Quantitative Analysis of

Core-Shell Nanoparticle Catalysts by

Scanning Transmission Electron Microscopy

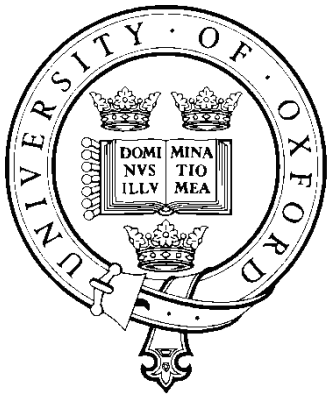

Haibo E

Corpus Christi College

University of Oxford

A thesis submitted for the degree of

Doctor of Philosophy

Hilary 2013

Abstract

Quantitative Analysis of Core-Shell Nanoparticle Catalysts by Scanning Transmission Electron Microscopy

H. E
Corpus Christi College
Thesis submitted for the degree of Doctor of Philosophy, Hilary Term 2013

This thesis concerns the application of aberration corrected scanning transmission electron microscopy (STEM) to the quantitative analysis of industrial Pd-Pt core-shell catalyst nanoparticles. High angle annular dark field imaging (HAADF), an incoherent imaging mode, is used to determine particle size distribution and particle morphology of various particle designs with differing amounts of Pt coverage. The limitations to imaging, discrete tomography and spectral analysis imposed by the sample's sensitivity to the beam are also explored.

Since scattered intensity in HAADF is strongly dependent on both thickness and composition, determining the three dimensional structure of a particle and its bimetallic composition in each atomic column requires further analysis. A quantitative method was developed to interpret single images, obtained from commercially available microscopes, by analysis of the cross sections of HAADF scattering from individual atomic columns. This technique uses thorough detector calibrations and full dynamical simulations in order to allow comparison between experimentally measured *cross section* to simulated ones and is shown to be robust to many experimental parameters. Potential difficulties in its applications are discussed. The cross section approach is tested on model materials before applying it to the identification of column compositions of core-shell nanoparticles.

Energy dispersive X-ray analysis is then used to provide compositional sensitivity. The potential sources of error are discussed and steps towards optimisation of experimental parameters presented. Finally, a combination of HAADF cross section analysis and EDX spectrum imaging is used to investigate the core-shell nanoparticles and the results are correlated to findings regarding structure and catalyst activity from other techniques.

The results show that analysis by cross section combined with EDX spectrum mapping shows great promise in elucidating the atom-by-atom composition of individual columns in a core-shell nanoparticle. However, there is a clear need for further investigation to solve the thickness / composition dualism.

List of Publications

Some of the work contained in this thesis has been published elsewhere in peer reviewed journals and conference proceedings. A list of these publications is given here.

Peer Reviewed Journal Articles

H. E, K. E. MacArthur, T. J. Pennycook, E. Okunishi, A. J. D'Alfonso, N. R. Lugg, L. J. Allen and P. D. Nellist, *Probe integrated scattering cross sections in the analysis of atomic resolution HAADF STEM images* Ultramicroscopy, (2013) *Accepted*

Conference Proceedings

H E, P D Nellist, A J D'Alfonso and L J Allen, *Quantitative techniques for aberration corrected HAADF STEM of nano-materials*, Journal of Physics: Conference Series, vol. 371, 012054 (2012)

H E, P D Nellist, S Lozano-Perez and D Ozkaya, *Quantitative analysis of core-shell catalyst nanoparticles for industrial applications*, Journal of Physics: Conference Series, vol. 371, 012027 (2012)

H E, P D Nellist, S Lozano-Perez and D Ozkaya, *Towards quantitative analysis of core-shell catalyst nano-particles by aberration corrected high angle annular dark field STEM and EDX*, Journal of Physics: Conference Series, vol. 241, 012067 (2010)

Published Abstracts

H E, P D Nellist, S Lozano-Perez , D Ozkaya, A J D'Alfonso and L J Allen *Quantitative Analysis of HAADF-STEM Images of Core-Shell Nanoparticles*, Proc 17th International Microscopy Congress (IMC), Rio de Janeiro, Brazil (2010)

Acknowledgements

I have been fortunate to work with and learn from a great number of eminent people during the course of my time in Oxford. I could not have completed this work without their help.

First and foremost, I would like to thank my supervisors. I am grateful to the indefatigable Pete Nellist, not only for the many hours he has spent patiently teaching me to be a better scientist: editing posters, presentations and papers, discussing ideas, promoting my curiosity and sanding down the rough edges, but also his understanding and support in the challenges outside of work. His wisdom and guidance and wit have been invaluable. I am grateful to Sergio Lozano-Perez for sharing his expertise, his kindness and his continual support; he has always miraculously found time for me while juggling many commitments. I am grateful to Dogan Ozkaya for his guidance, not only in science but also everything else in life. His frankness, enthusiasm and unwavering humour have been sources of both sober reflection and inspiration. I could not have wished for a better triumvirate.

I would like to thank Les Allen and Adrian D'Alfonso for their help with the simulation work and mathematics. Their attention to detail and "getting it right" is unparalleled; collaborating with them has been a privilege and honour. My thanks also go to Eiji Okunishi and Tim Pennycook for their contributions to the microscopy and Katherine MacArthur and, in particular, Lewys Jones for their contributions to the whole project.

Andrea Russell and her group in Southampton have kindly furnished me with many samples and extensive knowledge about catalysts and X-ray techniques. Thanks to Anna Wise and Beatrice Tessier in particular for their work. The kind people at Johnson Matthey Technology Centre who have shared their insights, knowledge and biscuits with me, in particular: Sarah Ball, Greg Goodlet, Sarennah Longworth-Cook, and Steve Spratt, thank you. My colleagues in Oxford have given me many hours of support, humour and fruitful discussions: Valeria Nicolosi, Peng Wang, Rebecca Nichols, Juan Lozano, Gavin Behan, Eireann Cosgriff, Fang Li, Aleksey Shmeliov, George Theodossiou, Jack

Severs, Gareth Hughes, Karleen Dudeck, Ron Doole, Neil Young, Judy Kim, Lionel Gontard and Steve Lett. The list is long but distinguished.

I would like to acknowledge the financial support of the EPSRC and Johnson Matthey and also the Department of Materials at the University of Oxford. Corpus Christi College have also been generous in their financial support for travelling to far-flung, beach-ridden conferences.

Finally, I am indebted to my family and my friends for my health and happiness. To those people who have helped me through a challenging and amazing journey, I would like to offer my heartfelt gratitude for your friendship: Julia Kleindienst*, Filip Jejina, Felix Day*, Becca Darley*, Anna Ferrari, Tree Roberts*, Marek Buchman*, Tadas Zgirskis, Andy Stewart*, Seb Farquhar, Marja Verbon, Karolina Wartolowska*, Judith Robinson, Annemari Ferreira*, Louise Bartelt, Arnaud Debauge, Jono Lain, Chris Foster and all the others who have kept me smiling and laughing and well fed. Those* in particular who have helped to read and helped me to edit this thesis; your attention to detail is impressive and your time and efforts are greatly appreciated.

I dedicate this thesis to my parents; I could not have been more blessed with two people who have such strength of character and kindness. I am, every day, grateful for their unwavering support, their love for and belief in me

"It is not the critic who counts; not the man who points out how the strong man stumbles, or where the doer of deeds could have done them better. The credit belongs to the man who is actually in the arena, whose face is marred by dust and sweat and blood; who strives valiantly; who errs, who comes short again and again, because there is no effort without error and shortcoming; but who does actually strive to do the deeds; who knows great enthusiasms, the great devotions; who spends himself in a worthy cause; who at the best knows in the end the triumph of high achievement, and who at the worst, if he fails, at least fails while daring greatly, so that his place shall never be with those cold and timid souls who neither know victory nor defeat."

- Theodore Roosevelt, Paris April 1910

"Oh come on, don't be as negative as an electron!"

"Not everything that counts can be counted and not everything that can be counted counts."

(Sign hanging in Albert Einstein's office at Princeton)

"心底无私天地宽"

Contents

Outline

Chapter 1 provides an overview of the motivation for the work. Important concepts in heterogeneous catalysis are presented, along with the questions that govern the understanding of their functionality. Methods for analysis of catalysts, in particular nanoparticles, are discussed. Preliminary work is carried out with conventional electron microscopy techniques, which are shown to be inadequate for answering the questions posed.

In Chapter 2, scanning transmission electron microscopy (STEM) is introduced and the suitability of aberration corrected high angle annular dark field (HAADF) STEM for imaging this system is described. Energy dispersive X-ray (EDX) analysis is introduced and posited as a complementary technique to HAADF STEM.

In Chapter 3, HAADF imaging is used to determine the size distributions and structure of core shell nanoparticles of various designs for the first time. The results are compared with those obtained from X-ray methods and electrochemical tests and shown to give novel insights into the deposition of Pt on the Pd core. The problem of nanoparticle stability is investigated and the potential damage mechanisms discussed in light of those that might limit the usefulness of characterisation by electron microscopy. Pushing the spatial resolution, the first atomic resolution images of this system is presented. Qualitative conclusions are drawn from the scattering intensity and an attempt is made to extract information about the 3D morphology of nanoparticles and shell coverage.

Chapter 4 contains a discussion of the drive towards atomic scale quantification. The novel technique necessary to perform quantitative HAADF STEM imaging on a factory standard microscope is described. The various experimental considerations to control and account for sources of error are presented. Finally, theoretical basis for the simulation of electron microscopy images is described.

Chapter 5 presents the novel concept of absolute probe integrated HAADF scattering cross sections, which is a robust measure of atomic resolution intensity. The theoretical framework is newly derived and the validity of the various assumptions is tested with simulations. Factors affecting the interpretability of the signal are discussed. As a proof of principle, cross section analysis is applied to identification of single isolated atoms a model sample of a 2D layered material, MoS_2, to demonstrate

its practical usage. A library of cross sections for Pd/Pt core shell nanoparticles is compiled for use in later work.

Chapter 6 presents novel approach of cross section analysis applied to atomic resolution HAADF STEM images of core-shell nanoparticles. The various limitations to atom-by-atom compositional sensitivity due to experimental uncertainties are discussed. A particle is imaged at two tilts in order to attempt discrete tomography, but is hampered by sample stability.

In Chapter 7, focus is turned to EDX analysis, which aims to shed further light on the compositional variation in core-shell nanoparticles. The limitations and difficulties of obtaining good spectra from small particles are discussed and suggestions made for optimisations.

In Chapter 8, the techniques in the previous chapters are brought together to show the application of HAADF cross section analysis coupled with EDX mapping. Key questions about the morphology and shell coverage of catalysts of different designs are addressed, as well as the effects of fuel cell cycling.

The author's conclusions and suggests for future work are given in the Chapter 9.

Declaration

The work presented in this thesis is entirely my own, except for the assistance and collaborative work mentioned in the text. I declare that the work in this dissertation has not been previously submitted for examination for a degree to this or any other university and that it is less than 40,000 words, excluding tables, bibliographies and appendices.

Chapter 1

Introduction

1.1 Motivation and Aims

The research in this thesis examines the application of aberration corrected scanning transmission electron microscopy to core-shell nanoparticles for heterogeneous catalyst applications. Where the core is a base metal and the shell is a precious metal, the design offers more efficient precious metal usage and also improved catalyst functionalities. Characterisation of the size, shape and shell coverage of individual particles is vital to understanding their catalytic properties and thus to the design of more effective catalysts.

Conventional microscopy techniques are sufficient for the identification of size and shape, but mapping short range compositional variations, as could comprise a shell structure, in such nanoparticles is extremely challenging and beyond the scope of all but the most advanced microscopes. The development of spherical aberration correction, and the resultant reduction in probe size and increase in probe current, has opened the door to routine high spatial resolution imaging and potentially also to elemental maps of nanoparticles. With these smaller, brighter probes, the possibility of atomic resolution, column-by-column composition identification appears, tantalisingly, within reach.

The research carried out aims to investigate the factors that affect the materials questions that govern effective catalysis. On the medium resolution level, particle size distribution is investigated between different designs and pre- and post-cycling. Also, the morphology of the particles is studied. With higher resolution, the surfaces are explored in terms of faceting, planes and steps. In terms of the shell

distribution, the variation in coverage is crucial to an understanding of the catalyst's efficacy. The possibility of extracting quantitative information and perhaps even atom-by-atom composition of individual columns in a particle is pursued.

In this chapter, the background of nanoparticle catalysis, particularly core-shell Pt-Pd nanoparticles, is explored. Initial characterisation by conventional techniques is then presented, highlighting the need for more advanced methods.

1.2 Catalysts

Coined by Jöns Jakob Berzelius in 1836 [1], a catalyst is a substance that enables a chemical reaction to occur faster than the corresponding un-catalysed reaction, without itself being consumed or chemically changed. Though a catalyst does not appear in the stochiometric equation for the overall reaction, it is nevertheless involved directly in the reaction. It acts to lower the heights of reaction activation barriers (See Figure 1.1) by providing alternative pathways for a part, or all, of the reaction. This allows industrially important reactions to occur at much lower temperatures.

Despite their wide use[1], very little of how catalysts work is understood. A major aim of the current research in the field is to understand the relation between structure and function.

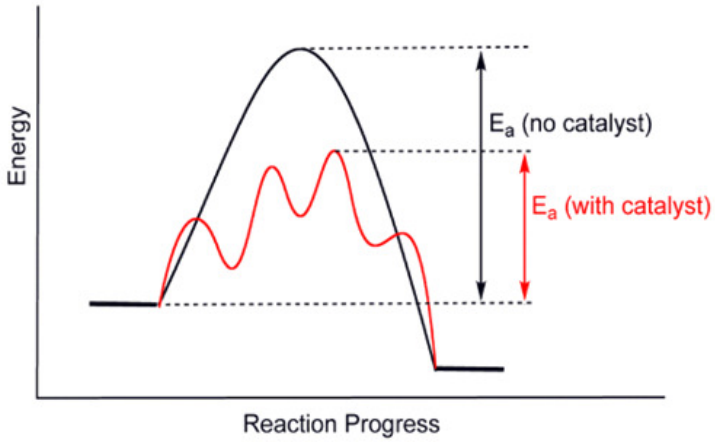

Figure 1.1 A catalyst lowers the activation energy E_a of a reaction pathway by offering an alternative pathway.

[1] 75% of all chemicals are produced industrially with the aid of catalysts. This figure is over 90% in newly developed processes[70].

Catalysis, important to industrial applications, can be categorised into two main types: heterogeneous and homogeneous. Most industrial catalysts are heterogeneous; they are typically solids that act in a different phase to their reactants. In industry, these nano-particles of catalysts are commonly fixed on an inert support and exposed to catalysis medium. [2].

Two main factors are important in the efficacy of a catalyst [3]:

- *activity* of a catalyst is the reaction rate per unit area of active surface
- *selectivity* is the rate of formation of a desired product with respect the overall conversion of the initial reactants.

Both dynamical properties are important in the design and synthesis of an economical and effective catalyst. Historically catalysts were found by empirical methods and improved through a process of trial and error. Even small changes in the sample preparation route can produce a significant change in the catalytic response [4] making their behaviour difficult to predict.

In heterogeneous catalysis most of the actual reaction mechanisms are not yet fully understood. The reactant molecules are thought to adsorb to the catalyst surface at certain sites, known as 'active sites'[5]. Doing so weakens or breaks bonds within the molecules causing the reaction to occur more readily. Since the reactions happen at the surface of the catalyst, the most obvious step towards increasing activity is to increase the surface area exposed by using small particles [6].

This surface based mechanism lends itself to utilising the large surface area offered by nanoparticles [6]. On these small nanoparticle crystals, the surface typically comprises of flat planes of atoms, steps and sometimes missing atoms. However, it is well known that only certain planar surfaces provide active sites for certain species. Other orientations may enhance (promote) the reaction of undesired products, or may even be completely inactive. The availability of active sites for specific reactions is vital in the efficacy of a catalyst in both activity and selectivity.

A plethora of parameters can affect a nanoparticle's catalytic performance: ranging from the seed crystal[2] [7], particle size and shape, local surface composition, chemical bonding, support material and particle-support interactions, surface structure. All these parameters are subject to change during the processes of synthesis, use and subsequent catalyst regeneration[3] [8]. Catalyst particles are normally dispersed on a porous and inert substrate, often an oxide. The presence of strong particle-support interactions have been demonstrated [9]; changing the support produces widely varying activities and selectivities.

1.3 Platinum group metal catalysts

The platinum group metals (PGMs) are six transition metals clustered together in the periodic table with similar physical and chemical properties: high melting points, extreme corrosion resistance, oxidation and reduction properties [10].

For these assets, they are still one of the most important sets of catalysts, despite their high cost (see Table 1.1). They are vital for accelerating fundamental reactions such as oxidation, dehydrogenation and isomerisation, which make up in total 25% of global industry output [2] and are still used because there is no comparable alternative.

Metal		Atomic number	Price ($/100g pure)
Ruthenium	Ru	44	1,400
Rhodium	Rh	45	13,000
Palladium	Pd	46	5,833
Osmium	Os	76	7,700
Iridium	Ir	77	4,200
Platinum	Pt	78	13,000

Table 1.1 Cost of pure platinum group metals, as indicated by www.chemicool.com in Feb 2013. The cost of Pt and Rh are significantly higher than the other PGMs and include the cost of purification from bulk.

[2] A seed crystal is the nanoparticle used to initiate the growth of a nanostructure.
[3] Regeneration is the process whereby the catalyst is heated in a clean environment in order to burn off contaminants and dirt that have built up on the surface during use and which are inhibiting catalytic activity, or 'poisoning' the catalyst.

1.3.1 Application to proton exchange membrane fuel cells

Platinum-based catalysts are particularly high profile for their applications to catalytic converters and fuel cells [11]. Much attention has been given to alternative energies and greener fuels in recent years due to the increasing awareness of the fuel crisis and climate change problems [12]. Proton exchange membrane fuel cells (PEMFC[4]) represent one of the most readily viable solutions and alternatives to the combustion engine. As an electrical power source, it is an alternative energy source to traditional fossil fuels and further benefits the environment by being zero-emission [13].

The fuel cell was first demonstrated in 1839 by Sir William Grove [14,15] and the catalyst for this reaction has not changed since the 19th century, since Pt is still the most stable under the corrosive environment of the low-temperature fuel cell [13]. PEMFCs rely on platinum in the form of nanoparticles supported or embedded in porous carbonaceous support to catalyse the reactions at both the anode and cathode (See Figure 1.2) so that they can proceed at sufficiently low operating temperatures to allow industrial usage. Typically, nanoparticles and the support are designed to maximise the surface area of platinum available to the gases that form the reaction.

At the negative anode, hydrogen is oxidised, separating the proton (as an H^+ ion) from the electron.

$$H_2 \rightarrow 2H^+ + 2e^- \qquad 1.1$$

The electron is blocked by the membrane and carried to the external circuit (where it can be utilised, for example, to turn a motor) and then rejoins the cathode side of the fuel cell. The proton migrates through the membrane directly to the cathode. At the cathode, oxygen from the air is reduced and combines with the H+ ion to produce water.

$$O_2 + 4H^+ + 4e^- \rightarrow 2H_2O \qquad 1.2$$

The catalyst is particularly essential at the cathode to prevent the reduction of the O_2 to hydrogen peroxide, the other energetically favourable reaction [16] as H_2O_2 can dissolve the membrane and cause the fuel cell to fail. The desired reaction at the cathode is net exothermic and produces a potential of about 1.2V [17] and so several fuel cells can be combined to form a stack.

[4] Alternatively called polymer electrolyte membrane

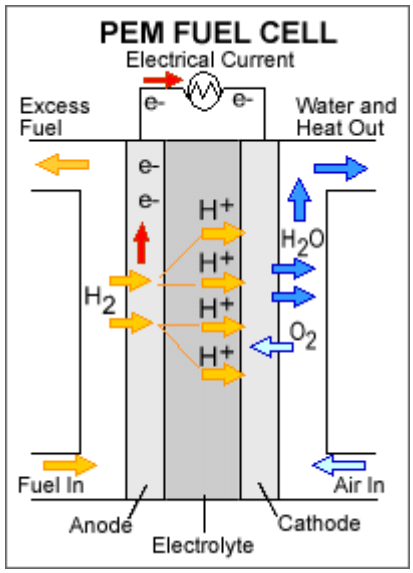

Figure 1.2 Schematic of PEM fuel cell[5].

However, there is a significant difference between the performance of a cell and the theoretical cell voltage due to the activation of the cathode catalyst and the slow kinetics of the oxygen reduction reaction (ORR) [11].

Currently, the major factor inhibiting commercial use of the fuel cell is the lack of an alternative, more economical catalyst. The expense of platinum and the cost of loading the fuel cell with sufficient material to achieve the necessary reaction rates are still prohibitive for large scale production. The total content of PGMs in these fuels cells has decreased by more than 80% since 2005, chiefly by improvements in nanoparticle design [18]. However, the best Pt activity is only a third[6] of the target defined by the US Department of Energy in order to represent a realistic alternative to the internal combustion engine [11]. Thus the major drive in catalytic design is to increase the activity at least three fold, so that one third as much Pt is needed.

[5] Image reproduced from http://www1.eere.energy.gov/hydrogenandfuelcells/fuelcells/fc_types.html
[6] 0.15 A/mg Pt at 900mV, 80°C, 150kPa$_{abs}$ O_2 compared to the target 0.44 A/mg Pt

1.4 Improvements to catalyst design

To achieve economical Pt loadings, either a higher reaction mass activity for Pt-based catalysts or better utilization of the precious metals is needed. As a further complicating issue, small amounts (ppm) of CO in H_2 poisons the catalyst surface severely [17], blocking the desired catalysed pathway and reducing the activity of the catalyst.

Pt-based alloys, such as PtCo and PtSn, have been shown to be more tolerant of poisoning [19,20]. In addition, some alloys of PtCo also show enhanced activity due to the modified electronic structure at the surface of the catalyst [21].

1.4.1 Surface adsorption and active sites

Understanding the location and formation of active sites on catalysts surfaces [22,23] and the surface adsorption mechanisms of the reactant species is the key to understanding the factors that govern selectivity and activity.

Early studies by [24] were performed by applying a combination of chemisorptions and Low Energy Electron Diffraction (LEED) to extended surfaces. Chemisorption of oxygen was observed not to occur on low Miller Index planes of Pt, but readily on remarkably thermally stable low index (111) and (100) terraces of constant width, linked by steps of monatomic height. Hydrogen also showed preferential adsorption at steps but only adsorbed on flat surfaces at temperatures in excess of 1000K.

Scanning probe techniques combined with density functional theory (DFT) calculations have been used to confirm the importance of steps and kinks. The tops of monatomic steps have been identified as the most reactive sites for O_2 dissociation on Pt (111) [25,26]. In addition, stepped structures on platinum-group metals have been shown theoretically to be crucial for both the activity and the selectivity of NO reduction to N_2, by increasing the strength of bonds to NO, N and O [27]. Problematically steps have also been shown experimentally and theoretically to be the most reactive sites for the oxidation of CO on Pt [19,22,26], an active poison for the catalyst.

1.4.2 Size effects

Since catalytic reactions happen at the surface of the catalyst, metal in the bulk that is not exposed to the reactant gasses is essentially wasted. Decreasing the size of PGM particles increases the surface area to volume ratio and thus decreases the amount of precious metal needed for the same activity.

However, as the size of catalyst particles decreases, "size effects" lead to anomalous behaviour not seen in the bulk material due to the large proportion of surface atoms and the increased surface free energy. In a bulk material these surface atoms are negligible to the calculations of free energy but at the nanometre scale they have a larger impact to both the structure and properties of the material and can lead to, for example, contraction of the lattice [28,29] and structural instabilities, as thermodynamics dictates a driving force to minimise the high surface energy.

Small particles of face-centred cubic metals can adopt complex structures based on twinned subunits, which minimise the surface energy [7,30,31]. Small particles have also been seen to exhibit a depression of melting temperature; this can be seen to significantly drop off below a particle diameter of 20nm [32]. This information led to a study on the melting and structural rearranging of particles under the electron beam [33,34] in high kV microscopes. The effect can be reduced if the particles are encased with surfactants [35], though this would be detrimental to the catalytic properties.

1.5 Core-shell heterogeneous catalysts

Recently, much attention has been given to core-shell structures in which a base metal core is surrounded by a catalyst metal shell. These structures offer even more efficient use of precious metals than just reduction of size, since the expensive precious metal only comprises a thin shell around a cheaper core. They have also been seen to show increased activity and selectivity[36–40] and reduction of the poisoning effects from adsorption of unwanted species [41]. Typically, the coverage is described by the number of monolayers that cover the surface, where one monolayer is a complete coverage of the surface by a shell of one atom thick (see Figure 1.3).

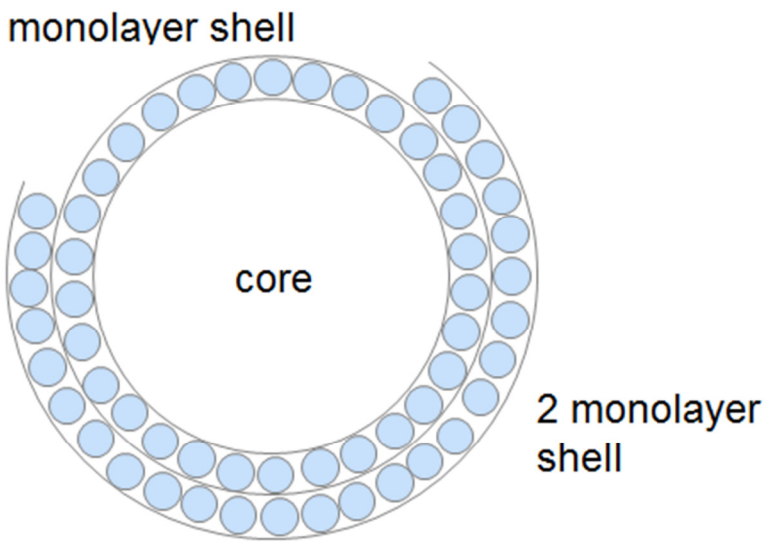

Figure 1.3 A monolayer (ML) shell is one where a single layer of shell atoms (blue) covers the surface of the core. Two monolayers is a coverage of the core's surface with two atomic layers of the shell.

Ru-Pt core-shell nanoparticles have been shown to exhibit an increased activity for oxidation of CO and at lower temperatures than RuPt alloys and pure Pt particles [42]. DFT calculations showed that this was due to an increased availability of CO-free Pt surface sites and a hydrogen-mediated low temperature CO oxidation process.

To improve the efficacy of the Pt catalyst in the hydrogen fuel cell's ORR reaction, a Pd core is advantageous not only for the close lattice match of the two elements but has also been shown to increase the activity as well as the selectivity. In rotating disk measurements, core-shell structures of a monolayer shell of Pt over a Pd(111) face had the highest activity of the common core-shell structures (See Figure 1.4) [43] and a 1.5x improvement on pure Pt (111). Mixed monolayer of Pt and transition metal elements improved both mass-specific activity by 20 times over that of pure and also the stability during oxidation [44].

This improvement is attributed to the effect on the electronic structure of the surface metals due to the structure and alloying effects of the different core metal. The d-band centre of the metal is shown by DFT calculations to be correlated with the O_2 dissociative adsorption energy and thus the activity

towards the oxygen reduction reaction (ORR), which is the bottleneck for the effectiveness of the reaction [25].

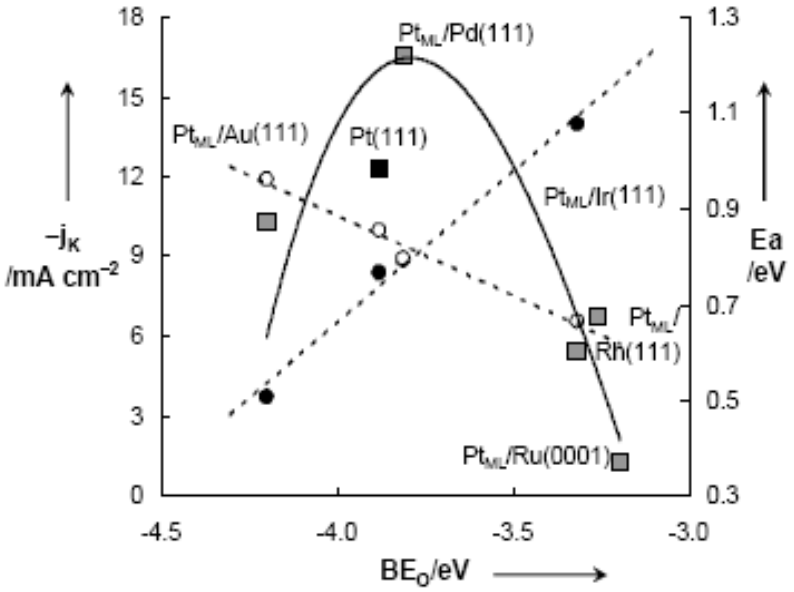

Figure 1.4 ORR activity (□), activation energies for O2 dissociation (o), activation energies for OH adsorption (o) for various Pt-based core-shell catalyst structures (adapted and reprinted with permission from [45])

To complicate matters, alloying at the core-shell boundaries has been seen as a function of decreasing particle size [46]. When core sizes fall below 4.6nm in diameter, Au and Ag are nearly randomly distributed within the particle. For larger particles, boundaries are maintained to within one monolayer. X-ray Absorption Fine Structure (XAFS) was used to deduce structural information. Though the technique averages over all of the X-ray excited from atoms in the entire sample, a large percentage of the atoms in the nanoparticles are at the interface, so the information obtained is sensitive to the bimetallic interfacial structure. However, this approximation does not give a very clear picture of what a typical structure would look like.

1.6 Methods of characterisation

The development of bimetallic heterogeneous catalysts has historically been achieved mainly through chemical intuition and empirical synthesis approaches. However, recent advances in analytical techniques [47] and first-principle calculations [48] have opened up the opportunity for more directed design.

It is clear that understanding the structure of nanoparticles is vital to explaining their catalytic behaviour; there is a need for accurate, local, high-resolution characterisation. With as few as 1 to 4 monolayers comprising the shell, core-shell nanoparticles are the most promising new development direction for efficient precious metal usage in catalysts and have been seen to give increased activity and selectivity. However, with such large compositional variations on a very short spatial scale, these particles present a challenge to characterisation.

Characterisation techniques for catalysts fall under two main categories:

- Averaging, bulk techniques give information about the whole system, including the support, across a statistically large number of particles. However, the flip side of this is that the information is averaged over the entire sample size and so no localised information can be acquired and explicit detail of individual structures not attainable. These include, amongst others:
    - cyclic-voltametry (CV)
    - X-ray photon spectroscopy (XPS)
    - extended X-ray absorption fine structure (EXAFS)
    - small angle X-ray spectroscopy (SAXS)
    - optical spectroscopy
- Higher resolution localised techniques give information about the specific atomic configuration of individual particles. Chief amongst these are:
    - scanning tunnelling microscopy (STM) and atom probe
    - scanning electron microscopy (SEM)
    - transmission electron microscopy (TEM)

  Some of these are highlighted here (for the others, see Appendix A)

1.6.1 Electrochemical techniques

Cyclic-voltammetry (CV) is an electrochemical test commonly used to probe the activity of a catalyst [1,49]. The potential of a working electrode, with the catalytic sample adsorbed onto the surface, is swept back and forth between two voltages and the current measured to determine the electrode's voltage-current characteristics and thus the redox processes happening at the electrode. The reverse current sweep can be used to establish how reversible any changes are, by comparing to the forward sweep.

1.6.2 X-ray photoelectron spectroscopy (XPS)

X-ray photoelectron spectroscopy (XPS) is a surface sensitive technique, useful for probing the first 10 atomic layers of a sample. This makes it ideally suited for determining the surfaces of catalysts and potential core-shell structures of larger particles on the order of 100nm [50]. However, smaller nanoparticles, where 10 layers comprise the whole particle, are beyond the scope of this technique. It can be used, together with inductively coupled plasma emission spectroscopy (ICP-ES, see Appendix A.2), as an initial screening to detect if there is an average core shell structure for larger particles. However, spatial resolution is in practice limited to the scale of microns.

1.6.3 X-ray characterisation (XRD, EXAFS, WAXS, SAXS, ASAXS)

Powder X-ray diffraction (XRD) is the most accessible X-ray technique because of its rapid, non-destructive analysis of complex multi-component samples without the need for extensive sample preparation. Every possible crystal orientation is represented in the sample so the orientation averaging results in the diffraction space to act as a single crystal. It is used to obtain various phases that may be present in the nano particles as well as providing average crystallite size in a sample. It is however not straightforward to study core-shell using XRD since there is no direct information about the surfaces.

Extended X-ray absorption fine structure (EXAFS) [51] provides information on local atomic co-ordination structure and bonding within the material [52]. The identity of, number of and distance to neighbouring atoms of individual atoms can be found, averaged over the whole sample. This is

frequently used to determine whether or not multiple element particles are random alloys or show a higher degree of order, for example core-shell structures. They are also very suited to studying the catalysts in-situ, since an electrochemical cell can be made up to sit in the beam line [53].

Wide angle X-ray scattering (WAXS) can be used to determine the nature of the crystal structure, its lattice parameter, crystallite size and the different phases present, whether amorphous or crystalline [54]. Small angle X-ray scattering (SAXS) can further be used to determine information about the size and shape of a sample, as well as the polydispersity [55]. Anomalous SAXS (ASAXS) can also provide element specific information on top of SAXS insights [56].

1.7 Electron microscopy (EM)

Electron microscopy is the chief characterisation technique that can be used to provide chemical *and* physical information about individual components of a nanoparticle [57] and is often the one of choice in research in industry. It has been used extensively for examining nanoparticle sizes, positions, morphologies and compositions [see for example 64,65].

The electron's short wavelength makes it more capable of observing objects at the nanometre scale. The fundamental deBroglie relation of the wavelength λ to the particle's momentum:

$$\lambda = \frac{h}{p} \tag{1.3}$$

can be written for relativistic fast electrons accelerated by a potential V as:

$$\lambda = \frac{h}{\left[2m_e eV\left(\frac{1+eV}{2m_e c^2}\right)\right]^{\frac{1}{2}}} \tag{1.4}$$

where e is the charge on the electron and $m_e c^2$ is its rest energy, and h is Plank's constant. A sense of scale can be garnered by considering the wavelength of 3.7pm for an electron accelerated through a potential of 100keV.

1.7.1 Scanning electron microscopy (SEM)

SEM is often considered a technique for the study of bulk materials. Resolution is limited as it suffers from the problems of multiple scattering events and beam spreading effects within the specimen; a typical resolution in a 20kV SEM is 1.5 - 3.5nm [60].

With the development of in-lens detectors, the backscattered signal has been more effectively collected, enabling weakly scattering samples, such as nanoparticle catalysts, to be imaged. As a Rutherford like scattering process, this technique is particularly suited to the heavy PGM elements used for heterogeneous catalysis (see section 1.1.2).

The use of the secondary electron signal can also provide strong topographical information since only electrons typically within a few nanometers of the surface are able to escape. Recently, a number of scanning electron microscopes have had a secondary electron detectors fitted allowing simultaneous high resolution and secondary electron imaging. Secondary electron signals have been detected of Pt particles on a γ-alumina support [61] and Au-Pd particles on TiO_2 [51]

Small Pt-Pd core-shell particles, 3-10 nm in diameter, on the surface of a industrial carbon pallet, were observed in a Zeiss Ultra 55 SEM at Johnson Matthey Technology Centre. The secondary electron signal shows the presence of nanoparticles on the support (see Figure 1.5). The backscattered signal is a strongly chemically sensitive technique so it is possible to get a good idea of the distribution of particles on the composition of the surface of the support (see Figure 1.6), clearly distinct from the underlying support. By overlaying two images at a tilt difference of 2 degrees, coloured in cyan and red, it is possible to see the 3D relief of the structure in an anaglyph (see Figure 1.7).

These images are at the limits of the capabilities of conventional SEM. The inadequate source brightness contributes low signal to noise and the typically low accelerating voltage mean that there is not the resolution to image individual atomic sites. Further, the limit of resolution and contrast means that it is not possible to image core-shell structures.

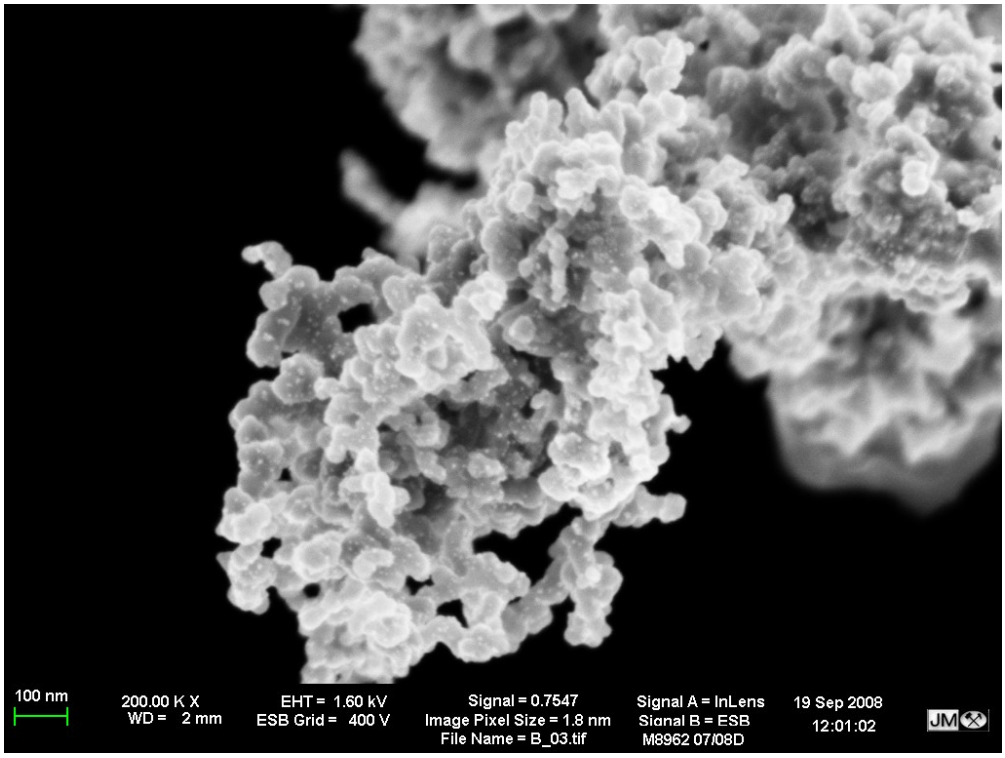

Figure 1.5 Secondary electron image of core-shell nanoparticles of Pt-Pd on industrial electroconductive carbon pallet (Ketjen) black taken by Zeiss Ultra 55 SEM with in-lens detector

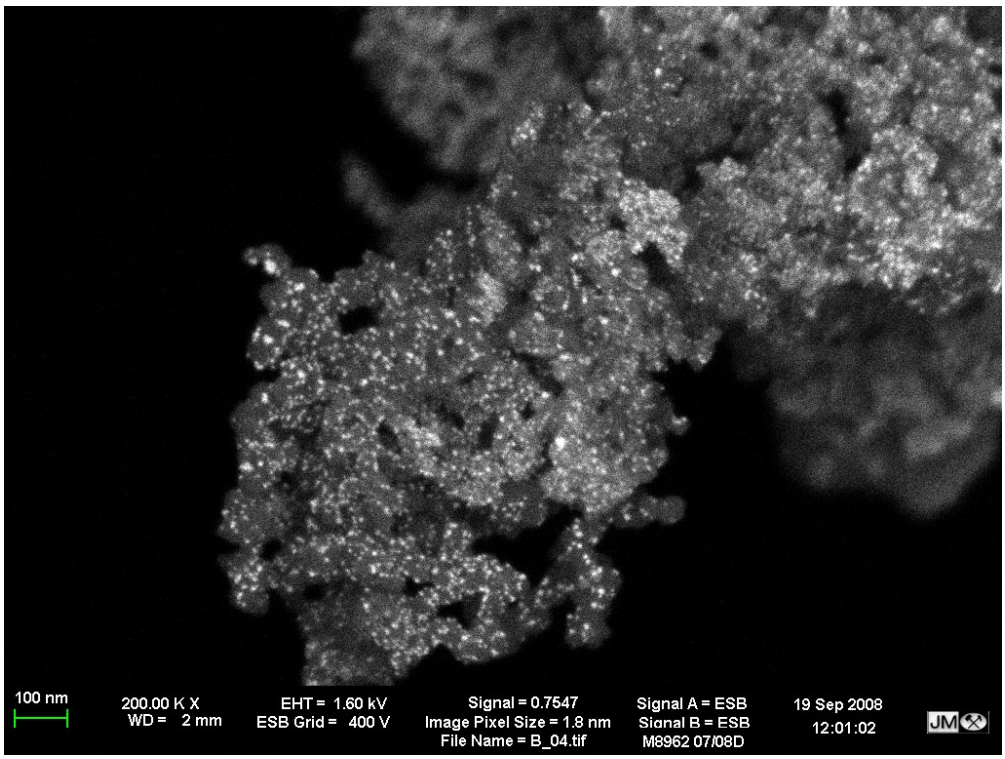

Figure 1.6 Backscattered electron image of the same area. The heavy Pt-Pd nanoparticles are easily visible due to the Rutherford like scattering mechanisms of BS-SEM.

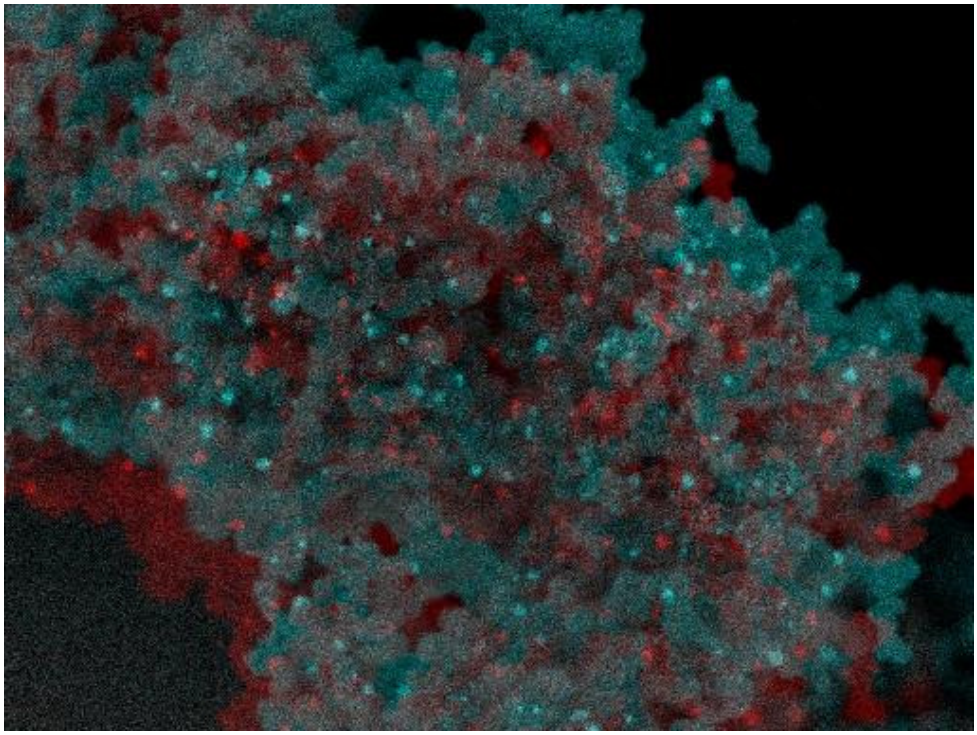

Figure 1.7 Backscattered SEM anaglyph (red/cyan stereograph). Two micrographs are recorded at a 2 degree tilt difference and false coloured red and cyan and displaced to create a pseudo—3D image when viewed through red/cyan filters.

1.7.2 Transmission electron microscopy (TEM)

Since the invention of the transmission electron microscope (TEM) by Ernst Ruska in 1939 (for a history of key milestones in EM see [62]), the technique has been widely applied to the imaging of catalyst [47].

Bright field (BF) conventional TEM imaging is suitable for recording images of catalyst nanoparticles when the particle density is not too high, scattering from the support material is weak or uniform, and atomic-resolution is not required. Investigations of similar core-shell nanoparticles to those in Figure 1.5 were carried out on an FEI Tecnai F20 with a super twin FEG at Johnson Matthey Technology Centre (see Figure 1.8). Though the resolution is much improved compared to SEM characterisation, it is still not possible to distinctly identify the core-shell structure.

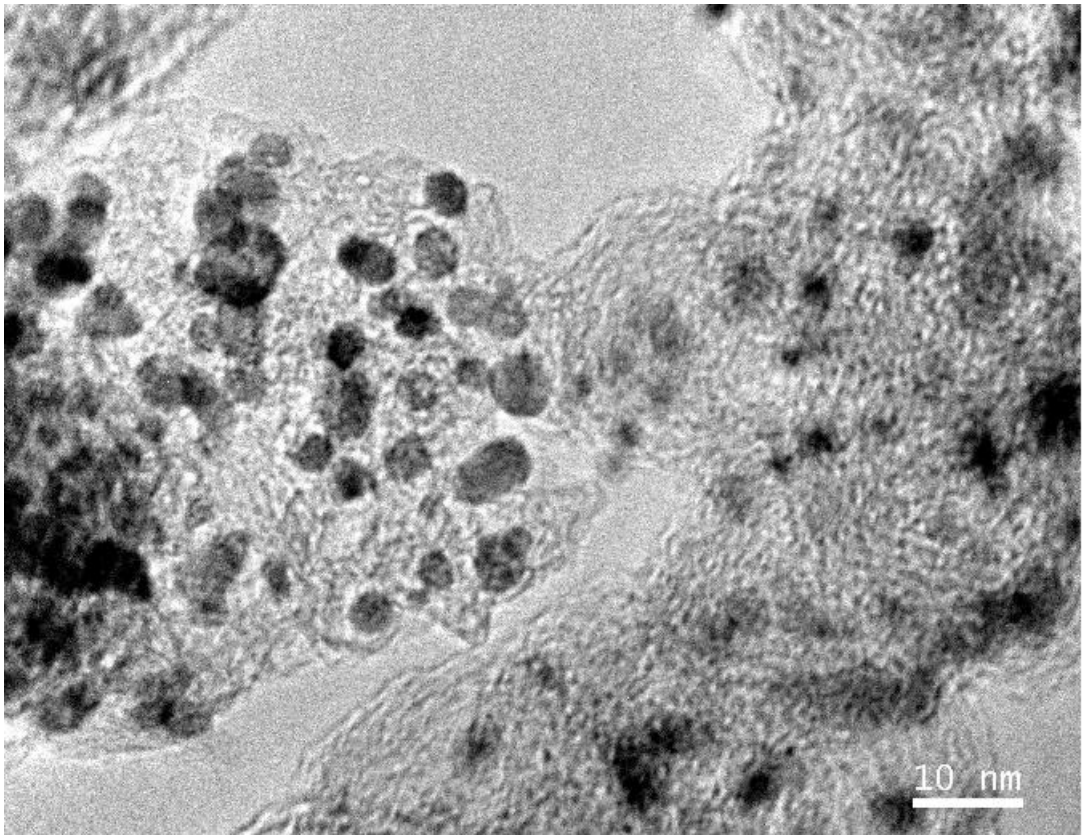

Figure 1.8 Bright field TEM image of Pt-Pd core shell nanoparticle on industrial carbon black taken using a FEI Tecnai F20 super twin field emission S/TEM. It is possible to see the individual nanoparticles but diffraction contrast from individual particles makes it difficult to observe core shell structure. There is no clear indication of core-shell structure and intensity is difficult to interpret. While particle size analysis is possible, structural detail is difficult to obtain as atomic resolution is not achieved.

An image created using a diffracted beam is a dark field (DF) image. Single-beam DF imaging can offer advantages over BF imaging for detecting small particles and assessing their structure and shape [63]. The overall intensity in a DF image is generally lower than in a BF image, but the corollary of low intensity is high contrast. A DF image also shows only certain crystal domains. As a result, although the detectability of particles is improved in a DF image, not all particles in the field of view are imaged.

Historically, high resolution TEM (HRTEM) has been a major contributor to the characterization of nanoscale particles and their supports [33,35], and real-time high-resolution studies of Pt crystals have been used to image dynamic events, including crystal growth, coalescence and atom displacement induced by the electron beam [34].

Conventional HRTEM relies on coherent interference to form a phase contrast image. The contrast transfer function of the microscope contains many oscillations, which lead to contrast reversals and lateral delocalisation of the information in the image with thickness and defocus. Though it has been shown that delocalisation can be useful in giving qualitative information about the orientation of the particle and also quantitative information about the absolute defocus value, it is still a limiting factor when it comes to image interpretation [64].

With supported particles the information from the support and the nanoparticles will overlap producing Moiré type fringes which do not necessarily represent lattice information. Fuel cell nanoparticles are supported on a conducting and theoretically amorphous carbon support, but there will always be areas with some graphitisation which will confuse the image. Model catalysts of metallic nanoparticles on spherical or cubic supports mitigate this problem [57] but are one further step away from understanding industrially relevant catalysts.

Simulations are therefore generally required to relate experimental images to structural models. Focal series exit wave restoration can be used to calculate the three dimensional structure of Pt nanoparticles [65,66], showing surface features such as steps, step vacancies and kinks (See Figure 1.9 and section 3.1 for more discussion).

Charge-couple device (CCD) cameras are often employed in HRTEM, requiring corrections for noise and the CCD response function [67]. Another unresolved issue that further encumbers quantitative interpretation of HRTEM images is the fact that image contrast in transmission electron microscopy is typically approximately three times lower than theory would predict. The discrepancy is known as *Stobbs factor*, and is present for both crystalline and amorphous samples, as well as for both thin and thick samples. Good reviews on the topic are [68,69]. In addition, the image is not easily interpretable, especially in terms of chemical composition, without extensive simulations and a complementary spectroscopic technique.

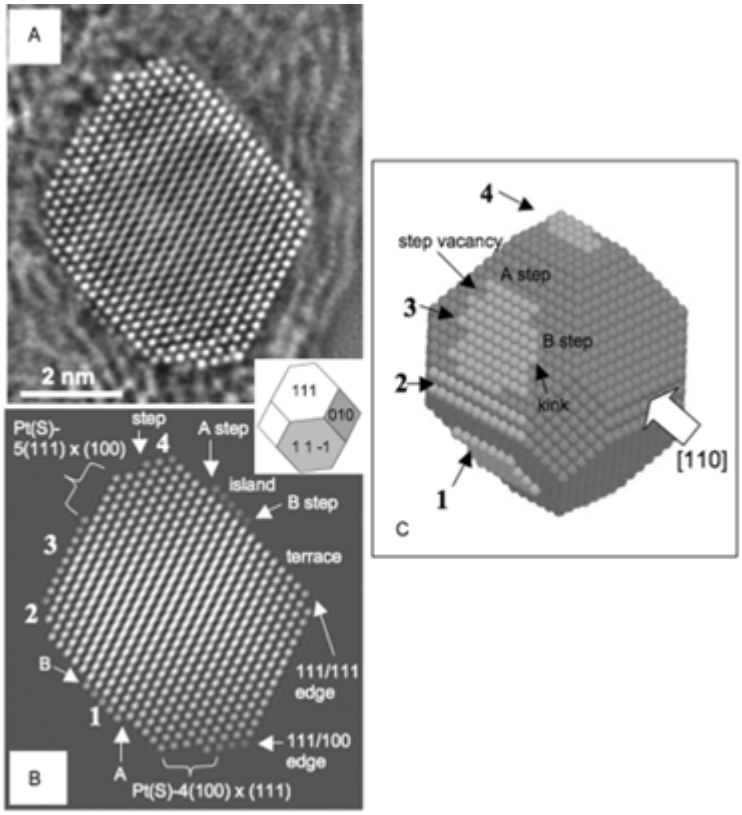

Figure 1.9 A) Restored phase of a 6-nm Pt particle obtained by applying spherical aberration correction and through-focus exit wavefunction restoration. **B)** Best-fitting simulated phase. **C)** Three-dimensional atomic model used to calculate the best-fitting phase in part (B). The large white arrow indicates the direction of the electron beam. The inset overlapping parts (A, B) shows the crystallographic details of the particle. In parts (B, C), 1-4 correspond to the same features on the surface of the particle. Steps and terraces are shown on the surface of the particle where the notation Pt(S)-n(xyz) x (uvw) refers to the micro-facets. n is the number of atoms in the terrace with Miller index (xyz) and (uvw) is the index of the step (Reprinted with permission from [66]).

1.8 Conclusions

Heterogeneous catalysts, specifically platinum group metal core-shell nanoparticles for fuel cell applications are an increasingly important material as effective catalysis for fuel cells. Core-shell interaction gives rise to increased activity and selectivity. Understanding and thus improving the performance of the catalysts requires not only a thorough understanding of the structure and morphology of the nanoparticles but also the location and extent of the shell coverage.

The spatial resolution limits of methods such as electrochemical and bulk averaging characterisation require alternate techniques to give specific, local information about structure and shell coverage. Initial investigations of Pd-Pt core-shell nanoparticles with conventional microscopy techniques show that SEM lacks the lateral resolution for atomic resolution detail and TEM has complicated image interpretability due to the phase contrast nature of image formation.

Aberration corrected HAADF STEM, the topic of the next chapter, is a more straight-forward technique. Utilising the recent improvements of electron optics to provide atomic resolution imaging and spectroscopy, atom-by-atom details of the surfaces of these PGM fuel cell nanoparticle catalysts can be achieved.

References

[1] B. Lindström, L. Pettersson, A brief history of catalysis, CatTech. 7 (2003) 130–138.

[2] C.H. Bartholomew, R.J. Farrauto, Fundamentals of Industrial Catalytic Processes, Wiley, 2005.

[3] P. Gai, E. Boyes, Advances in atomic resolution in situ environmental transmission electron microscopy and 1Å aberration corrected in situ electron microscopy, Microscopy Research and Technique. 72 (2009) 153–164.

[4] R.C. Tiruvalam, J.C. Pritchard, N. Dimitratos, J.A. Lopez-Sanchez, J.K. Edwards, A.F. Carley, et al., Aberration corrected analytical electron microscopy studies of sol-immobilized Au + Pd, Au{Pd} and Pd{Au} catalysts used for benzyl alcohol oxidation and hydrogen peroxide production, Faraday Discussions. 152 (2011) 63.

[5] H.S. Taylor, A Theory of the Catalytic Surface, Proc R Soc A. 108 (1925) 105–111.

[6] A. Datye, D. Smith, The Study of Heterogeneous Catalysts by High-Resolution Transmission Electron MicroscoDV, Catalysis Reviews. 34 (1992) 129–178.

[7] J. Elechiguerra, J. Reyes-Gasga, M. Yacaman, The role of twinning in shape evolution of anisotropic noble metal nanostructures, J. Mater. Chem. 16 (2006) 3906–3919.

[8] W. Zhou, I.E. Wachs, C.J. Kiely, Nanostructural and chemical characterization of supported metal oxide catalysts by aberration corrected analytical electron microscopy, Current Opinion in Solid State and Materials Science. 16 (2012) 10–22.

[9] A. Kulkarni, M. Chi, V. Ortalan, N.D. Browning, B.C. Gates, Atomic resolution of the structure of a metal-support interface: triosmium clusters on MgO(110)., Angewandte Chemie. 49 (2010) 10089–92.

[10] K. Hoppstock, B. Sures, Platinum Group Metals, Elements and Their Compounds. (2008).

[11] H.A. Gasteiger, S.S. Kocha, B. Sompalli, F.T. Wagner, Activity benchmarks and requirements for Pt, Pt-alloy, and non-Pt oxygen reduction catalysts for PEMFCs, Applied Catalysis B: Environmental. 56 (2005) 9–35.

[12] H. Liu, C. Song, L. Zhang, J. Zhang, H. Wang, D. Wilkinson, A review of anode catalysis in the direct methanol fuel cell, Journal of Power Sources. 155 (2006) 95–110.

[13] T.R. Ralph, M.P. Hogarth, Catalysis for Low Temperature Fuel Cells, Platinum Metals Review. 46 (2002) 3.

[14] R.W. Grove, On Voltaic Series and the Combination of Gases by Platinum, Philosophical Magazine and Journal of Science. XIV (1839) 127–130.

[15] R.W. Grove, On a Gaseous Voltaic Battery, Philosophical Magazine and Journal of Science. XXI (1842) 417–420.

[16] J. Rosenthal, D.G. Nocera, Role of proton-coupled electron transfer in O-O bond activation., Accounts of Chemical Research. 40 (2007) 543–53.

[17] G. Hoogers, D. Thompsett, The role of catalysis in proton exchange membrane fuel cell technology, CatTech. 3 (1999) 106.

[18] Fuel Cell Technologies Program, U.S. Department of Energy. (2011).

[19] P. Liu, A. Logadottir, J.K. Nørskov, Modeling the electro-oxidation of CO and H2/CO on Pt, Ru, PtRu and Pt3Sn, Electrochimica Acta. 48 (2003) 3731–3742.

[20] E.M. Crabb, R. Marshall, D. Thompsett, Carbon Monoxide Electro-oxidation Properties of Carbon-Supported PtSn Catalysts Prepared Using Surface Organometallic Chemistry, Journal of The Electrochemical Society. 147 (2000) 4440.

[21] V.R. Stamenkovic, B.S. Mun, M. Arenz, K.J.J. Mayrhofer, C.A. Lucas, G. Wang, et al., Trends in electrocatalysis on extended and nanoscale Pt-bimetallic alloy surfaces., Nature Materials. 6 (2007) 241–7.

[22] J. Yates, Surface chemistry at metallic step defect sites, Journal of Vacuum Science & Technology A. 13 (1995) 1359–1367.

[23] M. Yacamán, J.A. Ascencio, M.J. Yacamán, H.B. Liu, J. Gardea-Torresdey, Structure shape and stability of nanometric sized particles, Journal of Vacuum Science & Technology A. 19 (2001) 1091.

[24] B. Lang, R. Joyner, G. Somorjai, Low energy electron diffraction studies of high index crystal surfaces of platinum, Surface Science. 30 (1972) 440–453.

[25] P. Gambardella, Ž. Šljivananin, B. Hammer, Oxygen dissociation at Pt steps, Physical Review Letters. 87 (2001) 1–4.

[26] P.J. Feibelman, B. Hammer, J.K. Nørskov, F. Wagner, M. Scheffler, R. Stumpf, et al., The CO/Pt(111) Puzzle †, The Journal of Physical Chemistry B. 105 (2001) 4018–4025.

[27] Z. Liu, J. Wainright, M. Litt, R. Savinell, Study of the oxygen reduction reaction (ORR) at Pt interfaced with phosphoric acid doped polybenzimidazole at elevated temperature and low relative humidity, Electrochimica Acta. 51 (2006) 3914–3923.

[28] C. Solliard, M. Flueli, Surface stress and size effect on the lattice parameter in small particles of gold and platinum, Surface Science. 156 (1985) 487–494.

[29] W. Qi, M. Wang, Y. Su, Size effect on the lattice parameters of nanoparticles, Journal of Materials Science Letters. 2 (2002) 877 – 878.

[30] S. Ino, S. Ogawa, T. Taoka, H. Akahori, A Study of Multiply-Twinned Particles by 1000 kV Electron Microscope, Japanese Journal of Applied Physics. 11 (1972) 1859.

[31] K.E. MacArthur, N.P. Young, "Ex-Situ"Annealing and Structural Transformations in Gold Nanoparticles, Journal of Physics: Conference Series. 371 (2012) 12068–12072.

[32] P. Buffat, J.J.-P. Borel, Size effect on the melting temperature of gold particles, Physical Review A. 13 (1976) 2287–2298.

[33] L. Marks, D. Smith, Direct Atomic Imaging of Solid Surfaces II. Gold (111) Surfaces During and After in Situ Carbon Etching, Surface Science Letters. 143 (1984) 495–508.

[34] L.R. Wallenberg, J.-O. Bovin, A. Petford-Long, D. Smith, Atomic-resoultion Study of Structural Rearrangements in small platinum crystals, Ultramicroscopy. 20 (1986) 71–75.

[35] N. Long, R. Marzke, M. McKelvy, W. Glaunsinger, Characterization of Pt microcrystals using high resolution electron microscopy, Ultramicroscopy. 20 (1986) 15–20.

[36] R. Narayanan, M. a. El-Sayed, Shape-Dependent Catalytic Activity of Platinum Nanoparticles in Colloidal Solution, Nano Letters. 4 (2004) 1343–1348.

[37] S. Zhou, B. Varughese, B. Eichhorn, G. Jackson, K. McIlwrath, Pt-Cu core-shell and alloy nanoparticles for heterogeneous NO(x) reduction: anomalous stability and reactivity of a core-shell nanostructure., Angewandte Chemie (International Ed. in English). 44 (2005) 4539–43.

[38] M. Hu, K.P. Giapis, J. V. Goicochea, D. Poulikakos, Surface segregation of bimetallic alloys in nanoscale confinement, Applied Physics Letters. 97 (2010) 153107.

[39] J. Zhang, F.H.B. Lima, M.H. Shao, K. Sasaki, J.X. Wang, J. Hanson, et al., Platinum monolayer on nonnoble metal-noble metal core-shell nanoparticle electrocatalysts for O2 reduction., The Journal of Physical Chemistry. B. 109 (2005) 22701–4.

[40] D. Wang, H.L. Xin, R. Hovden, H. Wang, Y. Yu, D.A. Muller, et al., Structurally ordered intermetallic platinum-cobalt core-shell nanoparticles with enhanced activity and stability as oxygen reduction electrocatalysts., Nature Materials. 12 (2012) 81–87.

[41] C.J. Zhong, M.M. Maye, Core–Shell Assembled Nanoparticles as Catalysts, Advanced Materials. 13 (2001) 1507.

[42] S. Alayoglu, A.U. Nilekar, M. Mavrikakis, B. Eichhorn, Ru – Pt core – shell nanoparticles for preferential oxidation of carbon monoxide in hydrogen, Nature Materials. (2008) 333–338.

[43] J. Zhang, Y. Mo, M.B. Vukmirovic, R. Klie, K. Sasaki, R.R. Adzic, Platinum Monolayer Electrocatalysts for O 2 Reduction: Pt Monolayer on Pd(111) and on Carbon-Supported Pd Nanoparticles, The Journal of Physical Chemistry B. 108 (2004) 10955–10964.

[44] J. Zhang, M.B. Vukmirovic, K. Sasaki, A.U. Nilekar, M. Mavrikakis, R.R. Adzic, Mixed-metal Pt monolayer electrocatalysts for enhanced oxygen reduction kinetics., Journal of the American Chemical Society. 127 (2005) 12480–1.

[45] J. Zhang, M.B. Vukmirovic, Y. Xu, M. Mavrikakis, R.R. Adzic, Controlling the catalytic activity of platinum-monolayer electrocatalysts for oxygen reduction with different substrates., Angewandte Chemie (International Ed. in English). 44 (2005) 2132–5.

[46] T. Shibata, B.A. Bunker, Z. Zhang, D. Meisel, C.F. Vardeman, J.D. Gezelter, Spontaneous Alloying of Au−Ag Nanoparticles, Journal of the American Chemical Society. 124 (2002) 11989–11996.

[47] A. Datye, Electron microscopy of catalysts: recent achievements and future prospects, Journal of Catalysis. 216 (2003) 144–154.

[48] A. Hellman, E.J. Baerends, M. Biczysko, T. Bligaard, C.H. Christensen, D.C. Clary, et al., Predicting catalysis: understanding ammonia synthesis from first-principles calculations., The Journal of Physical Chemistry. B. 110 (2006) 17719–35.

[49] A.S.A. Khan, R. Ahmed, M.L. Mirza, Evaluation of Catalytic Activity of Pt and Pt-Ru Catalysts for Electro-oxidation of Methanol in Acid Medium by Cyclic Voltammetry, Portugaliae Electrochimica Acta. 27 (2009) 429–442.

[50] A.M. Venezia, X-ray photoelectron spectroscopy (XPS) for catalysts characterization, Catalysis Today. 77 (2003) 359–370.

[51] F. Krumeich, S. Marx, A. Baiker, R. Nesper, Characterization of AuPd Nanoparticles by Probe-Corrected Scanning Transmission Electron Microscopy and X-ray Absorption Spectroscopy, Zeitschrift Für Anorganische Und Allgemeine Chemie. 637 (2011) 875–881.

[52] R.F. Egerton, Electron energy-loss spectroscopy in the TEM, Reports on Progress in Physics. 72 (2009) 016502.

[53] A.E. Russell, B. Tessier, A. Wise, A. Rose, S.W. Price, P.W. Richardson, et al., In Situ XAS Studies of Core-Shell PEM Fuel Cell Catalysts: The Opportunities and Challenges, in: ECS Transactions, The Electrochemical Society, 2011: pp. 55–67.

[54] S. Alayoglu, P. Zavalij, B. Eichhorn, Q. Wang, A.I. Frenkel, P. Chupas, Structural and architectural evaluation of bimetallic nanoparticles: a case study of Pt-Ru core-shell and alloy nanoparticles., ACS Nano. 3 (2009) 3127–37.

[55] H. Borchert, E. V Shevchenko, A. Robert, I. Mekis, A. Kornowski, G. Grübel, et al., Determination of nanocrystal sizes: a comparison of TEM, SAXS, and XRD studies of highly monodisperse CoPt3 particles., Langmuir: The ACS Journal of Surfaces and Colloids. 21 (2005) 1931–6.

[56] G. Goerigk, H.-G. Haubold, O. Lyon, J.-P. Simon, Anomalous small-angle X-ray scattering in materials science, Journal of Applied Crystallography. 36 (2003) 425–429.

[57] A. Datye, A. Logan, K. Blankenburg, D. Smith, Characterization of surface structure in heterogeneous catalysts by high-resolution transmission electron microscopy, Ultramicroscopy. 34 (1990) 47–53.

[58] M. Yacamán, High resolution topographical images of small metal particles, Applied Physics Letters. 30 (1977) 359–360.

[59] J. Turkevich, J. Hillier, Electron microscopy of colloidal systems, Analytical Chemistry. 21 (1949) 475–485.

[60] D.C. Joy, Beam interactions, contrast and resolution in the SEM, Journal of Microscopy. 136 (1984) 241–258.

[61] J. Liu, J. Cowley, High-angle ADF and high-resolution SE imaging of supported catalyst clusters, Ultramicroscopy. 34 (1990) 119–128.

[62] F. Haguenau, P.W. Hawkes, J.L. Hutchison, B. Satiat-Jeunemaître, G.T. Simon, D.B. Williams, Key events in the history of electron microscopy., Microscopy and Microanalysis. 9 (2003) 96–138.

[63] N.R. Avery, J. V Sanders, The structure of metallic particles in dispersed catalysts, Journal of Catalysis. 18 (1970) 129–132.

[64] L.C. Gontard, R.E. Dunin-Borkowski, M.J. Hÿtch, D. Ozkaya, Delocalisation in images of Pt nanoparticles, Journal of Physics: Conference Series. 26 (2006) 292–295.

[65] L.C. Gontard, L.-Y. Chang, R.E. Dunin-Borkowski, a I. Kirkland, C.J.D. Hetherington, D. Ozkaya, The application of spherical aberration correction and focal series restoration to high-resolution images of platinum nanocatalyst particles, Journal of Physics: Conference Series. 26 (2006) 25–28.

[66] L.C. Gontard, L.-Y. Chang, C.J.D. Hetherington, A.I. Kirkland, D. Ozkaya, R.E. Dunin-Borkowski, Aberration-corrected imaging of active sites on industrial catalyst nanoparticles., Angewandte Chemie (International Ed. in English). 46 (2007) 3683–5.

[67] R.R. Meyer, J. Sloan, R. Dunin-Borkowski, Discrete Atom Imaging of One-Dimensional Crystals Formed Within Single-Walled Carbon Nanotubes, Science. 289 (2000) 1324–1326.

[68] M. Hÿtch, W.M. Stobbs, Quantitative comparison of high resolution TEM images with image simulations, Ultramicroscopy. 53 (1994) 191–203.

[69] A. Howie, Hunting the Stobbs factor., Ultramicroscopy. 98 (2004) 73–9.

[70] J. Hagen, Industrial Catalysis: A Practical Approach (Google eBook), John Wiley & Sons, 2006.

Chapter 2

Scanning transmission electron microscopy

An incident electron beam on a sample can interact with a sample in various ways to produce a multitude of signals (see Figure 2.1). In this section, we consider the signals that have been scattered by the sample and are collected in transmission: elastically and inelastically scattered and also characteristic X-rays.

The scanning transmission electron microscope (STEM) is discussed and some of the major landmarks in its development highlighted, especially with respect to catalyst nanoparticles. The image formation mechanisms are presented and the incoherent nature of HAADF STEM images discussed. The limitations to the achievable spatial resolution are described, along with the recent improvements due to aberration correction. Additionally, methods for obtaining three-dimensional structural information explored. The methods for obtaining chemical information are then presented, along with techniques to quantify the compositional ratios within a sample.

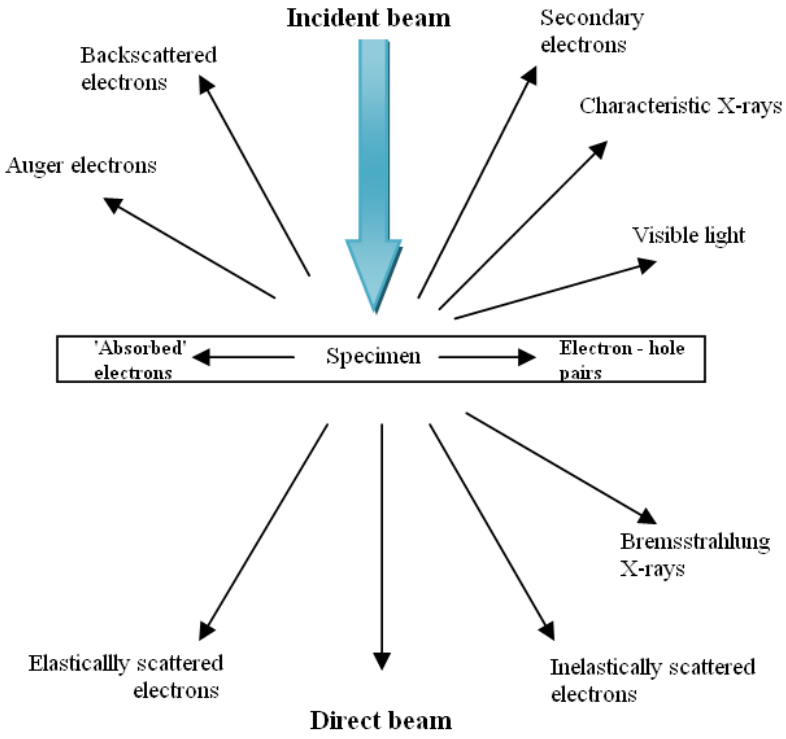

Figure 2.1 The various channels of scattering due to beam-sample interactions

2.1 The scanning transmission electron microscope

Although the design of the electron microscope is traditionally considered to originate with Knoll and Ruska's microscope [1], the scanning transmission electron microscope (STEM) was first designed and constructed by Baron Manfred von Ardenne in Berlin in 1937 [2]. The design borrows heavily from that of the scanning electron microscope (SEM); the STEM utilises a convergent beam of electrons that are focused to form a spot or *probe* on the sample. Less than 9 months after the initial paper of 1938, von Ardenne demonstrated a resolution of 10nm [3]. Sadly, von Ardenne's STEM equipment was destroyed in an air raid in 1944 and von Ardenne himself seconded to the nuclear weapons program [4].

Development was halted until the work of Crewe et al, 20 years later, who successfully developed the high vacuum conditions necessary to incorporate a field emission gun (FEG) as the electron source [5–8]. The FEG, either a Schottky thermally assisted one or a cold FEG, combined with a high resolution

pre-specimen objective lens to demagnify the source, was the means by which resolution of 5Å was achieved [9] and single atoms of thorium and uranium imaged on light substrates [10].

In the STEM, an illuminating probe is raster scanned across the sample by a set of deflector coils (as in an SEM) and an image is recorded pixel-by-pixel from the collected scattered intensity that is transmitted through the specimen. Unlike the SEM, the detector is placed in the diffraction plane post-specimen. The vital electron optical elements, which form the probe and focus it on the sample, are located on the pre-specimen side of the sample. A schematic is shown in Figure 2.2.

Since there is no need for imaging lenses after the specimen, a variety of different detectors can then be used to collect a variety of signals such as electron energy-loss spectra (EELS) and energy dispersive X-ray spectra (EDX), often simultaneously. One of the key benefits is that both imaging and microanalysis can be performed simultaneously and so STEM has been useful as an analytical machine in both materials science [11–14] and biology [15].

STEM was originally developed with the investigation of heavy atoms on thin light supports in mind [6] and was immediately used to image single heavy atoms of uranium on thin carbon substrates [10]. Even before atomic resolution in crystalline samples was readily achievable, the strong dependence of signal intensity on atomic number (see Section 2.1.2) meant that single atoms in catalyst samples were imaged [16]. Early experiments demonstrated that individual platinum and rhodium atoms could be imaged on crystalline (alumina) supports. Treacy and Rice used HAADF to estimate the number of atoms in a supported catalyst cluster [17]. By making assumptions about particle shape, they used the digitized image to attempt to calibrate imaged intensity as a per-atom increment. They calculated that Pt clusters containing as few as three atoms on a 200A thick γ-alumina substrate would be detectable using a probe of 3.5Å.

Under optimum conditions, single atoms, dimers and trimers could be distinguished [18]. Later, micro-diffraction patterns of individual nanoparticles were also acquired in order to estimate their internal structure from the diffraction spot arrangement [19,20].

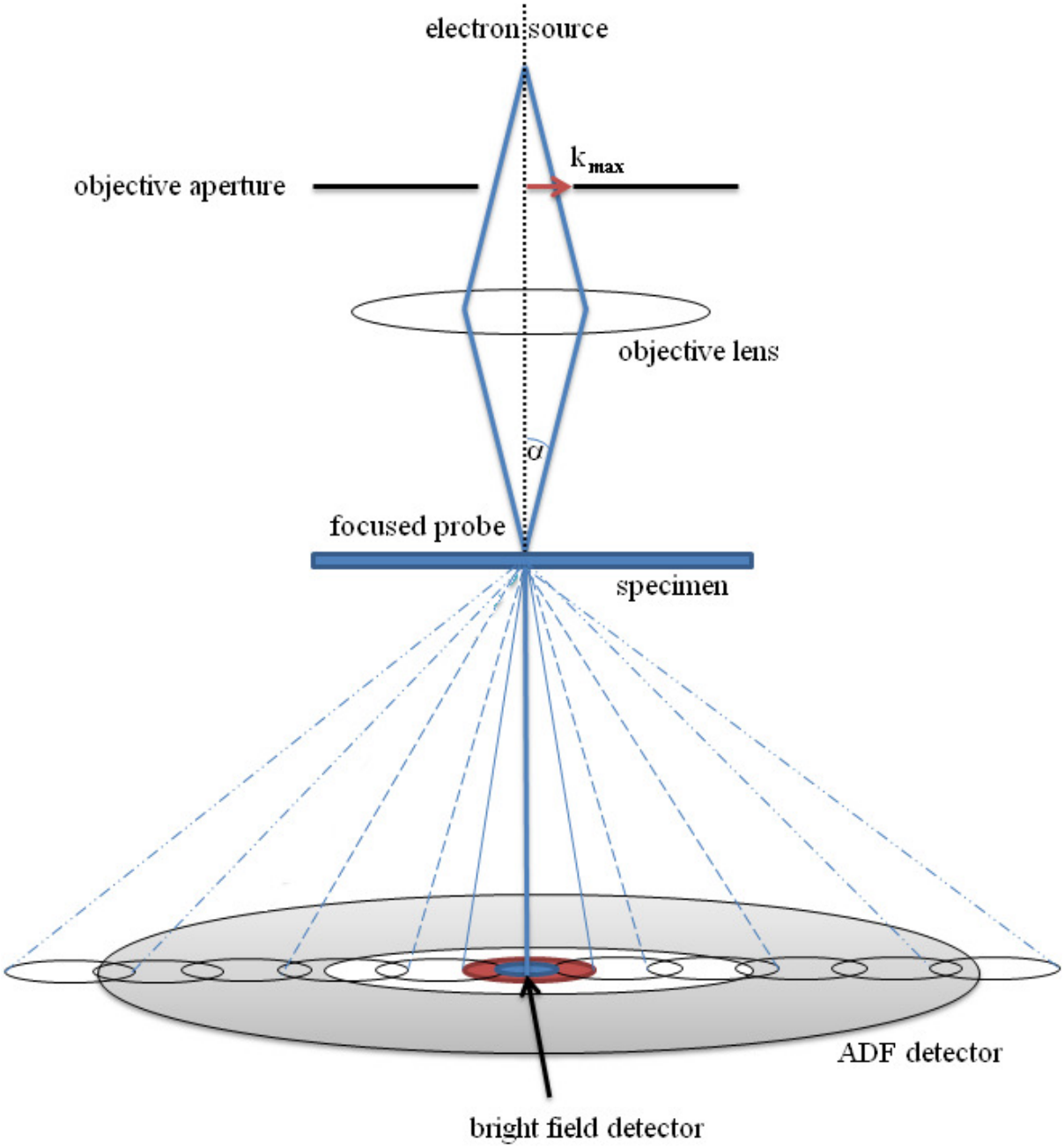

Figure 2.2 Schematic of image formation in a STEM, showing the on-axis small bright-field detector and the larger annular dark-field detector (shaded). The electron source, typically a field emission gun, emits a beam of electrons, which pass through the objective aperture and is focused by the objective lens to form a probe in the sample. The bright field detector on the beam axis records phase contrast images from diffracted discs at each probe position, whereas the ADF detector returns the total signal scattered onto it from diffuse intensity at high angles. The diffracted angles are greatly exaggerated here to aid visualization. The ADF detector typically collects beams of much higher order, though this depends on the apparent "camera length" used.

2.1.1 Bright field STEM and reciprocity

Using a small detector on the optic axis, the interference between overlapping Bragg disks can give phase contrast images (see Figure 2.2). By reciprocity, the elastic scattering events gives comparable contrast and phase contrast information to that of a bright-field TEM image even though the image is being created pixel by pixel as the probe is scanned across the specimen.

The bright field detectors collect electrons scattered to small angles from the optic axis, typically less than 5mrad. As elastic scattering can be considered to be time reversible, it can be convenient to consider STEM as the reciprocal of CTEM [21]. Thus the image forming lenses in the CTEM correspond to the probe forming lenses of the STEM.

2.1.2 High angle annular dark field and Z-contrast

An annular dark field (ADF) detector is defined by both an inner and outer angular radius. The contrast of ADF images can be manipulated by changing the range of detection angles collected [22,23]. This can be achieved by using post specimen lenses, which refocus the image at apparently different camera lengths.

High Angle ADF (HAADF) imaging relies on the collection of signal scattered to the ADF detector at high angles (typically >80mrad), missing the coherent bright field scattering in the centre disc (See Figure 2.2). So long as the inner radius is sufficiently large, scattering from the nucleus dominates. This so called Rutherford scattering has a strong dependence on the atomic number Z of the sample, with heavier atoms scattering more strongly than lighter ones. For example, by using a detector with an inner collection angle of 100mrad, the dimensions of Re clusters have been imaged with a precision of ± 2 atoms [24].

At first the Z-contrast image was conceived as a ratio between the total elastic cross-section from the annular detector ($\sim Z^{3/2}$) and total inelastic scattering intensity from an axial electron loss signal ($\sim Z^{1/2}$ for small thicknesses). This gave images with an intensity ~Z. Much debate has arisen over the exact number of the exponent, which is now commonly agreed to be around $Z^{1.7}$ (nearer the Z^2 of Rutherford scattering) once screening effects of the atomic potential are taken into account [25].

While this dependence allows for direct interpretation of images as brighter spots correspond to heavier atoms, intensity is thus a function of both composition and thickness, making image interpretation non-trivial. Images are essentially 2D projections of 3D object of unknown chemical composition. Furthermore, the dependence on thickness is itself non-linear [26,27], as will be discussed in Chapter 5.

2.1.3 Loss of coherence in HAADF STEM

Unlike the BF process, the HAADF imaging process is incoherent, making qualitative image interpretation more intuitive than for CTEM images. The contrast transfer function for ADF does not have fast oscillations, which lead to contrast reversals with defocus and thickness.

The incoherent image intensity $I(\boldsymbol{r}_\perp, z)$ can be described by a convolution of the probe intensity profile with a discrete object function sharply peaked at the projected atomic sites [28]:

$$I(\boldsymbol{r}_\perp, z) = O(\boldsymbol{r}_\perp, z) \otimes |P(\boldsymbol{r}_\perp, z)|^2 \qquad 2.1$$

where $O(\boldsymbol{r}_\perp, z)$ is the object function[1] describing the sample being imaged and $P(\boldsymbol{r}_\perp, z)$ describes the probe function. Note that the convolution is with a probe intensity and as such is real positive definite, not the complex amplitudes convolved in the BF imaging condition [29].

Originally, the explanation for this loss of coherence was that, at high enough angles, scattering would be dominated by incoherent thermal diffuse scattering (TDS) from the collective oscillations of excited phonons in the sample [21]. Later, it was found that incoherent images can be obtained even when the detector collects zero-order Laue zone disks, indicating that TDS is not a prerequisite for incoherent imaging but that the geometry of the detector is responsible for transverse incoherence in a Z-contrast image [30]. TDS due to phonon scattering is however still important for breaking longitudinal coherence along the columns [31] (and is discussed in more detail in Section 5.4.2).

[1] For a discussion of the object function, see [120]

However, as is often stressed, to fully understand the images, the correct modelling of TDS must be incorporated [32,33] and a dynamical theory is needed to fully take into account both elastic and inelastic scattering and channelling effects [34–39].

2.1.4 Channelling of probe down a column

Electron channelling is the process whereby the potential of the atomic column attracts the electrons and channel them to the exit surface. In essence, the atoms earlier in the column act as lenses to focus the beam down columns [37,40,41]. It is responsible for the agreement of the object function approximation with experiment, even at large thicknesses. However, the object function approximation is essentially a thin specimen scattering approximation and fails to accurately describe thicker specimens where dynamical scattering is prevalent [42]. For nanoparticles, considered a thin sample, and thus weakly scattering, the object function approximation can be useful in quantitative analysis (see Chapter 5).

Channelling is responsible for mitigating the adverse effects of geometric beam broadening well into the sample by keeping the electrons “on column” for much longer. Nevertheless, the probe can still introduce artefacts in HAADF images, e.g. from subsidiary maxima of the incident probe exciting neighbouring columns, and also de-channelling effects as the probe spreads off the column, so called “cross-talk” [43]. Deconvolution of the probe can be used to remove such artefacts [44] but is sometimes not possible in reality when the probe function is not known or difficult to determine. Moreover, oscillations of the probe function can potentially give rise to scattering that varies depending on column compositin.

2.2 The electron probe

In practice, the profile of the probe is a non-uniform disc with a width typically commensurate with the achievable resolution in a STEM. Its exact shape and size is difficult to determine and is primarily limited by the size of the source itself and the aberrations in the objective lens used to demagnify it to create the probe.

As the resolution depends on the wavelength of the electrons, increasing the accelerating voltage improves the resolution but often at the cost of possible increased specimen damage due to the higher energy of the fast electrons.

Yet the relativistic wavelength of an electron accelerated by a voltage of 200kV is approximately 2.5pm, which is far smaller than the resolution of current microscopes. It is well known that resolution is fundamentally limited by electron optics: electron lenses suffer from inherent aberrations due to the helical paths followed by the charge particles subject to the electromagnetic fields of the lenses. In a landmark paper in 1936, Scherzer proved that unlike glass lenses, skilful design cannot eliminate spherical or chromatic aberrations of a rotationally symmetric, static, space-charge-free, dioptic lens for electron beans [45].

Although STEM has been successful in imaging single isolated atoms and small clusters on supports, the limits to its resolution have until recently, prevented the technique from achieving routine atomic resolution imaging and spectroscopy. For core-shell catalyst nanoparticles, where variation in composition is across very short distances on small structures, atomic resolution is vital to understanding their catalytic behaviour.

Spherical aberration or C_s is a third order aberration (see Equation 2.2) and is the dominant inhibitor to resolution. The fundamental physics of charged particle optics means that rays at higher spatial frequencies, passing through the outer edges of the lens, will be pre-focused relative to the focal point in the Gaussian image plane, where the unaberrated rays would be focussed (see Figure 2.3). The displacement in that plane can be written geometrically as a function of the ray angle θ as:

$$\Delta x = C_s \theta^3 \qquad 2.2$$

Underfocussing the lens by a certain amount to bring the so called ‘disc of least confusion’ to the sample surface can also partially compensate for spherical aberration (see Figure 2.3 and Eq.2.4).

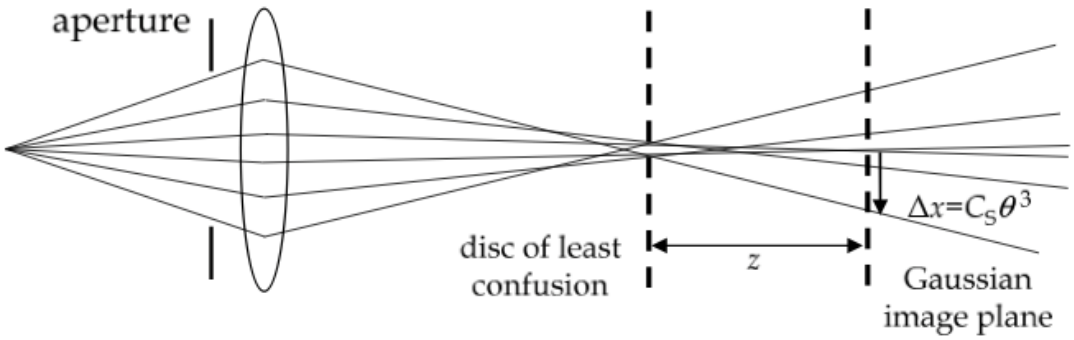

Figure 2.3 Ray diagram of a STEM setup showing the effects of spherical aberration. The Gaussian image plane is the one where unaberrated rays, passing through the centre of the lens, are focussed. The disc of least confusion is the underfocussed point with the smallest beam diameter and the displacement of the aberrated rays in the Guassian image plane is the cube of the ray angle. (Image reproduced from [46])

The effect of aberrations on the size of the probe is deleterious. If the probe is considered to be a superposition of plane waves with different transverse components $k_\perp$ then the function $\chi(\boldsymbol{k}_\perp)$ describes the phase shift due to circularly symmetric aberrations:

$$\chi(\boldsymbol{k}_\perp) = \pi\Delta f\lambda|\boldsymbol{k}_\perp|^2 + \frac{1}{2}\pi C_s\lambda^3|\boldsymbol{k}_\perp|^4 + \frac{1}{3}\pi C_C\lambda^5|\boldsymbol{k}_\perp|^6 + O(|\boldsymbol{k}_\perp|)^{higher} \qquad 2.3$$

where Δf is the defocus value, the shift of the probe relative to the entrance surface of the specimen. This aberration is the easiest to adjust in experimental practice, by compensating with the objective lens, and is not a limiting factor to resolution.

The coefficient C_s is the third order aberration, commonly termed spherical aberration and has been the largest limiting factor to resolution[2] [47] until recently [36,48,49]. The optimum defocus for an objective lens with a certain level of spherical aberration is given by [46]:

$$\Delta f_{opt} = -0.71(\lambda\, C_s)^{\frac{1}{2}} \qquad 2.4$$

[2] Other forms of aberrations, e.g. chromatic or C_c aberrations exist but the STEM is relatively robust to these [121]

As is evident from Equation 2.3, as the spatial frequency $\boldsymbol{k}_{\perp}$ becomes large, the phase shift becomes large. Thus it becomes necessary to use an aperture to limit the higher order beams to some k_{max} in the front focal plane. The size of this so called semi-angle of convergence α is given by the relation

$$\alpha \approx \lambda\, k_{max} \qquad 2.5$$

Restricting the higher order aberrated beams in this way allows for the probe to be purely limited by diffraction but also restricts the number of electron that can pass through the aperture by limiting the beam current.

And the corresponding maximum objective aperture size is:

$$\alpha = 1.3 \left(\frac{\lambda}{C_s}\right)^{\frac{1}{4}} \qquad 2.6$$

The diffraction limited version of Equation 2.3 gives rise to a full width half maximum (FWHM) of diffraction limited STEM probe of diameter d_{diff}:

$$d_{diff} = 0.43\ (\lambda^3\ C_s)^{\frac{1}{4}} \qquad 2.7$$

which is smaller than in TEM (where the pre-factor is 0.66). Thus STEM imaging can surpass the classical TEM information limit of a microscope if both the sample and the specimen holder are sufficiently stable against drift [50].

2.3 Spherical aberration correction

Scherzer later proposed designs for various corrected lenses, where one or more of the four requirements are abandoned, notably the limitation of round lenses. Recent advances in aberration correction using non-circular lenses have overcome this [51].

This permits the use of a larger probe convergence angle for an aberration-free probe, resulting in a smaller and more intense probe [52]. Since the objective aperture size, α, is inversely proportional to the probe size (see Eq. 2.12). In the electron optic framework, this essentially increases the numerical

aperture of the objective lens allows more beam current through for the same amount of source demagnification.

Greater lateral spatial resolution and better signal to noise ratios in both HAADF imaging and spectroscopic techniques are therefore possible. More intense probes thus allow higher-order orientations of crystals to be imaged at atomic resolution [53].

2.4 Brightness and probe current

To get a better handle on the importance of aberration correction and how it has opened up the possibilities for quantitative analysis at atomic resolution, it is useful to consider the fundamental trade-off between the imaging resolution[3] and the probe current, as the two are inversely proportional. Figure 2.4 demonstrates that probe current increases with increasing probe size, and thus decreasing resolution. This crucial relationship is explored and the relationship derived here to illustrate the importance of aberration correction to the atomic resolution study of nanoparticles.

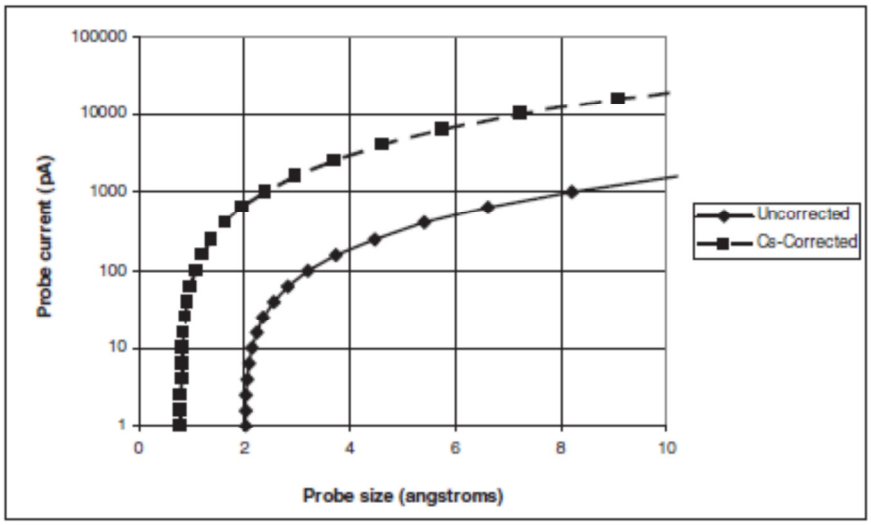

Figure 2.4 Plot of the probe size for incoherent STEM imaging versus beam current for Oxford-JEOL 2200MCO and an uncorrected instrument of the same brightness. (Image reproduced from [46]).

[3] secondary complications to image interpretation also arise due to the partial coherence of the source

The purpose of the condenser lens (often called CL1) is to demagnify the electron source as much as possible in order to reduce the deleterious effects of partial source coherence from the finite physical size of source [46]. The stronger the lens setting, the higher the demagnification, and consequently a smaller the probe size is possible and higher spatial resolution can be achieved. However, more demagnification also results in lower current in the probe since the objective aperture will block more of the electron beam. By weakening the condenser lens, the probe current can be increased significantly (see Figure 2.5), but at the cost of spatial resolution.

As nanoparticles are small in volume, the amount of signal generated for a given probe current and exposure time is necessarily lower than for a bulk sample. Low count statistics and poor signal to noise thus hinder the possibilities of quantitative analysis. To improve these issues, it is possible to either increase the acquisition time, which is often not practically feasible, or increase the probe current, which is explored here.

The number of incident electrons on a sample in a given time, i.e. the probe current, can be adjusted by several methods. Fundamentally, it is limited by the brightness of the electron source, which is dependent on the material and the anode extraction voltage of the electron gun. The brightness, B, of the electron source, or current per unit area per unit solid angle subtended by the beam, is a conserved quantity in an electron optic system[4] and so can be usefully employed to calculate the probe current available. It is given by the relationship:

$$B = \frac{I}{A\Omega} \qquad 2.8$$

where I is the emission current, A is the area of the source over which the electrons are emitted and Ω is the solid angle into which the electrons are emitted.

The introduction of an objective aperture limits the beam and thus the solid angle to $\pi\alpha^2$, where α is the size of the objective aperture. The brightness can be expressed in terms of the diameter of the source d_{src} by substituting in

[4] More accurately, brightness is conserved at planes conjugate to the electron source (i.e. at any beam crossover planes) so long as only geometric optics is considered and diffraction effects are neglected.

$$A = \frac{\pi d_{src}^2}{4} \tag{2.9}$$

to give

$$B = \frac{I}{\left(\frac{\pi d_{src}^2}{4}\right)(\pi \alpha^2)} \tag{2.10}$$

Rearranging Eq. 2.10, it is clear that to maximise probe current for a constant brightness[5], two things can be done:

$$I = \frac{B\pi^2 d_{src}^2 \alpha^2}{4} \tag{2.11}$$

The size of the source d_{src} can be increased, but this will be at the expense of resolution. Alternatively, the size of the objective aperture α can be increased, but this is limited by aberrations as set out in Eq. 2.6. In the diffraction limited regime [54], where the image of the demagnified source is smaller than the diffraction limit, the resolution of the probe is as expressed in Eq. 2.7 and is essentially constrained by the size of the objective aperture. However, once the image of the source is larger than the diffraction limit, the probe size is traded for the probe current, by the relationship with brightness (Eq. 2.11 rearranged):

$$d_{src} = \sqrt{\frac{4I}{B\pi^2\alpha^2}} \tag{2.12}$$

Assuming that both the source image and probe shapes are approximately Gaussian in form, the combined probe size can be obtained by adding d_{src} and d_{diff} in quadrature:

$$d_{probe}^2 = d_{diff}^2 + d_{src}^2 \tag{2.13}$$

which can be graphically seen in Figure 2.4. Note the diffraction-limited regime on the left, where probe current does not depend on the size of the probe is greatly increased for C_s aberration corrected instruments.

[5] Brightness is a fundamental constant of the instrumentation and has already been significantly improved beyond the original TEM construction by the development of the cold FEG, as discussed in Chapter 3.

Thus it can be clearly seen that the chief gain of aberration correction is the increase in probe current available due opening up the objective aperture to the higher convergence angles. The larger objective apertures allow an increase in the numerical aperture of the lens, essentially letting more of the beam through. This not only gives finer probes that allow higher-order orientations of crystals to be imaged at atomic resolution, but also an increase in probe current which improves the signal to noise possible in spectroscopy. Given the small volume of nanoparticles, the scattering from the sample is necessarily weak. Thus a smaller, more intense probe is vital if the atomic structure is to be studied quantitatively.

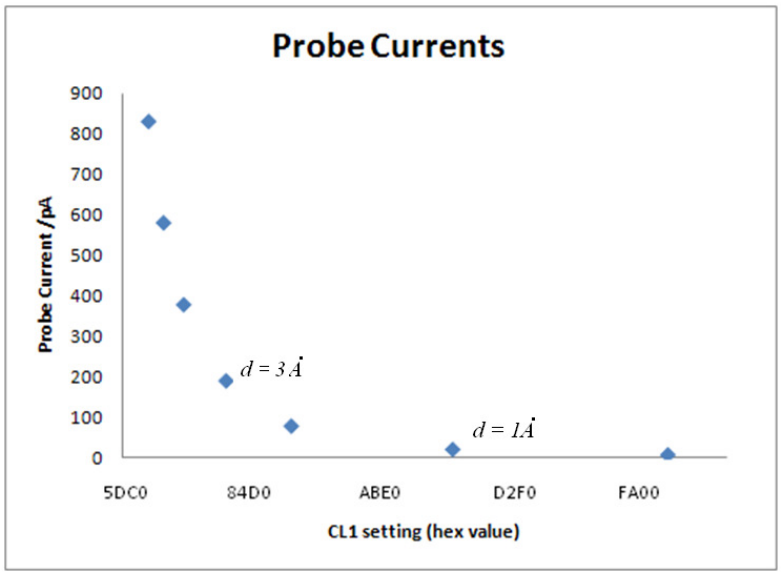

Figure 2.5 Probe current on the Oxford-JEOL 2200MCO decreases with increasing demagnification of the electron source due to stronger excitation of the CL1 (condenser) lens of the microscope. The known probe diameters of 1Å and 3 Å, measure by imaging Si(110) are marked.

In STEM, images of silicon <111> with 1.92 Å spacings were obtained as early as 1990 with an uncorrected microscope (C_s = 0.7 mm) operating at 100 kV in both axial BF and ADF modes [55]. With the advent of C_s-correctors, sub-Å probes can be obtained using microscopes operating at 120 kV [56,57]. Image resolution has been continually pushed by STEM instruments: from the direct imaging of the Si<112> dumbbells at 78pm [52] to the 63pm of wurtzite GaN in <211> [58]. Most recently the first sub-50pm resolution has been demonstrated [59].

10 nm gold islands on amorphous carbon, as well as single atoms and clusters of 2 and 3 atoms, have been distinguished using Cs-corrected HAADF STEM [57]. Single atom contrast was sufficiently high to allow the motion of atoms under the electron beam to be followed. The structures of individual bimetallic clusters of $Ru_{10}Pt_2$ were determined from Cs corrected HAADF images [60]. More ambitiously, gold nanoparticles on heavy supports (TiO_2) have been explored [61,62].

Since C_s correction has been successfully implemented the next focus for instrumentation improvements is towards monochromation or C_c correction in order to minimise the effect of beam spreading due to energy dispersion within the beam.

2.5 Three dimensional information

Beyond the considerations of lateral spatial resolution in the image plane, it is important to obtain accurate three-dimensional information about the morphologies of heterogeneous catalyst nanoparticles since the structure and surfaces of the nanoparticle plays a crucial role in the activity and selectivity of the catalyst [63]. The shapes of Pt nanoparticles have been inferred by comparing pendellösung fringes in weak-beam dark-field images with multi-beam simulations [20]. Similarly, HRTEM images of Au particles have been matched to multislice simulations [64]. These are lengthy procedures, with the added complication that only certain crystals can be imaged successfully using weak-beam dark-field imaging or particles must be oriented close to a high-symmetry zone axis for HRTEM imaging.

One of the fundamental problems with the transmission nature of (S)TEM is the reduction of a 3-dimensional structure into a 2-dimensional image which can cause considerable structure interpretation problems. Understanding of the atomic structure of nanoparticles has been long considered critical to understanding the activity and selectivity of the catalyst.

2.5.1 Tomography

In materials science, X-ray tomography allows 3D-structures to be imaged with a resolution of no better than 50nm [65]. Atom-probe field ion microscopy (APFIM) allows three-dimensional characterization at the atomic level, but can only be applied to certain samples. Bulk samples can be studied by slice sectioning with a focused-ion beam microscope and imaging successive slices with an SEM [66].

Electron tomography has been used in the biological sciences for more than 30 years[67]. The mathematical background to the recovery of three-dimensional information from two-dimensional images dates back to the work of Radon [68]. In general, the tomographic reconstruction algorithms require that the specimen be tilted about the eucentric axis of the specimen holder rod over a tilt range that is as close to ± 90º as possible. This greatly limits the feasibility of using this technique for beam sensitive samples.

However, the application of HAADF STEM tomography to heterogeneous catalysts has been demonstrated [69]. It has been shown that the spatial distributions of Pd-Ru bimetallic nanocatalysts within the pores of a SiO_2 matrix can be determined by tomography [70]. And more local details such as lamellar twinning can be investigated (See Figure 2.5) [71]. Once the 3D shape has been reconstructed important information such as surface area, volume and thickness distributions can be measured .[72]

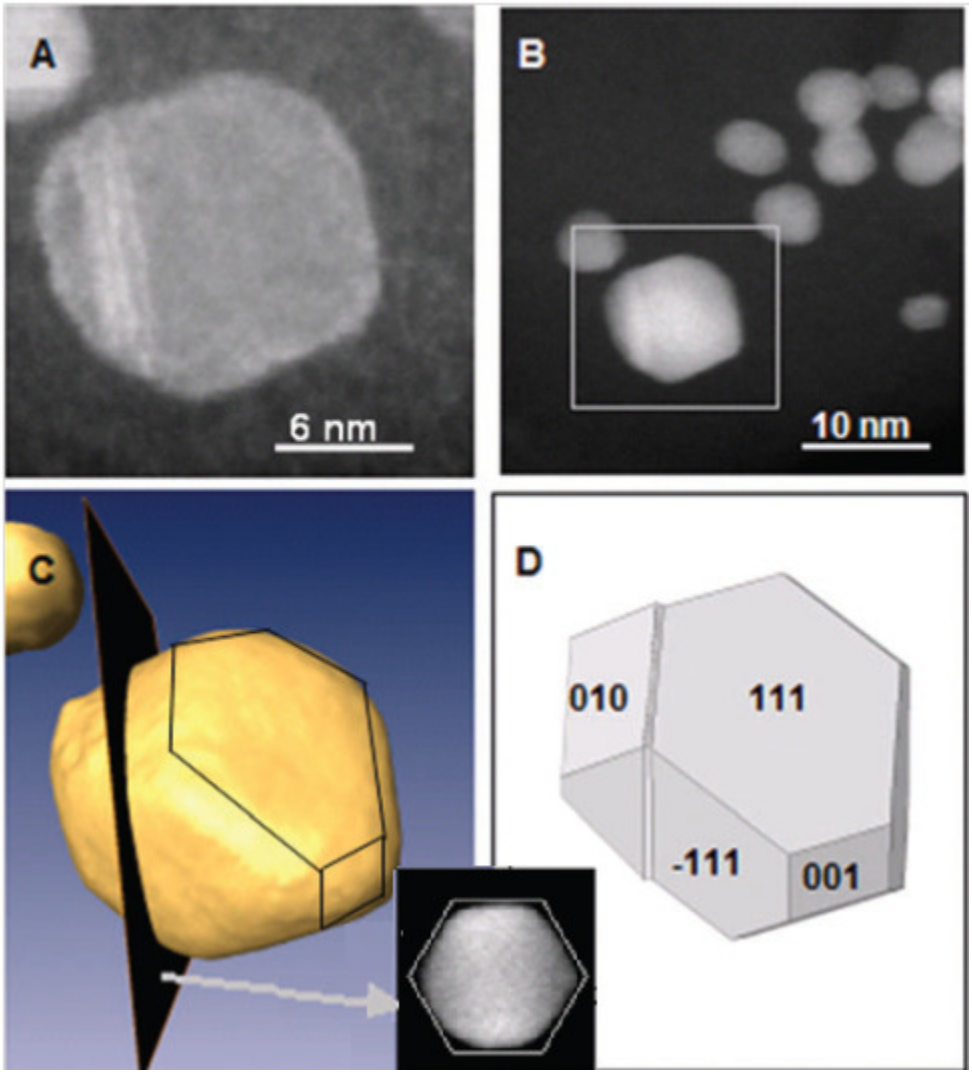

Figure 2.6 a) ADF STEM image of the Pt particle shown in (b), bright phase contrast in the particle arises from lamellar twinning. **(b)** HAADF STEM image of Pt particles taken from a tilt series acquired. **(c)** isosurface visualization of the three-dimensional shape of the particle determined using HAADF STEM tomography. **(d)** Corresponding view of the inferred modified Wulff construction. The inset shows that a section taken through the reconstruction at the position of the twin is approximately hexagonal in shape. (Adapted and reprinted with permission from [71]).

A recent reconstruction technique called compressed sensing (CS-ET) has been proposed, based on utilising images in which only a limited number of pixels contain non-zero values, has been shown to demonstrate improved reconstruction for fewer images [73] .

2.5.2 Discrete tomography

Discrete tomography is a technique where the number of images of different tilts required to elucidate 3D information can be as few as two, even in the presence of noise or defects, through the use of prior knowledge [74]. Atomic resolution discrete tomography uses the prior that the atoms in the sample all lie on atomic lattice sites, there are no vacancies and number and height of edges should be minimised. Further assumptions about the crystallographic structure allowed a reconstruction a 3D structure for an embedded silver nanoparticle [75] and the core of a core-shell semi-conductor nanocrystals [76] from just two low index atomic resolution projections. The number of atoms was estimated by a statistical parameter estimation method (see Chapter 5 for further discussion of the technique).

2.5.3 Optical sectioning

In STEM electron microscopy, the short depth of field of aberration-corrected STEM microscopes promises to allow the acquisition of three-dimensional information at atomic resolution via depth sectioning [77]. Recently depth sectioning has been shown to work in the confocal mode [78]. However, these techniques are limited by the depth of field, which is of the order of 10nm [79].

2.6 Compositional analysis

Given that image intensity in HAADF STEM is a function of both thickness and composition, use of another technique to complement imaging with compositional information is a practical approach to solving real materials problems [80].

Inelastic scattering processes, where an incident electron ionizes an atom in the sample by removing an inner shell electron from the atom, are another source of information about the sample. The incident electrons from the beam can be inelastically scattered in processes that generate X-rays, other secondary electrons or Auger emission or processes that arise due to the collective behaviour of many atoms or electrons (such as phonons). The detection of the scattered electrons themselves or the generated signals contain much compositional sensitivity as they are directly related to the chemistry of the sample.

2.6.1 EELS

The most common absorption spectroscopy is electron energy loss spectroscopy (EELS). In this method, the energy losses of the incident electrons themselves due to interaction with the sample can be recorded directly and analysed. They are collected and dispersed by a magnet in a spectrometer and the spectra can be readily analysed.

EELS has more easily provided good spatial and chemical resolution [81–84] compared to Energy Dispersive X-ray (EDX) analysis. Atomic resolution EELS was reported as early as 1993 [85] but with the popularisation of aberration correction, two-dimensional mapping has become accessible [86]. Layered manganite $La_{1.2}Sr_{1.8}Mn_2O_7$ imaged at atomic resolution [87] was quickly superseded by the mapping of atoms in two dimensions of a $La_{0.7}Sr_{0.3}MnO/SrTiO_3$ interface [88].

EELS usually provides better spatial resolution and detection limits than EDX [89]. However, palladium, platinum and other heavy elements have energy loss peaks higher in energy (see Figure 2.7). For thin samples such as nanoparticles which have low count statistics by nature of their size, the EELS signal for these elements is often lost in poor signal to background noise [90].

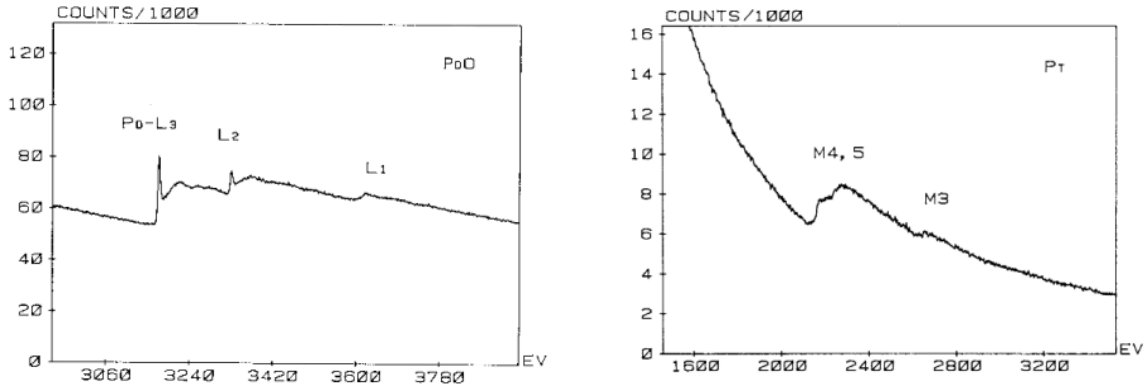

Figure 2.7 (left) Pd and **(right)** Pt peaks from the Gatan EELS Atlas. Pd M4,5 at 334.7eV and Pt M4,5 can be found at 2122eV. These spectra are from bulk samples; low count statistics from nanoparticle specimens would hinder the quantification of these peaks.

2.7 EDX

The other commonly used technique in analytical microscopy is energy dispersive X-ray (EDX) analysis. This technique, in contrast to EELS, is an emission spectroscopy technique. Once a core electron in an atom in the specimen is excited out of an inner shell by the high energy incident radiation, an outer (often L or M) shell electron relaxes down to the vacant shell, filling the hole (see Figure 2.8).

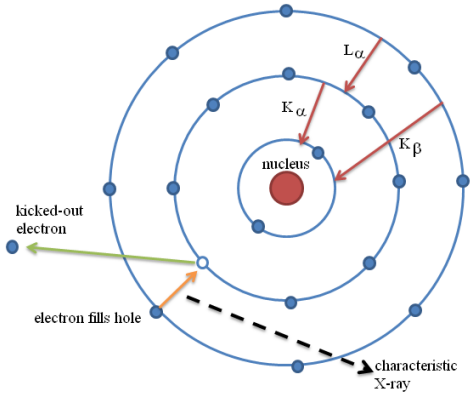

Figure 2.8 The ionization process. Where external stimulation kicks out and electron and the relaxation of an outer shell electron to fill the created hole radiates an X-ray of a characteristic energy.

The emitted X-ray has a characteristic energy equal to the difference in the two shell energies. Ionised atoms of Pd and Pt emit characteristic X-ray at different energies (see Table 2.1)

Element	X-ray	Energy /keV	Relative Intensity
Pd	K	21.12	100
	$L_{\alpha 1}$	**2.84**	**100**
	$L_{\alpha 2}$	2.83	11
	$L_{\beta 1}$	**2.99**	**53**
Pt	K	66.25	100
	$L_{\alpha 1}$	**9.44**	**100**
	$L_{\alpha 2}$	9.36	11
	$L_{\beta 1}$	**11.07**	**67**
	$L_{\beta 2}$	11.25	23
	$L_{\beta 3}$	12.94	13
	M_{α}	**2.05**	**100**

Table 2.1 Photon energies of the characteristic X-rays for Pd and Pt that are commonly detectable in a STEM. The relative intensity is shown with an intensity of 100 assigned to the strongest line in each shell for each element. The X-ray energies marked in bold are the ones typically considered experimentally.

In order to ionize an atom, the incident electron needs to transfer an amount of energy to the atom that is at least equal to the critical ionization energy (E_c). E_c increases as electrons are more tightly bound to the nucleus, thus inner K shell electrons have a higher E_c than outer L shell ones. Heavier atoms with a higher Z number have more protons and thus a stronger attractive nuclear field. This means that their E_cs are larger.

The cross section for ionization does not vary substantially as a function of incident electron energy but it does vary with the ratio of beam energy E_0 to the critical ionization energy E_c, the so called overvoltage *U* (see Figure 2.9). If the E_0 is too close to E_c, there is a low probability of ionization, which would limit elemental detectability in the sample.

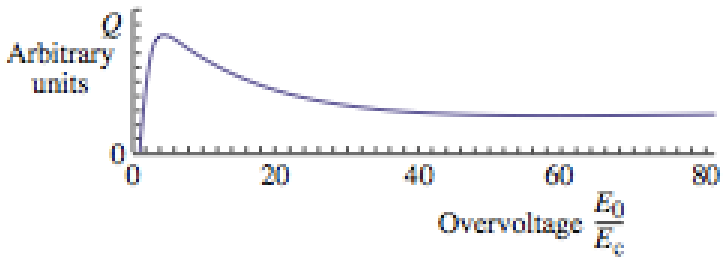

Figure 2.9 The variation of ionization cross section (here, *Q*) with overvoltage. Ionization is most probable at approximately ~5x the critical ionization energy E_c. (Image reproduced from [91])

The total ionization cross section (σ) is well described by the Bethe model:

$$\sigma_T = \left(\frac{\pi e^4 b_s n_s}{E_0 E_c}\right) \log\left(\frac{c_s E_0}{E_c}\right) \qquad 2.14$$

Where n_s is the number of electrons in the ionized shell and b_s, c_s and n_s are shell-specific constants. There is clearly a maximum in ionisation probability at ~$5E_c$ but in practice, a thorough understanding of the ionisation is overshadowed by the need to improve the detection and analysis methods.

2.7.1 Bremsstrahlung X-rays

Electrons decelerated by the Coulomb field of the nucleus of the sample atoms also produce an X-ray. This creates a continuum of bremsstrahlung[6] X-rays since the electron can be decelerated by any amount of interaction up to the energy of the beam. They create a broad, featureless background that sits on top of the sharp peaks of the characteristic X-rays in the X-ray spectra (see Figure 2.10).

[6] From the German for "braking radiation"

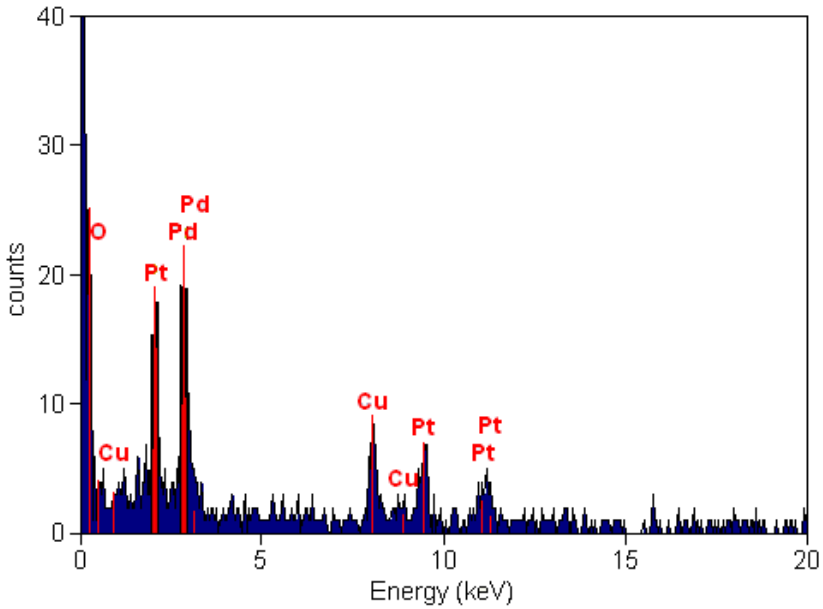

Figure 2.10 Typical EDX spectrum from a Pt/Pd nanoparticle. The increased background at lower energies is an indication of Bremmstrallung.

The likelihood of bremsstrahlung is well described by the Kramers cross section:

$$N(E) = \frac{KZ(E_0 - E)}{E} \qquad 2.15$$

Where *N(E)* is the number of X-rays of an energy *E* generated by electrons of energy E_0 and *K* is the Kramers constant and *Z* is the atomic number of the atom. Removing the contribution from this background is essential for accurate interpretation of the relative number of X-rays detected.

2.7.2 Compositional sensitivity

Fluorescence yield describes the probability that an ionization event results in the emission of a characteristic X-ray and not an Auger electron. It is the ratio of X-ray emission to inner shell ionization events and is a strong function of atomic number:

$$\omega = \frac{Z^4}{a + Z^4} \qquad 2.16$$

a is approximately 10^6 for K shell. This means that EDX is not a suitable technique for light elements[7] but are well suited for the heavier elements often used in catalysis (see Table 2.2).

Element	Z	ω
Pd	46	0.82
Pt	78	0.97

Table 2.2 Fluorescence yield for Pd and Pt K shell, calculated using equation 2.16

2.7.3 EDX of nanoparticles

There are very few examples of STEM-EDX of nanoparticles [92–95] since only a fraction of the X-rays generated are collected in a TEM and the small volume of the nanoparticles means that only a small number of atoms are excited and thus the number of X-rays generated is severely limited. Early maps produced by Lyman et al. [93] in 1987 showed that the maximum number of counts from a probe position corresponding to an area of the Pd particle was only 36, compared to a background count of 7; such poor signal to noise makes quantification difficult.

Recently a combination of aberration corrected HAADF STEM and EDX was used to map Pt-Pd core-shell nanoparticles [96]. While Sanchez et al chose to image at atomic resolution to show 2nm nanoparticles in great spatial detail, the identification of a core-shell structured was based on knowledge of their synthesis methods and broad-beamed EDX at low resolution showing the presence of both elements in the sample at large.

Recently EDX maps of core-shell Au-Pd bimetallic nanoparticle systems were shown [97]. However, X-ray signal is traded for atomic resolution so none of the images show the precise location of columns of atoms [98].

[7] X-rays from elements below beryllium (Be has Z=4) are in fact undetectable.

2.7.4 PCA and MSA

Within a data cube of spectra, there is often redundant information, which can be used to reduce the level of noise in individual spectra. Principle component analysis (PCA), in particular multivariate statistical analysis (MSA), have been readily employed in electron microscopy of biological macromolecules [99] but only later applied to STEM-EDX [100].

The technique factors the spectra into a set of orthogonal information components (eigenspectra), each of which correspond to an independent source of information. The eigenvalue solutions can then be used to extract maximum signal information and allow rare events to be seen by finding the independently varying parameters.

This technique has allowed the first atomic resolution EDX maps to be shown [101], though of bulk crystal. It is especially useful for systems where there is poor count statistics and thus low signal to noise, such as nanoparticles, where the interaction volume is necessarily small due to the size of the sample.

2.7.5 Spatial resolution

Spatial resolution is limited by the size of the probe and STEM can therefore in principle provide higher spatial resolution that TEM. Even without aberration correction, EDX was used to obtain the Pt and Re mass fraction in bimetallic particles with sizes of between 0.5 and 2.5 nm [94] and Pt concentration was investigated as a function of particle size. However, as explored in Section 2.4, increased spatial resolution is often at the expense of probe current.

EDX mapping has demonstrated that sulphur is localised on the nanoparticles in ‘poisoned’ catalysts [89] and more recently, EDX of 5nm core-shell nanoparticles mapping has been able to differentiate the layered structure very effectively [102]. However, the atomic columns aren’t resolved due to the trade-off between resolution and counts.

With aberration correction, the possibilities for a higher currents, higher resolution probes, have renewed interest in EDX as a high resolution compositional detection tool [103–105]. With probes now routinely Å-sized and brighter electron sources, larger X-ray signals and shorter acquisition times

can be achieved [106]. Atomic resolution EDX has recently been demonstrated on strontium-titanate mapping both the strontium and titanium sub-lattices [107]

2.7.6 Silicon drift detectors

The development of the new generation of EDX detectors has greatly improved the detection capabilities of EDX. Silicon drift detectors have a greater sensitivity [103,108] and are now commonly used on new analytical microscopes. This is now also combined with much larger solid angle of collection: by placing the detector closer to the pole piece or by using multiple detectors, up to 1.3 steradians (sr) can be achieved, where previously only 0.3sr solid angle was possible [109–111].

The transversal field generated by a series of ring electrodes causes charge carrier to 'drift' to a small collection electrode, a technique previously used in particle physics, allowing significantly higher count rates and a low capacitance of the detector. Like traditional Si(Li) detectors, the incoming photon is energy is measured by the amount of ionisation it produces in the detector material. Since SDDs use a higher purity material with a low leakage current, Peltier cooling can be used in place of a large liquid nitrogen tank, which improves the mechanical stability of the detector.

Tran et al. are among the first to apply these new detectors to nanoparticles [112], allowing them to map their Cu-Au nanoparticles ranging 1-10nm in diameter. They are now standard on all new analytical instruments.

2.8 EDX quantification

Ideally, the detector geometry and detection efficiency must also be included in quantification calculations including area and collection angle. In addition, accurate compositional analysis must take into account the self-absorption and re-florescence of X-rays within the sample [113].

This requires knowledge of local thickness and density, which cannot be measured simultaneously with an EDX spectrum. This is so that a ZAF correction can be made to account for the **Z**-number of

the specimen, the **A**bsorption of X-rays in the sample before they get to the detector, and the **F**luorescence of secondary X-rays of a different element.

For nanoparticle systems which are thin samples, it is reasonable to assume no absorption and re-florescence will take place and thus the only correction that needs to be taken into account is that of the atomic number Z.

2.8.1 Cliff Lorimer k-factor method

Most EDX software with built-in quantification use Cliff-Lorimer k-factors [114] to determine the compositional ratio of elements. They relate the weight fraction of the elements C, to measured characteristic X-ray intensities I, above background:

$$\frac{C_A}{C_B} = k_{AB}\frac{I_A}{I_B} \qquad 2.17$$

Tables of k-factors are often used when determining compositional ratios from the spectra. Most software pages included with EDX detectors calculate the quantification from spectra using artificial k-factors. These can be determined theoretically to 10% error [115] or experimentally to 1% error using standard samples of known composition [116].

A standards approach to EDX quantification involves selecting known samples with very similar density and thickness at a range of compositions to create a calibration curve and therefore an experimental k-factor (with ~±1% error). Unfortunately some standards may not be available and even if not k-factor calculation is a time consuming procedure.

The DTSA software developed for simulation of SEM and TEM X-ray analysis [117] uses existing Monte Carlo packages [118] to simulation electron and X-ray transport in solid materials. Both characteristic X-ray generation as a result of electron-induced inner shell ionisation and Bremsstrahlung X-ray generation resulting from electron deceleration are modelled. The software allows experimental k-factors generated from standard samples of known composition alloys to be used. Unfortunately, experimental k-factors require multiple samples of known composition and often

the precise factors are not available for the particular sample investigated, since they change with composition [119].

2.8.2 ζ--factor method

Watanabe and Williams [104] proposed an iterative ζ-factor method, which also takes into account self-absorption. This method uses pure element standard samples as references and allows for composition and mass-thickness to be determined simultaneously. In addition, various detector parameters such as spatial resolution, analytical sensitivity and detector efficiency, can also be determined from a single spectrum.

Whilst this method may seem less trivial as it requires thickness and calibration and current measurements as well as having the same limitations for multiple element systems it does have a significant advantage that pure element thin films can be used as standards [103]. Pure elements are often more routinely available. This method proves much more accurate than the k-factor method; however it requires a standard to be calibrated with every experiment.

2.9 Conclusions

The bright, small probe and the incoherent image formation mechanisms make aberration corrected HAADF STEM a powerful tool in the investigation of the detailed structure of nanoparticles. Previous work in the field of nanoparticles and catalysts show that it is particularly suited to this kind of material sample.

While HAADF STEM gives great lateral spatial resolution, the combined contributions to the detected intensity from both thickness and composition make chemical identification difficult. EDX and other spectroscopic techniques can provide a complement with more directly interpretable chemical information (as explored in Chapter 7). However, the poor generation and collection statistics from thin samples such as nanoparticles with their small, finite volumes means, even with the smaller probes and increased probe currents afforded by aberration correction, spatial resolution is often necessarily traded for beam current and signal.

Combining these two techniques, and together with tomography and detailed simulations, single atom mapping of core-shell nano-particles seems a not impossible dream.

HAADF STEM imaging will be applied in the next chapter to investigate catalyst samples of various designs (Chapter 3). In order to understand the structure and composition of catalyst core-shell nanoparticles, the solution of a 3 dimensional structure at the atomic level from a two dimensional image must be extracted. With careful calibrations and matching to simulation work (discussed in Chapter 4), column by column analysis (as proposed in Chapter 5) of HAADF STEM images is presented in Chapter 6 and combined with EDX in Chapter 8.

References

[1] E. Ruska, M. Knoll, Die magnetische Sammelspule für schnelle Elektronenstrahlen, Z. Techn. Physik. 12 (1931) 389–400.

[2] A.V. Crewe, High-resolution Scanning Transmission Electron Microscopy, Science. 221 (1983) 325–330.

[3] M. von Ardenne, Das Elektronen-Rastermikroskop. Praktische Ausführung, Z. Tech. Phys. 19 (1938) 407–416.

[4] C.W. Oatley, The early history of the scanning electron microscope, J. Appl. Phys. 53 (1982) R1–13.

[5] A. V. Crewe, A new kind of scanning micrsoscope, J. Microscopie. 2 (1963) 369–371.

[6] A. V. Crewe, A High-Resolution Scanning Transmission Electron Microscope, Journal of Applied Physics. 39 (1968) 5861.

[7] A. V. Crewe, Electron Gun Using a Field Emission Source, Review of Scientific Instruments. 39 (1968) 576.

[8] A. V. Crewe, A Simple Scanning Electron Microscope, Review of Scientific Instruments. 40 (1969) 241.

[9] A.V. Crewe, J. Wall, A scanning microscope with 5 Å resolution, Journal of Molecular Biology. 48 (1970) 375–393.

[10] A. Crewe, J. Wall, J. Langmore, Visibility of single atoms, Science. 168 (1970) 1338–1340.

[11] S.J. Pennycook, Z-contrast stem for materials science, Ultramicroscopy. 30 (1989) 58–69.

[12] S. Pennycook, High angle dark field STEM for advanced materials, Journal of Electron Microscopy. 43 (1996) 36–43.

[13] S.J. Pennycook, M. Varela, C.J.D. Hetherington, A.I. Kirkland, Materials Advances through Aberration-Corrected Electron Microscopy, MRS Bulletin. 31 (2006) 36–43.

[14] M. Varela, A.R. Lupini, K. van Benthem, A.Y. Borisevich, M.F. Chisholm, N. Shibata, et al., Materials characterisation in the aberration-corrected scanning transmission electron microscope, Annual Review of Materials Research. 35 (2005) 539–569.

[15] A. a Sousa, R.D. Leapman, Quantitative STEM mass measurement of biological macromolecules in a 300 kV TEM., Journal of Microscopy. 228 (2007) 25–33.

[16] M.M.J. Treacy, Howie, A, C.J. Wilson, Z contrast of platinum and palladium catalysts, Philosophical Magazine A. 38 (1978) 569–585.

[17] M.M.J. Treacy, S.B. Rice, Catalyst Particle Sizes from Rutherford Scattered Intensities, Journal of Microscopy. 156 (1989) 211–234.

[18] P.D. Nellist, S.J. Pennycook, Direct Imaging of the Atomic Configuration of Ultradispersed Catalysts, Science. 274 (1996) 413–415.

[19] W. Monosmith, J. Cowley, Electron microdiffraction from very small gold particles, Ultramicroscopy. 12 (1984) 177–183.

[20] M. Yacamán, J. Dominguez, Characterization of small platinum particles supported on graphite by electron microscopy, Journal of Catalysis. 64 (1980) 213–222.

[21] A. Howie, Image contrast and localized signal selection techniques, Journal of Microscopy. 117 (1979) 11–23.

[22] J. Liu, J. Cowley, High-angle ADF and high-resolution SE imaging of supported catalyst clusters, Ultramicroscopy. 34 (1990) 119–128.

[23] D.O. Klenov, S. Stemmer, Contributions to the contrast in experimental high-angle annular dark-field images., Ultramicroscopy. 106 (2006) 889–901.

[24] A. Singhal, J. Yang, J. Gibson, STEM-based mass spectroscopy of supported Re clusters, Ultramicroscopy. 67 (1997) 191–206.

[25] P. Hartel, H. Rose, C. Dinges, Conditions and reasons for incoherent imaging in STEM, Ultramicroscopy. 63 (1996) 93–114.

[26] S. Hillyard, R. Loane, J. Silcox, Annular dark-field imaging: Resolution and thickness effects, Ultramicroscopy. 49 (1993) 14–25.

[27] S. Hillyard, J. Silcox, Thickness effects in ADF STEM zone axis images, Ultramicroscopy. 52 (1993) 325–334.

[28] S. Pennycook, D. Jesson, High-resolution incoherent imaging of crystals, Physical Review Letters. 64 (1990) 938–941.

[29] P.W. Hawkes, J.C.H. Spence, eds., Science of Microscopy, New York, NY, Springer New York, 2008.

[30] D.E. Jesson, S.J. Pennycook, Incoherent Imaging of Crystals Using Thermally Scattered Electrons, Proceedings of the Royal Society A: Mathematical, Physical and Engineering Sciences. 449 (1995) 273–293.

[31] B. Rafferty, P.D. Nellist, S.J. Pennycook, On the origin of transverse incoherence in Z-contrast STEM., Journal of Electron Microscopy. 50 (2001) 227–33.

[32] C. Dwyer, J. Etheridge, Scattering of A-scale electron probes in silicon, Ultramicroscopy. 96 (2003) 343–360.

[33] S.D. Findlay, Quantitative structure retrieval using scanning transmission electron microscopy., Acta Crystallographica. Section A, Foundations of Crystallography. 61 (2005) 397–404.

[34] K. Ishizuka, N. Uyeda, A new theoretical and practical approach to the multislice method, Acta Crystallographica Section A. 33 (1977) 740–749.

[35] A. Amali, P. Rez, Theory of Lattice Resolution in High-angle Annular Darl-field Images, Microsc. Microanal. 3 (1997) 28–46.

[36] K. Ishizuka, Prospects of atomic resolution imaging with an aberration-corrected STEM., Journal of Electron Microscopy. 50 (2001) 291–305.

[37] C. Rossouw, Channelling effects in atomic resolution STEM, Ultramicroscopy. 96 (2003) 299–312.

[38] Y. Peng, P.D. Nellist, S.J. Pennycook, HAADF-STEM imaging with sub-angstrom probes: a full Bloch wave analysis, Journal of Electron Microscopy. 53 (2004) 257–66.

[39] P. Voyles, Imaging individual atoms inside crystals with ADF-STEM, Ultramicroscopy. 96 (2003) 251–273.

[40] P. Wang, a Bleloch, U. Falke, P. Goodhew, Geometric aspects of lattice contrast visibility in nanocrystalline materials using HAADF STEM, Ultramicroscopy. 106 (2006) 277–283.

[41] D.O. Klenov, S.D. Findlay, L.J. Allen, S. Stemmer, Influence of orientation on the contrast of high-angle annular dark-field images of silicon, Physical Review B. 76 (2007) 1–7.

[42] P. Rez, Can high-angle annular dark field scattering be represented by a local operator?, Ultramicroscopy. 81 (2000) 195–202.

[43] P. Voyles, Depth-dependent imaging of individual dopant atoms in silicon, Microscopy and Microanalysis. 10 (2004) 291–300.

[44] K. Watanabe, T. Yamazaki, I. Hashimoto, M. Shiojiri, Atomic-resolution annular dark-field STEM image calculations, Physical Review B. 64 (2001) 1–5.

[45] O. Scherzer, Uber einige Fehler von Elektronenlinsen, Arbeit. (1936) 593.

[46] S.J. Pennycook, P.D. Nellist, eds., Scanning Transmission Electron Microscopy, Springer, 2011.

[47] P. Hawkes, The long road to spherical aberration correction, Biology of the Cell. 93 (2001) 432–439.

[48] O. Krivanek, N. Dellby, A. Spence, R. Camps, L. Brown, Aberration correction in the STEM, Institute of Physics Conference Series. 153 (1997) 35–40.

[49] P.W. Hawkes, Aberration correction past and present., Philosophical Transactions. Series A, Mathematical, Physical, and Engineering Sciences. 367 (2009) 3637–64.

[50] P. Nellist, J. Rodenburg, Beyond the conventional information limit: the relevant coherence function, Ultramicroscopy. 54 (1994) 61–74.

[51] O. Krivanek, Towards sub-Å electron beams, Ultramicroscopy. 78 (1999) 1–11.

[52] P.D. Nellist, M.F. Chisholm, N. Dellby, O.L. Krivanek, M.F. Murfitt, Z.S. Szilagyi, et al., Direct sub-angstrom imaging of a crystal lattice., Science. 305 (2004) 1741.

[53] A. Bleloch, A. Lupini, Imaging at the picoscale, Materials Today. 7 (2004) 42–48.

[54] Lord Rayleigh, On the theory of optical images with special reference to the microscope, Philos. Mag. 42(5) (1896) 167–195.

[55] P. XU, E. Kirkland, J. Silcox, R. Keyse, High-resolution imaging of silicon (111) using a 100 keV STEM, Ultramicroscopy. 32 (1990) 93–102.

[56] P.E. Batson, N. Dellby, O.L. Krivanek, Sub-ångstrom resolution using aberration corrected electron optics, Nature. 418 (2002) 617–20.

[57] P. Batson, Aberration correction results in the IBM STEM instrument, Ultramicroscopy. 96 (2003) 239–249.

[58] R. Erni, M. Rossell, C. Kisielowski, U. Dahmen, Atomic-Resolution Imaging with a Sub-50-pm Electron Probe, Physical Review Letters. 102 (2009) 1–4.

[59] H. Sawada, Y. Tanishiro, N. Ohashi, T. Tomita, F. Hosokawa, T. Kaneyama, et al., STEM imaging of 47-pm-separated atomic columns by a spherical aberration-corrected electron microscope with a 300-kV cold field emission gun, Journal of Electron Microscopy. 58 (2009) 357–61.

[60] E. Ward, I. Arslan, P. Midgley, Direct visualisation, by aberration-corrected electron microscopy, of the crystallisation of bimetallic nanoparticle catalysts, Chem. Commun …. (2005) 5805–5807.

[61] N. Shibata, S.D. Findlay, S. Azuma, T. Mizoguchi, T. Yamamoto, Y. Ikuhara, Atomic-scale imaging of individual dopant atoms in a buried interface., Nature Materials. 8 (2009) 654–8.

[62] S.D. Findlay, N. Shibata, Y. Ikuhara, What atomic resolution annular dark field imaging can tell us about gold nanoparticles on TiO(2) (110), Ultramicroscopy. 109 (2009) 1435–46.

[63] L. Marks, Experimental studies of small particle structures, Reports on Progress in Physics. 57 (1999).

[64] J. Ascencio, M. Pérez, M. José-Yacamán, A truncated icosahedral structure observed in gold nanoparticles, Surface Science. 447 (2000) 73–80.

[65] W.K. Epting, J. Gelb, S. Litster, Resolving the Three-Dimensional Microstructure of Polymer Electrolyte Fuel Cell Electrodes using Nanometer-Scale X-ray Computed Tomography, Advanced Functional Materials. 22 (2012) 555–560.

[66] L. Holzer, F. Indutnyi, P.H. Gasser, B. Münch, M. Wegmann, Three-dimensional analysis of porous BaTiO3 ceramics using FIB nanotomography., Journal of Microscopy. 216 (2004) 84–95.

[67] A. Koster, U. Ziese, Three-dimensional transmission electron microscopy: a novel imaging and characterization technique with nanometer scale resolution for materials science, The Journal of Physical Chemistry B. 104 (2000) 9368–9370.

[68] J. Radon, On the Determination of Functions from Their Integral Values along Certain Manifolds., IEEE Transactions on Medical Imaging. 5 (1986) 170–6.

[69] M. Weyland, P.A. Midgley, J.M. Thomas, Electron tomography of nanoparticle catalysts on porous supports: A new technique based on Rutherford scattering, The Journal of Physical …. 105 (2001) 7882–7886.

[70] M. Weyland, Electron tomography of catalysts, Topics in Catalysis. 21 (2002) 175–183.

[71] L.C. Gontard, R.E. Dunin-Borkowski, M.H. Gass, A.L. Bleloch, D. Ozkaya, Three-dimensional shapes and structures of lamellar-twinned fcc nanoparticles using ADF STEM., Journal of Electron Microscopy. 58 (2009) 167–74.

[72] S. Sueda, K. Yoshida, N. Tanaka, Quantification of metallic nanoparticle morphology on TiO(2) using HAADF-STEM tomography., Ultramicroscopy. 110 (2010) 1120–1127.

[73] Z. Saghi, D.J. Holland, R. Leary, A. Falqui, G. Bertoni, A.J. Sederman, et al., Three-dimensional morphology of iron oxide nanoparticles with reactive concave surfaces. A compressed sensing-electron tomography (CS-ET) approach., Nano Letters. 11 (2011) 4666–73.

[74] K.J. Batenburg, S. Bals, J. Sijbers, C. Kübel, P. a Midgley, J.C. Hernandez, et al., 3D imaging of nanomaterials by discrete tomography., Ultramicroscopy. 109 (2009) 730–40.

[75] S. Van Aert, K.J. Batenburg, M.D. Rossell, R. Erni, G. Van Tendeloo, Three-dimensional atomic imaging of crystalline nanoparticles., Nature. 470 (2011) 374–7.

[76] S. Bals, M. Casavola, M.A. van Huis, S. Van Aert, K.J. Batenburg, G. Van Tendeloo, et al., Three-dimensional atomic imaging of colloidal core-shell nanocrystals., Nano Letters. 11 (2011) 3420–4.

[77] A.Y. Borisevich, Depth sectioning of aligned crystals with the aberration-corrected scanning transmission electron microscope, Journal of Electron Microscopy. 55 (2006) 7–12.

[78] E.C. Cosgriff, a J. D'Alfonso, L.J. Allen, S.D. Findlay, a I. Kirkland, P.D. Nellist, Three-dimensional imaging in double aberration-corrected scanning confocal electron microscopy, part I: elastic scattering, Ultramicroscopy. 108 (2008) 1558–66.

[79] G. Behan, E.C. Cosgriff, A.I. Kirkland, P.D. Nellist, Three-dimensional imaging by optical sectioning in the aberration-corrected scanning transmission electron microscope., Philosophical Transactions. Series A, Mathematical, Physical, and Engineering Sciences. 367 (2009) 3825–44.

[80] C. Colliex, N. Brun, Multi-dimensional and multi-signal approaches in scanning transmission electron microscopes, … of the Royal …. (2009).

[81] R.F. Egerton, M. Malac, EELS in the TEM, Journal of Electron Spectroscopy and Related Phenomena. 143 (2005) 43–50.

[82] J. LeBeau, S. Findlay, Quantitative HAADF-STEM and EELS, Microscopy and …. 14 (2008) 2007–2008.

[83] L.J. Allen, A.J. D'Alfonso, S.D. Findlay, J.M. LeBeau, N.R. Lugg, S. Stemmer, Elemental mapping in scanning transmission electron microscopy, Journal of Physics: Conference Series. 241 (2010) 012061.

[84] O.L. Krivanek, M.F. Chisholm, M.F. Murfitt, N. Dellby, Scanning transmission electron microscopy: Albert Crewe's vision and beyond, Ultramicroscopy. (2012).

[85] N.D. Browning, M.F. Chisholm, S.J. Pennycook, Atomic Resolution chemical analysis using a scanning tranmission electron microscope, Nature. (1993).

[86] M. Bosman, V. Keast, J. García-Muñoz, A. D'Alfonso, S. Findlay, L. Allen, Two-Dimensional Mapping of Chemical Information at Atomic Resolution, Physical Review Letters. 99 (2007) 086102.

[87] K. Kimoto, T. Asaka, T. Nagai, M. Saito, Element-selective imaging of atomic columns in a crystal using STEM and EELS, Nature. 450 (2007) 702–704.

[88] D.A. Muller, L.F. Kourkoutis, M. Murfitt, J.H. Song, H.Y. Hwang, J. Silcox, et al., Atomic-scale chemical imaging of composition and bonding by aberration-corrected microscopy., Science (New York, N.Y.). 319 (2008) 1073–6.

[89] J.J. Friel, C.E. Lyman, X-ray mapping in electron-beam instruments., Microscopy and Microanalysis. 12 (2006) 2–25.

[90] R. Darji, A. Howie, Scattering corrections in small particle imaging, Micron. 28 (1997) 95–100.

[91] D.B. Williams, C.B. Carter, Transmission Electron Microscopy: A Textbook for Materials Science, Springer; 2nd ed. 2009 edition, 2009.

[92] C. Lyman, Microanalysis of catalysts by analytical electron microscopy, Journal of Molecular Catalysis. 20 (1983) 357 – 368.

[93] C. Lyman, H. Stenger, J. Michael, Analytical electron microscopy of a sulfur-poisoned palladium catalyst with a dedicated STEM, Ultramicroscopy. 22 (1987) 129–133.

[94] R. Prestvik, Bimetallic Particle Formation in Pt–Re/Al2O3Reforming Catalysts Revealed by Energy-Dispersive X-Ray Spectrometry in the Analytical Electron Microscope, Journal of Catalysis. 176 (1998) 246–252.

[95] J. Liu, Scanning transmission electron microscopy and its application to the study of nanoparticles and nanoparticle systems., Journal of Electron Microscopy. 54 (2005) 251–78.

[96] ergio I. Sanchez, M.W. Small, J. Zuo, R.G. Nuzzo, Structural Characterization of PtPd and PdPt CoreShell Nanoclusters at Atomic Resolution, Journal of the American Chemical Society. 131 (2009) 8683–9.

[97] A. Herzing, M. Watanabe, J.K. Edwards, M. Conte, Z.-R. Tang, G.J. Hutchings, et al., Energy dispersive X-ray spectroscopy of bimetallic nanoparticles in an aberration corrected scanning transmission electron microscope, Faraday Discussions. 138 (2008) 337.

[98] J. Titchmarsh, EDX spectrum modelling and multivariate analysis of sub-nanometer segregation, Micron. 30 (1999) 159–171.

[99] M. Van Heel, J. Frank, Use of multivariate statistics in analysing the images of biological macromolecules, Ultramicroscopy. 6 (1981) 187–194.

[100] J.M. Titchmarsh, S. Dumbill, Multivariate statistical analysis of FEG-STEM EDX spectra, Journal of Microscopy. 184 (1996) 195–207.

[101] M. Watanabe, D.. Williams, Atomic-level detection by X-ray microanalysis in the analytical electron microscope, Ultramicroscopy. 78 (1999) 89–101.

[102] F.L. Deepak, R. Esparza, B. Borges, X. Lopez-Lozano, M. Jose-Yacaman, Direct Imaging and Identification of Individual Dopant Atoms in MoS 2 and WS 2 Catalysts by Aberration Corrected Scanning Transmission Electron Microscopy, ACS Catalysis. 1 (2011) 537–543.

[103] D.B. Williams, High resolution X-ray mapping in the STEM, Journal of Electron Microscopy. 51 (2002) 113S–126.

[104] M. Watanabe, D.B. Williams, The quantitative analysis of thin specimens: a review of progress from the Cliff-Lorimer to the new zeta-factor methods., Journal of Microscopy. 221 (2006) 89–109.

[105] M. Watanabe, D.W. Ackland, a. Burrows, C.J. Kiely, D.B. Williams, O.L. Krivanek, et al., Improvements in the X-Ray Analytical Capabilities of a Scanning Transmission Electron Microscope by Spherical-Aberration Correction, Microscopy and Microanalysis. 12 (2006) 515.

[106] L.J. Allen, Electron microscopy: new directions for chemical maps., Nature Nanotechnology. 3 (2008) 255–6.

[107] L.J. Allen, A.J. D'Alfonso, B. Freitag, D.O. Klenov, Chemical mapping at atomic resolution using energy-dispersive x-ray spectroscopy, MRS Bulletin. 37 (2012) 47–52.

[108] G. Lutz, Silicon drift and pixel devices for X-ray imaging and spectroscopy., Journal of Synchrotron Radiation. 13 (2006) 99–109.

[109] K. Keil, R. Fitzgerald, K.F.J. Heinrich, Celebrating 40 Years of Energy Dispersive X-Ray Spectrometry in Electron Probe Microanalysis: A Historic and Nostalgic Look Back into the Beginnings, Microscopy and Microanalysis. 15 (2009) 476–483.

[110] J. McCarthy, J. Friel, P. Camus, Impact of 40 Years of Technology Advances on EDS System Performance, Microscopy and Microanalysis. 15 (2009) 484–490.

[111] N.W.M. Ritchie, D.E. Newbury, J.M. Davis, EDS measurements of X-ray intensity at WDS precision and accuracy using a silicon drift detector., Microscopy and Microanalysis. 18 (2012) 892–904.

[112] D.T. Tran, I.P. Jones, J. a. Preece, R.L. Johnston, C.R. Brom, TEM characterization of chemically synthesized copper–gold nanoparticles, Journal of Nanoparticle Research. 13 (2011) 4229–4237.

[113] M. Watanabe, Z. Horita, M. Nemoto, Absorption correction and thickness determination using the zeta factor in quantitative X-ray microanalysis, Ultramicroscopy. 65 (1996) 187–198.

[114] G. Cliff, G.W. Lorimer, The quantitative analysis of thin specimens, Journal of Microscopy. 103 (1975) 203–207.

[115] M. Watanabe, D.B. Williams, Y. Tomokiyo, Comparison of detectability limits for elemental mapping by EF-TEM and STEM-XEDS, Micron. 34 (2003) 173–183.

[116] M. Watanabe, A. Burrows, A.A. Herzing, C.J. Kiely, D.B. Williams, G. Hutchings, et al., High Resolution X-Ray Elemental Mapping of Nanoparticles in the STEM, Microscopy and Microanalysis. 10 (2004) 468–469.

[117] D.E. Newbury, R.L. Myklebust, Simulation of electron-excited X-ray spectra with NIST-NIH Desktop Spectrum Analyzer (DTSA), Surface and Interface Analysis. 37 (2005) 1045–1053.

[118] N.W.M. Ritchie, A new Monte Carlo application for complex sample geometries, Surface and Interface Analysis. 37 (2005) 1006–1011.

[119] D. Williams, D. Ackland, M. Watanabe, Quantification of X-ray Spectrum Images in the Analytical Electron Microscope: Progress Toward Single-Atom-Detection Limits, Microscopy and Microanalysis. 13 (2007) 1348–1349.

[120] P.D. Nellist, S.J. Pennycook, Accurate structure determination from image reconstruction in ADF STEM, Journal of Microscopy. 190 (1998) 159–170.

[121] P.W. Hawkes, J.C.H. Spence, eds., Science of Microscopy, New York, NY, Springer New York, 2008.

Chapter 3

HAADF STEM of catalyst nanoparticles

In this chapter, HAADF STEM is used to study various core-shell particle designs pre- and post- fuel cell cycling. The size distribution, morphology, Pt shell coverage is investigated qualitatively. This is related to, and compared with, information about their activity and stability gained from XRD, EXAFS, WAXS, SAXS and electrochemical techniques. Finally the beam sensitive nature of these nanoparticles is discussed.

3.1 Catalysts studied in this thesis

In this dissertation palladium core, platinum shell particles supported on an amorphous carbon matrix were investigated. A controlled surface reaction forms a Pd hydride which reacts with a $Pt(acac)_2$ precursor [1] to deposit Pt as a shell around a 3nm Pd core [1]. The amount of $Pt(acac)_2$ was varied to achieve the desired coverage of monolayers of Pt according to the equation:

$$mass_{precursor} = \frac{wt\%_{Pd} \times mass_{Pd/C} \times D \times RMM_{Pt(acac)_2}}{RMM_{Pd}} \quad 3.1$$

Where $wt\%_{Pd}$ is the Pd loading of the mass of Pd catalyst on the carbon support ($mass_{Pd/C}$), D is the dispersion[2] of Pd, and RMM is the relative molecular mass.

[1] (acac) = acetylacetonate, a common bidentate ligand
[2] Dispersion is defined as the proportion of surface atoms with respect to the total number of atoms.

The crystalline structure of both Pt and Pd is face-centred cubic (see Figure 3.1) and the lattice parameters are 3.92Å and 3.89 Å respectively. The lattice mismatch means there is likely to be a strain at the interface of the Pd and Pt core shell boundary.

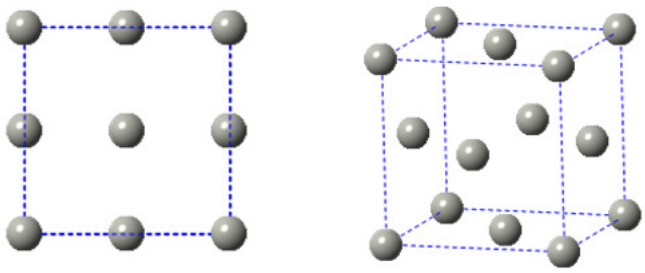

Figure 3.1 Crystal structure of a unit cell of a face centred crystal, which applies to both Pd and Pt: in the <001> orientation (left) and rotated to show the atoms in the centre of each face (right).

Nanoparticles of fcc metals do not form perfect spheres as it is thermodynamically more favourable to be faceted. Common facets are low index planes of {100}, {111} [23]. Very occasionally facets of higher index planes such as {411} are observed but are usually very small micro-facets. It is more energetically favourable for particles of this size to have steps and kinks that terminate lower index planes or terraces [15]. The notation *n(xyz) x (uvw)* is typically used, where *n* is the number of atoms in a terrace with Miller index *(xyz)*, and *(uvw)* is the index of the step joining terraces.

Several nominal design in thicknesses of Pt shell were considered: ½ monolayer (ML), 2ML and 4ML, where a monolayer is considered to be a complete coverage of the Pd core by one atom thick of Pt. Catalysts were investigated fresh (as synthesised) and post cycling. Electrochemical aging was performed by potential cycling the catalysts 1000 times between 0.6 and 1.0V at 20 mV s^{-1} in oxidising conditions of 1 molar H_2SO_4 at 80°C in a custom designed miniaturised fuel cell. All electrochemical preparations were performed by Anna Wise at the University of Southampton [2,3].

In order to relate the observations of the catalysts to their performance, a brief sketch of their electrochemical characteristics is given here. Samples were prepared by Beatrice Tessier and Anna Wise. For more detail of the work performed by Beatrice Tessier and Anna Wise, see [3,4].

In general, the core-shell designed catalysts show improved activity compared to pure Pt/C and the 2ML design showed dramatically improved stability (see Figure 3.2). XRD and SAXS data showed that particle size increased with shell thickness and from ICP data, it was seen that shell thickness is increased on smaller cores than on larger cores.

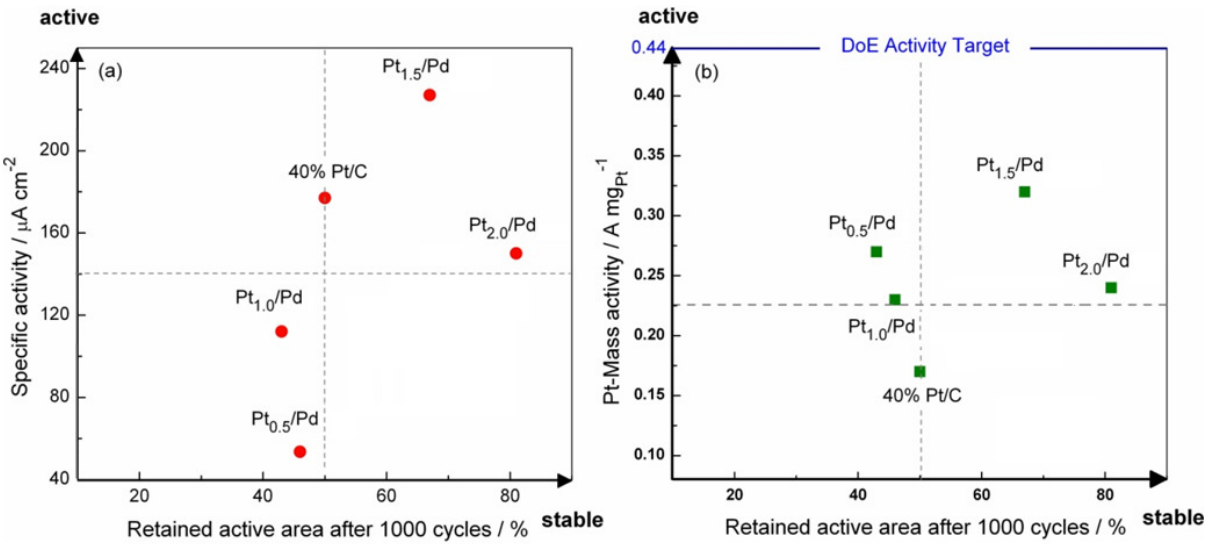

Figure 3.2 Specific activity (current / active surface area of catalyst) and mass activity (current / mass of catalyst) of various designs of core-shell particles as a function of their stability to potential cycling. Core-shell particles with 1.5ML of Pt around a Pd core are shown to be the most active, but those with 2ML are the most stable. For industrial purposes, where stability is of paramount importance, the 2ML design is thus superior (Figure adapted from [4]).

A loss of electrochemical area[3] (ECA) was seen in all of the catalyst samples subjected to potential cycling. EXAFS, WAXS and electrochemical techniques showed that the decrease in ECA was reduced with increasing shell thickness and was attributed to the dissolution of Pd in the acid. For the 4ML design only, the loss of ECA was found to be due to Ostwald ripening [5]. The coordination numbers and Pd-Pd bond length variations observed in the EXAFS suggested a loss of Pd from the system.

Further, a study of the lattice parameters measured from EXAFS indicated the likely formation of smaller or hollow particles on all samples. No direct evidence was seen of particle growth in all

[3] The surface area of a catalyst that is electrochemically active is a good measure of the catalytic activity

samples except the 4ML design, suggesting that coalescence either had not occurred with cycling or could not be detected using these techniques, and that agglomeration of the particles altered by dissolution was possible. Cyclic voltammetry also suggested that there were no isolated Pt particles on the carbon support and that the Pt shell and Pd core behaved as one phase.

3.2 Sample preparation

The freshly synthesised samples were received in powder form and the cycled samples as electrode buttons. The powder was broken up by several methods in order to isolate thinner areas of carbon so that particles could be imaged individually. They were either:

- Crushed between glass slides
- Crushed between static free weighing paper
- Suspended in a low boiling point solvent (e.g. ethanol) and then sonicated with a Hielscher UP100H at a frequency of 30kHz, 100% amplitude, continuous cycle for 20s.

The dispersion was then drop cast deposited on copper TEM grids covered with holey carbon film. The cycled catalyst coated on the electrode button was scraped off using a clean surgical blade and then prepared in the same way.

The first two methods were the most convenient but often led to large variation in the coverage of the sample on the grid and thick areas where the powder was not broken up as effectively. The method of sonication provided the best method for achieving thinner regions from the agglomerated bulk powder (see Figure 3.3) but required longer baking of the sample by heating to 80^{o}C in high vacuum to remove any latent hydrocarbons which could cause carbon contamination growth under the beam.

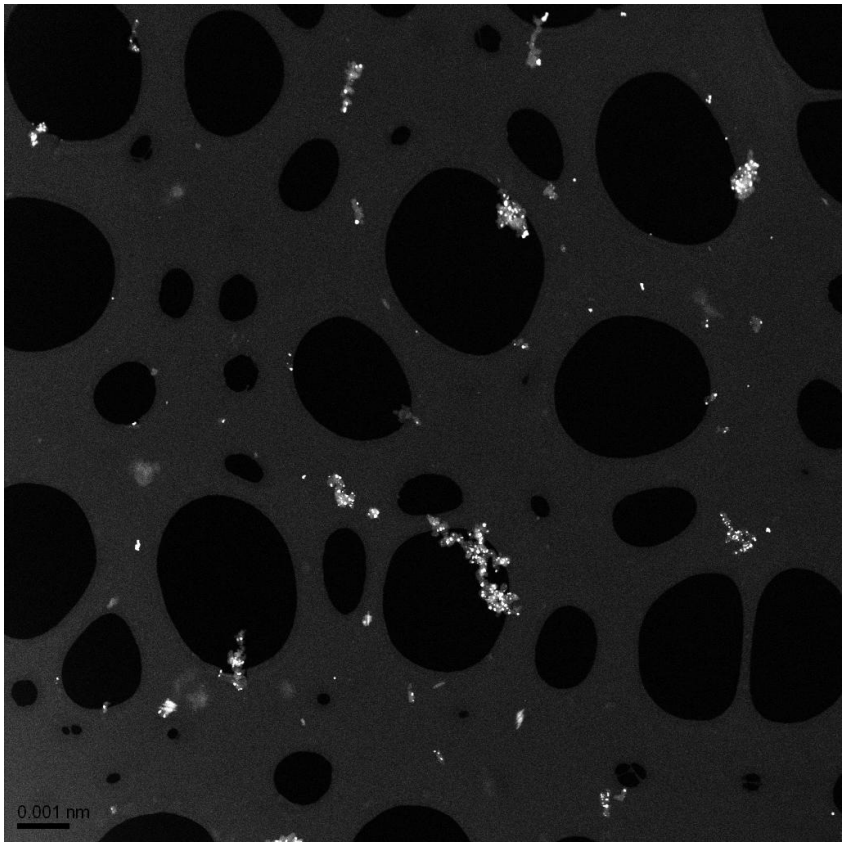

Figure 3.3 HAADF SETM image of smaller pieces of powdered sample, broken up by sonication in ethanol and drop cast onto a hole carbon TEM grid.

Further refinement of the method by using a micromanipulator to deposit the broken up powdered sample onto specific areas of a TEM finder grid enabled the same particle to be located across different experiments and also allowed several samples to be held on the same grid.

3.3 Instrumentation

Three instruments were used chiefly in this thesis (See Figure 3.4):

- JEOL JEM-3000F, an uncorrected FEG TEM/STEM
- Oxford JEOL 2200MCO, a probe forming and image forming (double) spherical aberration corrected FEGTEM with a CEOS hexapoles lens system [6]
- JEOL ARM-200F, a probe corrected STEM with a cold FEG source. The instrument has a built-in system of thermal and magnetic shielding and customised mechanical stability enhancements through the wider column and the hydraulically damped user console. This greatly improves the stability of the microscope and thus the achievable resolution and quality of acquired images. A later upgrade of the EDX system replaced the original SSD detector with 0.22str solid angle with a Centurio detector with 0.8str solid angle.

The details of the various operating parameters and specifications are given in Appendix B. The JEOL ARM-200F microscope was operated by Eiji Okunishi at the JEOL EM facility in Tokyo, Japan. All other data was taken by the author unless otherwise stated.

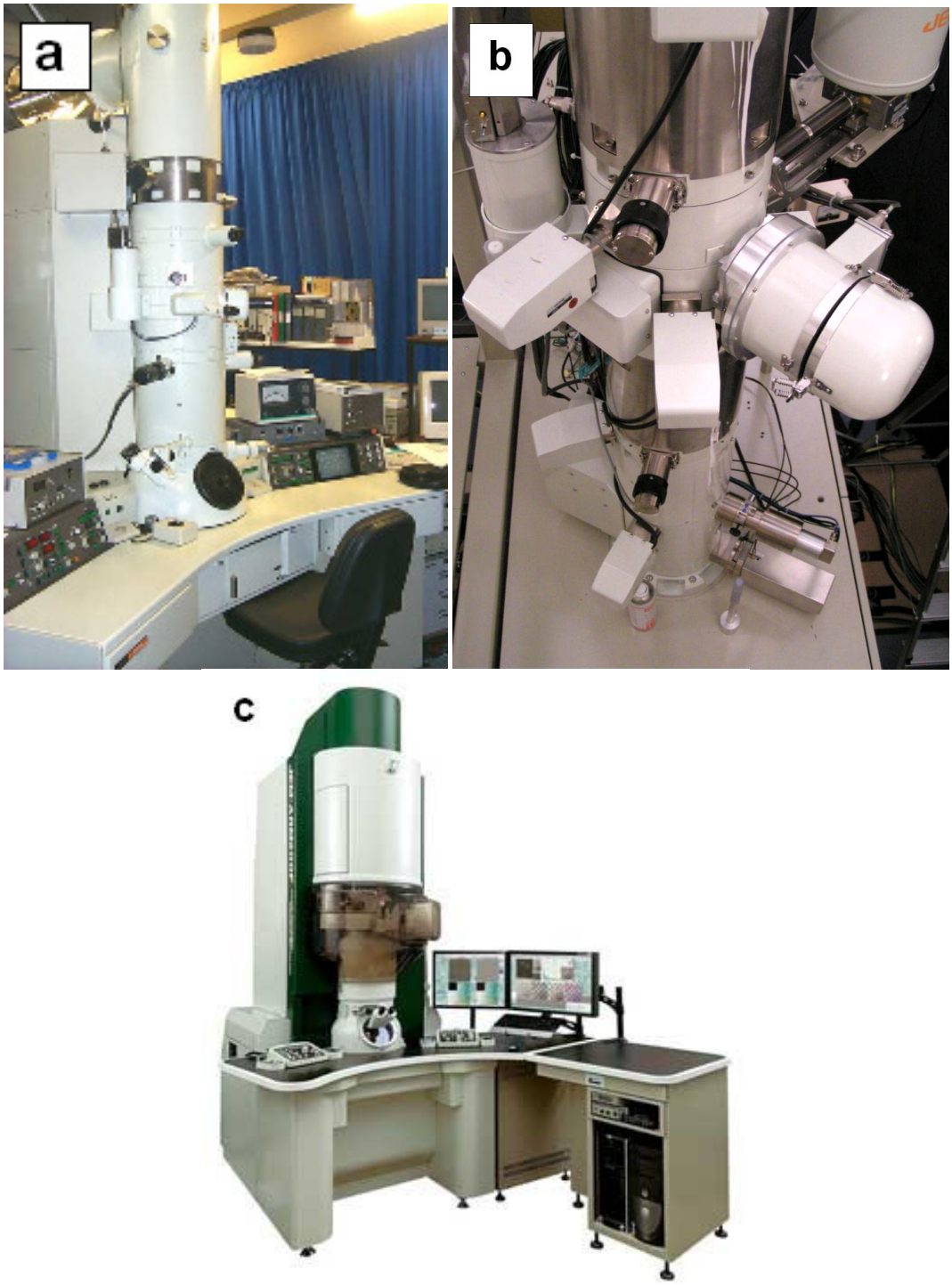

Figure 3.4 Microscopes used in this thesis, clockwise from top left: (a) JEOL JEM 3000F; (b) Oxford-JEOL 2200 MCO instrument from above; (c) JEOL ARM 200F; (Images reproduced from Oxford University Materials Department website and JEOL promotional literature).

3.4 Distribution on support

Given the projection of the 3D to a 2D image, it is not always possible to tell whether the particle is lying above, below or embedded in the support. Studies in TEM have been carried out using the delocalised fringes of the graphitised carbon with defocus to investigate this [7]. Because the lighter carbon of the support is weakly scattering in HAADF STEM, observations of particles at the edges of the support can be to elucidate which surfaces of the particles are available for catalytic activity. Figure 3.5 shows that particles sit on top of the carbon black and have at least one side in contact with the support. As the Pt is deposited onto the Pd cores after the Pd is formed on the carbon support, this means that full 360° shell coverage of the particle is unfeasible.

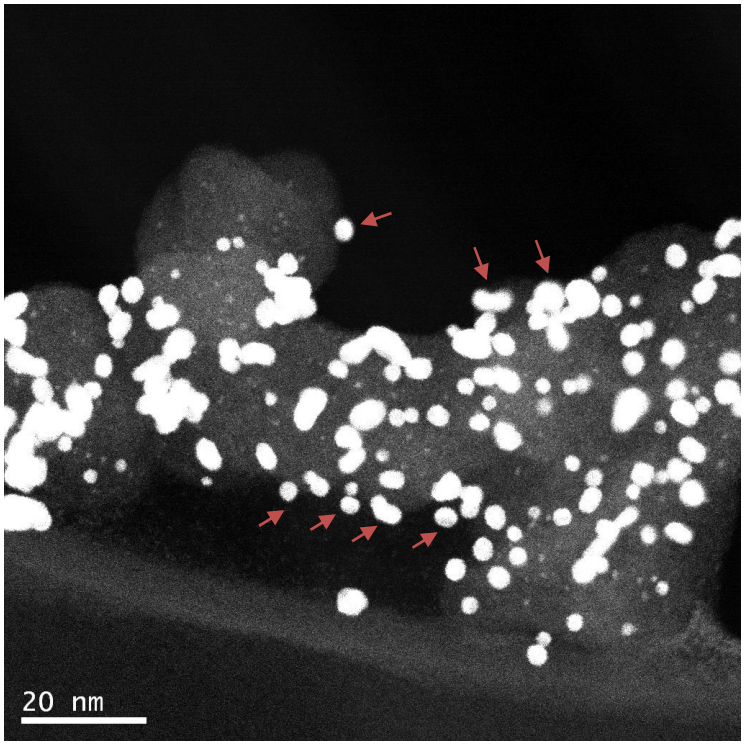

Figure 3.5 HAADF STEM image of a catalyst sample typical of the kind studied, taken with the Oxford-JEOL 2200MCO. The particles indicated with a red arrow are clearly sitting on the surface of the carbon support and not embedded within it.

EXAFS studies inferred that there was no change in the density of the distribution of particles in the sample with cycling and so loss of ECA was attributed to dissolution of Pd from the particle. HAADF STEM images confirm that there is an obvious depletion of nanoparticles from the support after cycling.

3.5 Particle size distribution

The particle size distribution was estimated from medium magnification HAADF STEM images each of various catalyst designs pre and post cycling (Table 3.1). Those particles that were out of focus or obfuscated by other overlapping particles were discarded. In each sample between 100 and 300 particles were investigated to give reasonable statistics.

The analysis was performed in Gatan's Digital Micrograph (DM) software. First a low pass Butterworth filter [8] was applied to the image using a custom DM script to smooth the pixilation noise. Then, an intensity thresholding was used to segment the particles from the support, before variables such as area, perimeter, length, and breadth were measured. An alternative particle size analysis software was written in Matlab (see Appendix C), adapted from the local thresholding method for TEM images in [9] but found to be useful TEM but not for HAADF STEM. This is likely due to the increased ease of edge detection of dark features on a light background typical of bright field TEM images compared to light features on a dark background typical of dark field images.

3.5.1 Equivalent circular diameter (ECD)

The ECD is a standard measurement for a range of particle size techniques. In DM, the number of pixels within an identified particle is counted to give an "area" A, which can be scaled by the pixel dimension to give an area in nm^2. This can then be used to calculate the ECD by the formula:

$$ECD = 2\sqrt{\frac{A}{\pi}} \qquad 3.2$$

The catalysts with thicker shell designs had a larger average diameter but also a larger range of sizes. Cycling marginally increases the size of the particles for 2ML and 4 ML designs and significantly more for the 0.5ML design.

While this definition of diameter gives a good grasp on the particle size, it does not take into account the variation in morphology as the particles are assumed to be circular. As is evident from the micrographs (see for example, Figure 3.5), the catalysts tend to be oblate.

Catalyst	Mean ECD (nm)	standard deviation (nm)	error on mean (nm)	# particles
Pd core	3.84	2.13	0.13	284
0.5 ML	3.78	2.37	0.18	165
1 ML	4.02	2.81	0.21	180
2 ML	4.27	3.07	0.17	246
4 ML	4.41	3.11	0.24	173
0.5 ML cycled	4.13	3.82	0.28	188
2 ML cycled	4.52	4.52	0.35	168
4 ML cycled	4.59	2.81	0.21	178

Table 3.1 Average particle diameter of various catalyst designs pre-cycled, post-cycled. The mean size increases with increasing shell coverage and also with cycling.

3.6 Particle morphology

The shape of the nanoparticle determines the nature of the surface sites available for catalysis. As the micrographs show, particles are rarely spherical, in part due to the synthesis method where the Pd core is supported on one side in the carbon, so growth of the particles and the Pt deposition is limited on one side by the carbon.

The Feret diameter is a common measure of the size of a non uniform object[4]. It can be defined as the distance between two parallel tangential lines of a particle's outline, and as such is often called the *calliper diameter*.[5]

[4] Other diameters exist, including Martin, the Krumbein and the Heywood diameters, see [27]
[5] Interestingly, from Cauchy's second theorem, it can be shown that the Feret diameter averaged over all directions in a convex 2D object is equal to the ratio of the object perimeter and π.

3.6.1 Aspect ratio and flakiness

Aspect ratio[6] is the ratio of the length L to the breadth B of the particle image and gives a sense of the shape of the particle. The breadth is taken here as the minimum Feret diameter and the length the maximum Feret diameter. Flakiness is the ratio of the breadth to the thickness. Since the thickness of the particle is difficult to discern in a projected image, this parameter is of little use in this chapter, but is introduced here for completeness and explored later in chapters 6 and 8.

The mean aspect ratio was constant, within the associated error, across all the designs and also post-cycling (see Table 3.2). The 1ML design showed the largest ratio, with mean length 1.46 that of its mean breadth. The 2ML showing the smallest at 1.33 (see Figure 3.6). Since the difference is so marginal, it would be difficult to attribute any differences in catalytic performance to the aspect ratio.

Catalyst	Mean Aspect Ratio	standard deviation	error on the mean
Pd core	1.42	0.71	0.04
0.5 ML	1.35	0.71	0.06
1 ML	1.46	0.83	0.06
2 ML	1.33	0.57	0.04
4 ML	1.54	0.61	0.05
0.5 ML cycled	1.32	0.83	0.06
2 ML cycled	1.33	0.95	0.07
4 ML cycled	1.39	0.63	0.05

Table 3.2 Mean aspect ratio across the different catalyst samples

[6] Confusingly, the conventional understanding of aspect ratio from image processing as the maximum to the minimum Feret diameter is contradicted by ISO 9276-6 which inverts the relationship to keep the value between 0 and 1. This bureaucracy is ignored in this work.

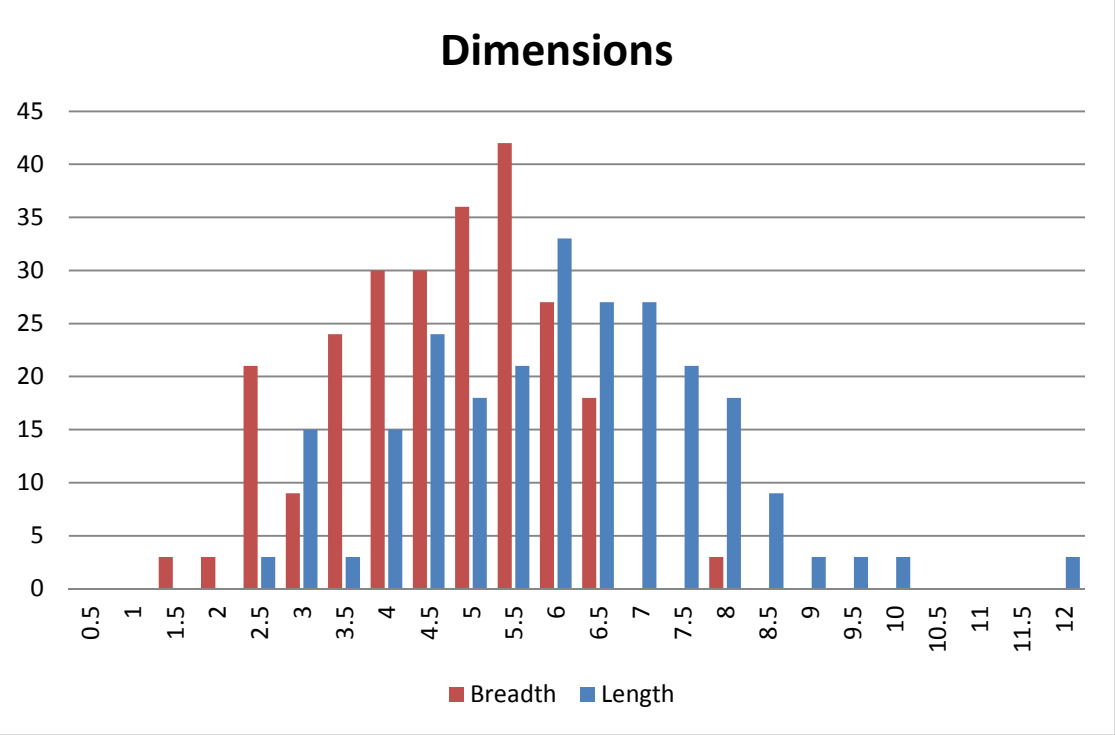

Figure 3.6 Histogram distribution of the maximum (length) and minimum (breadth) Feret diameter of the 2ML design catalyst, showing the large variance in the size of the particles

3.6.2 Roundness

Roundness is a useful parameter to describe a particle shape on the mesoscale, where a circle has a value of 1. Confusingly, several definitions exist; the relationship between the perimeter squared and the projected area is used here:

$$Roundness = \frac{4\pi A}{P^2} \qquad 3.3$$

Both the perimeter and projected area can be accurately measured, whereas the length of a particle is subject to variation depending on the direction chosen. In addition, this gives a gauge of the convexity or concavity of the particle.

All particles show a similar measure of mean roundness of 0.8, which indicates a convex shape. However, there is significant variance in the statistics. This could be potentially due to the pixilation of the images or the roughness of the particle outline defined by the thresholding, which will both give an increased measure of perimeter for smaller particles. The standard error on the mean is on the order of

0.05, which indicates that the calculated mean roundness is a good representation of the statistical mean.

The roundness of the freshly synthesised particles is uniform across the designs with the exception of the 4ML particles, which show more convexity. This is not clearly understood and might be due to the additional Pt deposition causes more islands of Pt on the surface facets of the Pd core. Curiously, the roundness of the 4ML design increases with cycling, which is unexplained.

While the 0.5ML particle becomes rougher with cycling, the 2ML design retains its roundness, supporting the electrochemical observation that it is the most stable to potential cycling.

Catalyst	Mean Roundness	standard deviation	error
Pd core	0.81	0.56	0.03
0.5 ML	0.84	0.68	0.05
1 ML	0.80	0.72	0.05
2 ML	0.86	0.55	0.04
4 ML	0.74	0.43	0.03
0.5 ML cycled	0.67	0.73	0.05
2 ML cycled	0.89	1.07	0.08
4 ML cycled	0.82	0.08	0.05

Table 3.3 Measure of mean roundness across the catalyst samples

3.6.3 Faceting

At higher resolutions it is clear that the particles are in fact not round but faceted, with low energy surfaces of {111}, {100} (see Figure 3.7). This allows for the identification of active sites and strongly preferred catalytic surfaces [10–12].

Furthermore, the intensity of the core regions in some particles suggests that there has been depletion of Pd (see Figure 3.8, red arrow) which corresponds to the EXAFS observations. Most particles show a shell like structure on three of four sides, which corresponds to the partial embedding of the particle on the carbon (the undecorated side).

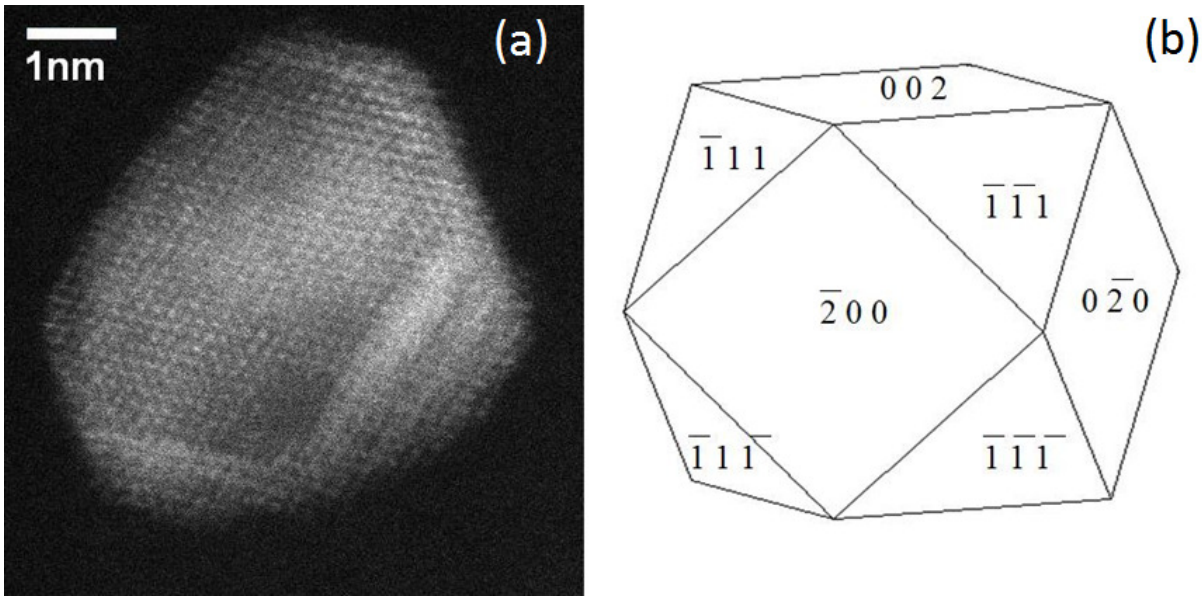

Figure 3.7 (a) Faceted particle imaged at 200kV on the Oxford JEOL 2200MCO. **(b)** Model nanoparticle with low energy surfaces.

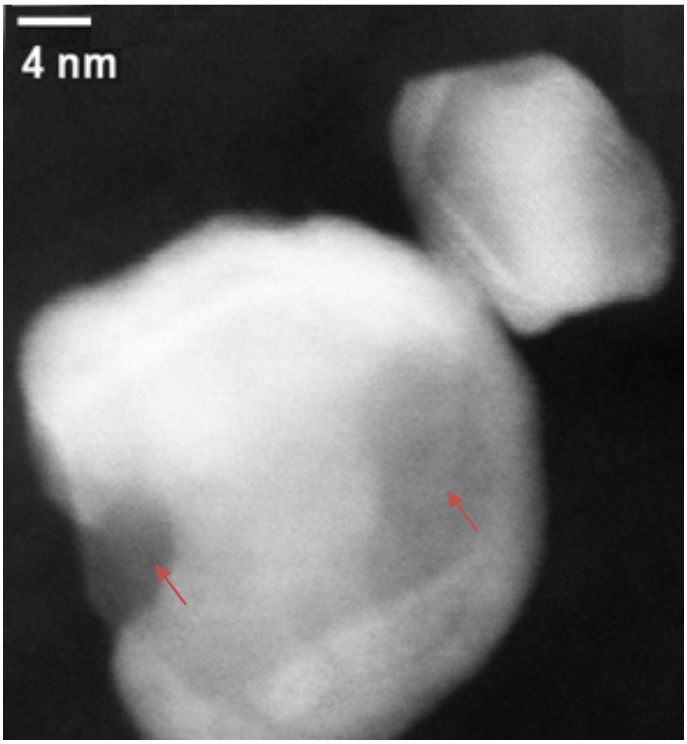

Figure 3.8 Some particles show decreased scattering from larger areas, potentially due to hollow centres (indicated by the red arrows)

3.7 Pt shell coverage

Catalytic processes are primarily concerned with the surface atoms of nanoparticle catalysts; therefore it is important to understand the precise nature of the shell coverage and thickness. Even while individual columns are not resolved, the contrast of Pt around the Pd core can often be clearly delineated at lower resolution.

Preferential deposition on the low co-ordination sites, such as edges and corners of particles, occurs (see Figure 3.9). This has been demonstrated by Coq et al. for the deposition of germanium on rhodium [13] and Candy et al for tin on rhodium [14]. Complete shell coverage is not seen, indicated by the bands of intensity on the bottom left of Figure 3.9, which suggest decoration on stepped edges across a facet. This corresponds to increased activity since active sites are higher in number at stepped edges [15].

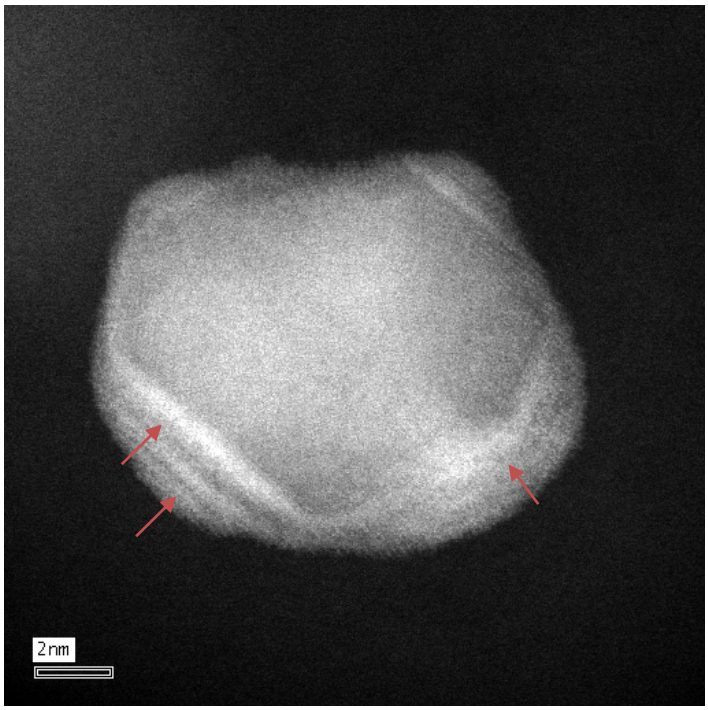

Figure 3.9 Edge decoration of a 2ML design nanoparticle, indicated by the red arrows. The brighter intensity is indicative of a higher Z element scattering since the morphology of the nanoparticle makes contrast due to a thickness change highly unlikely.

The 2ML designed particle in Figure 3.10 shows bright intensity at the edges. The two neighbouring columns highlighted by the red arrows suggest a composition change as the difference in intensities (shown in the line profile) rule out a cliff edge due to thickness and is more likely to be due to Pt decoration.

There is also a large uniform intensity region when viewed along the [110] direction perhaps suggesting large (110) facets. Facets of (110) are thermodynamically less favourable in fcc structures than (111) and (100). However, it is possible that a large (110) facet is terminated by stepped edges onto (100) and (111) faces. Evidence of this is seen in projection (top left of particle in Figure 3.10, indicated by the red box)

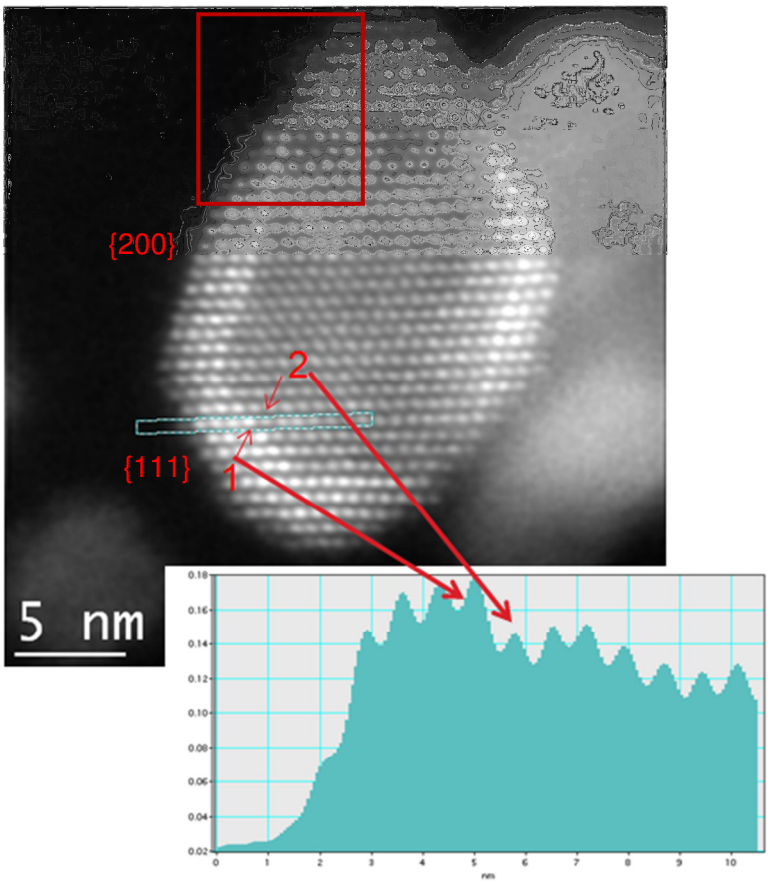

Figure 3.10 Calibrated HAADF image of a core-shell nanoparticle with 2ML design showing clear core-shell structure. Adjacent columns indicated by 1 and 2 show a significant decrease in scattered intensity, as can be seen clearly from the line scan (inset). The red box shows areas of stepped structure in projection.

While the Pt coverage of 2ML design was found by surface sensitive techniques such as high sensitivity low energy ion scattering (HS-LEIS) to be 65 % [4,16], it is not possible to tell from a

single image what the thickness of the shell is without comparison to simulations; the projection of the 3D structure means that neighbouring columns of bright intensity could correspond not to a shell thickness but a thinly decorated facet.

Moreover, given that the amount of Pt used in the synthesis process is chosen for complete shell coverage, and the observed paucity of the shell coverage, which seems often to be limited to edge decoration, the question arises: where has the Pt gone?

The location of the Pt cannot be answered by single images of particles alone without further analysis. Compositional data is required and will be explored in the following chapters. In the meantime, the deleterious effects of the beam on the sample are explored to highlight the delicacy of the structure of these nanoparticles and underscore why it is necessary to extract as much information as possible from single images and limited beam exposure.

3.8 Beam-Particle Interactions

As with all characterisation techniques there is the necessity to understand if and how the technique itself might affect the material's structure.

3.8.1 Particle Stability

This is particularly important when investigating nanoparticles, as the high surface area to volume ratio causes excess free surface energy and therefore surface mobility during imaging (see Figure 3.11). Moreover, the existence of melting point depression [see for example 11–13] means that nanoparticles are even less stable as size decreases.

This excess energy is thought to be responsible for the high catalytic activity witnessed in nanoparticles, not present in the bulk material [20] but can cause distortion of the sample during imaging and analysis such that the image may no longer correspond to the sample imaged over the course of the acquisition.

3.8.2 Beam damage to sample

While aberration correction offers many benefits to microanalysis, the flip side of the coin is that the same features, the high current density due to the improved brightness and smaller probe, also cause problems to beam sensitive samples.

3.8.2.1 Knock-on damage

The atomic displacement caused by collisions of the electron beam is termed knock-on damage. Excessive knock due to a prolonged exposure of the focussed beam can further result in drilling of holes in the sample. Knock on is known to decrease with increase in atomic number and also to decrease with decreasing accelerating voltage [21]. Thus voltages of less than 100kV are recommended to reduce this type of damage.

		Ag	**Pt**
Atomic number (Z)		47	78
T_d (eV)		28	33
T_s (eV)		3.0 – 6.0	5.9 – 11.8
T (eV)	**100kV**	2.23	1.23
	200kV	4.89	2.69
	300kV	7.90	4.37
	400kV	11.3	6.26

Table 3.4 The comparison between maximum transferable kinetic energy T at different accelerating voltages with T_d the displacement and T_s the exit surface sputtering energies (data summarised from [22]). Pt should theoretically not sputter or displace. No data is available for Pd, but the trends are monotonic. Ag is one atomic number heavier than Pd and so is a useful point of comparison here. This suggests that sputtering of Pd is a real concern at beam energies greater than 100kV. However, this data is from bulk samples, nanoparticles are subject to weaker bonds than bulk crystal so the likelihood of displacement and sputtering is still real.

3.8.2.2 Sample heating

The energy imparted to the sample by the incident electron beam can cause the particle to heat up by exciting phonon modes in the crystalline sample. While the phonons don't contribute significantly to TDS, since the frequency of oscillations is low, increases in temperature allows the particle to reconstruct into other structures [23]. This can be clearly seen in Figure 3.12. To the author's

knowledge, there has been no study done on the temperature increase due to the incident electron beam, although the effects can clearly be seen experimentally. Secondary processes such as defect aggregation may also be driven by temperature.

Radiolysis is another common damage mechanism characterised by ionisation and the dissociation of bonds due to inelastic scattering with the atomic electrons[24]. Its effects are inversely proportional to the accelerating voltage. However radiolysis in conducting metal nanoparticles, with their high electron density, is quickly quenched as broken bonds will heal on the order of femtoseconds [25]. If it was a dominant damage mechanism, this could be observed in changes of the fine structure of EELS spectra since the bonding states would be changed.

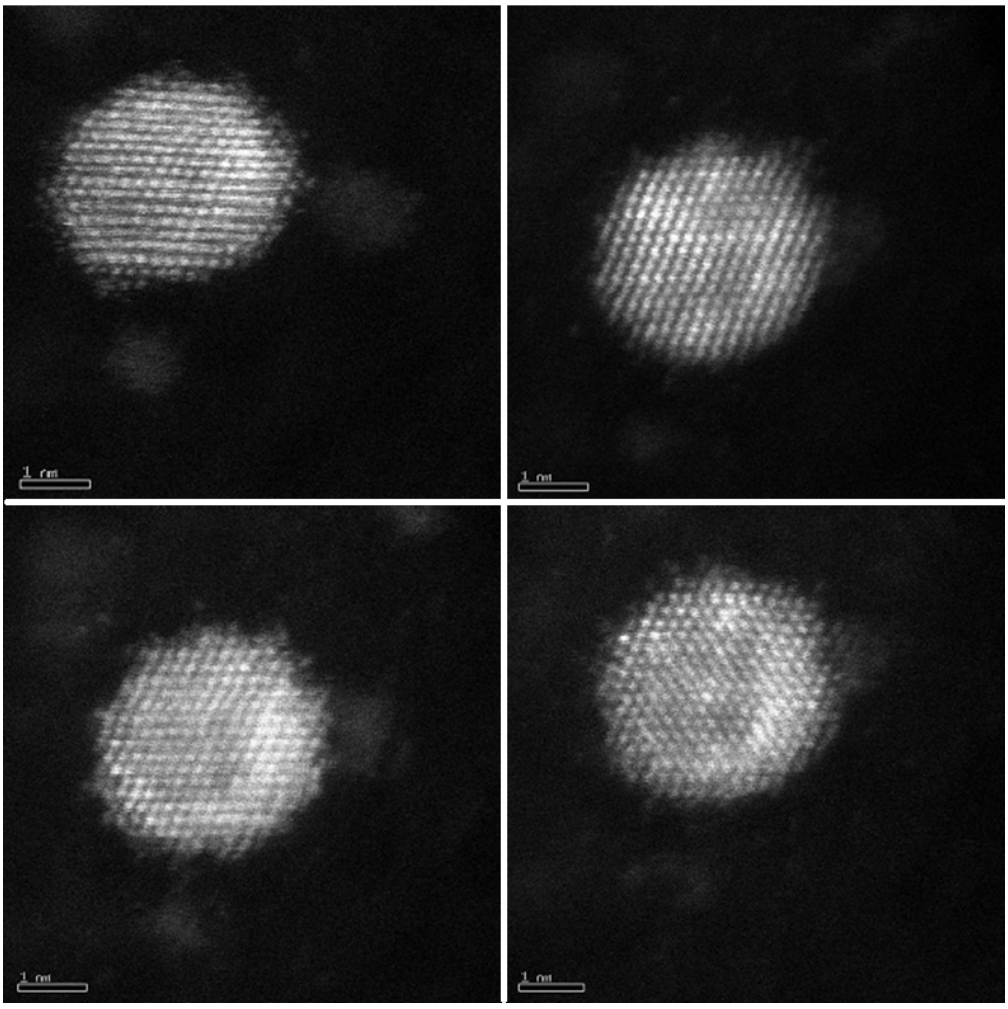

Figure 3.11 Consequtive images of the same particle taken on the Oxford JEOL 2200MCO at 200kV showing mobility of surface atom and particle reconstruction due to heating. Interestingly, the Pt segregation can be seen to change over time under the beam.

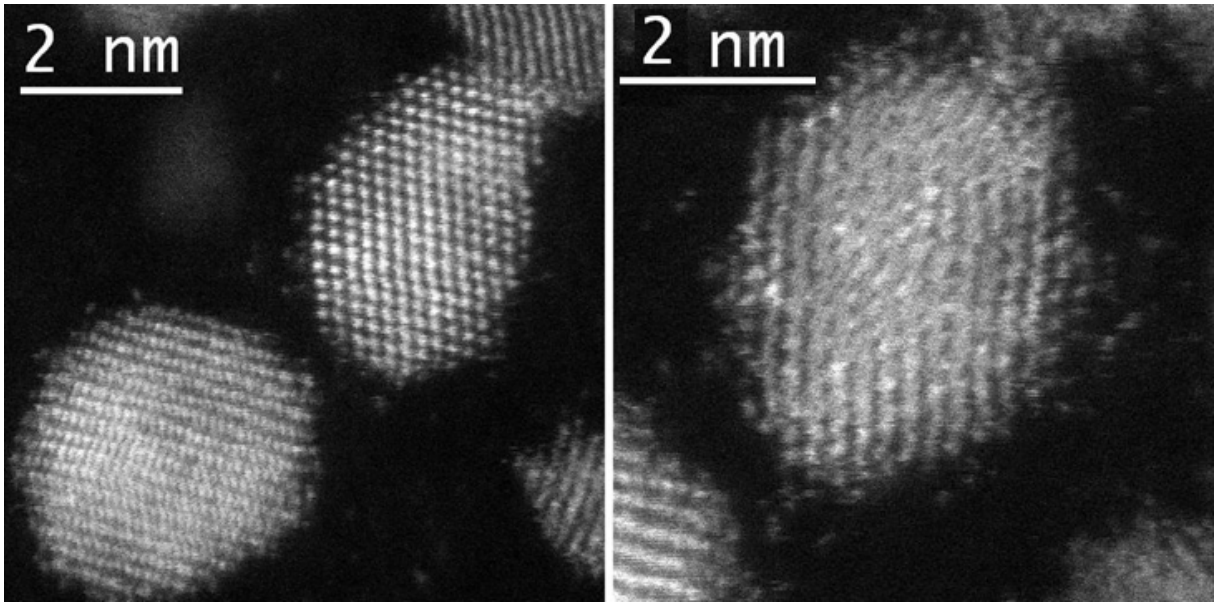

Figure 3.12 2ML nanoparticle imaged with the Oxford JEOL 2200MCO. Even within the time taken to acquire two successive frames (~10s) it is clear that particle has reconstructed, especially at the surface. Image size of 512 x 512 pixels with pixel dwell time of 38µs.

3.8.3 Contamination

Attraction of hydrocarbons to the negative electron beam, where they are cracked and deposited under the beam, causes the accumulation of a layer of amorphous carbon contamination on the sample. This makes the sample thicker and reduces image contrast. Problematically it also decreases the effect of channelling since the atomic columns are no longer directly coupled to the beam. The beam would have to traverse the amorphous carbon first, where it is prone to spreading, thus reducing the available resolution. Contamination can be reduced by gentle plasma cleaning of the sample or baking in vacuum, often at temperatures of about 80°C. Often, the main culprit is the TEM grid; treating the grid before the sample is deposited greatly reduces the contamination.

3.8.4 Mistilt and rotation

Nanoparticles on industrial carbon black are prone to movement under the beam. There are two mechanisms for this:

- the support itself is not firmly fixed to the carbon of the TEM grid and can often be protruding into vacuum.

- the particle is not fixed on the carbon support and can thus rotate under the beam

Figure 3.13 shows a 0.5ML design particle where an on axis image does not show clear core-shell structure (a). In the subsequent scan (b), the particle has rotated so that it is no longer on zone axis and strong channelling conditions around the edges show greater scattered intensity, which could be suggestive of the presence of a Pt shell. It must be remembered that channelling of the probe when imaging columns on-axis can boost the scattering strongly, so increased intensity may not necessarily be compositional in origin. Thus mistilt of particles can lead to misidentification of core-shell structure. This issue is explored in greater depth in Section 5.5.4.

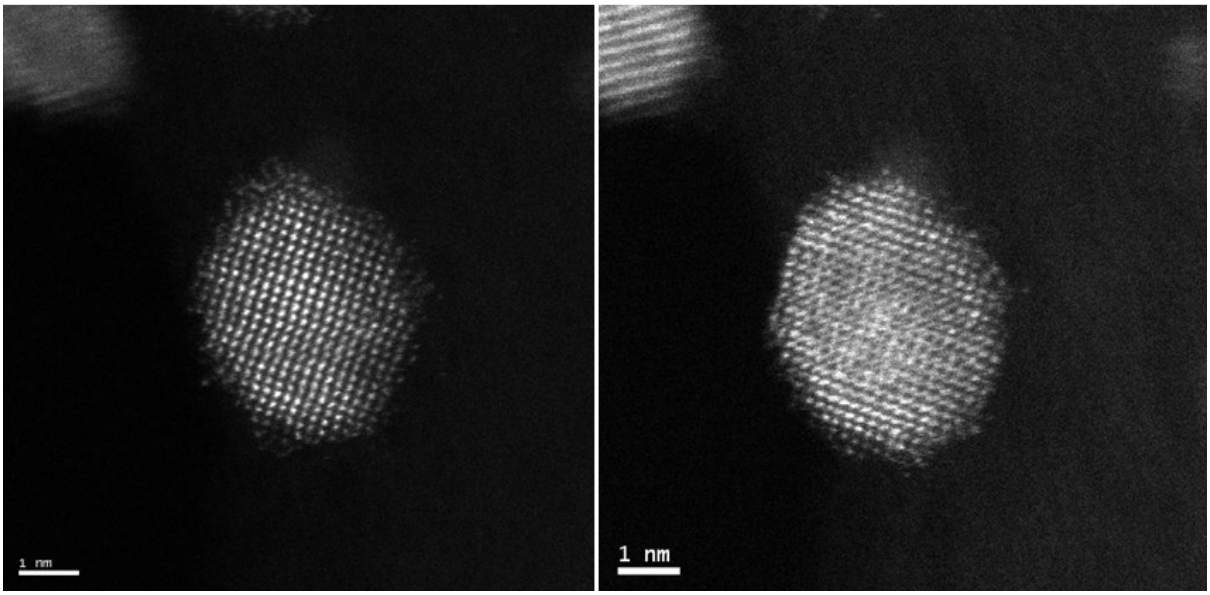

Figure 3.13 0.5ML particle imaged on axis and mistilted. The latter suggests the presence of a Pt shell, but care must be taken in interpretation to include the strong boost to scattering due to channelling effects

3.9 Particle structure with discrete tomography

A nanoparticle with 2ML shell design was imaged at atomic resolution with the JEOL ARM200F (see Figure 3.14) and then tilted to acquire another atomically resolved image from a different direction. The objective was to acquire a set of images from which a discrete tomography calculation could be run to determine the 3D shape of the particle (see Section 3.5.2).

The particle is imaged in the [110] direction, with {002} facets and {111} facets visible. The particle has formed a contact twin, with both crystals in some <110> orientation, as seen from the Fourier transform (FT) (see Figure 3.15). The mirror plane marked in green in Figure 3.14.

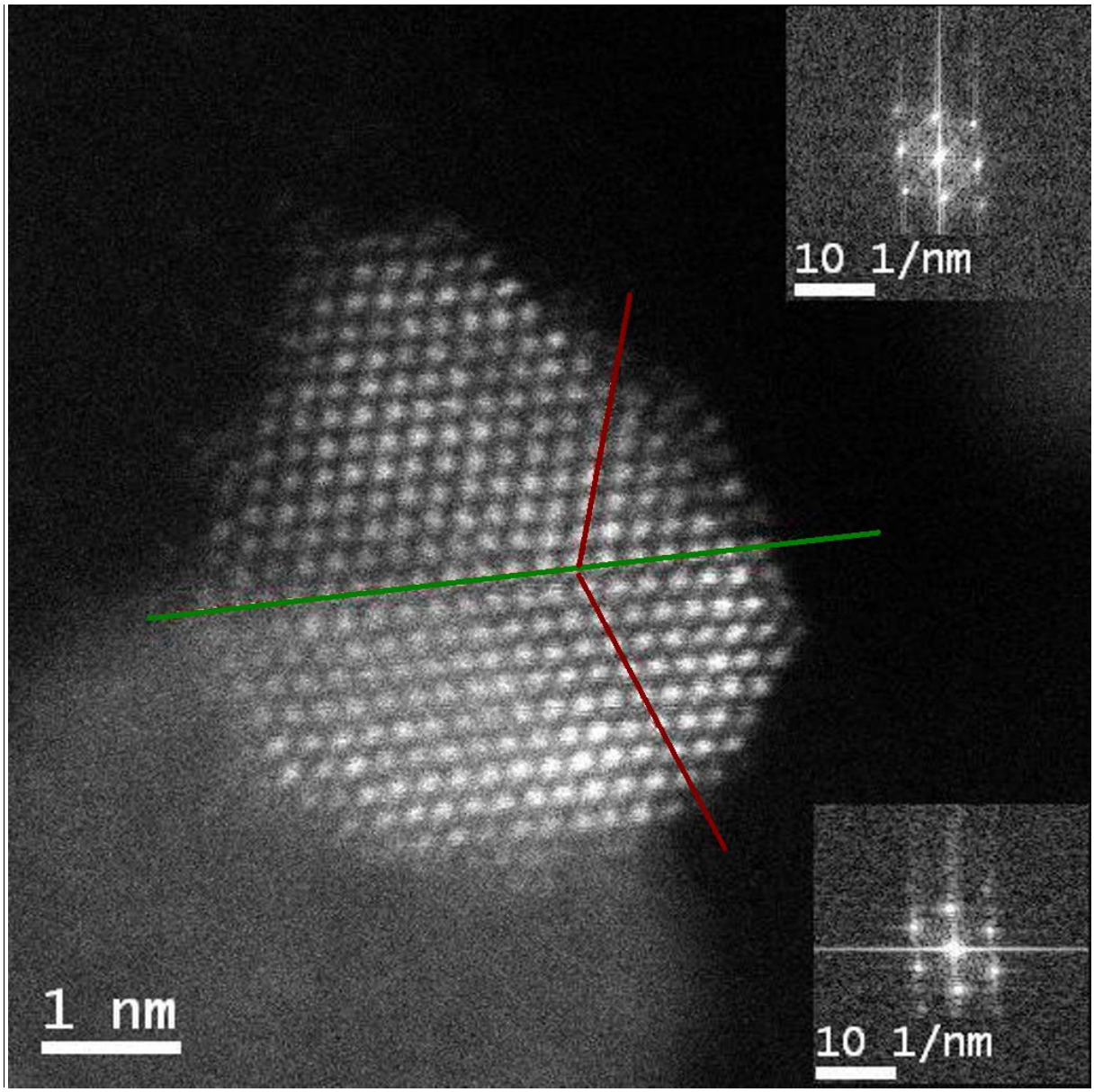

Figure 3.14 2ML design particle imaged at 200kV by a JEOL ARM-200F. Splitting of the {111} diffraction spots in the FFT (inset) shows that it is twinned. The non-split (200) spot shows that this is where the twin boundary is. A mirror plane twin boundary (green line) separates two nanocrystals, which are both in the <110> orientation. Planes of (111) are marked (red lines) to show the different orientations of the crystals.

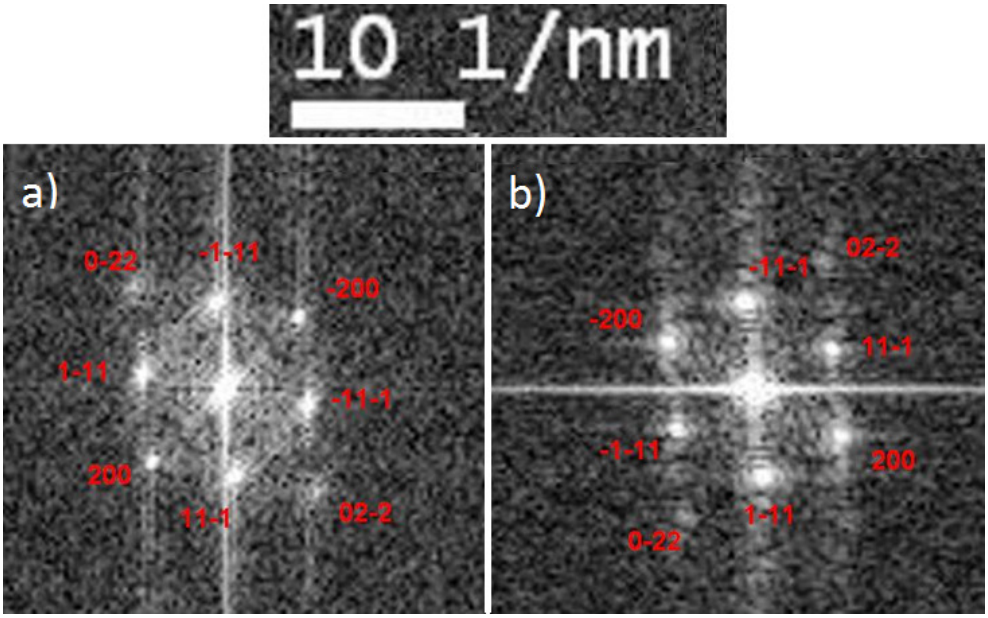

Figure 3.15 Indexing the Fourier spots shows that the two parts of the twin: (a) top crystal (b) bottom crystal, are both imaged down a <011> direction.

The spots in the FT can be indexed by comparing the Fourier transform of the respective areas to the well known diffraction patterns of FCC crystals (See Appendix D for more details). Note that the {100} spots are not visible experimentally since they are crystallographically forbidden[7] [26]. Either the distances from the zero spot to the index spot (see Table 3.4) or the angles between two non-symmetrically related spots of the Fourier transform (see Table C.1) can be used to index the pattern. Both methods confirm that the orientation is indeed <110>.

Index		Top grain		Bottom grain	
	Ideal	Measured (nm^{-1})	Ratio to $\bar{2}00$	Measured (nm^{-1})	Ratio to $\bar{2}00$
$\bar{2}00$	1	5.85	1	5.55	0.977
$\bar{1}1\bar{1}$	0.866	4.72	0.807	4.94	0.870
$11\bar{1}$	0.866	4.74	0.810	4.86	0.856
200	1	5.85	1	5.68	1
$1\bar{1}\bar{1}$	0.866	4.72	0.807	4.94	0.870
$\bar{1}\bar{1}1$	0.866	4.68	0.800	4.97	0.875

Table 3.5 Calculation of the crystal orientation of the two grains in Figure 3.15.

[7] FCC requires that the indices of the spots conform to $h + k + l = 2x$ where x is an integer.

The slight discrepancy between the measured and ideal distances shows that there could be some relaxation on the lattice, commonly seen in nanoparticles due to surface strain and could explain the enlarged bond lengths observed in the EXAFS data [3].Alternatively, this could also be due to scan distortion or drift from the imaging process itself.

Coincidence site lattice analysis was carried out to determine that the twin is a Σ3(111)[110] with one in every 3 lattice points common to both crystals (see Figure 3.16).

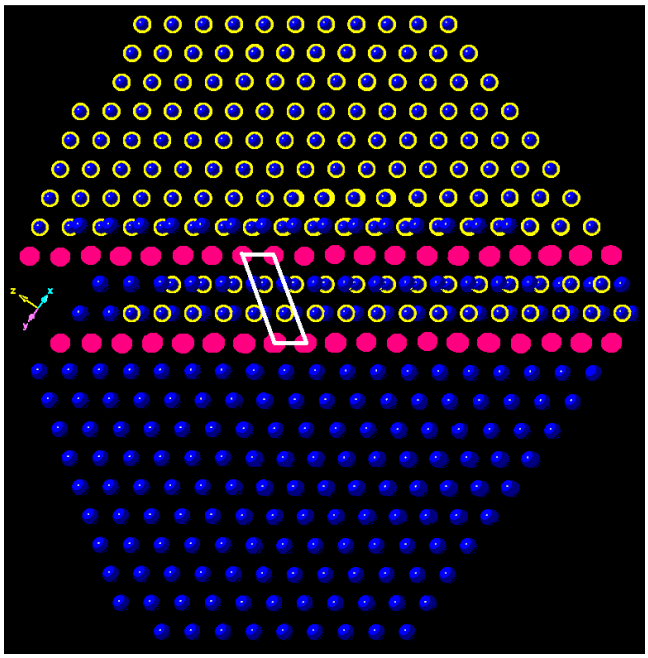

Figure 3.16 Coincident lattice site analysis shows that this is a simple Σ3(111) grain boundary. There is angle of 110 degrees between the two grains.

The sample was then tilted and another zone axis found in a different <110> orientation (see Figure 3.17). However, in this orientation, the twin boundary is no longer visible.

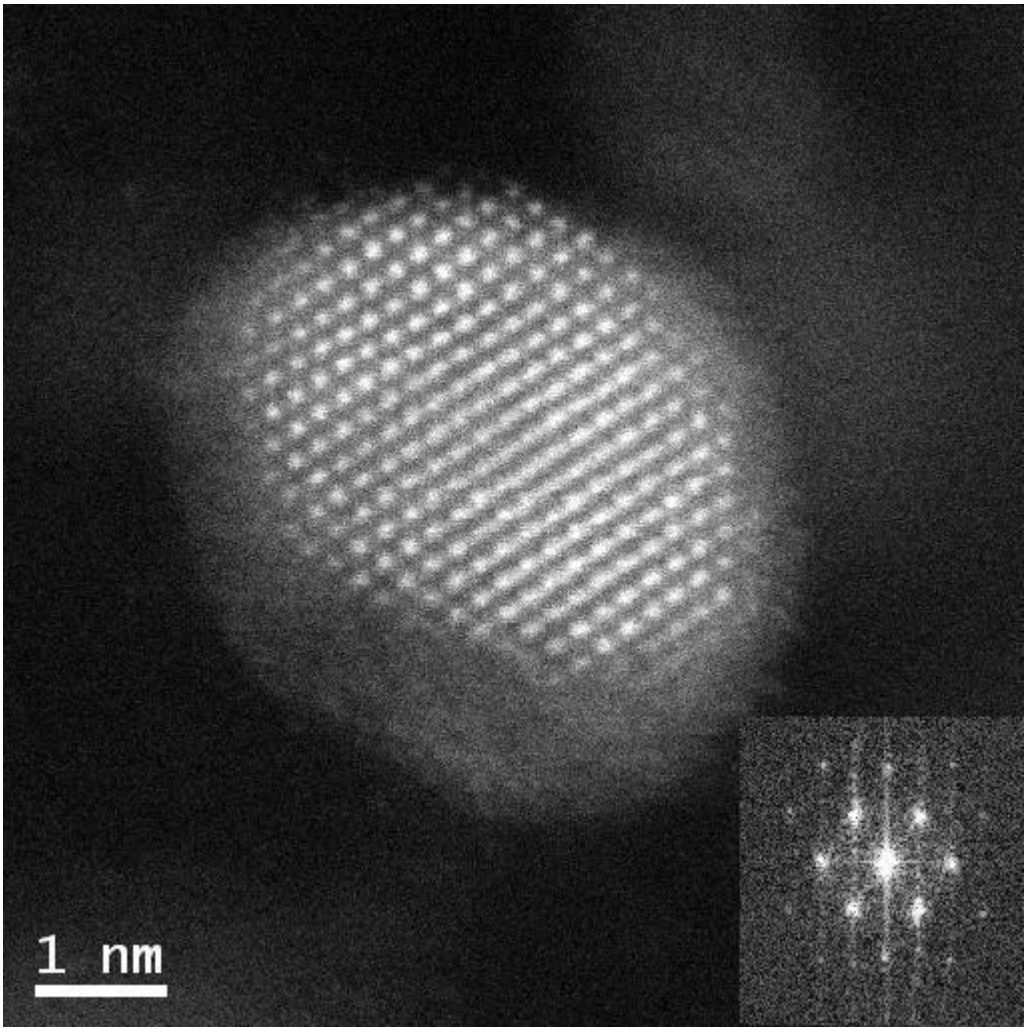

Figure 3.17 Tilted nanoparticle in another <110> orientation. The mistilt in the centre of the particle suggests that there is significant strain in the area, causing the columns to be slightly misaligned.

A crystal model was created using Crystal Maker to investigate the particle structure (see Figure 3.18). A FCC particle in the [110] orientation was made and then the top half rotated to form the twinning seen in Figure 3.14.

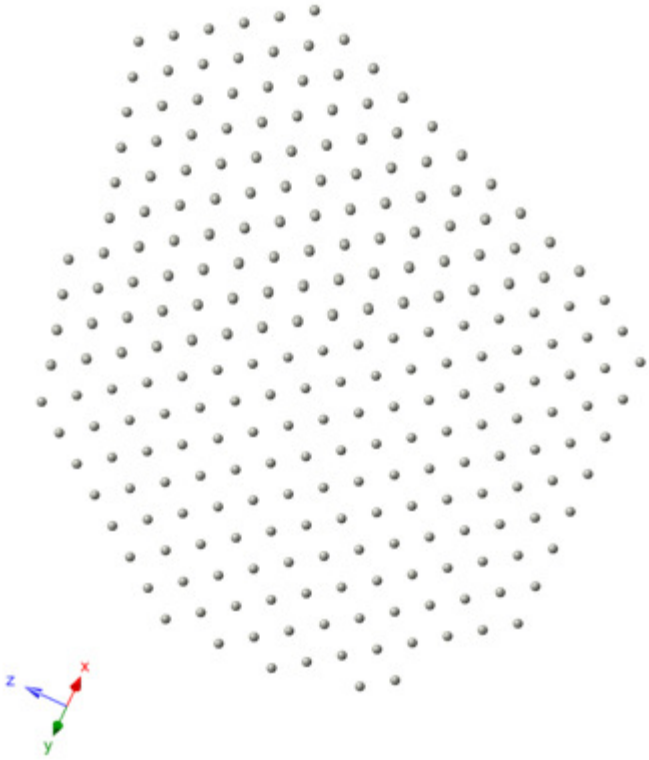

Figure 3.18 Model of the particle imaged in Figure 3.14 created using Crystal Maker.

Noting that the nanoparticle to the bottom left in Figure 3.14 is now underneath the particle in focus, and using this as a guide, the particle was tilted to find a match to Figure 3.17. The closet visual match (See Figure 3.19) is in the [1-11] orientation. This does not match the FFT of the experimental image, which is clearly <110> (See inset Figure 3.17).

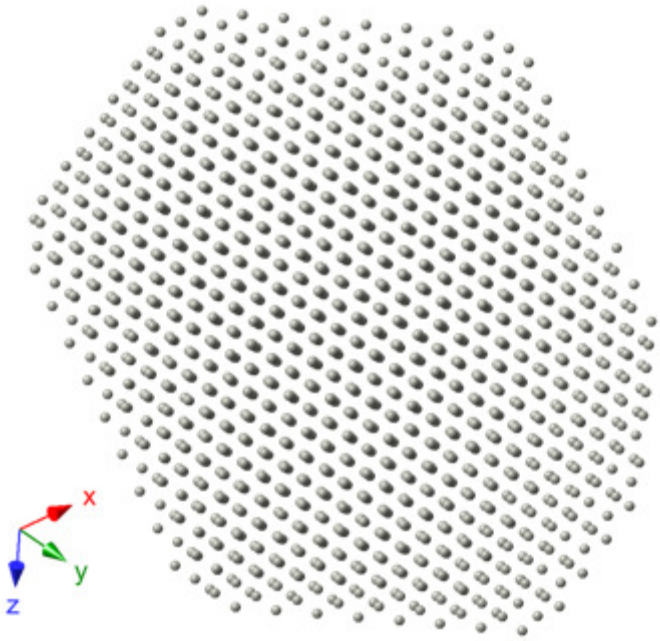

Figure 3.19 Closest match to particle in Figure 3.16 by matching the perimeter shape of the particle. However, the orientation here is <111>, whereas the experimental image shows an orientation of <110>. This mismatch is likely due to the particle reconstructing during the time under the beam while tilting to another zone axis.

Cycling through all possible <110> orientations, it was found that there is no <110> orientation that would match the second image acquired of the particle (see Table E.1 in Appendix E). It is therefore most probable that the particle underwent a reconstruction under the beam during the time take to tilt the sample and find another zone axis. This is a common occurrence for particles of this size since the energy imparted by the incident beam is enough to overcome the activation barrier and allow the particle to relax back down to a lower energy state by removing the twin boundary.

3.10 Conclusions

Characterising the physical structure of core-shell nanoparticles is vital to understanding their catalytic properties. Medium magnification HAADF STEM yielded particle size distribution for various catalyst designs and also allowed the aspect ratio and roundness of the particles to be investigated. The expected increase in mean particle size with thicker shells is observed. Post-cycling, all the catalytic designs showed an increase in size a decrease in aspect ratio.

However, though the Pt shell on Pd core design shows the increased electrochemical stability and catalytic activity, its functionality is not due to a purely core-shell type structure but a combination of step-type edge decoration of Pt.

Atomic resolution images were obtained of 2ML design particles, but the stability of the particle under the beam hampered analysis. While it is possible to tilt the particle to obtain atomic resolution images from two directions in order to perform a tomographic reconstruction, the process often exposes the sample to the beam for a prolonged period of time, which results in particle reconstruction. This prevented the structure from being solved by a discrete tomography approach.

Moreover, it is difficult to extract compositional information by comparisons of HAADF intensities alone as those particles that oriented on zone axis channel the beam down the columns and so appear brighter, thus making intensity not only dependent on thickness and composition but also on orientation. At atomic resolutions, even when on zone axis, the precise determination of thickness and composition is also not possible since both effects contribute to a single measurement of intensity.

References

[1] S.C. Ball, S.L. Burton, J. Fisher, R. O'Malley, B.C. Tessier, B. Theobald, et al., Structure and Activity of Novel Pt Core-Shell Catalysts for the Oxygen Reduction Reaction, ECS Transactions. 25 (2009) 1023–1036.

[2] A.E. Russell, B. Tessier, A. Wise, A. Rose, S.W. Price, P.W. Richardson, et al., In Situ XAS Studies of Core-Shell PEM Fuel Cell Catalysts: The Opportunities and Challenges, in: ECS Transactions, The Electrochemical Society, 2011: pp. 55–67.

[3] A. Wise, Characterisation of Bimetallic Alloy and Core-Shell Electrocatalysts, University of Southampton, 2012.

[4] B.C. Tessier, Preparation, Characterisation and Evaluation of Core-Shell Electrocatalysts for PEMFCs, University of Southampton, 2009.

[5] W. Ostwald, Studien über die Bildung und Umwandlung fester Körper, Zeitschrift Für Physikalische Chemie. 22 (1897) 289–330.

[6] M. Haider, P. Hartel, H. Müller, S. Uhlemann, J. Zach, Current and future aberration correctors for the improvement of resolution in electron microscopy, Philosophical Transactions. Series A, Mathematical, Physical, and Engineering Sciences. 367 (2009) 3665–82.

[7] L.C. Gontard, The application and development of novel TEM techniques to the study of Pt catalyst particles, 2007.

[8] S. Butterworth, On the Theory of Filter Amplifiers, Wireless Engineer. 7 (1930) 536–541.

[9] L. Cervera Gontard, D. Ozkaya, R.E. Dunin-Borkowski, A simple algorithm for measuring particle size distributions on an uneven background from TEM images., Ultramicroscopy. 111 (2011) 101–6.

[10] Z. Gu, P.B. Balbuena, Absorption of Atomic Oxygen into Subsurfaces of Pt(100) and Pt(111): Density Functional Theory Study, Journal of Physical Chemistry C. 111 (2007) 9877–9883.

[11] J. Zhang, Y. Mo, M.B. Vukmirovic, R. Klie, K. Sasaki, R.R. Adzic, Platinum Monolayer Electrocatalysts for O 2 Reduction: Pt Monolayer on Pd(111) and on Carbon-Supported Pd Nanoparticles, The Journal of Physical Chemistry B. 108 (2004) 10955–10964.

[12] A.-X. Yin, X.-Q. Min, Y.-W. Zhang, C.-H. Yan, Shape-Selective Synthesis and Facet-Dependent Enhanced Electrocatalytic Activity and Durability of Monodisperse Sub-10 nm Pt-Pd Tetrahedrons and Cubes., Journal of the American Chemical Society. 133 (2011) 3816–9.

[13] A.G.B. Coq, T. Tazi, F. Figueras, D.R. Salahub, Site segregation in small rhodium bimetallic aggregates: a combined catalytic and quantum chemical study, Journal of the American Chemical Societyi. 113 (1991) 1485.

[14] J.-P. Candy, B. Didillon, E.L. Smith, T.B. Shay, J.-M. Basset, Surface organometallic chemistry on metals: a novel and effective route to custom-designed bimetallic catalysts, Journal of Molecular Catalysis. 86 (1994) 179–204.

[15] L. Chang, L. Cervera-Gontard, C. Hetherington, A. Kirkland, D. Ozkaya, R. Dunin-Borkowski, Imaging Active Sites on Platinum Catalytic Nanoparticles Using Aberration-Corrected Electron Microscope, Microscopy and Microanalysis. 13 (2007) 866–867.

[16] ter Veen,H.R.J, Applications of High Sensitivity-Low Energy Ion Scattering (HS-LEIS) in heterogeneous catalysis, Catalysis Today. 140 (2009) 197 – 201.

[17] T. Shibata, B.A. Bunker, Z. Zhang, D. Meisel, C.F. Vardeman, J.D. Gezelter, Spontaneous Alloying of Au−Ag Nanoparticles, Journal of the American Chemical Society. 124 (2002) 11989–11996.

[18] D. Alloyeau, C. Ricolleau, C. Mottet, T. Oikawa, C. Langlois, Y. Le Bouar, et al., Size and shape effects on the order-disorder phase transition in CoPt nanoparticles., Nature Materials. 8 (2009) 940–6.

[19] C.Q. Sun, Y. Wang, B.K. Tay, S. Li, H. Huang, Y.B. Zhang, Correlation between the Melting Point of a Nanosolid and the Cohesive Energy of a Surface Atom, The Journal of Physical Chemistry B. 106 (2002) 10701–10705.

[20] F. Baletto, R. Ferrando, Structural properties of nanoclusters: Energetic, thermodynamic, and kinetic effects, Reviews of Modern Physics. 77 (2005) 371–423.

[21] R.F. Egerton, P. Li, M. Malac, Radiation damage in the TEM and SEM., Micron. 35 (2004) 399–409.

[22] C.R. Bradley, N.J. Zaluzec, Atomic sputtering in the Analytical Electron Microscope, Ultramicroscopy. 28 (1989) 335–338.

[23] N.P. Young, M. a van Huis, H.W. Zandbergen, H. Xu, a I. Kirkland, Transformations of gold nanoparticles investigated using variable temperature high-resolution transmission electron microscopy., Ultramicroscopy. 110 (2010) 506–16.

[24] R. Egerton, Mechanisms of Radiation Damage and Electron-Beam Fabrication, Microscopy and Microanalysis. 16 (2010) 1658–1659.

[25] R.F. Egerton, Mechanisms of radiation damage in beam-sensitive specimens, for TEM accelerating voltages between 10 and 300 kV., Microscopy Research and Technique. (2012).

[26] C. Hammond, The Basics of Crystallography and Diffraction (International Union of Crystallography Texts on Crystallography), OUP Oxford, 2001.

[27] Y. Arai, Chemistry of Powder Production, Springer, 1996.

Chapter 4

Techniques for Quantification

Electron micrographs are often in danger of being used as high resolution cameras to provide an image of results verified by other techniques. They can provide much more information if the images are treated as data sets and analysed as such quantitatively; the efforts in this direction is discussed in this chapter.

A method is presented, which has been developed for quantifying HAADF STEM images from any commercially available microscope by careful detector calibrations and probe current measurements. By placing the collected scattered intensity on an absolute scale, images can be scaled as a fraction of incident beam current and compared directly to simulations.

4.1 Quantification of HAADF STEM images

Quantitative STEM has been carried out since the 1970s [1,2] when Retsky and Isaacson independently compared the scattered intensity from single atoms and small clusters of Pt, Pd and other heavy metals to calculated values from first principle quantum mechanics, usually grounded in a Born approximation. They calibrated the response of their detectors with a systematic set of imaging using various probe currents.

Work on metallic nano-clusters has often assumed that the total integrated HAADF intensity of a cluster scaled linearly with the number of atoms [3,4]. Such an approach ignores the effects of channelling, which can be strongly seen when imaging a crystal along a low-order zone axis to achieve atomic resolution.

Comparison of experimental data with simulations have allowed for the study of more than single atoms, with crystals of various thicknesses imaged experimentally (see for example [5,6]). However, until recently, comparisons have all required an arbitrary scaling parameter to scale the experimental intensity values to the simulations as experimental datasets were not determined on an absolute scale.

4.1.1 Recent efforts in quantitative STEM

These comparisons are somewhat unsatisfactory for adequately explaining complicated real systems of materials. Even as early as 1996 Darji and Howie showed that some corrections of the direct image signal is often necessary because of additional scattering effects from the substrate [7]. The missing link between simulation and experiment of detector calibration lay dormant, except for a few instances, detailed here.

Singhal et al again reported absolute measurements of the scattering cross section in 1997 with the study of small Re particles using a calibrated HAADF detector [8]. Errors in the measured cross sections of the particles were divided into random errors produced by the sample, and systematic errors originating from detector asymmetries and the finite size of the probe. By measuring carefully detector efficiencies and the signal processing responses between the detector and computer, data was presented on an absolute scale. However, no simulations or calculations were presented to compare with the experiments.

Anderson et al were aware of the need for a detection system which counts individual electrons or knowledge of the signal processing between the detector and the computer in order to determine a set of relative or even absolute intensities [5]. They noted that the efficiency of scintillator of ADF detector must be known for absolute scaling and a parametric fit factor was used in end.

Yang et al produced a detailed analysis of the morphology of supported $PtRu_5$ on carbon black [9]. They refer to two methods of quantifying detector efficiency and thus scaling their experimental results absolutely. One follows the Singhal approach and the other is a custom method using carbon as an internal standard. They measure the carbon thickness by the attenuation of the main beam intensity

in a bright-field image. Once the thickness is known, they calculate the dark field intensity and compare it to the HAADF intensity from the same region.

LeBeau and Stemmer began a resurgence of interest in detector calibrations and quantification of the experimental image to an absolute scale in 2008 [10]. Following on from the work of Menard et al [11], by normalising the measured image intensities to the incident beam, the intensity of the image can be placed on an absolute scale. Fractional intensity images of a $SrTiO_3$ single crystal for varying thicknesses up to 120nm. Foil thickness was determined using the well known ratio of $\ln\left(\frac{I_t}{I_0}\right)$ in the EELS spectrum[1], which is very sensitive to thickness variations [12]. Full characterisation of the microscope and detector outputs was covered so direct comparison with simulation could be possible [13].

Spatial incoherence is known to reduce contrast and has been modelled previously by convolving the simulated HAADF images with a Gaussian envelope function [14,15]. LeBeau et al take this approach to match their data to simulations and subsequent studies with the same instrument and experimental conditions confirm that the finite source size of the probe is indeed 0.04nm [16,17].

Van Aert et al also presented quantitative atomic resolution mapping using similar methods of comparison of known and unknown compositions [18]. A statistical hypothesis testing algorithm was used to compare known atomic columns in the same sample with unknown ones to study the interface of a $LaAlO_3/SrTiO_3$ multilayer. However, the method has no treatment of TDS or dynamical effects and is restricted to systems where the thickness variation is negligible so known and unknown columns contain the same number of atoms.

Integration of the total intensity of atomic columns from a scaled image is used to investigate the thickness of the columns [19]. Statistical parameter estimation was used to extract various experimental parameters using a maximum likelihood fitting. The crux of the algorithm depends on an initial estimate, a so called 'cost function', of the number of distinct peaks in a histogram of the intensity of columns extracted from the image. The algorithm then looks for clustering of intensity values to determine the column thicknesses. This has been successfully implemented in conjunction

[1] I_t is the total area under spectrum and I_0 is the area under zero loss peak

with discrete tomography to determine the structure of model nanoparticles [19] (as detailed in Section 2.5.2) and also the core of a core-shell nanoparticle [20] .

A combination of sequential high resolution STEM images and multislice simulation has been successfully implemented by Ortalan et al on Ir-Rh cluster by using intensity ratios to predict possible combinations of Ir and Rh in each column [21]. This procedure was only possible due to the cluster investigated contained a maximum of 3 atoms per column; at larger particle sizes the number of possible combinations increases exponentially.

Molina et al have carried out quantitative mapping of InAsP alloys for quantum wire applications [22] by using a carefully controlled standards approach. Neither instrument calibrations nor simulations were carried out but instead a set of calibrated composition samples grown by molecular beam epitaxy were used as standards by which to quantify the experimental data. The extended crystal structure of the system allows for this straight-forward phenomenological method. Later, the average intensity of a unit cell is used to give a thickness calibration before estimating column compositions using a linear approximation of the dependence of intensity on thickness [23].

In this thesis, a novel method is developed, which combines a custom detector calibrations technique (see Section 4.2) and a column intensity analysis method (see Chapter 5) to quantify the intensity of scattering in experimental images. The experimental findings are compared to results obtained from an absorptive potential simulation method (see Section 4.4.5), which is ideally suited for nanoparticles.

4.2 Detector calibrations

Commercially available ADF detectors are typically made from YAP-Ce: $YAlO_3$ perovskite (YAP) doped with caesium as the scintillator material. The electrons incident on the material are converted to a photon cascade, which is collected by a photomultiplier tube [24] and converted to a current. This conversion can be controlled by a gain setting in the analogue to digital (A/D) convertor to give varying “contrast” to the image outputted. A constant voltage (DC offset) may be added by a preamplifier, which is termed a “background” signal. The output is read by the imaging hardware that digitizes the signal using an analogue-to-digital converter. Each probe position is then recorded as a

"pixel" value in the image. The intensity measured in this image depends on the operating conditions of the detector and scintillator-photomultiplier combination.

In this section the method that was developed to measure the response efficiency of the ADF detector of any commercially available microscope is presented. The behaviour of the gain and offset of the analogue to digital convertors with varying incident beam currents is shown, highlighting the need to be careful with detector settings. All of these experiments were carried out on the Oxford-JEOL 2200 MCO to investigate the detector response with different gain settings on the A/D converter.

4.2.1 Detector mapping

The scintillator efficiency of the ADF detectors of the instruments used to carry out the experiments in this work is presented in Figures 4.1 and 4.2. For each experimental setup, a focussed probe of a known current was scanned across the detector. The sample is moved to an area of vacuum so that the measured response is purely due to the detector and not some area of the specimen.

In the Oxford-JEOL 2200MCO, the formation of a probe at the detector plane was accomplished by using both the upper and lower lenses in a confocal setup[2]. For the JEOL ARM-200F, the pre-specimen lenses were weakened to form the probe on the detector plane.

The post-specimen magnification is decreased until the detector is found and then post-specimen deflector coils (e.g. the PLA deflectors on the Oxford-JEOL instrument) used to move the detector image to the centre of the screen. Typical settings are: pre-specimen magnification of 250k and post-specimen magnification of 2M.

The contrast and brightness is then optimised for the detector map such that the signal is not saturated and the black level of the DC offset is not clipped when scanning over areas of vacuum. These A/D convertor settings are then used for the imaging of the particles. It is important to be aware of the exposure (pixel dwell time) and image size that is used for the detector map so that a one-to-one comparison of electron fluence can be made to the specimen images. It is usually convenient to map

[2] This can be set up in the JEOL software controls by selecting the "Alignment" mode

the detector with several pixel dwell time and image size combinations, which are often used for imaging (e.g. 512x512 pixel image with 38µs dwell time).

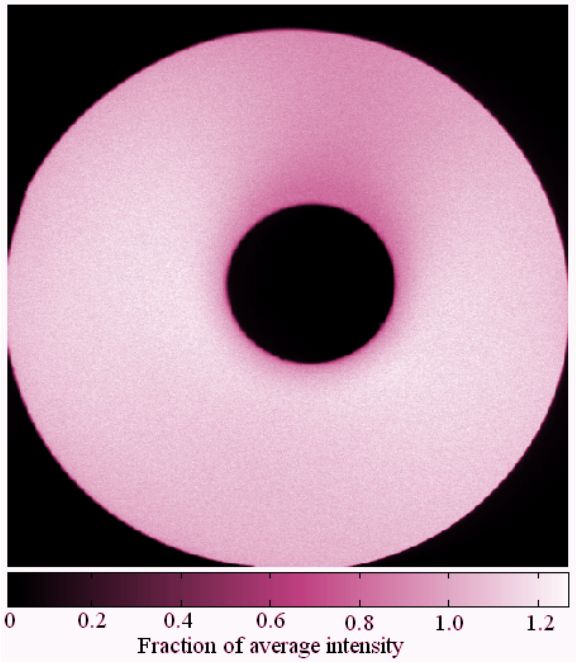

Figure 4.1 The detector scintillator efficiency of the ADF detector on the Oxford-JEOL 2200MCO as a function of probe position across the detector surface. The intensity is scaled to mean value across detector. Variations in efficiency are seen across the detector surface, in particular at low angles. Detector is also seen to be non-symmetric in outer angle, probably due to a manufacturing fault.

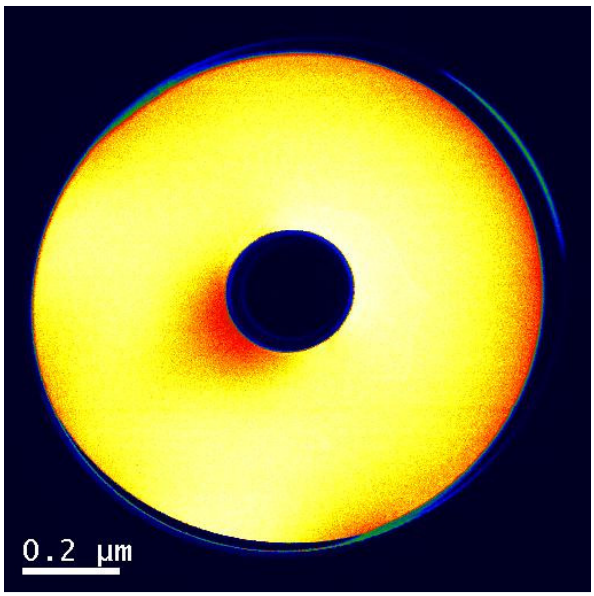

Figure 4.2 HAADF detector of the JEOL ARM-200F. The instrument is also equipped with a mid angle annular detector and also a bright field detector. The shadow of the electron pipe can be clearly seen at low angles and variations in detector efficiency at higher angles are not azimuthally symmetric

4.2.2 Detector non-uniformity

Variations can be seen across both detectors, especially at low angles; the detector response is not necessarily uniform in either the azimuthal or radial directions. Some shadowing from the electron pipe can be seen in the upper right quadrant of the Oxford-JEOL 2200MCO detector (see Figure 4.1) and in the lower left of the JEOL ARM-200F (see Figure 4.2). The effect of the detector non-uniformity was shown to affect the imaged intensity by 5% [25] and the contrast by up to 10% [26]. Thus all HAADF simulations should include a detector efficiency weighting factor or an accurate appraisal of the likely error due to detector non-uniformity.

In addition, the inner hole is not centrally placed with respect to the outer edge. However, the active area of the detector is limited by the ultra high resolution pole piece to approximately 180mrad at the camera length used for imaging. Since this means that the scattering to higher angles will fall completely on the detector, concerns that scattering is lost in some radial directions because of the mis-centering of the inner hole are mitigated. Moreover, since the scattered intensity drops off with increasing scattering angle, beyond 40mrad, the effect of an increase in the outer angle is neglibible [26]. What is of more importance is the accuracy of determining the inner angle.

4.2.3 Measuring the inner angle

The inner angle of the detector must be known to a great degree of accuracy in order to compare experiment to simulation since the signal collected by the detector is strong at lower angles. It has been reported in the literature that an uncertainty of a few mrad in the inner angle could produce a 10% error in the value of the peak intensity [26]. It has been further shown that the dependence of intensity on the inner angle is exponential and so must be carefully calibrated [27].

The imaged inner angle of the HAADF detector does not necessarily correspond to the active area since an aluminium electron pipe sits inside the inner hole. This electron pipe is typically 1mm in physical size which means the inner shadow is 3mm in radius, whereas the detector inner radius[3] is 4mm (see Figure 4.4). Thus extracting the inner angle value from an image of the detector may not be sufficiently accurate; a more experimental approach to measuring the inner angle is necessary.

[3] These figures correspond to the HAADF detector of the JEOL ARM 200F

A beam focussed at the ADF detector plane can be manually scanned across the hole in the detector using the post-specimen deflector coils. The point at which the detector registers a response is then recorded since this corresponds to the edge of the active area of the HAADF detector. The beam is then deflected in one direction across the detector hole until another response is recorded, following chord 1 in Figure 4.3. The middle point is then taken and the beam moved from one edge of the hole to the other in the perpendicular direction (following line 2 in Figure 4.3).

This allows the mid-point of the detector hole to be found and subsequently, two perpendicular diameters to be measured in units of deflector step sizes. Care was taken to include the diameter of the aperture in the calculations since signal would be detected once diametrically opposite sides of the aperture crossed onto the detector.

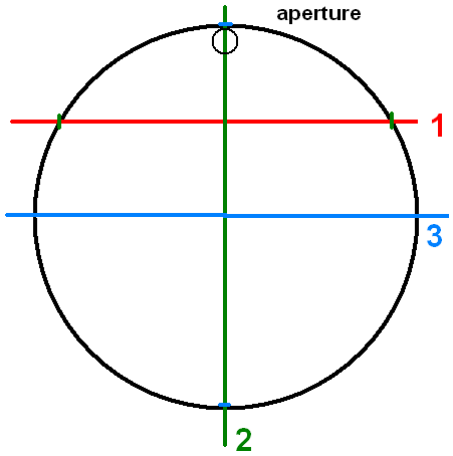

Figure 4.3 Measuring the inner angle of the Oxford-JEOL 2200MCO by scanning an aperture across the inner hole.

The number of steps can then be converted to milliradians by comparing to a calibration from an aperture of known size, itself calibrated from the CBED discs of a crystalline sample of $SrTiO_3$. The measured inner angle for the upper detector[4] on the Oxford-JEOL 2200MCO was 90mrad for a camera length of 100cm, and 91mrad for the JEOL ARM-200F at 6cm camera length (see Figure 4.4).

[4] The instrument is also equipped with a lower ADF detector after the Omega-filter; this was not used.

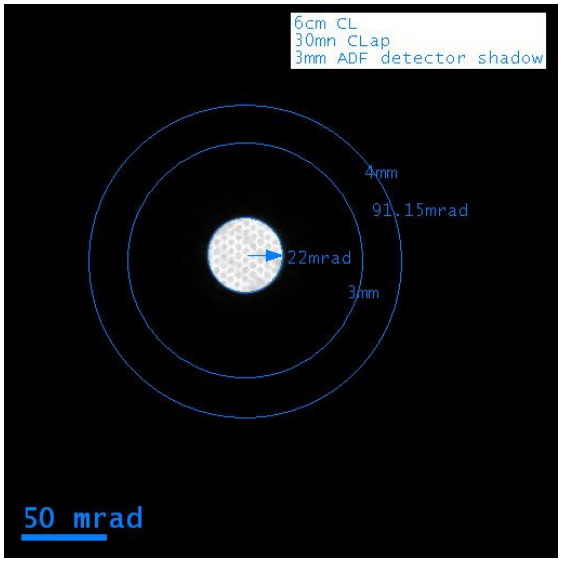

Figure 4.4 Inner angle of the JEOL ARM-200F's ADF detector. The physical size of the detector is shown in mm.

4.2.4 Detecting the HAADF Signal

Since the HAADF signal is typically only a small fraction of the primary beam current[5] [28], using the same beam current to map the detector and to image would result in either a saturation of the detector map image or a loss of dynamic range for the specimen image, unless the contrast of the A/C convertor was adjusted.

The amplifiers in the A/D convertor that digitise the current from the HAADF detector on commercially available instruments needs to be carefully calibrated in order to map the signal detected to an absolute value of fraction of incident beam current. While LeBeau and Stemmer used a custom built A/D convertor which they showed was linear in response [10], this cannot be guaranteed for all instruments. The two parameters of interest are the DC offset, which controls the background black level of an image and the gain, which varies the image contrast.

[5] The scattered intensity falls off with scattering angle and so the signal is stronger at lower angles, within the bright field regime.

4.2.5 Linearity of detector response with D.C. offset in A/D convertor

The D.C. offset (brightness) was measured by adjusting the settings with a beam of constant current. It was found that the A/D convertor behaviour varied linearly with offset (See Figure 4.5). This meant that adjusting the brightness requires only a subtraction of count values from the image.

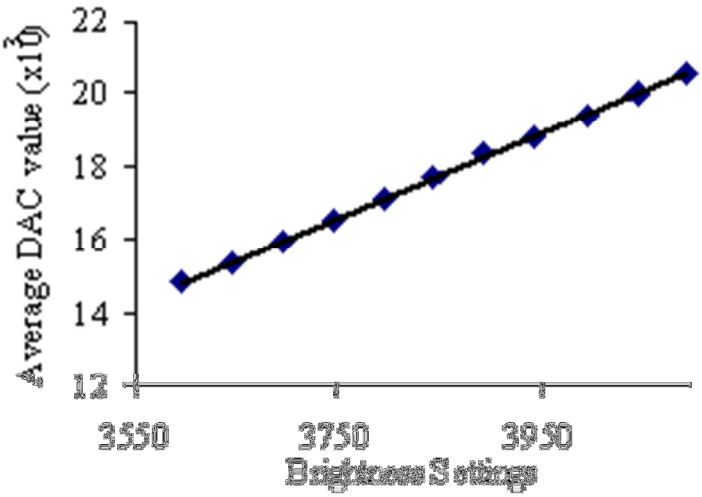

Figure 4.5 Linear behaviour of the analogue to digital convertor with brightness (offset).

4.2.6 Linearity of detector response with gain in A/D convertor

By sweeping over a range of contrast values, it is clear that the response is indeed nonlinear over even a short range of values (See Figure 4.6). Moreover, the trend is not linear with different brightness settings: the difference in successive brightness values at lower contrast settings is more significant than at higher contrast settings. This makes quantitative comparisons of image intensity across different gain settings not straightforward. Moreover, while the D.C. offset at a particular gain setting varies linearly (as in section 4.2.5), the combination of changing brightness and contrast (D.C. offset and gain) means that the brightness cannot be guaranteed to be linear.

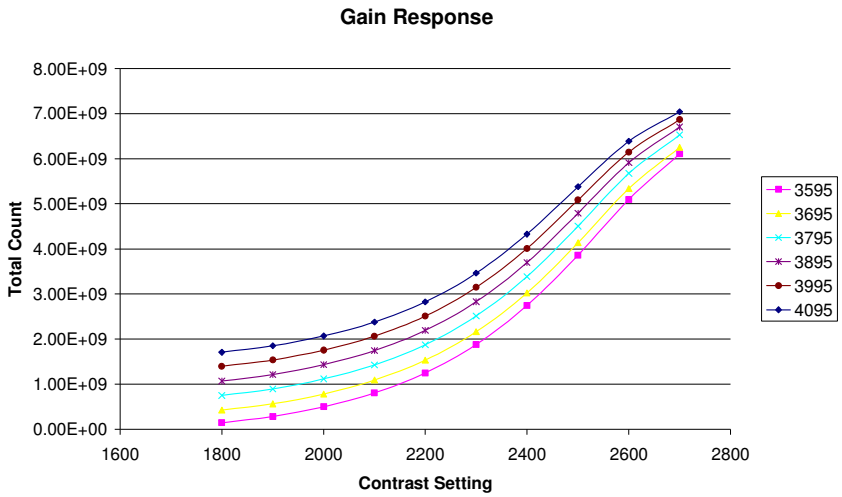

Figure 4.6 Non-linear response of the A/D convertor with contrast (gain) for the Oxford-JEOL 2200MCO microscope. Several brightness settings are explored ranging from 3595 to 4095 (nominal values on the JEOL system). Lower contrast settings show a larger difference between the responses at successive brightness settings than that observed for higher contrast settings. This further nonlinearity in the gain response with brightness further complicates interpretation of absolute scattering intensities.

Consequently, to aid experimental convenience the gain settings are kept the same across both the mapping of the detector and also the imaging of the sample. Thus vitally, the incident beam current should be reduced by a factor on the order of 10 when mapping the detector, in order to use a full dynamic range for the images of the sample and thus achieve good signal to noise.

Reduction of the beam current can be achieved by using a smaller objective aperture and by increasing the C1 lens excitation (often conveniently by selecting a smaller spot size in the microscope operating software). The exact reduction in current should be measured experimentally since even known aperture sizes can differ from their nominal size and shape. This is particularly important for a cold FEG instrument such as the JEOL ARM 200F, where probe current is not stable and decreases significantly with time from tip flashing.

4.2.7 Measuring probe current

The probe current measurement is carried out with the beam used for the detector mapping and also the beam used for imaging, so that the ratio of the beam currents can be used to calibrate the detector response.

The camera length is adjusted to the lowest setting (4cm on the Oxford-JEOL 2200MCO) so that the smallest beam can be produced to ensure that the whole beam profile falls in the Faraday cup (see Figure 4.7). This does not affect the beam current since the post-specimen lenses serve only to magnify the beam profile so long as the whole beam is collected. The PLA deflectors are used to move the beam until the signal from the Faraday cup is maximised.

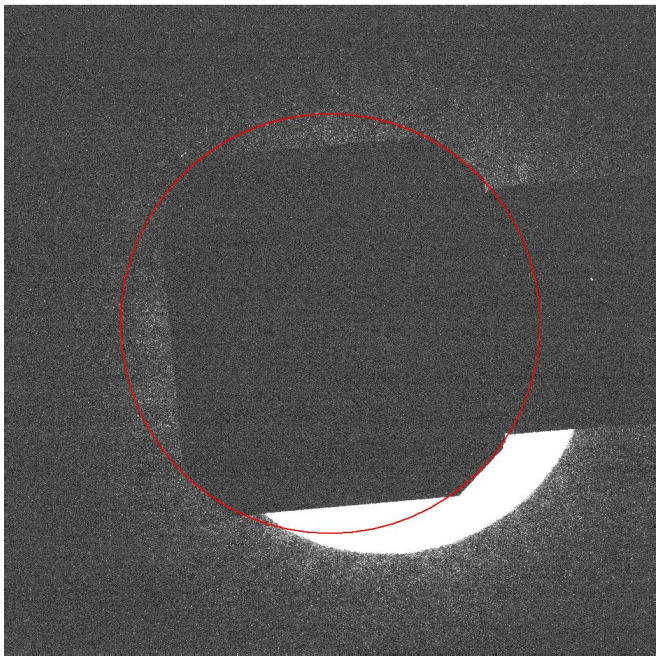

Figure 4.7 Shadow of the Faraday cage in the Oxford-JEOL 2200MCO.

A zero, "dark-current" is taken with the picoammeter, with the beam blanked and then a reading taken with the beam value open. All readings are averaged over several measurements to minimise shot noise (see Table 4.1).

	Picoammeter	Number of readings	Typical error
Oxford-JEOL 2200 MCO	Keithley 6487	100	± 0.08pA
JEOL ARM-200F	Advantest R8240	80	± 0.05pA

Table 4.1 Picoammeter settings used for measuring probe currents on the various microscopes used in this thesis.

4.2.8 Linearity of detector response to scattered signal

To verify that changing the probe current, and thus changes in the scattered intensity, does not lead to nonlinear behavior in the detector response, detector maps were imaged on the Oxford-JEOL 2200 MCO to investigate the detector response with different probe currents.

The incident probe current for three spot sizes were measured using a Faraday Cup. Apertures of known size were used to systematically decrease the incident probe current, while brightness and contrast settings were optimized for the highest beam current. The response of the detector to variations in incident probe current is linear (See Figure 4.8). Thus the intensity of HAADF images can be directly compared with simulation when probe current is reduced to allow for a better dynamic range in the thin sample images.

As mentioned previously in Section 3.4, it is possible to vary the probe current by manually adjusting the CL1 condenser lens settings (tantamount to changing the spot size). However, in order place the cross over at the correct height, in the objective lens, CL3 needs to be adjusted in the opposite direction to compensate. Alternatively, it is possible to increase the extraction voltage (A1) of the gun, as was performed on the JEOL ARM 200F, although this is not recommended since it could damage the electron source.

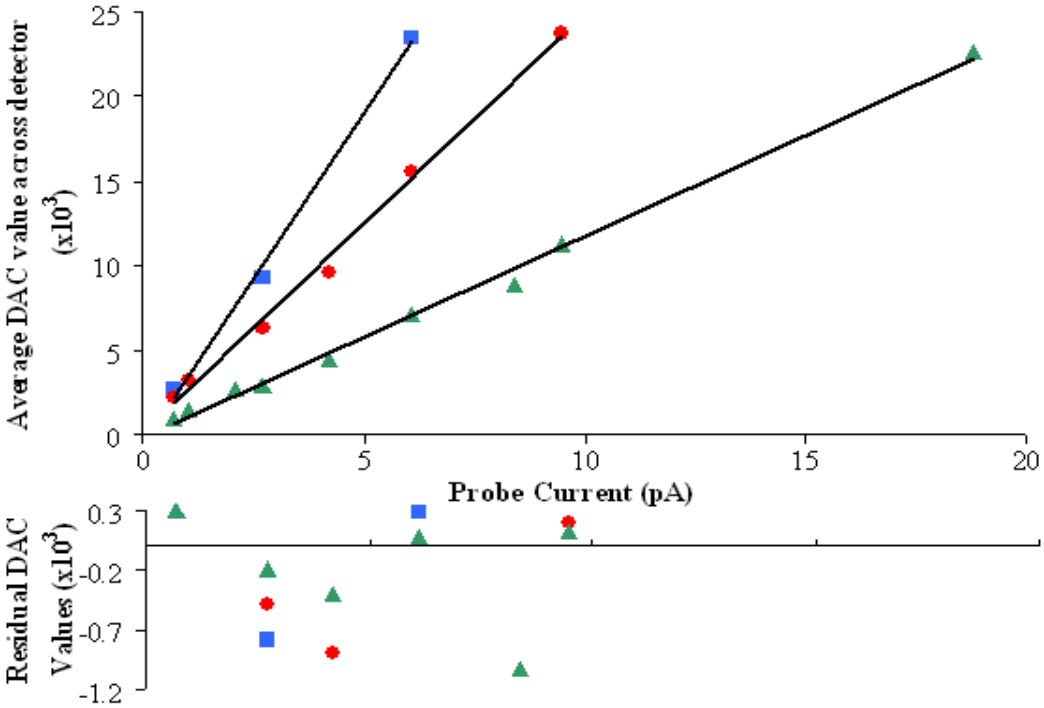

Figure 4.8 Response of the detector sensitivity to various probe currents is linear. The residuals show no systematic deviations.

4.3 Image Intensity Calibration

The recipe for scaling an image of a specimen to an absolute value is straightforward (a practical summary for experiments can be found in Appendix F). In order to transform the imaged intensity to a fraction of incident beam current, Int_{frac}, the following conversion needs to be performed:

$$Int_{frac} = Int_{Spec} \frac{I_{Det}}{I_{Spec} \times Int_{Det}} \tag{4.1}$$

where Int_{Spec} is the unscaled intensity collected from the scattering of the specimen in the raw experimental image; I_{Spec} is the probe current used to image the specimen in the experiment; and Int_{Det} is the mean intensity of the detector response when mapped with a probe current of I_{Det}.

Once a detector map is acquired as described in Section 4.2.1, the mean detector response (I_D) can be calculated by subtracting the mean value of the pixels from the detector map that correspond to the

detector from the mean value of the background pixels. Since the two regimes are well separated in values, this can be performed by representing the data as a histogram and thresholding to separate the detector response from the background (see Figure 4.9).

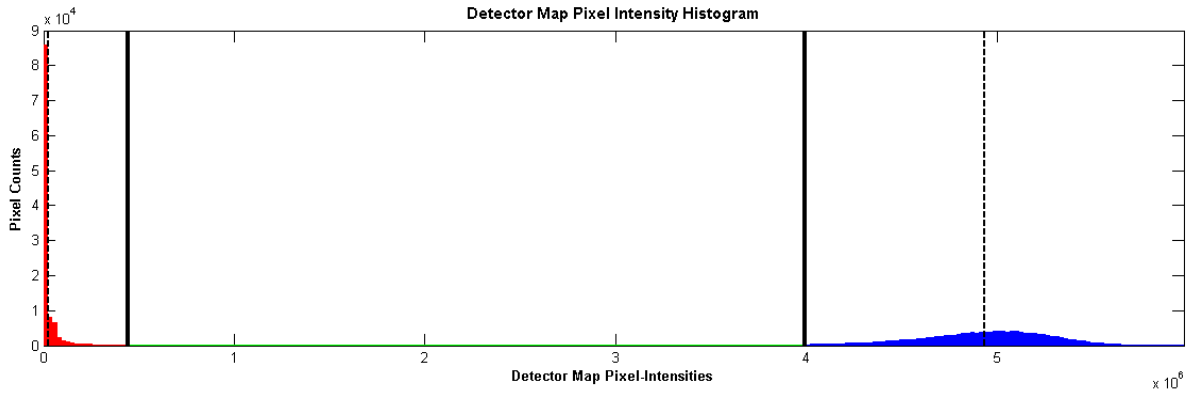

Figure 4.9 Histogram of the values of the detector map. The detector response (right) and background (left) are well separated in values.

It is vital to carefully note the beam current used to map the detector and also those of every image of the specimen. Though typically only one detector map is needed per instrument and scan setting[6], the beam current for imaging needs to be known for each image. The fluctuations in beam current for Schottkey FEGs is relatively small but for cold FEG instruments, the source deteriorates over time and probe current falls dramatically over a period of hours since flashing the tip. Errors in these values will greatly affect the accuracy of the results since errors of products are cumulative.

In order to achieve high resolution imaging of the specimen, the source demagnification is requisitely high and thus the probe current unavoidably low (see Section 2.4). Typical probe currents used for imaging nanoparticles tend to be around 10 - 20pA. This requires the beam current used to map the detector to be on the order of 1 - 2pA.

[6] a function of pixel dwell time, number of scanned probe positions

4.4 Simulation techniques

Once the HAADF images are calibrated so that they are represented on an absolute scale of fraction of incident beam current, it is possible to begin comparing images quantitative to each other and also to simulations. Here some of the major simulation techniques are presented and the case made for the absorptive potential approach for nanoparticle systems.

There are two main approaches to simulating electron microscopy images: Bloch wave and multislice approaches. Both are solutions to the Schrödinger equation and are equivalent given the right parameters [29]. A full derivation is outside the scope of this thesis but can be found in various places in the literature (see for example [30,31]).

4.4.1 Thermal diffuse scattering

The HAADF image intensity comprises both the scattering out to high angles of the elastic Bragg reflections and also crucially, the inelastic scattering of the diffuse TDS. The treatment of TDS requires careful calculation of the effects of the thermal vibrations of the specimen lattice

The Einstein approximation is usually invoked for the phonon dispersion relation for ease of calculation and reduction of computation time. This assumes that all atom vibrations are uncorrelated and their mean square displacement can be described by a Debye-Waller factor which thermally smears the atomic potential [32]; all the phonons in the sample are assumed to oscillate at the same frequency, independent of their wavelength. Though more sophisticated phonon models have been explored with a full Debye model phonon distribution [33] and with the inclusion of other inelastic scattering processes [34], the simple Einstein model is sufficient for most cases [31].

The Debye-Waller factor is defined as

$$M(\boldsymbol{q}) = 2\pi^2 < u^2 > q^2 \qquad 4.2$$

where $< u^2 > (T)$ is the projected mean square displacement of the atoms, which is a function of temperature *T*. These are parameterised by Sears and Shelly, and also by Gao and Peng [32,35] and were readily computed from the parameterisation for the simulations carried out in this thesis.

4.4.2 Multislice method

Cowley and Moodie proposed a physical optics approach for decoupling the phase shift due to scattering and propagation of fast electron travelling through solids to simplify simulations [36]. The sample is sliced in the direction perpendicular to that of the incident electron beam and a planar atomic potential used to describe each slice.

Each slice is then considered to be a weak phase object and the phase change due to the electron interacting with the atomic potential at one slice is calculated before the wavefunction is propagated to the next slice through free space by a Fresnel propagator, where another phase change is computed. Thus the exit wave from the previous slice is used as the incident wave on the next.

For thin slices (typically 2-5Å), this formulation is satisfactory and can prove to be extremely time-efficient for non-periodic samples compared to the Bloch wave solution. It is usually performed in reciprocal space via fast Fourier transforms (FFTs) to decrease calculation time. This contains an implicit periodicity so care must be taken to ensure periodic boundary conditions or non-overlap of non-periodic features.

4.4.3 Frozen phonon method

The frozen-lattice model, pioneered by Silcox and co-workers [37–40] is a popular semi-classical approach for calculating thermal diffuse scattering (TDS) in crystals. In this model, electron-phonon scattering is approximated as elastic scattering from static atoms displaced from their equilibrium positions. The final observed intensity is assumed to result from an ensemble average over atomic positions and is calculated by summing over many individual multislice simulations. A formal

comparison [41] of the frozen phonon with quantum-mechanical phonon excitation theory shows that they give identical results if:

- each thermal diffuse scattering calculation is considered incoherent with others
- the specimen thickness and the mean-free-path for the phonon excitation are both smaller than the distance travelled by the electron within the lifetime of the phonon.

The second condition is usually absolutely satisfied. Although atom vibration is a time-dependent process, the crystal lattice appears as if in a stationary instantaneous configuration for an incident electron since the interaction time of the electron with the crystal is much shorter than the vibration period of the crystal atom. An electron accelerated at 100keV goes through a 10nm thick layer in approximately 10^{-17}s; phonon vibration time is of the order of 10^{-13}s. The first can be precisely accounted for in the calculation with the introduction of the mixed dynamic form factor.

The frozen phonon formalism is readily implemented by a multislice technique [42] and popularised by Kirkland's book [43]. Quantitative matching with experimental observations has been obtained [39] and the model generally accepted [44].

However, since the calculation needs to run for several phonon configurations for each probe position, the computation time is often extensive and impractical. This has been greatly improved by the advent of GPU computers [25] and parallel clusters but the alternative method is particularly suitable for nanoparticle systems on desktop computers.

4.4.4 Bloch wave

A full Bloch wave analysis, proposed by Bethe [45], is the most physically intuitive way of describing a HAADF image (for a review, see [46]). The total wavefunction is derived from a coherent superposition of Bloch states: eigenstates of the fast electron coupled to eigenstates in the sample. These states are excited from a series of plane waves which cover the full range of angles within a focussed probe and are all phase-linked. Solving this problem involves inverting large matrices for

multiple angles, still a hugely computationally intensive process, though some progress was made to reduce the inverse complexity [47].

Inelastic scattering was initially described phenomenologically using the complex periodic potential $V_i(\mathbf{R})$. This later theoretically justified by Yoshioka quantum mechanically using a tight binding approximation [48]. Hall and Hirsch developed a theory to calculate the contribution of thermal diffuse scattering to the absorptive part of $V_i(\mathbf{R})$ in 1965 [49]. However, since it is impractical to numerically evaluate the convolution of several rapidly varying functions in 3 dimensions, most simulations are done using the various calculated and tabulated absorptive scattering factors [32,35]. Both these formulations were presented within the framework of the Bloch wave theory as an absorption process.

4.4.5 Absorptive potential

A faster, more practical approach based on an absorptive potential [49] was proposed by Pennycook and Jesson [50]. The atomic potential $V'(\mathbf{R})$, corresponding to the sample, is an effective absorption potential which directs the electron density in the elastic part of the wave function into the inelastic channel as inelastic scattering events occur [48]. In the single-channel[7] equation form, where the dominant absorption mechanism is thermal scattering, the total absorptive potential is well approximated by a local potential [51,52].

The integrated intensity falling on the HAADF detector is simply given by a sum of the probe intensity at each atomic column weighted by the corresponding TDS cross section of each atom, which is treated as individual scattering centres. The problem is thus simplified to an interaction between the elastic wavefunction and an effective interaction potential for inelastic scattering [53]. This approach was formulated into a multislice method for STEM simulations, which also included the detector geometry into the effective scattering potential [29].

However, the local approximation breaks down for structures thicker than 40nm as it does not take into account multiple scatterings; electrons removed from the elastic channel into the inelastic channel

[7] where inelastically scattered electrons are no longer considered to take part in subsequent elastic scattering and are essentially removed from the elastic channel

no longer take part in further elastic scattering [29]. It has, however, proven very effective for calculations of thin crystalline samples with weak scattering [13] and thus makes it ideal for systems with a limited number of atoms, such as nano-particles.

4.4.6 Available simulation codes

The simulations in this thesis were performed using the Melbourne STEM program developed by L J Allen, S D Findlay, M P Oxley and A J D'Alfonso [29,54]. The code requires the input of the co-ordinates of the sample in .xyz format with suitable mean squared displacement values to account for TDS. An example input file *is* given in Appendix G.1.

Parameters are required to define the probe and also the thickness of the slices in the multislice calculation. For a crystal, it is possible to tile a small input co-ordinate cell to create a larger supercell for adequate convergence of sampling for the calculation (see Appendix G.2). For a nanoparticle, a larger input cell is required with sufficient padding of empty space around the particle. This is necessary to prevent artefacts from the periodic boundary conditions required for the Fourier transforms performed in the calculation.

Other programs are available, often freely within the community. QSTEM is a frozen phonon code run in Matlab, developed from the popular Kirkland code by Cristoph Koch. STEMSim is another Matlab based code which performs frozen phonon, Bloch wave and also absorptive potential simulations. It is developed by Rosenauer et al.

4.5 Conclusions

Quantification of HAADF STEM images is shown to be vital to unlocking the true value of this technique in answering materials questions at a higher resolution.

A method to calibrate the ADF detector is developed which allows the scintillator response to be mapped relative to the incident beam current on the sample on all standard factory microscopes. Characterisation of the detector's A/D convertor with gain variations shows that there is significant nonlinear behaviour. This restriction necessitates the gain setting to be kept constant across the imaging of the detector and the sample and thus requires an increase in the probe current in order to achieve adequate dynamic range when imaging weakly scattering objects like nanoparticles (i.e. a lower probe current is needed to map the detector, a higher one to image the sample).

Though the detector response is non-uniform with probe position, the error associated with this variation is small compared to the potential error in uncertainty of the inner angle measurement. A method to ascertain the inner angle is detailed. Simulation techniques are then necessary to interpret the data quantitatively. Of the various available methods, the absorptive potential method is particularly suitable for nanoparticle systems.

References

[1] M. Retsky, Observed single atom elastic cross sections in a scanning electron microscope, Optik. 41 (1974) 127–42.

[2] M. Isaacson, D. Kopf, M. Ohtsuki, M. Utlaut, Atomic imaging using the dark-field annular detector in the stem, Ultramicroscopy. 4 (1979) 101–104.

[3] Z.Y. Li, N.P. Young, M. Di Vece, S. Palomba, R.E. Palmer, A.L. Bleloch, et al., Three-dimensional atomic-scale structure of size-selected gold nanoclusters, Nature. 451 (2008) 46–8.

[4] J.C. Yang, S. Bradley, J.M. Gibson, Rapid and Semi-automated Method for Analysis of the Number of Atoms of Ultra-small Platinum Clusters on Carbon, Microscopy and Microanalysis. 6 (2000) 353–357.

[5] S. Anderson, An approach to quantitative compositional profiling at near-atomic resolution using high-angle annular dark field imaging, Ultramicroscopy. 69 (1997) 83–103.

[6] D.O. Klenov, S. Stemmer, Contributions to the contrast in experimental high-angle annular dark-field images., Ultramicroscopy. 106 (2006) 889–901.

[7] R. Darji, A. Howie, Scattering corrections in small particle imaging, Micron. 28 (1997) 95–100.

[8] A. Singhal, J. Yang, J. Gibson, STEM-based mass spectroscopy of supported Re clusters, Ultramicroscopy. 67 (1997) 191–206.

[9] J. Yang, The oblate morphology of supported PtRu5 on carbon black, Materials Characterization. 51 (2003) 101–107.

[10] J.M. Lebeau, S. Stemmer, Experimental quantification of annular dark-field images in scanning transmission electron microscopy., Ultramicroscopy. 108 (2008) 1653–8.

[11] L.D. Menard, S.-P. Gao, H. Xu, R.D. Twesten, A.S. Harper, Y. Song, et al., Sub-nanometer Au monolayer-protected clusters exhibiting molecule-like electronic behavior: quantitative high-angle annular dark-field scanning transmission electron microscopy and electrochemical characterization of clusters with precise atomic stoichiom, The Journal of Physical Chemistry. B. 110 (2006) 12874–83.

[12] T. Malis, S.C. Cheng, R.F. Egerton, EELS log-ratio technique for specimen-thickness measurement in the TEM., Journal of Electron Microscopy Technique. 8 (1988) 193–200.

[13] J.M. Lebeau, S.D. Findlay, L.J. Allen, S. Stemmer, Quantitative Atomic Resolution Scanning Transmission Electron Microscopy, Physical Review Letters. 100 (2008) 1–4.

[14] D.O. Klenov, S.D. Findlay, L.J. Allen, S. Stemmer, Influence of orientation on the contrast of high-angle annular dark-field images of silicon, Physical Review B. 76 (2007) 1–7.

[15] P. Nellist, J. Rodenburg, Beyond the conventional information limit: the relevant coherence function, Ultramicroscopy. 54 (1994) 61–74.

[16] J. LeBeau, S. Findlay, X. Wang, A. Jacobson, L. Allen, S. Stemmer, High-angle scattering of fast electrons from crystals containing heavy elements: Simulation and experiment, Physical Review B. 79 (2009) 214110.

[17] J.M. Lebeau, S.D. Findlay, L.J. Allen, S. Stemmer, Position averaged convergent beam electron diffraction: theory and applications., Ultramicroscopy. 110 (2010) 118–25.

[18] S. Van Aert, J. Verbeeck, R. Erni, S. Bals, M. Luysberg, D. Van Dyck, et al., Quantitative atomic resolution mapping using high-angle annular dark field scanning transmission electron microscopy., Ultramicroscopy. 109 (2009) 1236–44.

[19] S. Van Aert, K.J. Batenburg, M.D. Rossell, R. Erni, G. Van Tendeloo, Three-dimensional atomic imaging of crystalline nanoparticles., Nature. 470 (2011) 374–7.

[20] S. Bals, M. Casavola, M.A. van Huis, S. Van Aert, K.J. Batenburg, G. Van Tendeloo, et al., Three-dimensional atomic imaging of colloidal core-shell nanocrystals., Nano Letters. 11 (2011) 3420–4.

[21] V. Ortalan, A. Uzun, B.C.B. Gates, N.D.N. Browning, Towards full-structure determination of bimetallic nanoparticles with an aberration-corrected electron microscope, Nature Nanotechnology. 5 (2010) 843–7.

[22] S.I. Molina, D.L. Sales, P.L. Galindo, D. Fuster, Y. González, B. Alén, et al., Column-by-column compositional mapping by Z-contrast imaging., Ultramicroscopy. 109 (2009) 172–6.

[23] D. Hernández-Maldonado, M. Herrera, P. Alonso-González, Y. González, L. González, J. Gazquez, et al., Compositional Analysis with Atomic Column Spatial Resolution by 5th-Order Aberration-Corrected Scanning Transmission Electron Microscopy, Microscopy and Microanalysis. -1 (n.d.) 1–4.

[24] E.J. Kirkland, M.G. Thomas, A high efficiency annular dark field detector for STEM., Ultramicroscopy. 62 (1996) 79–88.

[25] H. Katz-Boon, C.J. Rossouw, C. Dwyer, J. Etheridge, A method to determine the thickness profile of nanoparticles, Ultramicroscopy. 124 (2012) 61–70.

[26] S.D. Findlay, J.M. LeBeau, Detector non-uniformity in scanning transmission electron microscopy, Ultramicroscopy. 124 (2013) 52–60.

[27] L. Jones, K.E. MacArthur, Detector Non-uniformity, In Preparation. (n.d.).

[28] B. Rafferty, P.D. Nellist, S.J. Pennycook, On the origin of transverse incoherence in Z-contrast STEM., Journal of Electron Microscopy. 50 (2001) 227–33.

[29] S.D. Findlay, L.J. Allen, M.P. Oxley, C.J. Rossouw, Lattice-resolution contrast from a focused coherent electron probe. Part II, Ultramicroscopy. 96 (2003) 65–81.

[30] A. Amali, P. Rez, Theory of Lattice Resolution in High-angle Annular Darl-field Images, Microsc. Microanal. 3 (1997) 28–46.

[31] S.J. Pennycook, P.D. Nellist, eds., Scanning Transmission Electron Microscopy, Springer, 2011.

[32] V.F. Sears, S. a. Shelley, Debye–Waller factor for elemental crystals, Acta Crystallographica Section A Foundations of Crystallography. 47 (1991) 441–446.

[33] D. a Muller, B. Edwards, E.J. Kirkland, J. Silcox, Simulation of thermal diffuse scattering including a detailed phonon dispersion curve., Ultramicroscopy. 86 (2001) 371–80.

[34] A. Bleloch, M. Castell, A. Howie, C. Walsh, Atomic and electronic Z-contrast effects in high-resolution imaging, Ultramicroscopy. 54 (1994) 107–115.

[35] H.X. Gao, L.-M. Peng, Parameterization of the temperature dependence of the Debye–Waller factors, Acta Crystallographica Section A Foundations of Crystallography. 55 (1999) 926–932.

[36] J.M.J. Cowley, A.F.A. Moodie, The scattering of electrons by atoms and crystals. I. A new theoretical approach, Acta Crystallographica. 10 (1957) 609–619.

[37] S. Hillyard, J. Silcox, Thickness effects in ADF STEM zone axis images, Ultramicroscopy. 52 (1993) 325–334.

[38] S. Hillyard, R. Loane, J. Silcox, Annular dark-field imaging: Resolution and thickness effects, Ultramicroscopy. 49 (1993) 14–25.

[39] R.F. Loane, P. Xu, J. Silcox, Thermal vibrations in convergent-beam electron diffraction, Acta Crystallographica Section A Foundations of Crystallography. 47 (1991) 267–278.

[40] R. Loane, P. Xu, J. Silcox, Incoherent imaging of zone axis crystals with ADF STEM, Ultramicroscopy. 40 (1992) 121–138.

[41] Z.L. Wang, The `Frozen-Lattice' Approach for Incoherent Phonon Excitation in Electron Scattering. How Accurate Is It?, Acta Crystallographica Section A Foundations of Crystallography. 54 (1998) 460–467.

[42] E. Kirkland, Simulation of annular dark field stem images using a modified multislice method, Ultramicroscopy. 23 (1987) 77–96.

[43] E.J. Kirkland, Advanced Computing in Electron Micrscopy, 1st ed., New York, NY, Plenum Press, 1998.

[44] D. Van Dyck, Is the frozen phonon model adequate to describe inelastic phonon scattering?, Ultramicroscopy. 109 (2009) 677–682.

[45] H.A. Bethe, Theorie der Beugung von Elektronen an Kristallen, Ann. Phys (Leipzig). 87 (1928) 55–129.

[46] C. Humphreys, The scattering of fast electrons by crystals, Reports on Progress in Physics. 42 (2001).

[47] K. Watanabe, T. Yamazaki, I. Hashimoto, M. Shiojiri, Atomic-resolution annular dark-field STEM image calculations, Physical Review B. 64 (2001) 1–5.

[48] H. Yoshioka, Effect of Inelastic Waves on Electron Diffraction, Journal of the Physical Society of Japan. 12 (1957) 618–628.

[49] C.R. Hall, P.B. Hirsch, Effect of Thermal Diffuse Scattering on Propagation of High Energy Electrons Through Crystals, Proceedings of the Royal Society A: Mathematical, Physical and Engineering Sciences. 286 (1965) 158–177.

[50] S. Pennycook, D. Jesson, High-resolution incoherent imaging of crystals, Physical Review Letters. 64 (1990) 938–941.

[51] L.J. Allen, S.D. Findlay, M.P. Oxley, C. Witte, N.J. Zaluzec, Modelling high-resolution electron microscopy based on core-loss spectroscopy., Ultramicroscopy. 106 1001–11.

[52] S.D. Findlay, M.P. Oxley, L.J. Allen, Modeling atomic-resolution scanning transmission electron microscopy images, Microscopy and Microanalysis. 14 (2008) 48–59.

[53] L. Allen, T. Josefsson, Inelastic scattering of fast electrons by crystals, Physical Review B. 52 (1995) 3184–3198.

[54] L.J. Allen, S.D. Findlay, M.P. Oxley, C.J. Rossouw, Lattice-resolution contrast from a focused coherent electron probe. Part I., Ultramicroscopy. 96 (2003) 47–63.

Chapter 5

Probe Integrated HAADF Scattering Cross Sections

5.1 Cross sections in the literature

Quantitative image interpretation of STEM images has most commonly focussed on contrast and thus peak values, possibly as a legacy of standard image interpretation techniques in conventional TEM. A non-linear dependence of the peak intensity on the number of atoms in a column can be observed (see Figure 5.1) and the contribution to the intensity of impurity atoms can depend on their height within the column [1]. In such cases, a quantitative interpretation necessitates either a) a full comparison to image simulations or areas of known composition, or b) construction of a histogram of column intensities and then the identification of distinct clustering of intensity values.

Thus far, agreement between calculation and experiment requires knowledge of a significant number of imaging parameters, such as convergence angle, defocus and other residual aberrations [2]. In particular, a convolution with a Gaussian is routinely used to account for the finite size of the electron source and its broadening effect on the probe [3]. Often, the width of this Gaussian is found through an empirical fit to achieve an exact match of the simulations with the data [4], and subsequent experiments with different samples can then be used to show a consistent measure of the probe size of a particular instrument [5–7].

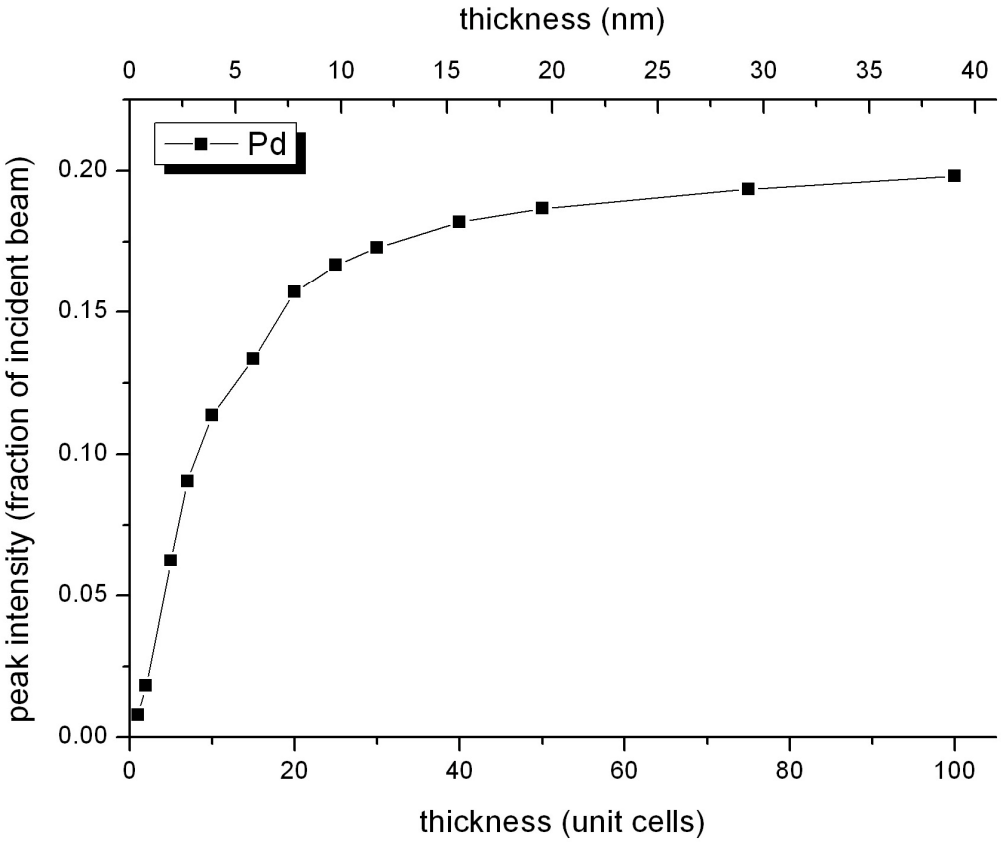

Figure 5.1 Simulations show that peak intensity (single pixel) of an atomic column in a crystal of Pd viewed along <100> is monotonic but non-linear with thickness.

The finite effective source size can be measured experimentally [8] but this varies depending on the demagnification given by the settings of the condenser lenses and objective lens. In addition, the measurement process may require changing samples or risks incurring sample damage. Furthermore, optimum focus is usually found by manual adjustment or choosing the image which maximises contrast in a through focal series [9]. The latter requires prolonged exposure of the specimen to the electron beam, problematic where issues of damage in beam sensitive samples are paramount, and the former is prone to human subjectivity. Thus it is vital to have a metric for comparing experiments to simulation that is robust to these experimental parameters since any error in defocus translates to a broader incident beam profile. Moreover, when observing samples from real materials problems, such as nanoparticles dispersed on a powder support in a heterogeneous catalyst system, variations in height preclude having a precise knowledge of the crucial defocus parameter.

For beam sensitive samples such as core-shell nanoparticles, a quantitative parameter that allows comparison between simulation and experiment, yet that is as robust to the widest range of imaging parameters as possible, is of vital importance.

Some recent studies of quantified HAADF image interpretation typically use the mean intensity, averaged over multiple columns or individual columns [5] or the 'intensity volume' of the column [14] to compare simulation to experiment. In 1973, Retsky used annular dark-field imaging in the STEM to measure elastic cross-sections of single atoms and found a good agreement with theoretical calculations [10]. Later studies showed interest in the idea of an integrated cross section [15] but with only the resolution to image clusters of heavy elements on a light matrix and without the resolution needed to isolate individual atomic columns in a structure [16]. Consideration of the total scattered HAADF intensity from an object has also been used previously to estimate cluster sizes and number of atoms in small particles using known cluster sizes as a metric to calibrate the intensities [17]. The idea of cross sections is used widely scattering physics (X-ray and neutron diffraction [18], electron energy-loss spectroscopy in electron microscopy [19]) and describes the effective area which corresponds to the probability of scattering or absorption.

In this thesis, the probe-position integrated HAADF cross section is simply referred to as the cross section; and it is an incoherent HAADF scattering cross section integrated over the probe positions that correspond to a feature such as a single column of atoms. The cross section quantity can be useful for the comparison of experimental data with simulation because the incoherent nature of HAADF detection allows for the absolute cross section to be independent from the form of the probe, as long as the signal from the whole atomic column is integrated, the columns are clearly resolved and the sample sufficiently thin.

This chapter shows that the cross section quantity is robust to most experimental parameters, being only significantly sensitive to accelerating voltage, detector angle, and the object itself, and circumvents lack of detailed knowledge of parameters that are difficult to determine, such as source coherence. The main sources of error in the quantitative analysis of atomic resolution HAADF STEM images are discussed. Lastly, the method is demonstrated by applying it to identification of single atoms in a bimetallic sample of Pt and Pd nanoparticles and the identification of layers in 2D layered materials.

5.2 Simulation methods

The simulations were performed using an absorptive potential multislice method [11,12], which has been shown to agree with the full frozen phonon calculation up to thicknesses of 25nm [6], sufficient for nanoparticle systems and thin layered specimens. Unless otherwise specified, they are performed for a 200kV instrument with HAADF detector inner and outer angles of 90mrad and 180mrad, corresponding to that of the Oxford-JEOL 2200-MCO double aberration corrected microscope.

The Debye-Waller factors that account for the thermal diffuse scattering were calculated using the Gao and Peng parameterisation [13] and a temperature of 300K chosen unless otherwise stated. All calculations, unless otherwise specified, were performed on a 3.112 x 3.112 nm^2 super-cell, sampled on a 512 x 512 mesh, which was found to be sufficient for convergence of the calculation for the thin specimens (see Appendix G for a more detailed discussion of sampling). Sub-slicing was increased until convergence in the multislice calculation to 4s.f. accuracy was reached; this typically corresponded to 6 subslices. Each slice was defined such that it contained one unit cell in thickness so that the atoms could be placed at the correct heights in the sample. 24 x 17 probe positions were used over one unit cell in the [110] direction and 24 x 24 probe positions in the [100] direction, in order to create an image with circular atoms while also minimising calculation time.

5.3 Mathematical treatment

The following derivation was carried out in collaboration with Les Allen, Adrian D'Alfonso and Nathan Lugg of the University of Melbourne.

It is convenient to start from Equation 5.7 in [20]**,** which allows a probe position dependent inelastic scattering cross section σ (in three dimensions) to be expressed as a 3 dimensional integral:

$$\sigma(\boldsymbol{R}) = \frac{2\pi}{h\nu} \iint \psi_0^*(\boldsymbol{R},\boldsymbol{r})\, W(\boldsymbol{r},\boldsymbol{r}')\, \psi_0(\boldsymbol{R},\boldsymbol{r}') d\boldsymbol{r}\, d\boldsymbol{r}' \qquad 5.1$$

Here $\boldsymbol{R}$ denotes the position of the probe, h is the usual Plank's constant and v is the relativistic velocity of the incident electrons. The term $W(\boldsymbol{r},\boldsymbol{r}')$ is the non-local potential representing the inelastic scattering of interest. The incident probe is represented by the wavefunction $\psi_0(\boldsymbol{R},\boldsymbol{r}')$, which is normalized as

$$\frac{1}{V}\int_V |\psi_0(\boldsymbol{R},\boldsymbol{r})|^2\, d\boldsymbol{r} = 1 \qquad 5.2$$

Here V is the volume of the specimen and the wavefunction is dimensionless.

The wavefunction can then be written in the form of a modulated plane wave as

$$\psi_0(\boldsymbol{R},\boldsymbol{r}) = \exp(4\pi i K z)\, \phi_0(\boldsymbol{R},\boldsymbol{r}_\perp, z) \qquad 5.3$$

where K is the wave number of the incident electron and the vector r in the wavefunction ϕ_0 has been decomposed into a vector orthogonal to the optical axis, and one which is along the z direction [20].

Then assuming that the potential representing the inelastic scattering can be projected, making a flat Ewald sphere approximation, and also supposing that the detector counting the inelastically scattered electrons spans a sufficiently large area in the diffraction plane (as discussed in Ref. [20]), Equation 5.1 reduces to the following form:

$$\sigma(\boldsymbol{R}) = \frac{4\pi}{hvt}\int_A \int_0^t |\phi_0(\boldsymbol{R},\boldsymbol{r}_\perp, z)|^2\, \widetilde{V}'(\boldsymbol{r}_\perp)\, d\boldsymbol{r}_\perp\, dz \qquad 5.4$$

The volume integral has been decomposed into integration over the area A that the specimen presents to the beam and its thickness t. After making the local approximation, $W(\boldsymbol{r},\boldsymbol{r}')$ becomes the local potential $V'(\boldsymbol{r})$. It is then integrated with respect to z over the thickness t of the specimen (and taken together with the factor of $1/t$ in the pre-factor, is the potential per unit length). In this paper $\widetilde{\boldsymbol{V}}'(\boldsymbol{r}_\perp)$ is the potential for incoherent inelastic scattering to the HAADF detector, which can be calculated, for example in a similar way to that described in Ref. [24].

A further approximation is made such that the probe wavefunction does not change significantly within the thickness of the sample. This is commonly termed the 'object function approximation' [21] and allows the probe wavefunction to be taken out of the integral over thickness to obtain:

$$\sigma(\boldsymbol{R}) = \frac{4\pi}{h\nu}\int_A |\phi_0(\boldsymbol{R},\boldsymbol{r}_\perp)|^2\, \widetilde{\boldsymbol{V}}'(\boldsymbol{r}_\perp)\, d\boldsymbol{r}_\perp \qquad 5.5$$

Assuming that the $\boldsymbol{R}$ dependence can be expressed as $\boldsymbol{r}_\perp - \boldsymbol{R}$ such that the incident STEM probe is invariant under translation across the sample, Equation 5.5 can be reformed to give:

$$\sigma(\boldsymbol{R}) = \frac{4\pi}{h\nu}\int_A |\,\phi_0(\boldsymbol{r}_\perp - \boldsymbol{R})|^2\, \tilde{V}'(\boldsymbol{r}_\perp) d\boldsymbol{r}_\perp \qquad 5.6$$

Now considering the fraction of incident electrons that is scattered to the HAADF detector; from the definition of the cross section $\sigma(\boldsymbol{R})$, this can be written as:

$$I(\boldsymbol{R}) \;=\; \frac{\sigma(\boldsymbol{R})}{A} \;=\; \frac{4\pi}{h\nu A}\int_A |\,\phi_0(\boldsymbol{r}_\perp - \boldsymbol{R})|^2\, \tilde{V}'(\boldsymbol{r}_\perp) d\boldsymbol{r}_\perp \qquad 5.7$$

Making the definition:

$$P(\boldsymbol{r}_\perp - \boldsymbol{R}) = \frac{|\,\phi_0(\boldsymbol{r}_\perp - \boldsymbol{R})|^2}{A} \qquad 5.8$$

which can be intuitively thought of as the fraction of the total incident electron current per unit area for a given location in the probe, Equation 5.7) becomes

$$I(\boldsymbol{R}) = \frac{4\pi}{h\nu}\int_A P(\boldsymbol{r}_\perp - \boldsymbol{R})\, \tilde{V}'(\boldsymbol{r}_\perp) d\boldsymbol{r}_\perp \qquad 5.9$$

The projected potential of a crystal in the local approximation can be expressed as a sum of many potentials of individual atomic columns α, centred at positions $\boldsymbol{R}_\alpha$

$$\tilde{V}(\boldsymbol{r}_\perp) = \sum_\alpha \tilde{V}'_\alpha(\boldsymbol{r}_\perp - \boldsymbol{R}_\alpha) \qquad 5.10$$

This is particularly useful when considering the composition of atomic resolution images. Here it is assumed that both the width of the potential of the column and probe itself are much smaller than the distance between columns. This is broadly true of on-zone axis crystals in aberration corrected instruments.

Substituting this expression into Equation 5.9) gives:

$$I(\boldsymbol{R}) = \frac{4\pi}{h\nu}\sum_{\alpha}\int_{A} P(\boldsymbol{r}_{\perp} - \boldsymbol{R})\ \tilde{V}'_{\alpha}(\boldsymbol{r}_{\perp} - \boldsymbol{R}_{\alpha})d\boldsymbol{r}_{\perp} \tag{5.11}$$

Note that the probe is centred on $\boldsymbol{R}$ and thus a contribution to the intensity is only apparent when the probe is in the vicinity of a column $\boldsymbol{R}_{\alpha}$ and zero elsewhere. Considering the contribution from a single column, it is possible to write $\boldsymbol{r'}_{\perp} = \boldsymbol{r}_{\perp} - \boldsymbol{R}_{\alpha}$:

$$I_{\alpha}(\boldsymbol{R}) = \frac{4\pi}{h\nu}\int_{A} P(\boldsymbol{r'}_{\perp} + \boldsymbol{R}_{\alpha} - \boldsymbol{R})\ \tilde{V}'_{\alpha}(\boldsymbol{r'}_{\perp})d\boldsymbol{r'}_{\perp} \tag{5.12}$$

Defining a new variable $\boldsymbol{R'} = \boldsymbol{R} - \boldsymbol{R}_{\alpha}$ such that $\boldsymbol{R} = \boldsymbol{R'} + \boldsymbol{R}_{\alpha}$, Equation 5.12 then becomes:

$$I_{\alpha}(\boldsymbol{R'}) = \frac{4\pi}{h\nu}\int_{A} P(\boldsymbol{r'}_{\perp} - \boldsymbol{R'})\ \tilde{V}'_{\alpha}(\boldsymbol{r'}_{\perp})d\boldsymbol{r'}_{\perp} \tag{5.13}$$

An integration is then performed over another area *A'* such that *A'* is centred on column α and $I_{\alpha}(\boldsymbol{R'})$ is negligible at the boundaries of A'. Here the assumption is made that the area A' contains all the image intensity associated with the column. This yields the following:

$$\int_{A'} I_{\alpha}(\boldsymbol{R'})d\boldsymbol{R'} = \frac{4\pi}{h\nu}\int_{A}\int_{A'} P(\boldsymbol{r'}_{\perp} - \boldsymbol{R'})\ \tilde{V}'_{\alpha}(\boldsymbol{r'}_{\perp})d\boldsymbol{r'}_{\perp}d\boldsymbol{R}' \tag{5.14}$$

By considering the integral over $\boldsymbol{R'}$ first, Equation 5.14) can be written as:

$$\int_{A'} I_{\alpha}(\boldsymbol{R'})d\boldsymbol{R'} = \frac{4\pi}{h\nu}\int_{A} \tilde{V}'_{\alpha}(\boldsymbol{r'}_{\perp})\int_{A'} P(\boldsymbol{r'}_{\perp} - \boldsymbol{R'})\ d\boldsymbol{R'}\ d\boldsymbol{r'}_{\perp} \tag{5.15}$$

At this point, the normalised probe function over the specimen can be considered in order to obtain an expression consistent with Equation 5. 2:

$$\int_{A'} P(\boldsymbol{r'}_{\perp} - \boldsymbol{R'})\ d\boldsymbol{R'} = 1 \tag{5.16}$$

This normalisation is a key step, as, by substituting Equation 5.16 into 5.15, this allows the integrated intensity of a column to be expressed as:

$$\int_{A'} I_{\alpha}(\boldsymbol{R'}) d\boldsymbol{R'} = \frac{4\pi}{h\nu} \int_{A'} \tilde{V'}_{\alpha}(\boldsymbol{r'}_{\perp}) d\boldsymbol{r'}_{\perp} \tag{5.17}$$

It can be clearly seen that the value has dimensions of [L^2] and this is then identified as the cross section of inelastic scattering to the HAADF detector integrated over probe positions that comprise an atomic column, the cross section:

$$\frac{4\pi}{h\nu} \int_{A'} \tilde{V'}_{\alpha}(\boldsymbol{r'}_{\perp}) d\boldsymbol{r'}_{\perp} = \Theta\ [L^2] \tag{5.18}$$

Experimentally, the probe is scanned over discrete probe positions which make up a pixelated STEM image, where each pixel has the total fraction of the incident probe that has scattered onto the HAADF detector from that probe position $\boldsymbol{R}$. Thus the integration in Equation 5.18 is, in practice, a discrete sum. Assuming that the image of a particular column α in an atomic resolution HAADF image is contained by some j pixels each with fractional intensity I_j and each of some area a_j, the total area of these pixels corresponds to the area A' in Equation 5.18. When this is summed, the product of these pixels with their area gives:

$$\Theta = \sum_{j} I_{\alpha,j}\, a_j \tag{5.19}$$

This is an integrated cross section of inelastic electron scattering to the HAADF detector identical to that used by Retsky [10]. In addition, this quantity is independent to the shape and form of the probe, simply by taking the product of the integrated (summed) fractional intensity of the pixels that comprise a column and assuming that the area of each pixel is a:

$$\Theta = a \sum_{j} I_{\alpha,j} \tag{5.20}$$

Given that this parameter is independent of the probe function, the dependence on probe shape and source coherence, which may be difficult to determine experimentally, can be strongly mitigated as long as a column is well resolved.

It is imperative to note that this treatment is valid for the circumstances where the probe function is considered invariant in z, i.e. thin specimens. For thicker samples, the variation of the probe in the sample becomes more significant and the object function treatment will naturally break down. The degree to which an integrated cross section quantity is useful under those conditions is explored in Section 5.5.

5.4 Cross section for single atoms

The sensitivity of the cross section of single atoms to common imaging parameters is investigated first. The key to measuring the cross section is to record an image on a calibrated intensity scale such that the intensity for any probe position is expressed as a fraction of the total incident current.

Simulations were performed using the absorptive potential code that showed the cross section for a single Pd atom imaged with a 200kV, aberration free probe of convergence semi-angle 25mrad, with a detector of collection angle range 90-180mrad, is 0.33 Mbarns (Mb) where 1 barn=10^{-28} m^2 . For a single Pt atom under the same conditions, the integrated cross section is 0.48 Mb. As can be seen in later sections, the cross section is robust to the precise form of the probe and thus the aberration and convergence semi-angle quantities for the simulations have been can be chosen reasonably arbitrarily.

5.4.1 The probe: defocus

The probe harbours some of the most influential and difficult to determine experimental parameters such as defocus and source size effects [8]. The defocus, which has been shown to greatly affect HAADF images [22] is considered first.

Simulations show that the peak image intensity of a single atom of Pt drops significantly with increased under-defocus of the probe into the specimen (see Figure 5.2). This is expected when imaging with a broadened defocused beam. However, the cross section is relatively insensitive, as long as the area of 'column integration' is sufficient such that the entire atom image is included. This breaks down as the beam becomes increasingly broad and intensity is lost to the outer edges of the integration box.

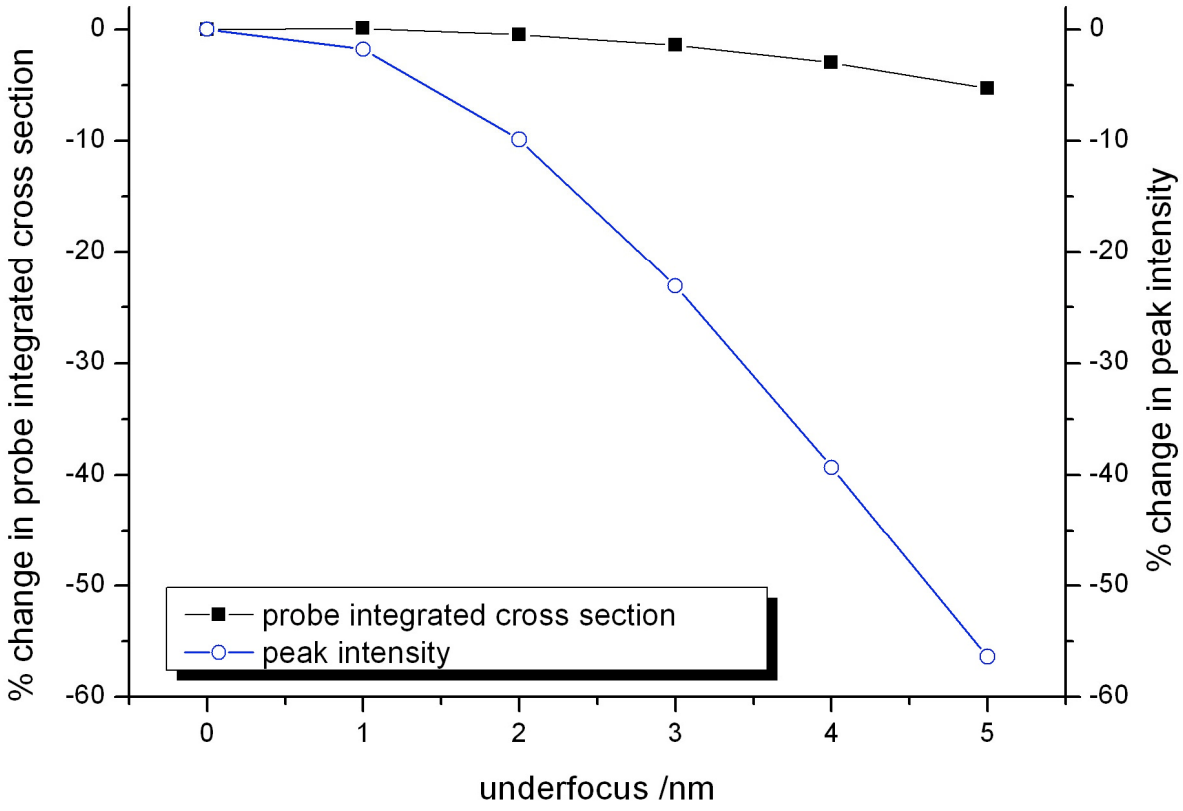

Figure 5.2 The relative change in peak and cross section values as a function of defocus for a single Pd atom. While the cross section is reasonably insensitive, the peak value falls off very rapidly. Variations of the cross section for large defocuses are due to the broadened beam no longer being included in the area of the integration box for the column of size 5Å^2, with sides of 2.25Å

5.4.2 The probe: source size and coherence

The intensity distribution in the probe is strongly dependent on the demagnified electron source distribution as imaged to form the probe, and other sources of loss of spatial coherence such as

instrument instabilities. The difficulty with measuring these parameters has often led to mismatches between experiment and simulation [23]. While many efforts have been made to characterise them [24,25], often the most practical way to account for their effects is to make a fit to the experimental images themselves. This is primarily done by combining unknown probe effects into a Gaussian convolution where the choice of the size of the Gaussian is determined by a variable fitting parameter or the match to images across several experiments [9].

By using the cross section as a metric for comparison between experiment and simulations, the dependence on spatial coherence is greatly reduced. As previously shown in Section 5.3, the cross section has no dependence on the probe. Applying a Gaussian convolution to account for the partial spatial coherence does not affect the cross section value of a single atom, whereas the peak value (and thus the contrast) drops significantly (see Figure 5.3). A convolution was performed with Gaussians of sizes covering the range typically reported in the literature [5,23], and the values compared to those of the original image.

5.4.3 The probe: convergence angle

Convergence angle (determined by the objective aperture size) has been found to greatly affect the intensity of HAADF images [26]. The cross section is seen to be insensitive to the size of the probe as long as the columns are well resolved (Table 5.1). Again, this is easily understood by the fact that the measured cross section is independent of the probe, as long as the columns are well resolved.

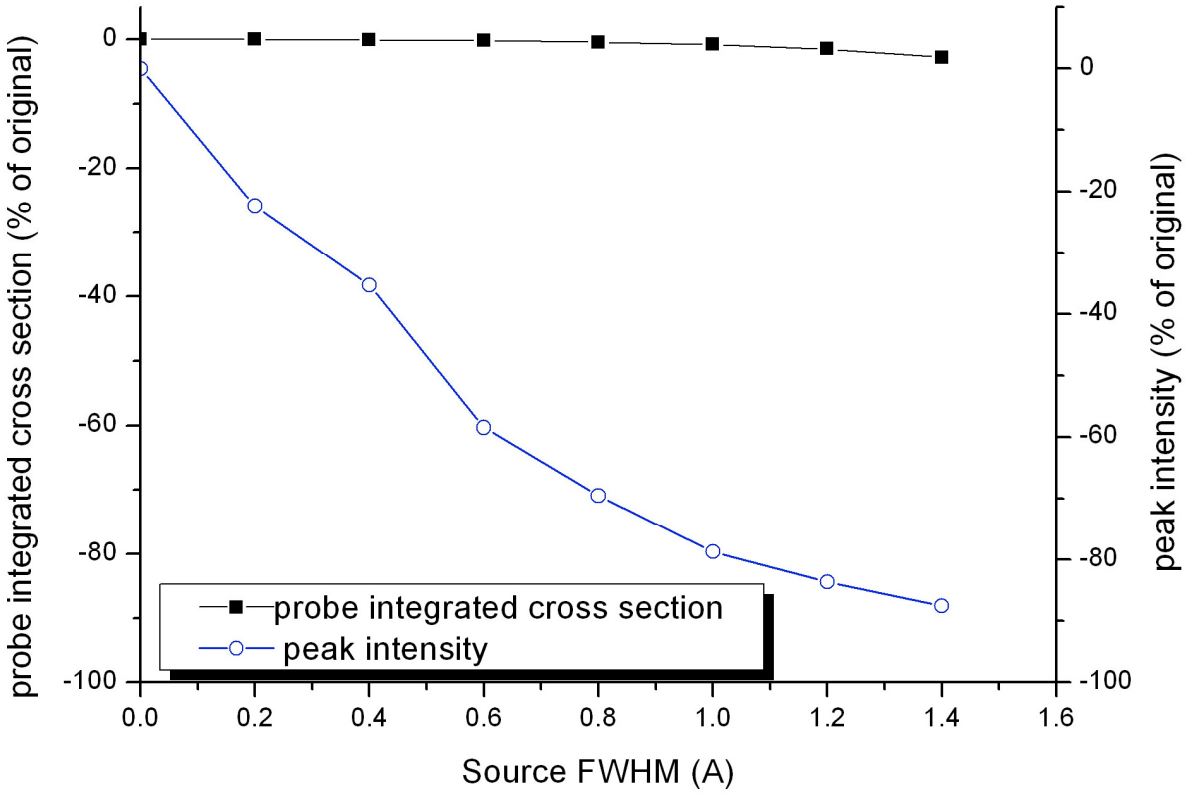

Figure 5.3 The relative change of cross section and column peak intensity with effective source size. The cross section is robust to a convolution with a Gaussian to account for the finite probe size, unlike the value of the peak intensity.

Aperture Size ($Å^{-1}$)	**Convergence Angle (mrad)**	**cross section (Mb)**	**% change**
0.8	20.1	0.477	0
0.9	22.6	0.486	1.7
1.0	25.1	0.483	1.2

Table 5.1 The variation of cross section with respect to convergence angle. The objective aperture size, which controls the convergence angle of the probe, has very little effect on the cross section of a single Pt atom.

5.4.4 Analysis parameters

One of the strengths of analysis by cross section is that this parameter is not sensitive to the number or size of pixels in both the simulation and experiment. As long as the integration is performed over the whole of the column, the size of the area of integration does not affect the value of the cross section significantly (See Table 5.2). Making use of an average intensity across the atomic column quantity would require accurate knowledge of the size of the integration box or pixel sizes to compare simulation to experiment.

Integration area (Å^2)	**cross section (Mb)**	**% difference**
Single Pt atom		
9.0	0.483	
5.1	0.475	-1.7
2.3	0.452	-6.5
*Single Au atom**		
2.3	0.564	25

Table 5.2 The change in cross section as a function of the area of the integration box around a single atom of Pt. As long as the whole column is included in the integration of intensities, the cross section does not vary significantly. The variation is small enough that it is still possible to distinguish between elements of successive Z-number (Pt Z=78, Au Z=79). *The percentage difference with respect to a single Pt atom of the same integration box size.

As more simulations are performed on desktop PCs, it is useful to conserve computing power by finding the minimum number of probe positions necessary. The cross section analysis is also robust to the number of probe positions imaged (See Table 5.3), which minimises the need for long calculations. As long as the probe sampling is sufficient to accurately capture the fluctuation of intensity across the atom or column, the cross section is insensitive to the effective pixel size used in the simulations.

The cross section values are sensitive enough to allow identification of different species of atoms that are Z=1 apart in atomic number (see Tables 5.2 and 5.3). It is thus tempting to consider the possibility of creating a periodic table of cross sections from simulations that allows easy comparison of experimental images to simulations. This is further discussed in Sections 5 and 6.

Pixel size (Å ^{2})	cross section (Mb)	% difference
Single Pt atom		
0.00055	0.4835	
0.04592	0.4828	0.14
0.25000	0.4772	1.3
0.36000	0.5891	22
Single Au atom		
0.00055	0.5462	13

Table 5.3 The change in cross section as a function of the pixel size of the image. Probe position sampling does not affect the cross section value as long as the columns are well resolved and appear to be circular. When the pixel size is large such that the atomic columns are no longer appear round in shape, the cross section value increases dramatically such that it is not possible to resolve atoms of neighbouring Z-number in composition (Au, Z=79).

5.5 Applicability of cross sections to imaging of crystals

While it is intuitive to understand why the cross section gives such a robust parameter when using the object function approximation, it must be kept in mind that the mathematical treatment in Section 5.3 has assumed that the probe does not change with respect to thickness in the specimen. Nonetheless, an cross section may still be defined in the case of a thicker crystal, but will now be influenced by channelling effects. For application to thicker samples, the strength of the cross section approach to crystals is empirically explored, particularly to what extent this method continues to have value.

Simulations show that the cross section is closer to being linear with thickness compared to peak intensity (Figure 5.4). This makes image interpretation considerably more straightforward. However, the relationship is not a linear one, thus matching between experiment and simulation is still necessary for a thorough quantification.

In this section some of the sources of error in comparing experiment to simulation are discussed: from errors in experimental measurements to errors in analysis.

5.5.1 Pure crystals

Both pure element crystals of Pt and Pd were simulated as a basis for comparison to experimental results. The calculated cross sections are show in Figure 5.4 as a function of crystal thickness.

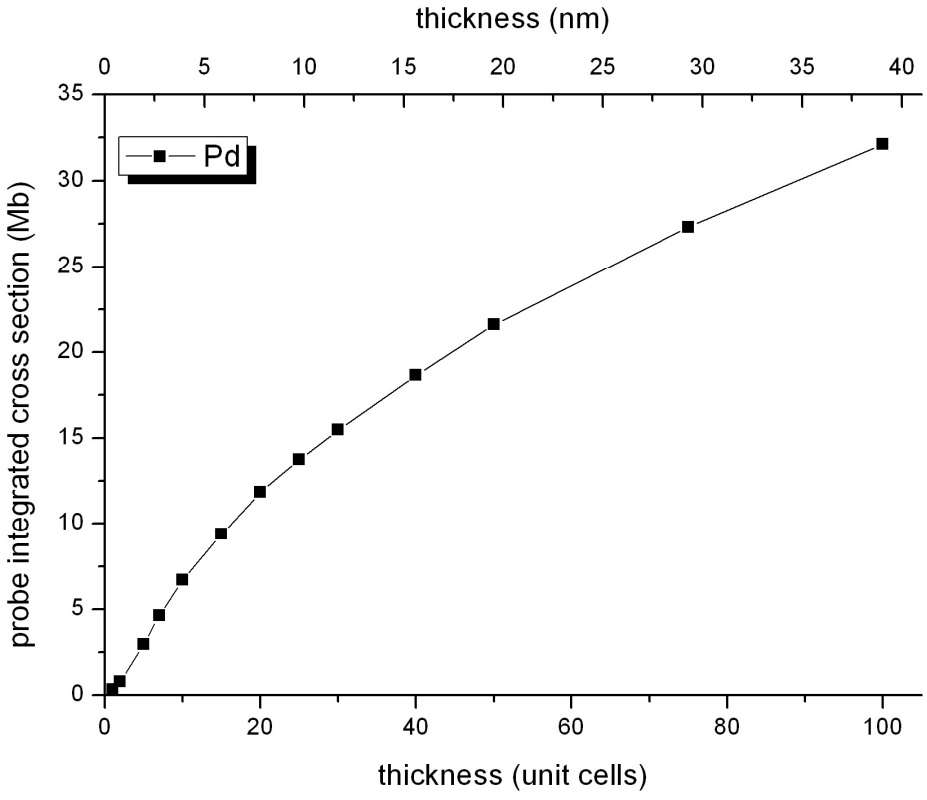

Figure 5.4 cross section of intensity scattered to the HAADF detector (integrated over probe positions) of an atomic column in a Pd crystal of orientation <100> as a function of thickness (as defined by Eqs. 18 and 19). The dependence is much closer to linear than that of peak intensity (compare with Figure 5.1).

It is clear from Figure 5.4 that the intensity is monotonic but nonlinear with thickness. Moreover, channelling effects mean that the scattering is enhanced beyond the linear addition of atomic scattering with $Z^{1.7}$ behaviour. The exponent of 1.7 is the usual Z^2 Rutherford scattering behaviour with the addition of screening effects from the atomic potential [27,28] and the plot scaled to the cross section of a single Pd or Pt atom.

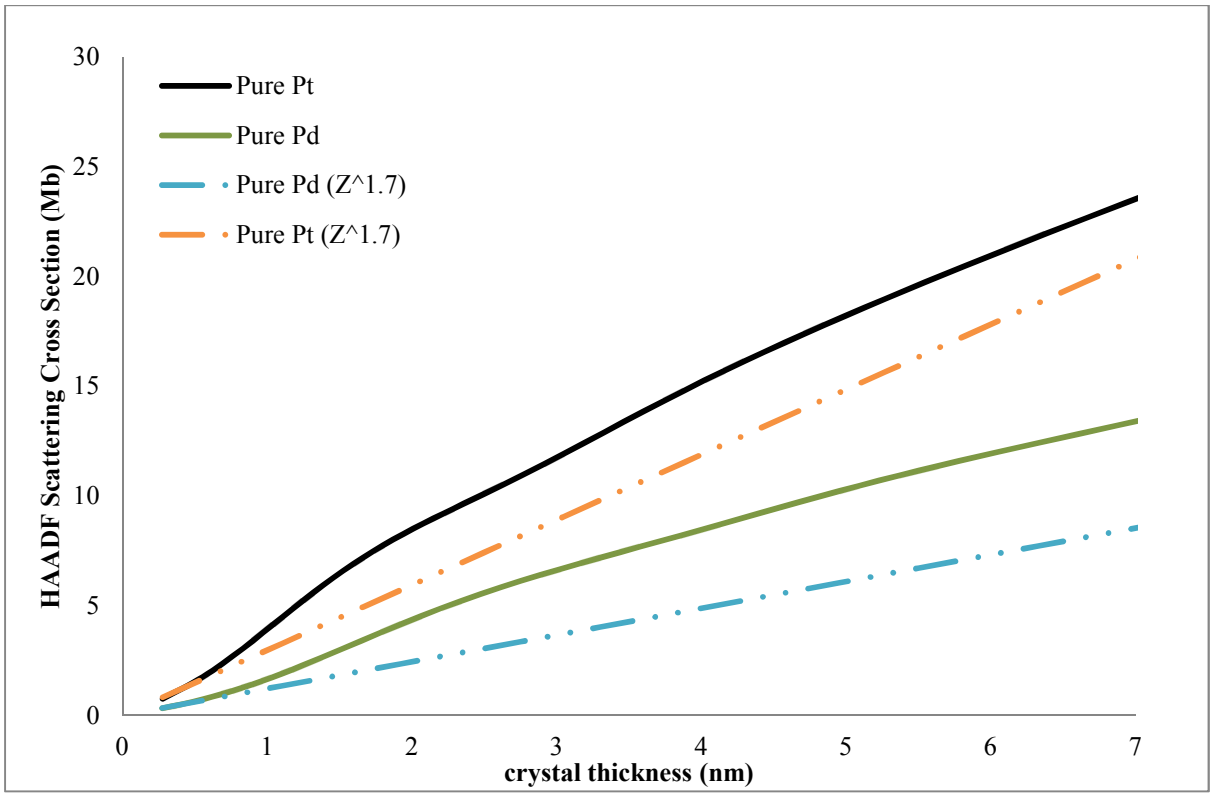

Figure 5.5 HAADF scattering cross section of crystals of pure Pt and Pd, both oriented in a [110] direction, calculated for a microscope at 200kV with detector angles of 91.15 – 180mrad. The dashed lines show the linear scaling of cross section without channelling effects, scaled to the scattering from a single atom of Pd or Pt.

5.5.2 Defocus in a crystal

Despite changes in defocus affecting the coupling of the incident probe into the channelling states, it is apparent that the cross section of a single column does not vary significantly with defocus (see Figure

5.5). As has been previously reported [29], optimum focus for peak intensity is in fact a few nm below the surface of a crystal. With increased defocus, the peak intensity drops rapidly to several tens of percent of maximum within a few nm. This creates significant difficulty in matching simulation to experiment if peak intensity or contrast is used as a measure of fit, whereas the probe position cross section remains robust. The robustness of the cross section to defocus, even in thicker crystals, suggests that it remains a useful quantity to use for matching with simulations.

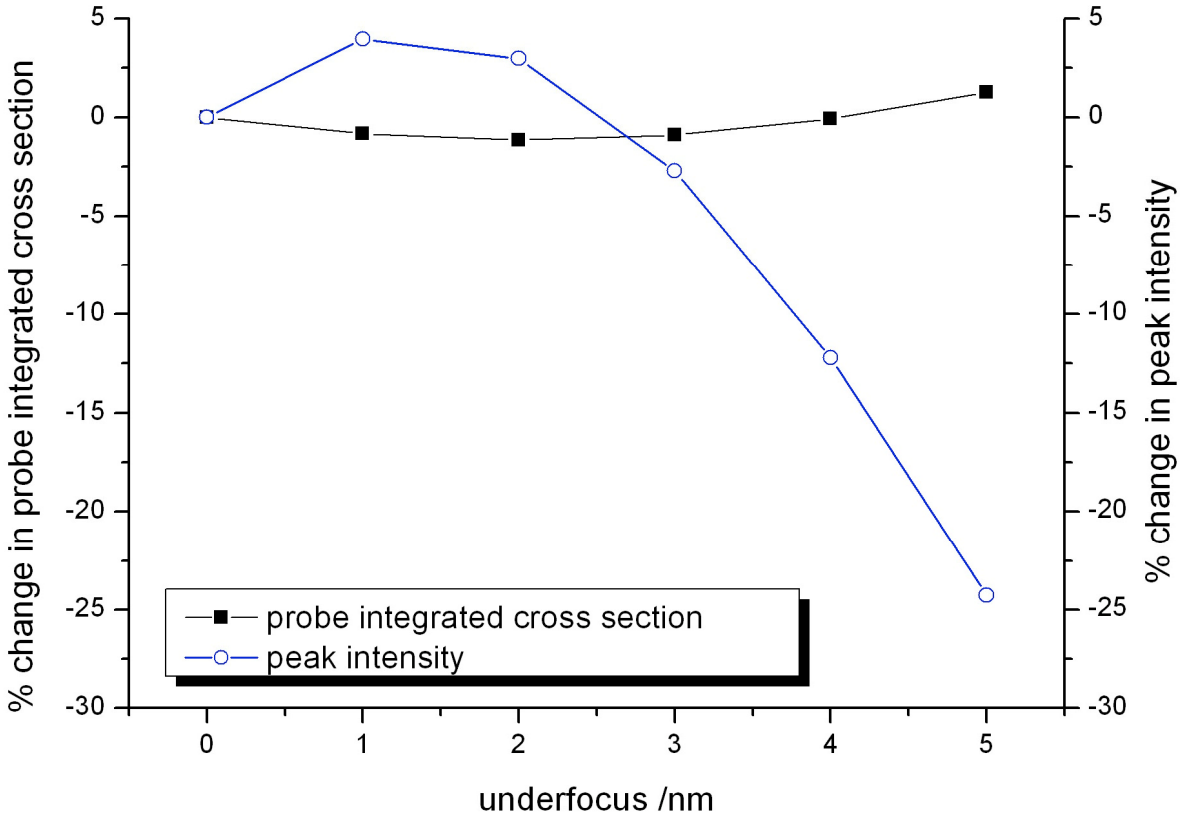

Figure 5.6 The cross section and peak intensity of a single column in a crystal of Pd <100>, of thickness 5nm, as a function of defocus. The cross section varies minimally with under-focus of the probe into the sample. However, the peak intensity shows significant deviation from the in focus value, both above and below the value.

5.5.3 Temperature and the Debye-Waller factor

Most simulations methods use the Einstein model for phonons, where Debye-Waller factors (DWF) or 'temperature factors', are typically calculated for bulk samples of pure element crystals. A recent contribution by Martin et al [30] suggests that an absorption potential method, which takes into account correlated atomic motion, agrees with the Einstein model. However, there is no guarantee that these parameterised factors are applicable to nanoparticles or thin, layered structures, where the behaviour of collective phonon excitations must naturally be very different. In fact, the well-known melting point depression of nanoparticle structures [31] suggests that this is the case.

Though X-ray methods have been used to experimentally find accurate DWF in samples that are also used in an electron microscopy study [7], this may not be feasible for small nanoparticle samples where spatial resolution is key and sample size limits the feasibility of X-ray methods sensitivity. Beam effects on nanoparticles can also cause structural changes corresponding to heating [32] which lead to difficulties in determining the temperature of the system and thus determining the DWF for simulations.

Crystals of Pd of varying thicknesses were simulated with DWFs at 300K and 600K (see Figure 5.7). The projected mean square displacement values used to calculate the DWF were 0.0059Å^2 and 0.0116Å^2 respectively. For thicknesses below 2nm, there is a far smaller difference between the two cross sections of a column of Pd (within 18%) whereas the peak intensity is found to vary more significantly (up to 28%). However, for thicker samples, the higher temperatures show attenuated high angle scattering from more vigorous vibrations of the atoms, since less of the beam is retained down the column.

It might be expected that there is only a small effect on thin samples due to errors in the Debye-Waller factors for the simulations. The effect of the DWF is to reduce the intensity in the coherent illuminating probe for subsequent layers in the sample, and so differences are seen predominantly in thicker samples.

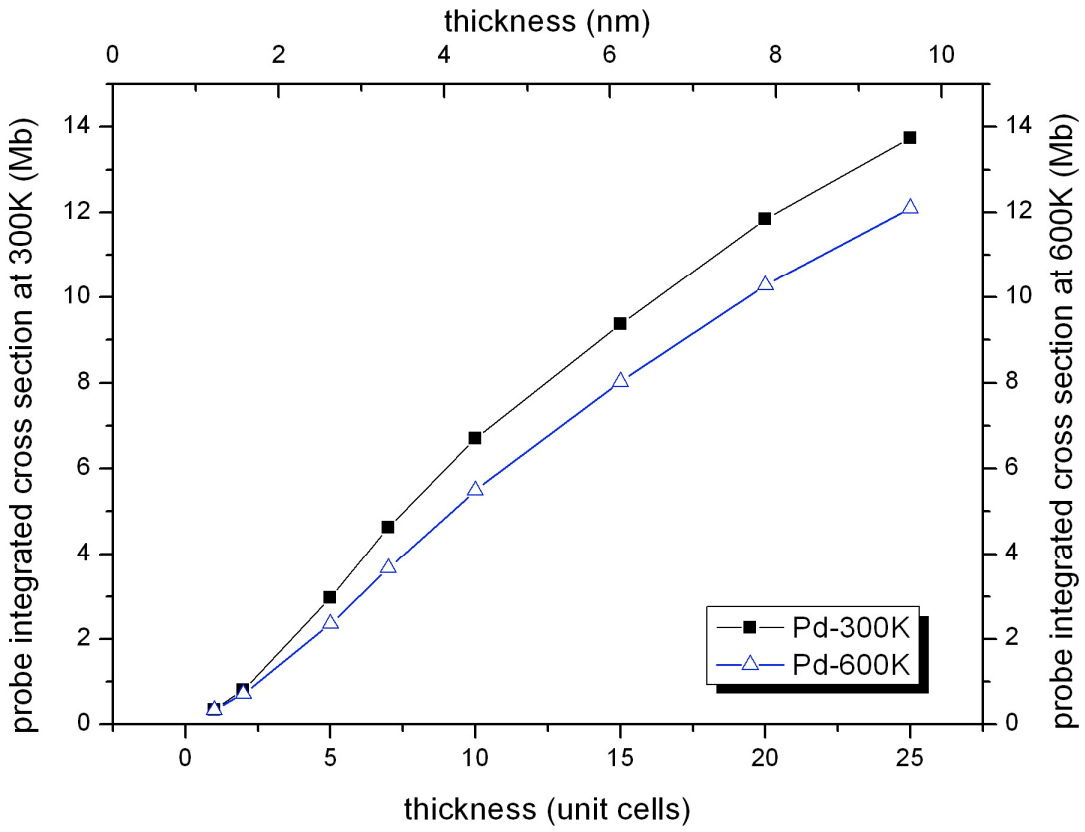

Figure 5.7 cross section versus thickness for two different temperatures. Below thicknesses of 2nm, a two-fold increase in the means square displacement values, corresponding to an increase in temperature from 300K to 600K, has little effect on the calculated cross section. For thicker crystals, the increased thermal motion attenuates the channelling of the beam.

5.5.4 Mistilt

It is commonly observed that HAADF-STEM intensities sharply increase when crystals are on zone axis due to channelling effects [33]. When a sample is mistilted off a zone axis, the intensity drops rapidly; even small amounts of mistilt, of the order of a few mrads, have been shown to greatly reduce the amount of contrast visible in high-resolution HAADF images [26,34]. LeBeau et al [35] have shown that using a position averaged CBED (PACBED) method, it is possible to determine mistilt to an accuracy of 3mrad readily and 1mrad by careful comparison of the PACBED symmetry. This however requires averaging the thickness over the area for the PACBED scanned, which is difficult for samples such as nanoparticles and further places limitations on beam sensitive samples.

Simulations of a single isolated Pd column of 10 atoms with a repeat distance of 3.89Å at various mistilts were carried out to investigate the influence of channelling as a function of tilt. The relative increase in the cross section due to channelling is shown as a fraction of the value for 10 times an individual Pd atom. A 60% increase in the cross section due to channelling can be observed when the atoms are aligned with the beam (see Figure 5.8).

By a mistilt of 4° (70mrad), the cross section plateaus out to the same value as 10 individual Pd atoms and, in fact, decreases to slightly less than the value of the sum of 10 Pd atoms as, for some angles, the channelling enhancement effect is overcome by absorption attenuating the beam for later atoms in the column. If channelling did not occur, it would be reasonable to expect that a well-aligned column of atoms, with little mistilt, would show slightly decreased cross section than 10 individual Pd atoms as more absorption would occur. Atoms earlier in the column scatter electrons from the beam away from further interaction with atoms later in the column.

Simulations of a crystal of a 5nm thick crystal of Pd (100) were carried out at various mistilts from the zone axis. It can be seen from Figure 5.9 that the cross section varies less significantly with mistilt compared to the peak. As the cross section captures all scattering to the HAADF detector from the column, a loss in peak intensity due to decreased channelling of the probe does not affect the scattering from the whole column as strongly.

A 7mrad mistilt in crystals of various thicknesses was simulated to investigate how the cross section varies with increasing thickness (see Figure 5.10). The difference between on-axis and mistilted cross sections is less than 2% for thin specimens under 1nm. As thickness increases, the difference is less than 10% but typically 6-7%. There is no linear or monotonic trend to the difference between on axis and off axis cross sections; this complicated behaviour is beyond the scope of the present work.

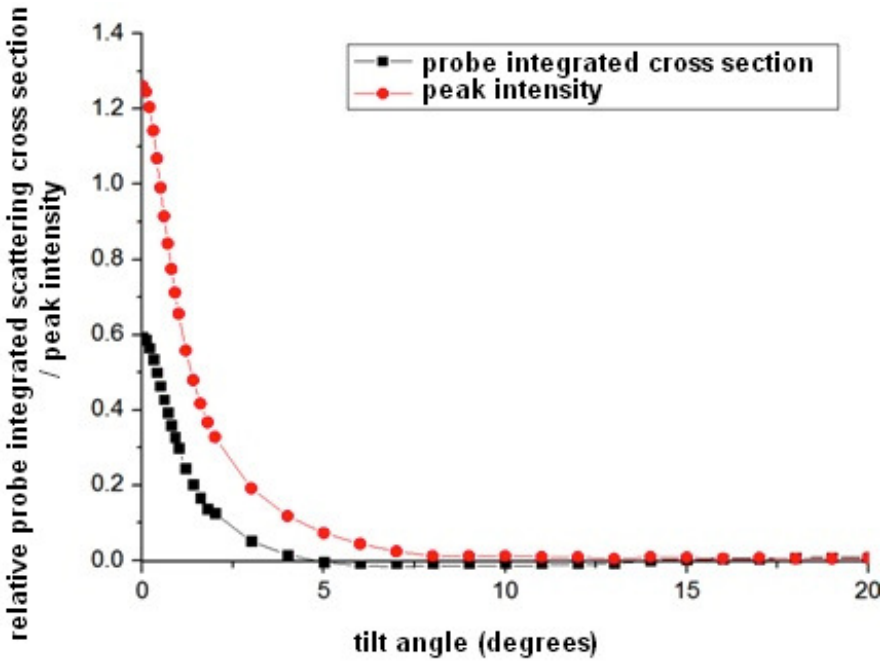

Figure 5.8 The fractional increase in cross section and peak values relative to the sum of 10 individual cross sections plotted as a function of tilt angle for a single isolated Pd column of 10 atoms, showing how they both decrease from the on axis case until reaching a plateau which is equal 10 times the cross section of an individual Pd atom, and no channelling is present. Credit: Katherine MacArthur.

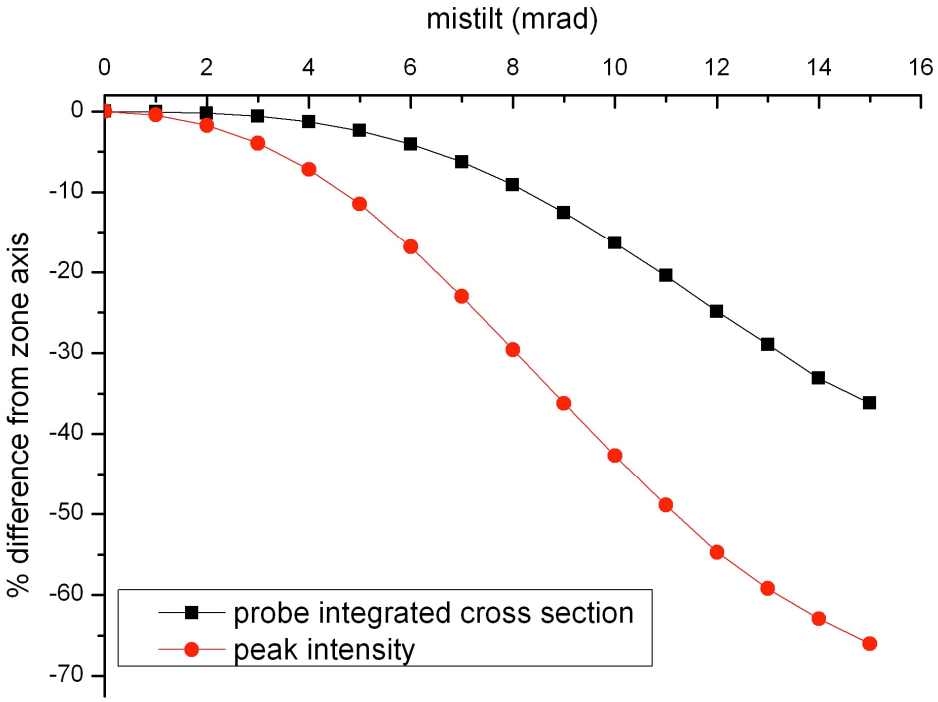

Figure 5.9 Simulation of the effect of mistilt on the cross section and peak intensity for a column in Pd <100>. Peak intensity drops off rapidly with mistilt away from zone axis whereas the cross section is much slower varying.

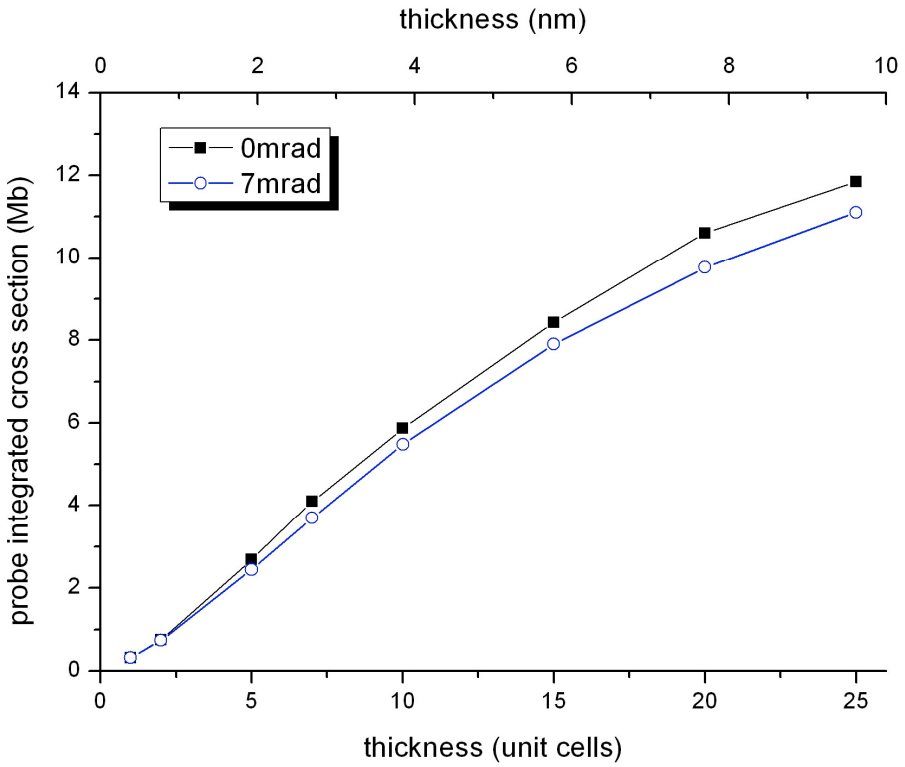

Figure 5.10 A mistilt of 7mrad is enough to see the effect of tilt in the image at thicknesses of 4nm of crystals of Pd along the <100> axis. The difference in cross section is less than 10% and typically on the order of 7% for crystals of up to 10nm thickness. For thinner specimens up to 1nm, the difference is less than 2%.

5.5.5 Cross-talk

In thicker crystalline samples, so-called "cross talk" between columns may occur as the probe de-channels or spreads geometrically, especially at larger convergence angles, and contributions from neighbouring columns can exist. This becomes a serious issue when assigning intensity to individual columns and has been carefully studied with respect to EELS analysis [36].

Given that it is required for columns to be well resolved and the whole probe to be included in the integrated area, it is necessary to include the background between columns as potential intensity from a probe of finite size. Given the finite size of the probe, any subsidiary maxima or probe tails that could excite scattering from neighbouring columns would affect the measured cross section at a particular probe position.

Furthermore, any potential "cross talk" between the columns, i.e. the effects of probe de-channeling [9,12,37,38] or spreading geometrically, will alter the measured intensity at a particular probe position, and thus the cross section value from that of an isolated column.

A nanoparticle often has neighbouring columns of different thickness due to its convex structure, and faceted sides. It is reasonable to assume that the thickness variations between neighbouring columns will be less than 4 atoms. This can be readily seen in the images acquired (see Figures 4.7, 4.10, 4.11, 4.14, 4.17) where the surfaces of some facets are clearly visible in projection. It is thermodynamically unlikely for an isolated column far from the edge of a particle to vary in height by two or more atoms, so called "cliff-edges" or "canyons". The effect of neighbouring columns of heights that differ by one atom needs to be well understood since they might have an effect on the calculated PI-CS value due to cross talk.

5.5.5.1 Neighbours of differing thicknesses

A wedge shape with different column thicknesses (see Figure 5.11) was simulated to explore the consequences of thickness variations of neighbouring columns (see Figure 5.12) in the [011] beam direction. The cross section value of each thickness was then compared to that of a pure crystal of the same thickness (see Figure 5.13).

It can be seen that there is variation on the order of 5% between the pure crystal cross section value and that of a column with neighbours of different heights due to cross talk. While there is no systematic trend in the difference, there is a marked increase in the difference as thickness increase beyond 4nm. The lack of a clear pattern in the variation could perhaps be attributed to the channelling pendellösung along the columns, such that intensity is bunched along the column at different depths into the crystal and so cross talk to different columns is not uniform with thickness.

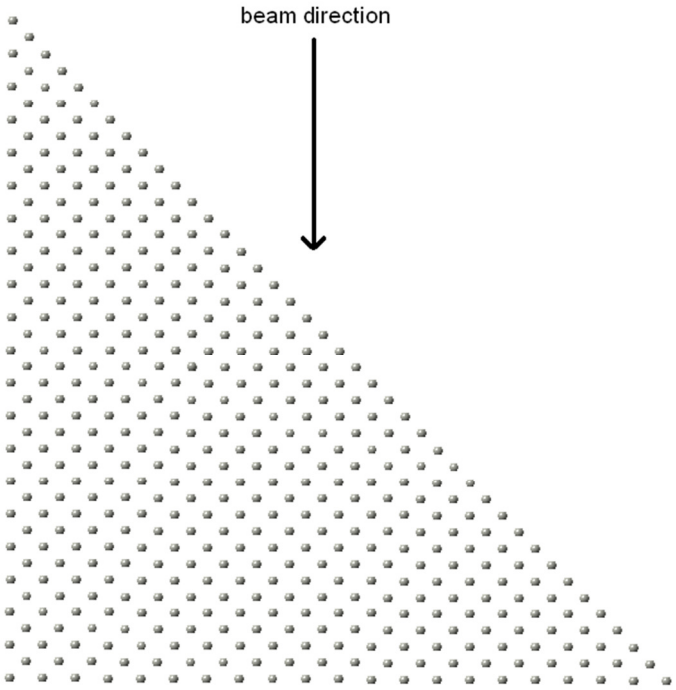

Figure 5.5.11 A wedge of Pd crystal in the [100] orientation used to investigate the effect of neighbouring atoms of different thicknesses. The beam direction is from the top, as shown.

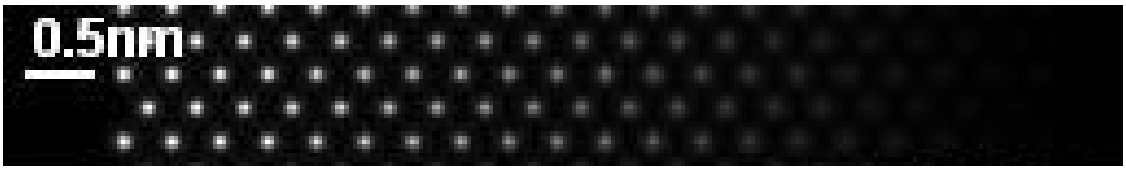

Figure 5.12 HAADF simulation of the wedge structure from Figure 5.11, showing the increase in brightness with thickness.

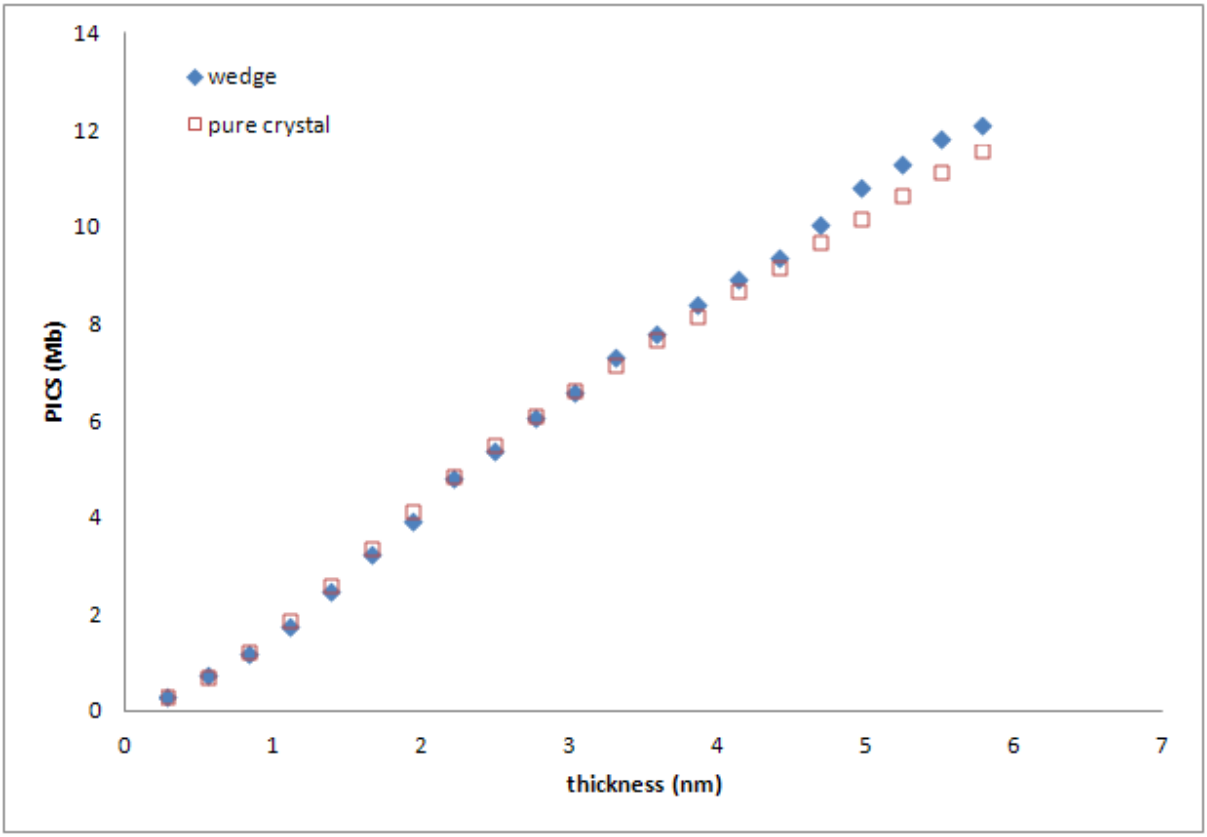

Figure 5.13 Plot of cross section for a pure crystal and the wedge structure. The effect of the neighbouring columns of different heights is small: on the order of 5% for thinner sections of the crystal. The effect becomes more pronounced at larger thicknesses.

It is evident that care is required in the matching of tabulated cross section values to experiments. At the very least, an uncertainty of 5% should be incorporated in the likely error when the identifying the column thickness and composition.

5.5.5.2 Neighbours of different compositions

Simulations of pure crystals of Pt and Pd of varying thicknesses were performed, as well as corresponding ones for a fictional "ordered alloy" of Pt and Pd where pure Pt and Pd columns alternate in a <100> view (see Figure 5.14).

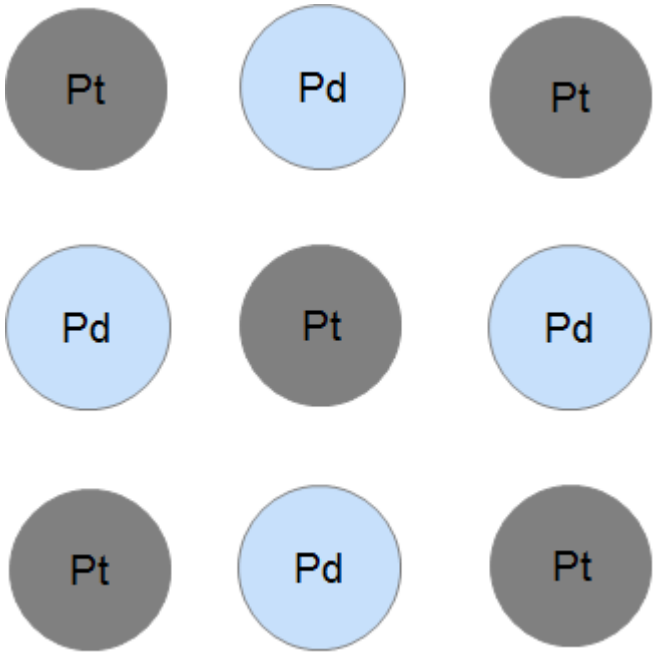

Figure 5.14 Ordered alloy system of pure Pt columns surrounded by pure Pd columns in a chequer-board pattern.

It was found that up to thicknesses of 10nm in <100> orientation of FCC crystals, the cross section value was affected by neighbouring columns of a different species by up to 11% for Pt and 16% for Pd (see Figure 5.15). The Pt loses intensity to the Pd columns, while the Pd gains intensity from the Pt columns. For thinner crystals, less than 4nm, the ordered alloy showed a 5% decrease in the cross section of Pt columns while the Pd gains on the order of 10% of its cross section value.

This poses a significant issue when comparing samples of over 4nm, which is approximately the depth of focus of the microscope used for these simulations, which suggests that unambiguous column-by-column comparison with simulation would not be straightforward and a full comparison with a model structure may allow clearer interpretations.

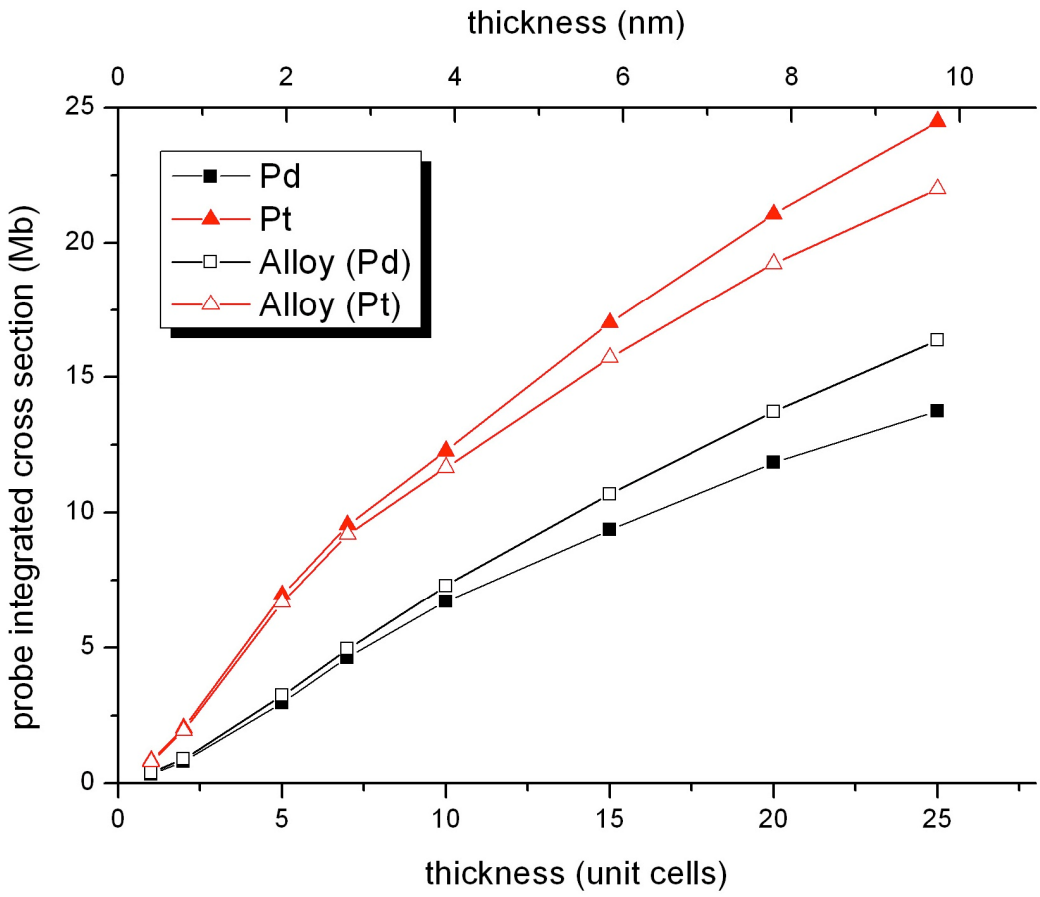

Figure 5.15 cross sections of an ordered alloy of neighbouring Pd and Pt columns and also pure Pd and pure Pt. With neighbours of different atomic species, the heavier Pt loses intensity to the lighter columns of Pd.

To investigate the role of neighbouring columns within a nanoparticle type geometry, a Pd cuboctohedral nanoparticle core with a monolayer Pt shell was simulated along the <110> projection. This work was carried out by Kate MacArthur of the University of Oxford. Comparison between the columns containing 3Pt and those containing Pt(2Pd)Pt demonstrated that the variation of cross section values due to differences in neighbouring columns within each group is 0.6%, sufficiently small that differentiation between each column type is possible (see Figure 5.16). As this difference is not obvious in the original image by inspection, analysis by cross section allows for identification of composition where qualitative analysis of structure does not.

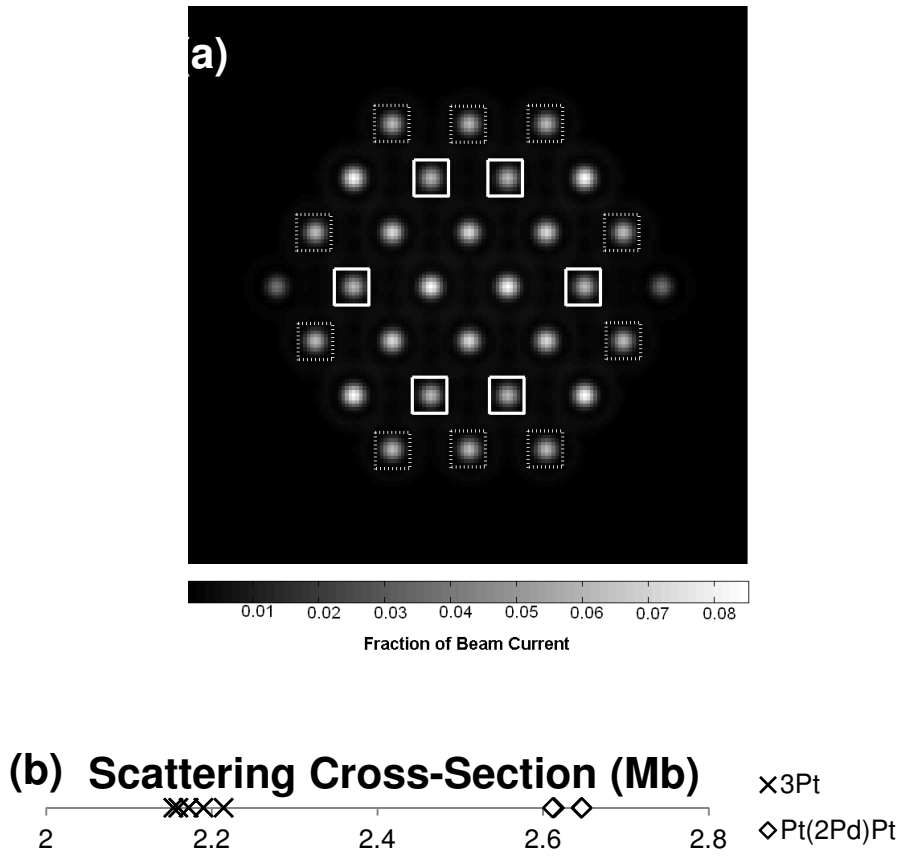

Figure 5.16 Simulation of a Pt(Pd) core-shell particle in <110> projection cross sections from two types of columns are shown: Pt(2Pd)Pt columns are indicated by the solid boxes in (a) and diamonds in (b); 3Pt are indicated by the dashed boxes in (a) and as X in (b). Differentiation between column types by cross section values is possible (b). There is, however, scatter of the cross section values depending on neighbouring configurations and discrete pixel sampling. This is likely due to the numerical error arising from the discrete pixel sampling. There are 6 pixels per Ångstrom and the cross section is taken with an integration circle of radius 5 pixels from the pixel with maximal intensity in the column. Credit: Katherine MacArthur.

5.5.6 Mixed composition columns

The scattered intensity is known to be sensitive to the height of dopant atoms [1,39] so a set of simulations was carried out to investigate the effect of a single dopant layer Pt at various heights in a 5nm thick slab of Pd crystal in the [100] orientation.

As can be seen from Figure 5.17, the peak intensity varies with the height of the dopant in a non-monotonic fashion, increasing to a maximum of 14.3% of the incident beam intensity at a depth of 5 unit cells (1.9nm) from the surface of the Pd crystal. This is a 10% increase on the value of 13.0% if

the Pt was placed at the entrance surface. After this maximum, the peak intensity drops off back to 13.3% of incident beam current.

The cross section shows a similar behaviour, except that the increase of the maximum is later: at 7 unit cells (2.7nm) into the crystal. The subsequent decrease is only 1.4% of the maximal value, compared to the 6.8% of the maximal value of peak intensity.

Although the peak intensity is more sensitive than the cross section to the position of the dopant in the column, the depth dependent variation is not a straight-forward one as there is not a clear one to one mapping of a peak intensity value to a particular position of the dopant in the column. One value of the cross section can also correspond to multiple positions of the Pt in the Pd column, however the range of possibilities is smaller since the maximum variation is only 7% of the value at the entrance surface, compared to a difference of 10% for the peak (see Figure 5.17).

This agrees with work carried out by Loane et al.[40] , who determined that the location of an atom within a column will affect its contribution to the total column intensity due to how focused the probe is when it reaches the atom. This so called ‘top-bottom effect’ means that an additional heavy atom within a column will have a much more marked effect on the column intensity if it is positioned on the exit surface, where the probe is more focused, than the entrance surface. Later work focused on the depth dependence of channelling and exploiting it to try and determine the exact depth location of dopant atoms in extended crystals, based on their contribution to intensity [39].

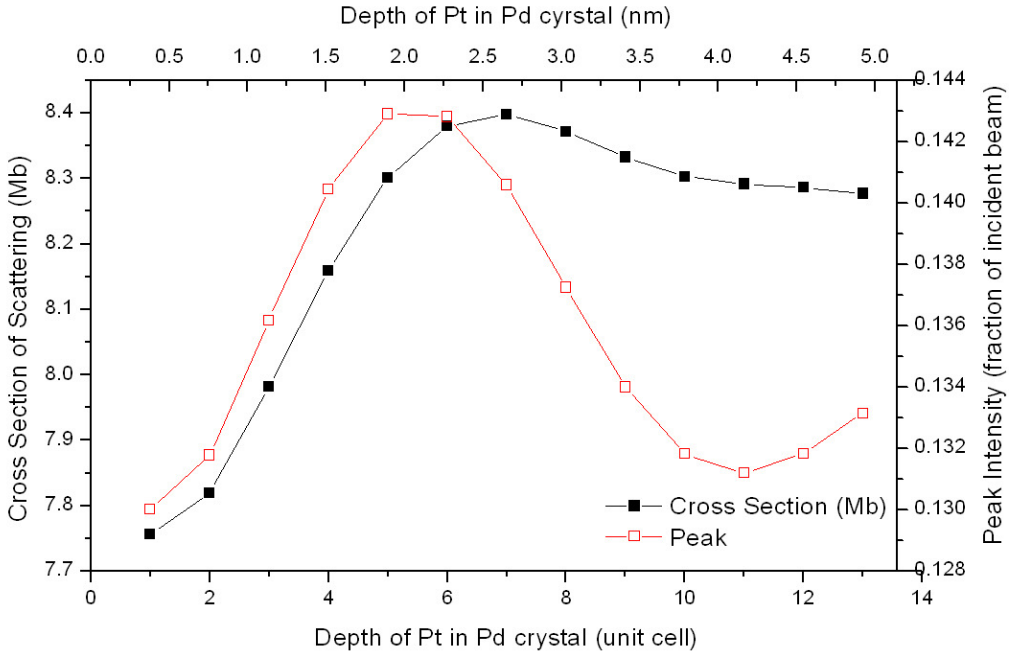

Figure 5.17 Variation in cross section and peak height as a function of the depth of a dopant Pt in a Pd crystal

5.6 Compiling a library of simulated cross section values

In order to match calibrated experimental cross section of columns to simulated values, the only required experimental parameters for calculating the cross section are detector angles and the accelerating voltage. The library of cross sections for the Pt and Pd core-shell nanoparticle system was compiled to match the experimental parameters of the JEOL ARM 200F at 200kV and 80kV and also the Oxford JEOL 2200MCO at 200kV. These parameters are given in Appendix B.

The orientations of nanoparticles observed experimentally are typically the [110] and sometimes the [100] directions and so these were the crystal orientations calculated. The lattice parameter of Pt and Pd used in this thesis are 3.92Å and 3.89 Å respectively. Thicknesses of up to 15nm were calculated (approximately 40 unit cells in the [100] direction and 50 unit cells in the [100] direction).

5.6.1 Assumptions made in cross section matching

While an exact matching would be ideal, the particulate nature of the sample structure means that thickness variations preclude the possibility of identifying the depth of the Pt in the column since there is no guarantee that neighbouring columns are identical in thickness. For the rest of this thesis, the following approach is taken to reduce the number of cross section value possibilities.

For the purpose of the core-shell samples, it is assumed that there is a maximum of 4 Pt atoms per column and that they are either arranged at the entrance surface or the exit surface or both, commensurate with a Pt shell of 2ML coating a Pd core, which is the maximum coverage of shell design imaged at high resolution. Other combinations of mixed column compositions are not considered due to the complexity of matching experimental values to simulated ones. This assumption is a reasonable one given that the Pt is deposited on the surface of the Pd core in a secondary step once the core has been formed. It is further reasonable that a complete shell seen in projection, at the edge of a particle, would comprise of purely Pt atoms.

5.6.2 Pt at entrance surface

The scattering cross section of columns of Pd in the <110> direction, topped with one, two and three Pt atoms was investigated. The results show that there is little variation in the contribution due to the extra Pt (see Figure 5.18), particularly at larger thicknesses. For thinner samples, less than 3nm, the capping Pt at the entrance surface does play a significant role in increasing the intensity and thus the measured cross section value.

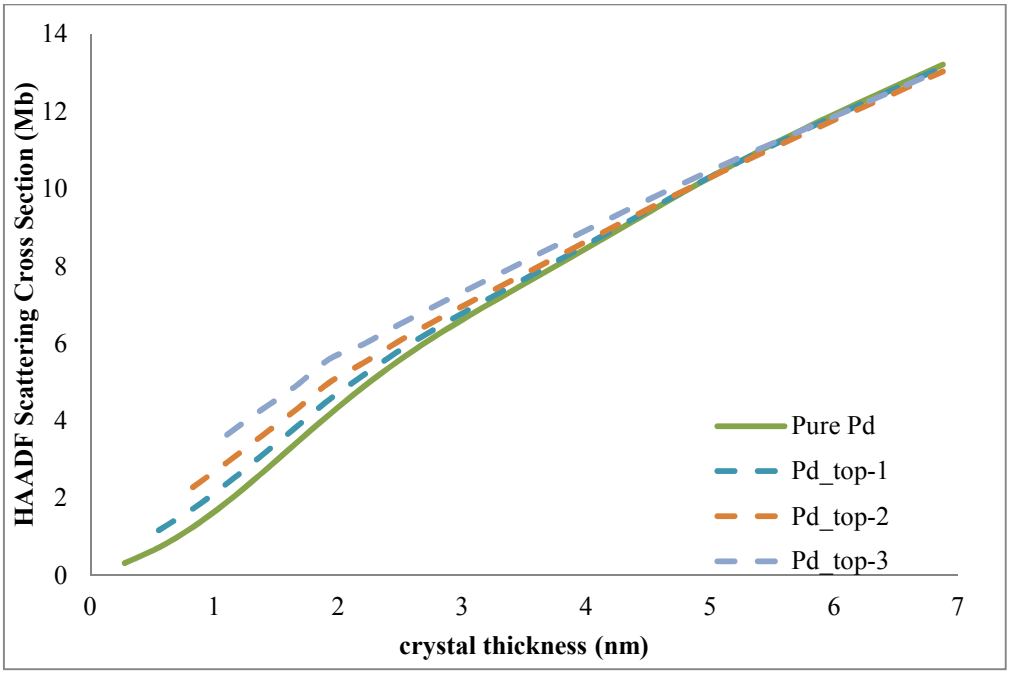

Figure 5.18 cross section of crystals of Pd, capped with Pt at the entrance surface

At thicknesses larger than 5nm, the effect of the number of Pt atoms at the start of the column becomes negligible as channelling effects dominate and the cross section values converge to that of a pure Pd column of the same thickness. In terms of image interpretation, this causes a major issue if the particles are thicker and the Pt located at the entrance surface as they will not be distinguishable from pure Pd columns.

5.6.3 Pt at exit surface

The scattering cross section of columns of Pd with one, two and three Pt atoms at the exit surface was investigated. The results show that there is clear increase in the cross section due to the extra Pt atoms and that the effect is monotonic and linear with increasing Pt doping. Further, it does not vary with thickness (see Figure 5.19). This is significantly larger than the effect seen when Pt is at the entrance surface of the Pd crystal and is again understood by considering the effects of channelling: since the Pd atoms act like mini-lenses to focus the probe down the column, stronger scattering lower in the column occurs.

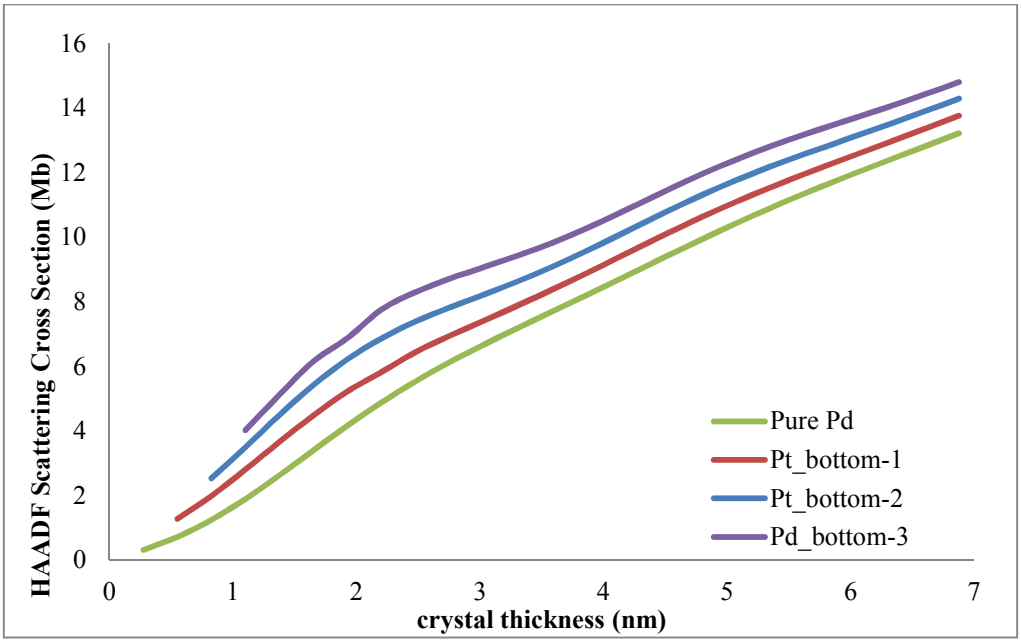

Figure 5.19 cross section of crystals of Pd capped with Pt at the exit surface

Thus it is possible to clearly determine the presence and number of dopant Pt atoms in a column at all thicknesses if the Pt is located at the exit surface of the crystal.

5.6.4 Pt in a sandwich structure

As can be expected from the results of Section 5.6.2, the effect of one or two Pt at the start and end of a column, a so-called "sandwich" configuration, does not significantly alter the cross section much from the value seen for the configuration of Pt atoms later in the column (see Figure 5.20). This further confirms that the substitution of one or two Pd atoms at the top of a column with Pt atoms has negligible effect on the cross section value for thicker samples and is only relevant for samples thinner than 3nm.

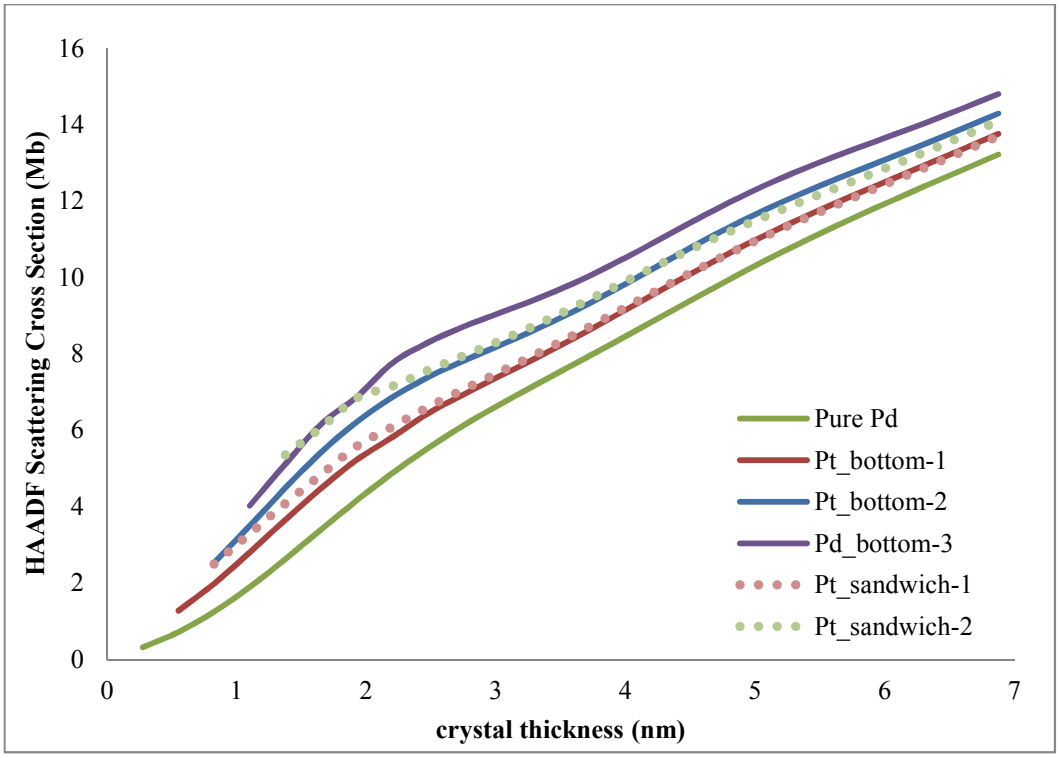

Figure 5.20 cross section of crystals of Pd capped with Pt both the entrance and exit surface (sandwich configuration) and at only the exit surface (bottom)

To complicate interpretation, the cross section values for thinner samples of 2 Pt at the entrance and exit surfaces are similar to that for a column with 3 Pt at the exit surface only. This raises the concern that unambiguous column composition identification by matching to cross section values is practically not feasible, certainly when experimental error is taken into account.

5.7 Experimental applications

Some initial investigations of the use of cross sections for the interpretation of experimental data is now presented. These investigations demonstrate some further experimental considerations in the application of the proposed approach.

5.7.1 Background subtraction

Images of many samples may have background intensity in the image arising from, for example, catalyst support materials or some carbon contamination, and thus background subtraction must be performed carefully since it greatly affects any comparison with simulation. Care must then be taken that contributions from contamination or a support is not attributed to the cross section value. The digital to analogue converter offset (constant background) can be taken into account by subtracting the black level of the detector map [41].

When considering nanoparticles, this is possible as contributions from the sample support can be taken into account by considering the complete surroundings of the cluster [42]. However, when the background is uneven across the length of the sample (e.g. increasing thickness of support), it is necessary to interpolate the background from one side of the sample to the other side. Purely subtracting the inter-column background can lead to underestimates of the scattering cross section, as the finite source size will engender significant intensity between columns, which must be attributed to the columns themselves. A method for doing this is discussed in Section 7.3.4.

5.7.2 Experimental uncertainty in detector quantification

Because of the possible nonlinear dependence of image intensity on the detector amplifier gain setting, either a custom converter needs to be added to microscopes [6] or small probe currents are needed to scan the detector during the calibration process [43]. In the latter approach, it is necessary to measure small beam currents using a Faraday cup and picoammeter. The error on reading such small currents

with standard picoammeters can be as large as 10%, since the probe currents are often as small as 1 or 2pA in order that the scattering from the samples in imaging does not saturate the detector response. This dominates the error on the cross section analysis.

Further, it has recently been pointed out that potential detector non-uniformity requires careful consideration [44,45], as variations in detector response across different scattering angles would lead to a difference in signals from different zone axes.

5.7.3 Identification of unknown elements

The cross section analysis method lends itself directly to identifying single atoms of unknown element where it would otherwise be difficult to garner information using spectroscopic methods due to poor signal to noise. Isolated atoms are similarly not affected by errors due to concerns of mistilt and cross talk. Similarly, as shown earlier in the paper, the cross section of thin sample was found to be robust to the Debye-Waller factor.

Several nanoparticles in a heterogeneous catalyst known to contain Pt and Pd were imaged. The sample had regions of isolated atoms on the carbon support surrounding the larger nanoparticles (see Figure 5.21). To attempt to identify whether the atoms are Pt or Pd, the cross section values were compared to simulated values at the given microscope accelerating voltage and HAADF detector collection angles. This study is similar to one presented by Isaacson et al. [46]; the difference being that here the investigation is on an actual bimetallic heterogeneous catalyst system rather than a model specimen.

Initial investigations at 200kV gave cross sections of the same order of magnitude as simulations for this accelerating voltage: 0.48Mb for single Pt and 0.33Mb for single Pd. There was, however, sufficient scatter in the data that distinction between elements or number of atoms was not possible (see Figure 5.22).

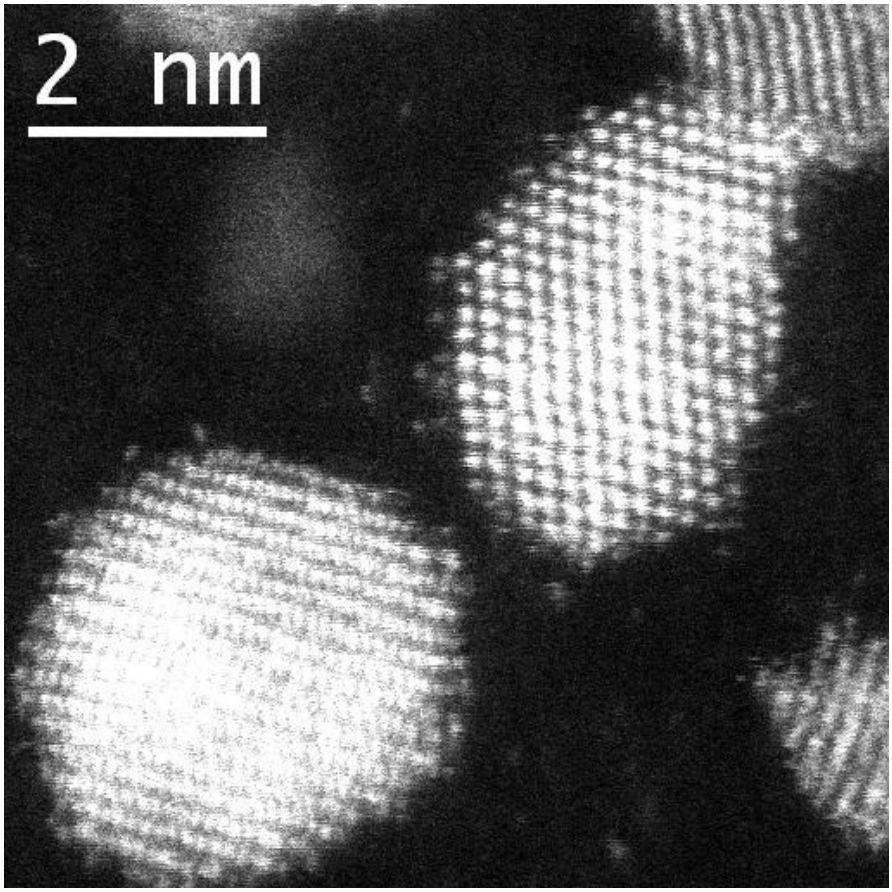

Figure 5.21 Heterogeneous catalysts of Pt and Pd on industrial carbon black support, imaged at 200kV on the Oxford-JEOL 2200MCO. Single atoms around the nanoparticles can be clearly seen.

The movement of unpinned atoms during scanning is the largest source of error. If the atoms move with the scanning probe direction, increased beam interaction will result in a larger cross section than calculated. Conversely, a movement of the atom away from the original position and out of the beam profile will reduce the measured cross section.

Further experiments were carried out at 100kV using a Nion UltraSTEM 100, at the UK SuperSTEM facility, to reduce the knock on effect of a high energy electron probe. Samples were prepared by Kate MacArthur and the instrument was operated by Tim Pennycook. At the lower accelerating voltage, atom movement was significantly reduced (see Figure 5.22) but not sufficiently for clear differentiation between elements. Sequences of images showed that the atoms are highly mobile on the carbon black support material used for this catalyst system, suggesting that general application of this

method will be dependent on degree to which the supporting material limits atom mobility. Single atoms on other supports, such as thin amorphous carbon films, may show lower mobility. Nonetheless, the clustering of the measured cross sections around the expected, simulated ones, is reassuring.

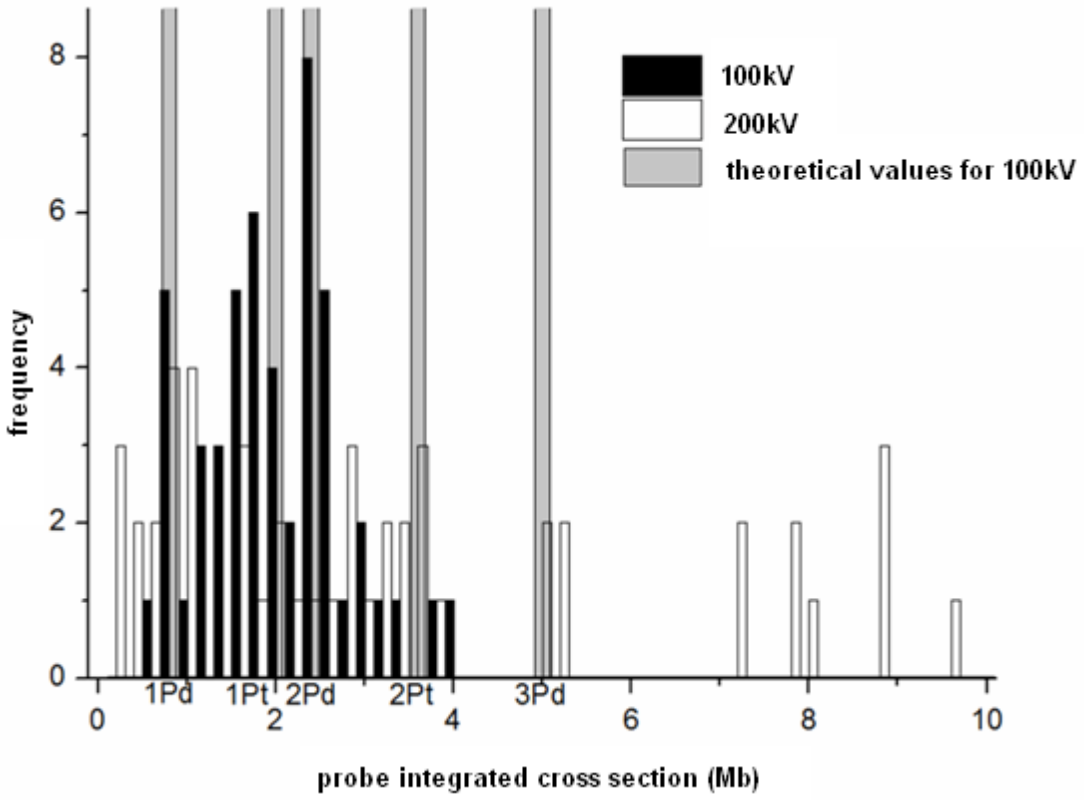

Figure 5.22 Histogram representing the distribution of the scattering cross sections of single atom species measure from experimental images. Black bars show data from images taken at 200kV and white bars show data from images taken at 100kV. The grey bars represent the location of theoretical values calculated for 100kV accelerating voltage. The large values of 7 – 10Mb could be due to movement of the atoms under the beam causing multiple scans of the same atom. Credit: Katherine MacArthur, Tim Pennycook.

5.7.4 Thin, layered materials

As a proof of principle, the cross section approach is applied to a real material with simpler morphology. Single layer materials offer the ideal test for quantitative analysis where the individual atoms are more fixed than small isolated atomic clusters. Thin sheets of MoS_2 were prepared by liquid exfoliation [47] and imaged using a JEOL ARM-200F at 80kV with inner and outer detector angles of 55mrad and 180mrad respectively. Calibrations for quantitative imaging were performed using probe currents of 2.6pA for the detector mapping and 33.8pA for imaging. Thus the gain and offset ('contrast' and 'brightness') of the analogue to digital convertor could be maintained at the same settings without the detector saturating and this provides a good dynamic range for the images without the need for a custom built analogue to digital convertor with a linear behaviour [43].

Careful background subtraction was necessary since the sample showed contamination in some areas (Figure 5.23, bottom left), which would greatly affect the measured cross section value. A background level was measured by averaging the intensity over a region immediately adjacent to the edge of the single layer in the top left of Figure 5.23. Only atoms far from edges and steps were considered as areas close to the edges of thin 2D sheets often have ad-atoms [48]. Only those in the top half of the image were investigated, where the sample was cleaner. The main sources of calculable errors were due to the accuracy of the picoammeter in the measuring of the small 2.6 ± 0.1pA current used to map the detector and due to the large variance of integrated intensities because of noisy data.

The structure of a single layer of MoS_2 has a layer of Mo atoms in a hexagonal lattice located at the A sites, sandwiched between two layers of S both at the B site (see overlaid positions in Figure 5.23). The average of 42 atomic sites gave a mean cross section of 6.0 ± 0.7 Mb. Comparison with theoretical cross section values revealed that the mid area atoms were single Mo (calculated cross section of 6.8 Mb), confirming that this is a monolayer. It was not possible to identify the S as the columns of S were not well resolved above the background. They would have had a smaller cross section of 4.3 Mb.

Cross sections of the brighter columns to the right of Figure 5.23 showed that these were a combination of two S and one Mo, as expected for a bi-layer of MoS_2. Because of channelling effects, Mo before two S has a theoretical cross section of 13.6Mb, whereas the two S before Mo has a cross

section of 12.3Mb. The mean cross section of 30 atomic sites in the "double layer" region was (11.4±0.9)Mb, which suggests that the configuration is two S before Mo (see Figure 5.24).

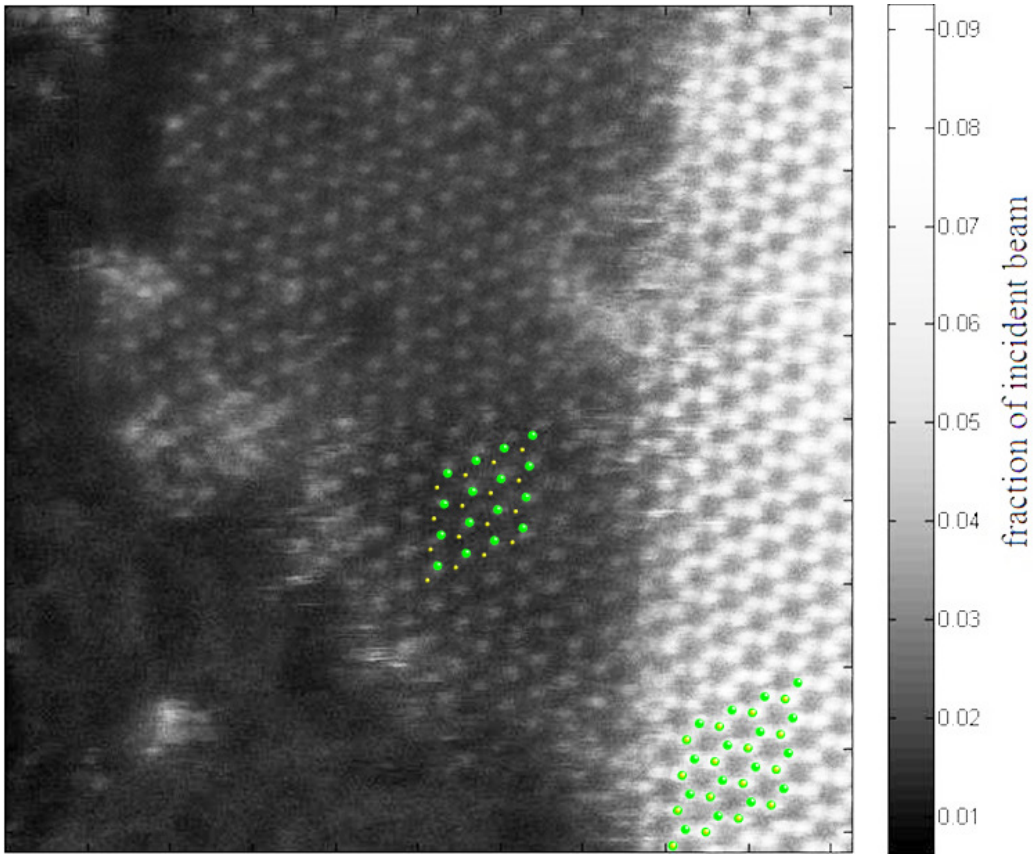

Figure 5.23 Calibrated HAADF STEM image of the edge of a MoS_2 flake showing monolayer (left, centre) and bilayer (right). The MoS_2 structure is overlaid in the bottom right corner with Mo sites shown in green and S in yellow. Sample kindly prepared by Aleksey Shmeliov.

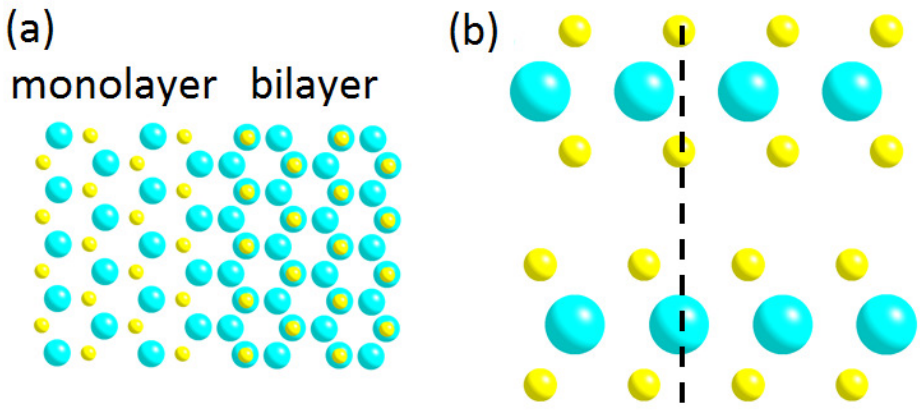

Figure 5.24 (a) structure of monolayer and bilayer in a 2H stacking formation **(b)** transactional view of stacking: 2 sulphur atoms (yellow) above a Mo atom (green) is indicated by the black dashed line.

5.8 Conclusions

The analysis of quantified atomic resolution HAADF STEM images can be carried out by integrating around well-resolved columns and this can be understood very intuitively in terms of the probe-position integrated cross sections of scattering to the HAADF detector, integrated over the probe positions encompassing a column of atoms.

Due to the transverse incoherent nature of HAADF STEM, it is found to be robust to parameters that affect probe size and shape such as defocus and source coherence. The main imaging parameter dependencies are on detector angle and accelerating voltage, which are well known. As long as the sample is thin enough that the probe does not vary through the thickness of the sample, the cross section is independent of the probe. Thus there is no reliance on any statistical or indirect fitting parameters or comparisons to known samples to compare simulation to experiment.

The cross section remains a robust parameter even in thicker crystals, and is a useful quantity for comparison with simulations. Though excellent progress has been made in quantitative interpretation of HAADF STEM images, some of the potential issues and causes of errors when comparing experimental data to simulations are still prevalent. These include the need for careful background subtraction, consideration of accurate Debye-Waller factors, sample mistilt and cross talk.

By calibrating the HAADF detector and using a cross section approach, comparisons of experimental images of isolated single atoms with simulated cross sections seems possible but is practically difficult in reality due to the mobility of the single atoms. However, thin, layered materials, where the atoms are less mobile, show excellent agreement to simulations.

In the next chapter, we apply the cross section analysis method to catalyst nanoparticles in order to elucidate structural and chemical information.

References

[1] P.M. Voyles, D.A. Muller, J.L. Grazul, P.H. Citrin, H.-J.L. Gossmann, Atomic-scale imaging of individual dopant atoms and clusters in highly n-type bulk Si, Nature. 416 (2002) 826–9.

[2] C. Dwyer, C. Maunders, C.L. Zheng, M. Weyland, P.C. Tiemeijer, J. Etheridge, Sub-0.1nm-resolution quantitative scanning transmission electron microscopy without adjustable parameters, Applied Physics Letters. 100 (2012) 191915.

[3] S.D. Findlay, N. Shibata, Y. Ikuhara, What atomic resolution annular dark field imaging can tell us about gold nanoparticles on TiO(2) (110), Ultramicroscopy. 109 (2009) 1435–46.

[4] J.M. Lebeau, S. Stemmer, Experimental quantification of annular dark-field images in scanning transmission electron microscopy., Ultramicroscopy. 108 (2008) 1653–8.

[5] J.M. Lebeau, S.D. Findlay, L.J. Allen, S. Stemmer, Standardless atom counting in scanning transmission electron microscopy, Nano Letters. 10 (2010) 4405–8.

[6] J.M. Lebeau, S.D. Findlay, L.J. Allen, S. Stemmer, Quantitative Atomic Resolution Scanning Transmission Electron Microscopy, Physical Review Letters. 100 (2008) 1–4.

[7] J. LeBeau, S. Findlay, X. Wang, A. Jacobson, L. Allen, S. Stemmer, High-angle scattering of fast electrons from crystals containing heavy elements: Simulation and experiment, Physical Review B. 79 (2009) 214110.

[8] C. Dwyer, R. Erni, J. Etheridge, Measurement of effective source distribution and its importance for quantitative interpretation of STEM images, Ultramicroscopy. 110 (2010) 952–957.

[9] D.O. Klenov, S. Stemmer, Contributions to the contrast in experimental high-angle annular dark-field images., Ultramicroscopy. 106 (2006) 889–901.

[10] M. Retsky, Observed single atom elastic cross sections in a scanning electron microscope, Optik. 41 (1974) 127–42.

[11] L.J. Allen, S.D. Findlay, M.P. Oxley, C.J. Rossouw, Lattice-resolution contrast from a focused coherent electron probe. Part I., Ultramicroscopy. 96 (2003) 47–63.

[12] S.D. Findlay, L.J. Allen, M.P. Oxley, C.J. Rossouw, Lattice-resolution contrast from a focused coherent electron probe. Part II, Ultramicroscopy. 96 (2003) 65–81.

[13] H.X. Gao, L.-M. Peng, Parameterization of the temperature dependence of the Debye–Waller factors, Acta Crystallographica Section A Foundations of Crystallography. 55 (1999) 926–932.

[14] S. Van Aert, K.J. Batenburg, M.D. Rossell, R. Erni, G. Van Tendeloo, Three-dimensional atomic imaging of crystalline nanoparticles., Nature. 470 (2011) 374–7.

[15] A. Singhal, J. Yang, J. Gibson, STEM-based mass spectroscopy of supported Re clusters, Ultramicroscopy. 67 (1997) 191–206.

[16] L.D. Menard, S.-P. Gao, H. Xu, R.D. Twesten, A.S. Harper, Y. Song, et al., Sub-nanometer Au monolayer-protected clusters exhibiting molecule-like electronic behavior: quantitative high-angle annular dark-field scanning transmission electron microscopy and electrochemical

characterization of clusters with precise atomic stoichiom, The Journal of Physical Chemistry. B. 110 (2006) 12874–83.

[17] N. Young, Z. Li, Y. Chen, S. Palomba, M. Di Vece, R. Palmer, Weighing Supported Nanoparticles: Size-Selected Clusters as Mass Standards in Nanometrology, Physical Review Letters. 101 (2008) 246103.

[18] R.G. Newton, Scattering Theory of Waves and Particles: Second Edition, 1982.

[19] R.F. Egerton, M. Malac, EELS in the TEM, Journal of Electron Spectroscopy and Related Phenomena. 143 (2005) 43–50.

[20] S.D. Findlay, M.P. Oxley, L.J. Allen, Modeling atomic-resolution scanning transmission electron microscopy images, Microscopy and Microanalysis. 14 (2008) 48–59.

[21] S.J. Pennycook, P.D. Nellist, eds., Scanning Transmission Electron Microscopy, Springer, 2011.

[22] K. Ishizuka, Prospects of atomic resolution imaging with an aberration-corrected STEM., Journal of Electron Microscopy. 50 (2001) 291–305.

[23] S.I. Molina, M.P. Guerrero, P.L. Galindo, D.L. Sales, M. Varela, S.J. Pennycook, Calculation of integrated intensities in aberration-corrected Z-contrast images., Journal of Electron Microscopy. 60 (2011) 29–33.

[24] C. Maunders, C. Dwyer, P.C. Tiemeijer, J. Etheridge, Practical methods for the measurement of spatial coherence--a comparative study., Ultramicroscopy. 111 (2011) 1437–46.

[25] C. Dwyer, R. Erni, J. Etheridge, Method to measure spatial coherence of subangstrom electron beams, Applied Physics Letters. 93 (2008) 021115.

[26] X. Wu, M.D. Robertson, M. Kawasaki, J.M. Baribeau, Effects of small specimen tilt and probe convergence angle on ADF-STEM image contrast of Si(0.8)Ge(0.2) epitaxial strained layers on (100) Si, Ultramicroscopy. 114 (2012) 46–55.

[27] P. Hartel, H. Rose, C. Dinges, Conditions and reasons for incoherent imaging in STEM, Ultramicroscopy. 63 (1996) 93–114.

[28] P.M. Voyles, Imaging Single Atoms with Z-Contrast Scanning Transmission Electron Microscopy in Two and Three Dimensions, Microchimica Acta. 155 (2006) 5–10.

[29] E.C. Cosgriff, V. Nicolosi, J.N. Coleman, P.D. Nellist, Quantification of ADF STEM images of molybdenum chalcogenide nanowires, Journal of Physics: Conference Series. 26 (2006) 280–283.

[30] A. V. Martin, S.D. Findlay, L.J. Allen, Model of phonon excitation by fast electrons in a crystal with correlated atomic motion, Physical Review B. 80 (2009) 024308.

[31] C.Q. Sun, Y. Wang, B.K. Tay, S. Li, H. Huang, Y.B. Zhang, Correlation between the Melting Point of a Nanosolid and the Cohesive Energy of a Surface Atom, The Journal of Physical Chemistry B. 106 (2002) 10701–10705.

[32] A.S. Barnard, N.P. Young, A.I. Kirkland, M.A. van Huis, H. Xu, Nanogold: a quantitative phase map., ACS Nano. 3 (2009) 1431–6.

[33] S. Pennycook, High angle dark field STEM for advanced materials, Journal of Electron Microscopy. 43 (1996) 36–43.

[34] S.E. Maccagnano-Zacher, K.A. Mkhoyan, E.J. Kirkland, J. Silcox, Effects of tilt on high-resolution ADF-STEM imaging., Ultramicroscopy. 108 (2008) 718–26.

[35] J.M. Lebeau, S.D. Findlay, L.J. Allen, S. Stemmer, Position averaged convergent beam electron diffraction: theory and applications., Ultramicroscopy. 110 (2010) 118–25.

[36] L.J. Allen, A.J. D'Alfonso, S.D. Findlay, J.M. LeBeau, N.R. Lugg, S. Stemmer, Elemental mapping in scanning transmission electron microscopy, Journal of Physics: Conference Series. 241 (2010) 012061.

[37] S. Hillyard, R. Loane, J. Silcox, Annular dark-field imaging: Resolution and thickness effects, Ultramicroscopy. 49 (1993) 14–25.

[38] C. Dwyer, J. Etheridge, Scattering of A-scale electron probes in silicon, Ultramicroscopy. 96 (2003) 343–360.

[39] P. Voyles, Depth-dependent imaging of individual dopant atoms in silicon, Microscopy and Microanalysis. 10 (2004) 291–300.

[40] R. Loane, E. Kirkland, J. Silcox, Visibility of single heavy atoms on thin crystalline silicon in simulated annular dark-field STEM images, Acta Crystallographica Section A. 44 (1988) 912–927.

[41] A. Rosenauer, K. Gries, K. Müller, M. Schowalter, A. Pretorius, A. Avramescu, et al., Measurement of composition profiles in III-nitrides by quantitative scanning transmission electron microscopy, Journal of Physics: Conference Series. 209 (2010) 012009.

[42] L. Cervera Gontard, D. Ozkaya, R.E. Dunin-Borkowski, A simple algorithm for measuring particle size distributions on an uneven background from TEM images., Ultramicroscopy. 111 (2011) 101–6.

[43] H. E, P.D. Nellist, S. Lozano-Perez, D. Ozkaya, Towards quantitative analysis of core-shell catalyst nano-particles by aberration corrected high angle annular dark field STEM and EDX, Journal of Physics: Conference Series. 241 (2010) 012067.

[44] H. Katz-Boon, C.J. Rossouw, C. Dwyer, J. Etheridge, A method to determine the thickness profile of nanoparticles, Ultramicroscopy. 124 (2012) 61–70.

[45] S.D. Findlay, J.M. LeBeau, Detector non-uniformity in scanning transmission electron microscopy, Ultramicroscopy. 124 (2013) 52–60.

[46] M.S. Isaacson, J. Langmore, N.W. Parker, D. Kopf, M. Utlaut, The study of the adsorption and diffusion of heavy atoms on light element substrates by means of the atomic resolution stem, Ultramicroscopy. 1 (1976) 359–376.

[47] V. Nicolosi, D.N. McCarthy, D. Vengust, D. Mihailovic, W.J. Blau, J.N. Coleman, Exfoliation of Mo6Sx I9-x nanowires in common solvents, The European Physical Journal Applied Physics. 37 (2007) 149–159.

[48] O.L. Krivanek, M.F. Chisholm, V. Nicolosi, T.J. Pennycook, G.J. Corbin, N. Dellby, et al., Atom-by-atom structural and chemical analysis by annular dark-field electron microscopy, Nature. 464 (2010) 571–4.

Chapter 6

HAADF cross sections of core-shell nanoparticles

In this chapter, the methodology of probe integrated cross sections for the analysis of Pt-Pd core-shell nanoparticles is explored. We present the calculation of a library of cross section values and investigate the feasibility of decoding the composition and thickness of atomic resolution images in a column by column manner. The sources of error are discussed and suggestions for minimising the uncertainty in composition and thickness identification are given.

The cross section approach is then applied to the analysis of an image of a pure Pt particle and also to a range of core-shell nanoparticles. The possibilities for answering important catalytic questions are explored and the practical limitations discussed.

6.1 Imaging particles

Particles that were free-standing were chosen to minimise the contribution to the HAADF intensity from other parts of the sample such as carbon support or neighbouring particles. Two microscopes were used to carry out the atomic resolution investigations: Oxford-JEOL 2200MCO and JEOL ARM-200F. Details of the microscopes are given in Appendix B along with the experimental setup used. The detectors for both were calibrated as detailed in Chapter 4 and HAADF imaging was performed at 200kV unless otherwise stated.

Wherever possible, particles were chosen that were 'fresh', i.e. had not been previously exposed to the electron beam and thus potentially altered or damaged by incident fast electrons. Attention was focused on the as-prepared 2ML design particles,[1] since they were shown to be the most catalytically favourable [12,13].

6.1.1 Background subtraction

Image interpretation of nanoparticles supported on industrial amorphous carbon black requires the careful removal of the contribution to the image from the support, so that the scattering from the carbon is not included in the value for the cross section of the column. Given the size of values that comprise the background signal in a typical HAADF image, especially where the substrate or other particles are also imaged, correct identification of the background is vital.

As seen in Section 6.6.4, where the particle is relatively free-standing and the height and thickness of the support underneath fairly uniform, this is easy to implement. The automated cross section calculator described in Section 5.5 copes very well with this and removes the background sufficiently well that there is good agreement between the range of values found in simulation and experiment.

However, where there are particles which lie underneath the one imaged, or the carbon support or possible contamination is non-uniform in thickness or height, the background identification is particularly difficult. As can be seen from Figure 6.1, this is not an unusual occurrence with these industrial nanoparticle samples as the loading density of the particles tends to be quite high.

As detailed in Section 5.1, the intensity between columns must be included in the cross section value since the finite size of the probe and various cross talk effects means that intensity detected off a column still corresponds to scattering from said column. Therefore, background subtraction needs to be performed away from the columns themselves but close enough to the particle that they represent a true measure of the background.

[1] i.e. non-cycled

Three different areas near to the particle were chosen and an averaged background manually subtracted from the cross section value of a column of interest (as respectively indicated by areas A, B, C and the red circle in Figure 6.1). The scattering cross-section of the column varies significantly, from 54.4% to 64.2% of the un-background-subtracted value (see Table 6.1), depending on the area chosen as background. This variation highlights the sensitivity of the cross section value to the correct identification of the background.

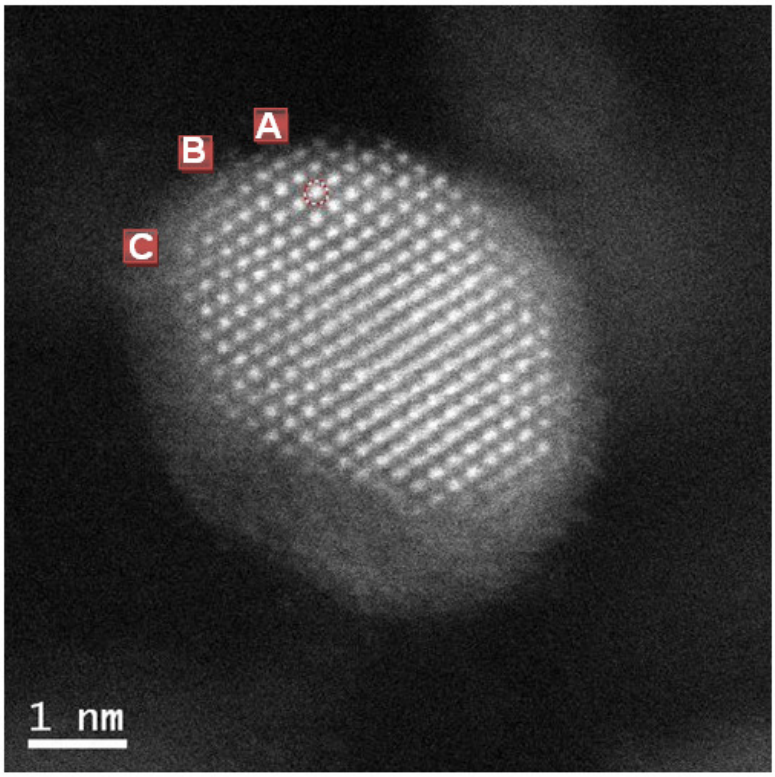

Figure 6.1 HAADF image of a 2ML design nanoparticle positioned above another particle (out of focus), a particularly challenging case for accurate background subtraction. The column circled in red is investigated with various background values subtracted from areas indicated by A, B and C

Background subtracted (fraction of incident probe)		Integrated intensity	Cross section (Mb)	% of original
0		13.7204	30.87	100
A	0.0295023	8.81044	19.82	64.2
B	0.0326981	8. 11682	18.26	59.1
C	0.0356996	7. 46563	16.80	54.4

Table 6.1 The influence of background subtraction on the cross section value

6.2 Automated cross section analysis

Integrating peaks of interest by hand would take a long time so a MATLAB program for automated peak identification and background subtraction was used to analyse the atomic resolution images [14]. The development of the code is attributed to Lewys Jones[2]. The program requires the input of the following parameters:

- detector inner and outer angles (mrad)
- beam currents used to map the detector and to image the specimen (pA)
- lattice parameter of particle (Å)
- the index spacing notation used to auto-calibrate the pixel size of the image from the diffractogram

The process of analysing an image is described in the following section with the example of a pure Pt particle. In the first instance, a particle of pure Pt was chosen to test the method as this negates the complication of compositional variation in the image interpretation. The sample was kindly supplied by Dogan Ozkaya at Johnson Matthey.

6.3 Pure platinum particle

6.3.1 Detector calibration

Pairs of images and detector images were recorded on the Oxford-JEOL 2200MCO with corresponding probe currents recorded. The detector map is loaded first and a histogram plotted to extract a figure for the detector response. The upper bound of the background signal of the vacuum (the dark reference) and lower bound of the detector response is manually selected and the mean value for each is calculated (see Figure 6.2). A 1% error in the mis-selection of the lower and upper bounds at this stage corresponds to a 0.1% difference in the final cross section value [15] and thus can be largely neglected in light of the magnitude of the other experimental errors.

[2] The code is available for download here: www.lewysjones.com, Absolute Integrator v1.1.3 was used in this thesis.

The difference between the two means is then taken as the detector response Int_{det} corresponding to the current used to map the detector:

$$Int_{det} = \overline{Int_{pixel}} - \overline{Int_{darkRef}} \qquad 6.1$$

This gives a single value for the detector response to be used as per Eq. 5.1 to calibrate the image of the sample.

Once the detector's sensitivity is known at particular a gain (contrast) and offset (brightness) settings, the recorded STEM image is recorded using the same settings. This avoids problems arising from any non-linearities in the A/D converter on factory standard instruments which don't have the custom A/D of the LeBeau and Stemmer experiments [16], as discussed in Section 4.2.4.

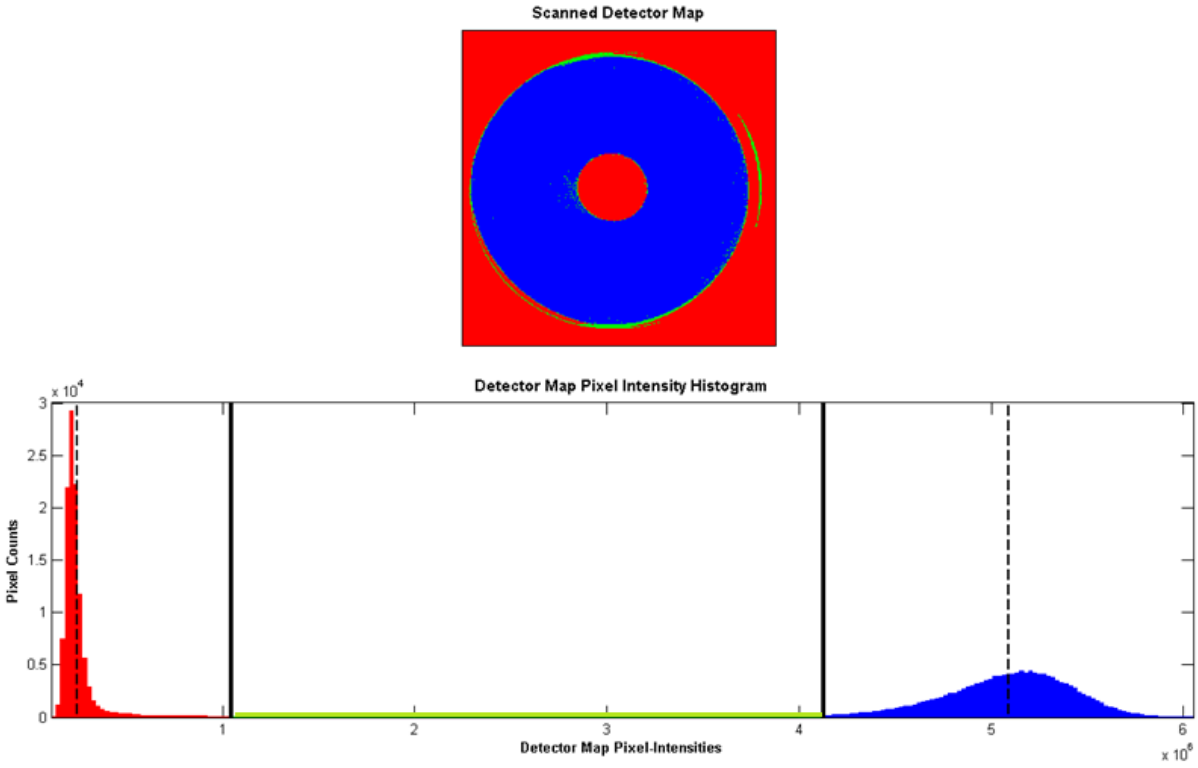

Figure 6.2 Detector calibration step. The image of the detector (top) is shown as a histogram (bottom) of intensity values, divided into three regions: vacuum (red, left), difference (green, middle) and detector (blue, right). The upper threshold for the vacuum level and lower threshold for the detector sensitivity level are selected manually and shown by the solid back lines. The dotted black lines show the resultant mean intensities of the vacuum dark reference and the detector sensitivity.

6.3.2 Image calibration

The image to be analysed is then loaded and calibrated as per Equation. 5.1 to give the intensities on an absolute scale of a fraction of the incident beam current.

The diffractogram is calculated (See Figure 6.3) and the spots indicated in the input file (e.g. “111” for a particle viewed in the [110] direction) are selected in order to calibrate the pixel size of the image. Two spots of the same index family (e.g. -111 and 1-11) are selected to increase the accuracy by averaging the values.

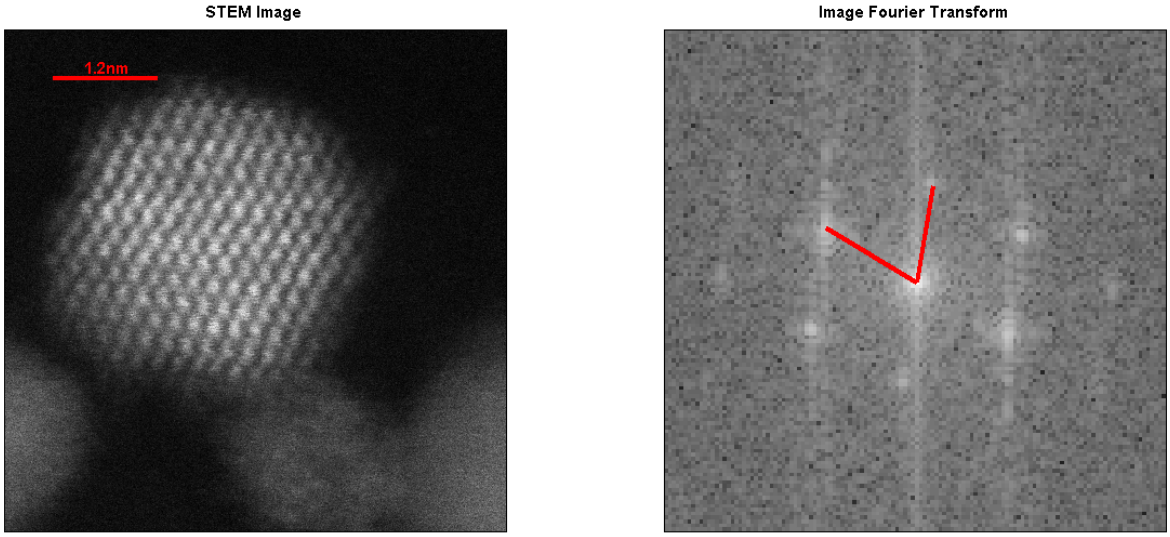

Figure 6.3 Calibration of the pixel size from the diffractogram. Calibrated image (left) and FT spots (right). The spots are selected manually with the cursor and the distance to the zero frequency maximum calculated (red lines).

In order to calibrate the size of the pixels in real space, e.g. Δx, it is convenient to do so from the FT as the inverse relationship between an image and its Fourier transform minimises the potential error in calibration: small distances in the real image (e.g. pixel size) correspond to large distances from the origin in the Fourier transform.

An image of dimensions $a_0 \times b_0$ in real space, with $N_x \times N_y$ pixels has pixel sizes of $\Delta x = \frac{a_0}{N_x}$ and $\Delta y = \frac{b_0}{N_y}$. The Fourier transform of this image will also have $N_x \times N_y$ pixels but the dimension of the image in reciprocal space is $\frac{N_x}{a_0} \times \frac{N_y}{b_0}$. And each pixel in the FT will be $\Delta k_x = \frac{1}{a_0}$ and $\Delta k_y = \frac{1}{b_0}$

The distance from the origin to a spot in the FT for a given diffraction pattern is known as:

$$|g_{hkl}| = \frac{1}{d_{hkl}} \tag{6.2}$$

Where

$$d_{hkl} = \frac{a}{\sqrt{h^2 + k^2 + l^2}} \tag{6.3}$$

where *a* is the lattice parameter for the crystal. In Figure 6.3, two 111 type spots are chosen to calibrate the image; in the [011] projection of an FCC system, the distance $|g_{111}|$ of a 111 spot from the origin is:

$$|g_{111}| = \frac{\sqrt{3}}{a} \tag{6.4}$$

From this, the size of the pixels in reciprocal space can be calculated since if $|g_{111}|$ corresponds to *n* pixels in the FT, then

$$\Delta k_x = \frac{|g_{111}|}{n} \tag{6.5}$$

And so

$$\Delta k_x = \frac{\sqrt{3}}{an} \tag{6.6}$$

The maximum frequency in reciprocal space (in the k_x direction) is the furthest pixel from the centre of the FT. Since the centre of the FT is placed in the middle of the image, this corresponds to

$$k_{max} = \frac{N_x \Delta k_x}{2} \tag{6.7}$$

The Nyquist limit[3], imposed by the discrete nature of the sampling, means that the maximum spatial frequency is limited by:

$$k_{max} < \frac{1}{2\Delta x} \tag{6.8}$$

From this, the minimum detectable separation distance in real space, i.e. the real space pixel size Δx, to be calculated:

$$k_{max} = \frac{1}{2\Delta x} = \frac{N_x \Delta k_x}{2} \tag{6.9}$$

So the pixel size is simply:

$$\Delta x = \frac{1}{N_x \Delta k_x} = \frac{an}{N_x \sqrt{3}} \tag{6.10}$$

It is important to note that an error of 1% in distance measured from the spot to the central maximum corresponds to a 5% error in the measured cross section. Since this affects the calculated pixel size, which is multiplied to get the cross section, this error scales exponentially and so the selection needs to be done carefully.

6.3.3 Peak finding

A box of size x pixels is scanned across the image and the highest intensity pixel found within this area of focus. This allows a map of peak positions to be found which is then used to determine the sites of atomic columns by attributing pixels to the nearest peak within a certain radius.

---

[3] The Nyquist-Shannon sampling theorem says that a signal can be reconstructed by sampling with a rate that is at least twice the maximum frequency. A more practical understanding is to say that the minimum detectable frequency in a real image is limited by 2 pixel widths.

For a fully automated approach, the box size can be iteratively increased until the number of feature peaks found converges and before the total number starts decreasing as the box becomes larger than the distance between neighbouring features and individual peaks are lost. From this, a map of identified peaks can be found (see Figure 6.4).

It has been shown that this method is significantly faster than other Fourier space peak finding methods [14]. Since the accurate identification of the location of the peak is of paramount importance in identifying the column itself and extracting a value for the total column intensity, a further refinement is necessary. This is carried out by fitting a 2D Gaussian profile over the identified peak positions and comparing this with the raw data. The location of the peak of the fitting Gaussian which best fits the raw data is used as the refined column location. This step is optional and is often not necessary for well resolved, high resolution images.

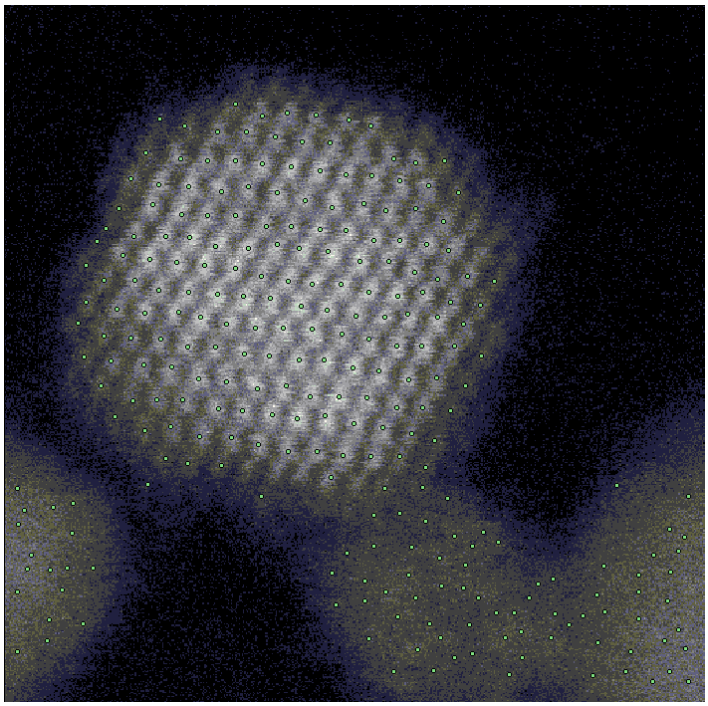

Figure 6.4 Peak identification, where green spots indicating the local maxima found by the algorithm. A straight forward threshold to select the peak intensities results in the automated method finding false positives in the out of focus particles to the bottom right and left. This is an unavoidable artefact of the automated algorithm.

6.3.4 Background subtraction algorithm

Next, the crucial step of background subtraction is performed. The method allows for a locally-responsive and spatially-varying background to be removed. An extended area of a fixed radius of one feature spacing is drawn around each column found in the peak identification. This creates a complete mask of the particle and any free atoms are encompassed in their own circle. This segments the image into two parts: sample plus background, and just background.

The pixels corresponding to sample and background are removed and the area of pure background is considered. A value for the background underneath the sample is then interpolated from the values at the edges of the particle mask. This is done by using the *roifill* function in Matlab's library to smoothly in-paint the region left by the sample by interpolating inwards from pixel values at the boundary edge by solving the Laplacian. This is iteratively Gaussian blurred until a converged solution is found. The background calculated is then removed from the raw data of sample + background, and the sample image returned (see Figure 6.5) such that all pixels which aren't attributed to the particle are zero in value.

From Figure 6.6, it is clear that misidentification of the intensity in the bottom right has labelled amorphous areas as atomic columns. This has meant that the background subtraction has not entirely "lifted out" the particle from the background as these areas were also considered part of the sample.

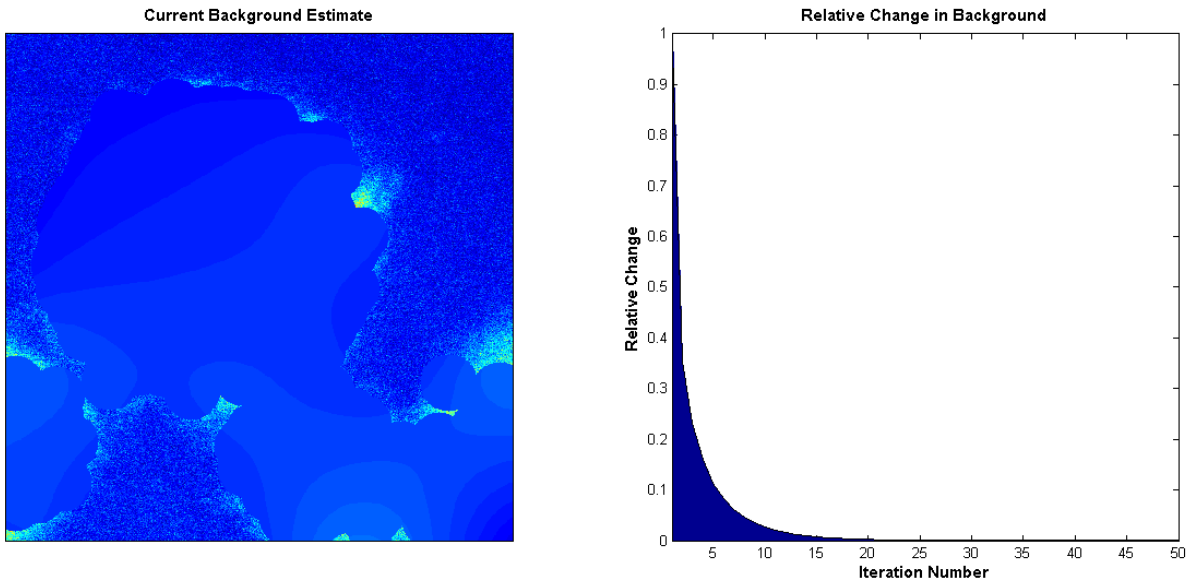

Figure 6.5 Screenshot of the iterative background subtraction. The mask of the particle is removed and a background interpolated iteratively from the remaining values (left). The relative change in the mean background value to test for convergence (right).

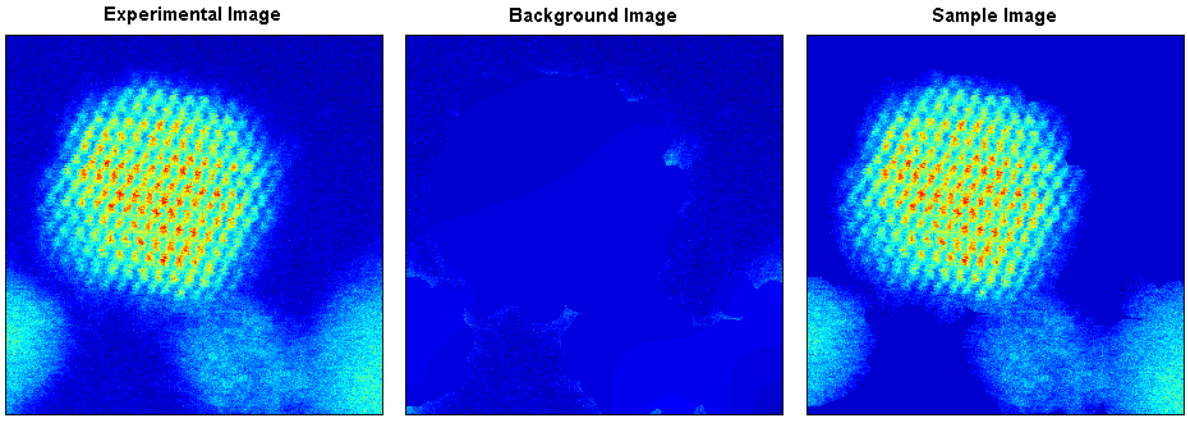

Figure 6.6 Raw experimental image (left), the removed background (middle) and the difference, which is the sample image (right).

6.3.5 Cross section determination

The sample image is then processed. The integration area corresponding to each column is a Voronoi polygon[4], where each point within the polygon is attributed to that atomic column by virtue of it being the closest peak to that point. The rationale behind this shape is to maximise the area of integration to satisfy the conditions for the cross section values that the probe function is negligible at the boundaries of the integration cell, without clearly impinging on the scattering from neighbouring columns. A limit of one lattice parameter is applied to the size of the radius of these polygons as it is unphysical to consider scattering further away from the column intensity. The effect of this can be seen at the edges of particles where the polygons are rounded.

The polygons are calculated from the locations of the atomic-columns by calculating the Euclidian distances of all the image pixels to the nearest identified column. In practice, this results in Euclidian allocation zones (EAZ) due to the pixilated nature of the raw data. At sufficient magnifications, these EAZs correspond well to true Voronoi polygons.

The contents of each EAZ is then integrated and multiplied with the area of each pixel calculated from the image calibration described in 6.3.1.2 to give an absolute value for the probe integrated scattering cross section to be compared to simulations. The results of this analysis can then be displayed as a histogram in order to identify clustering of values which might correspond to thickness variations (see Figure 6.7) or an interactive Matlab figure (see Figure 6.8) where the cross section values can be probed by selecting the regions with a cursor.

[4] Also called Thessian polygons or proximal polygons

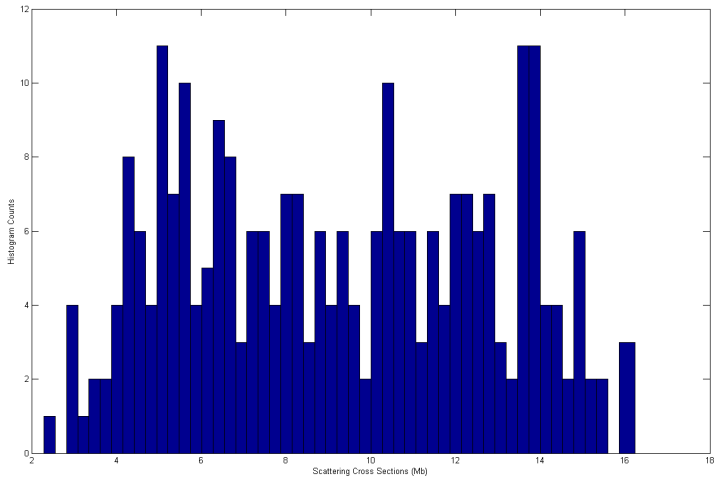

Figure 6.7 Histogram of calculated cross section values of identified columns, extracted from the image. There is some sense of clustering

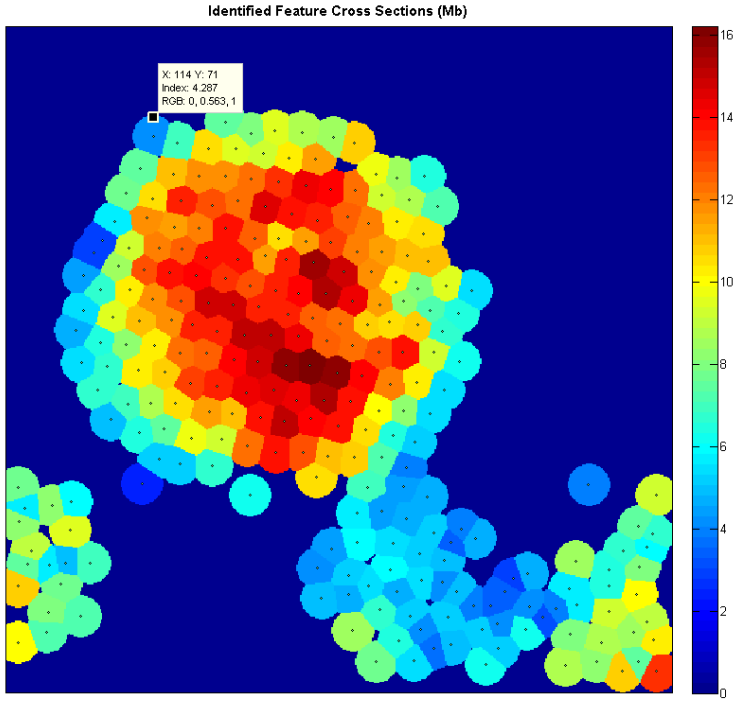

Figure 6.8 Identified cross sections, where each Voronoi polygon is coloured to represent the cross section value associated with that column.

Comparing cross section values to the library of simulated values, a map of possible thickness is obtained, as in Figure 6.9. Matches were found by using a lookup table to find the nearest value less than the measured cross section. Then the relative error of that value and one greater was calculated and the value corresponding to the smallest error chosen.

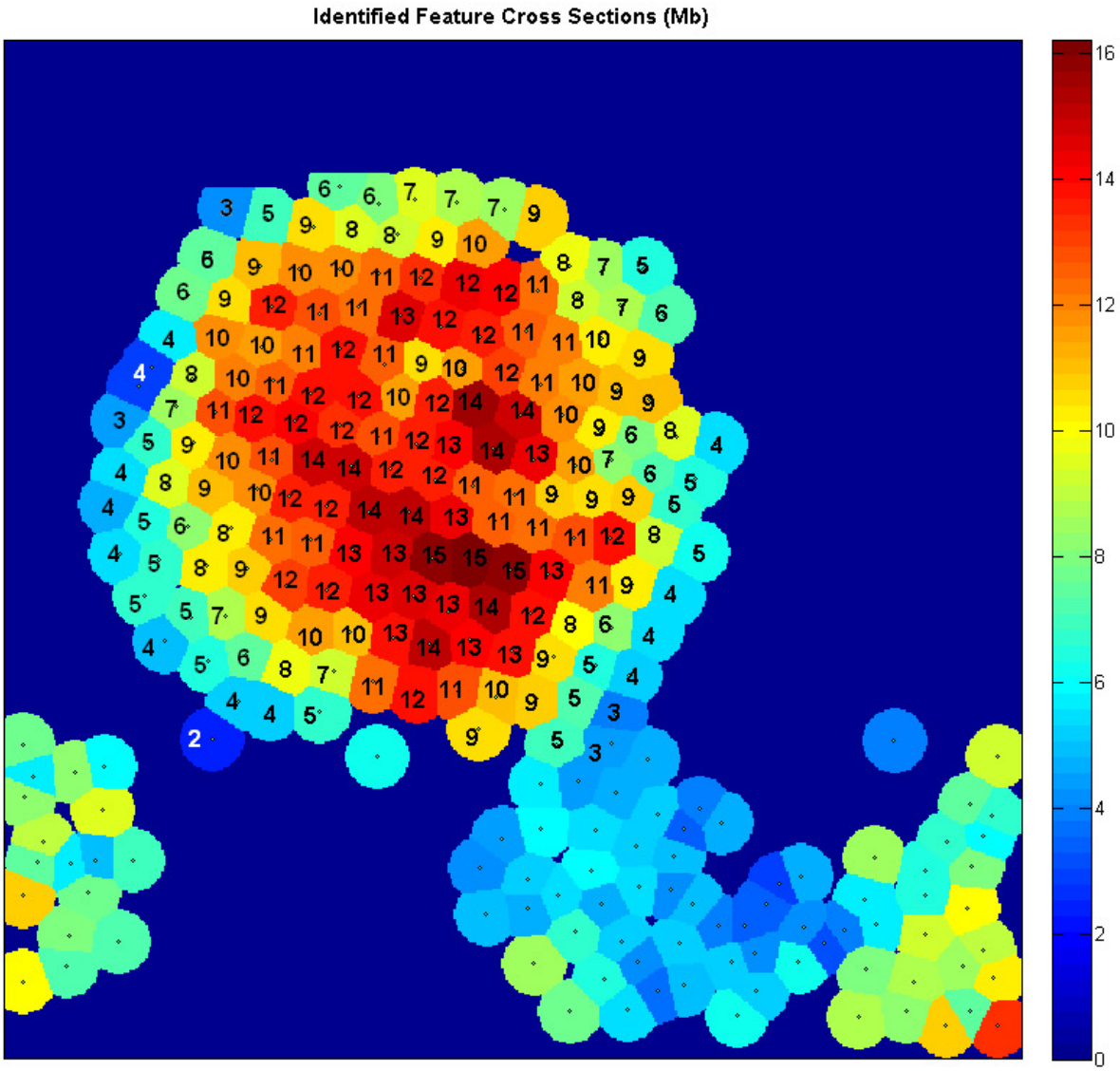

Figure 6.9 Thickness of columns by comparison of extracted experimental cross section values to a simulated library. The number of atoms in the column marked in black.

6.3.6 Crystal Maker model

A model of the particle was made using the Crystal Maker software by manually removing atoms from a bulk crystal until a column by column match to the thicknesses obtained from the cross section analysis gave a roughened particle.

Because of the large experimental error in measurement, the possibility of misidentification of the column composition is significant. Thus, the best likelihood estimate is made given assumptions made about the particle's 3D morphology. These assumptions are chiefly that the particle is:

- not hollow (so each column is continuous)
- no thicker in projection than it is wide in the image
- convex
- smooth (the difference in thicknesses between neighbouring columns is minimised)

Considerations of surface smoothness were further used to place the height of neighbouring columns relative to each other. Where the error on the cross section measurements allowed for a thickness of ±1 or 2 atoms, the thickness best suited to preserving an extended, smooth facet was chosen since this produced a thermodynamically more stable and thus more likely solution.

The best likelihood model can be seen in Figure 6.10, in the beam direction and rotated slightly to view the morphology.

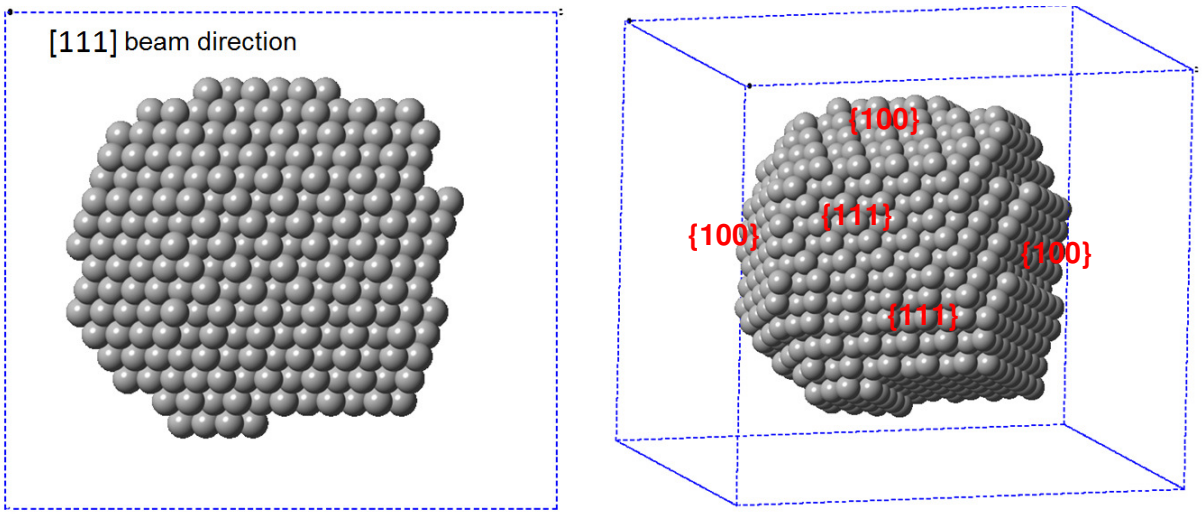

Figure 6.10 Model of particle imaged in 6.4 made from the analysis of cross section values, as show in Figure 6.9. Miller index families are shown in red (right)

This model with 1700 atoms was then used to simulate an image using the absorptive potential code. The dimensions of the supercell were 5.07nm x 5.64nm, sampled over a mesh of 1024 x 1024 pixels. 162 x 180 probe positions were plotted to give the output image of Figure 6.11.

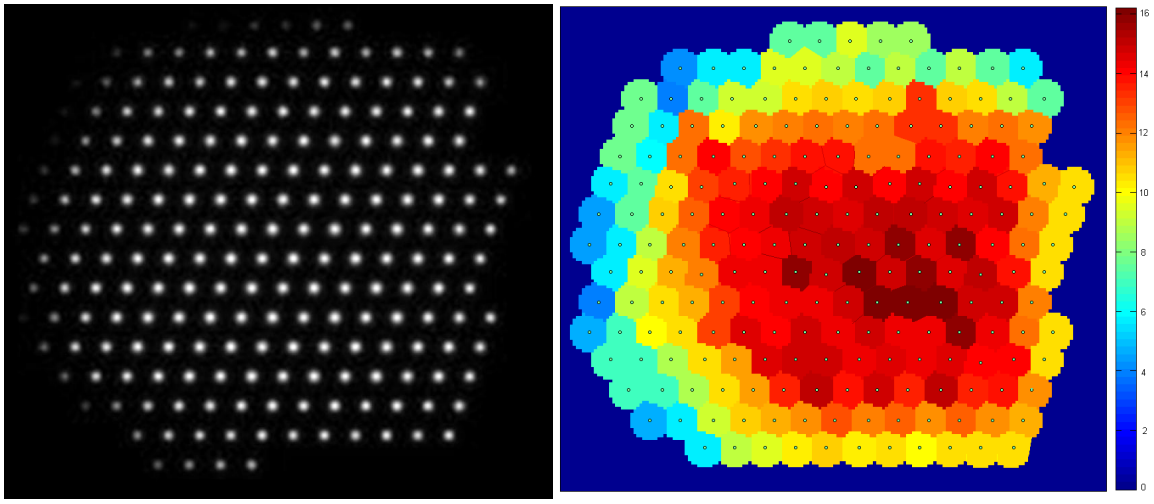

Figure 6.11 (a) Simulated image from the model shown in Figure 6.10. Sliced 23 times, 6 subslices. **(b)** cross section analysis of simulated image showing good agreement to the original image in Figure6.4.

Although there is not an exact match between the cross section values of the experiment and the simulated model, especially around the areas to the bottom right where the background subtraction is occluded by a neighbouring particle, there is good agreement in the number of atoms in each column (See Figure 6.11(b)). This is encouraging evidence that it is possible to get a good match between image and a model by matching experimental values to a library of column intensities.

6.4 Error Analysis

The combination of uncertainties in the experimental procedure limits the accuracy of the match to a theoretical cross section. The errors arise from many sources (see Table 6.2) and quantifying them allows an experimental uncertainty to be applied to the quantified analysis of the nanoparticles.

Error source	Scale	
	Typical error	**%**
probe current (detector)	± 0.05pA	5
probe current (image)	±0.05pA	0.3
detector inner angle	1mrad	5
detector outer angle	5mrad	*negligible*
Detector non-uniformity	-	5
mistilt	3mrad	5
pixel size calibration	0.1Å	1
background subtraction	constant	constant

Table 6.2 Potential sources of errors and their associate magnitudes as absolute values and percentages.

The errors are independent and thus combined in quadrature:

$$\Delta_{total} = \sqrt{\sum errors^2} \tag{6.6}$$

$$\sum errors = \Delta^2_{detectorCurrent} + \Delta^2_{imageCurrent} + \Delta^2_{innerAngle} + \Delta^2_{outerAngle} + \Delta^2_{DetNonUniform} + \Delta^2_{mistilt} + \Delta^2_{pixel} + \Delta^2_{background}$$

Typically, the combined error is on the order of 10%, with the dominant errors being the shot noise on the small probe current used to map the detector, the detector inner angle and non-uniformity and the potential for unidentified mistilt.

6.5 Core-shell Particles

The cross section analysis is now applied to a core-shell nanoparticle in order to investigate the feasibility of extracting information about the compositional makeup of atomic columns. Some particles show a very distinct segregation of Pt to a shell like structure (see Figure 6.12) but the thickness of the Pt coverage is difficult to ascertain in projection.

Unfortunately, the underlying particles to the right side make effective background subtraction intractable and thus over-aggressive removal of the background has led to artificially decreased cross section values to the right of the particle. However, those to the left are unencumbered by underlying variations in background and can be more readily analysed. Comparison by cross section (see Figure 6.14) reveals possibilities for compositions in neighbouring columns of 6.4Mb and 5.2Mb (marked 1 and 2). Within the 10% uncertainty of the experiment, each column has many possible combinations of thickness and composition (see Table 6.3).

Assuming that the two columns are located in the middle of a facet, it is thermodynamically unlikely that neighbouring columns would differ in height by many atoms. In addition, assuming that the particle is convex, the thickness of column 2 must be greater than or equal to that of column 1 since it is further away from the edge of the particle. Thus column 2 is most likely 8Pd or (7Pd + 1Pt at the top) and column one is thus constrained to be (6Pd + 2 Pt at the top) or (7Pd + Pt at the top) if the neighbouring columns are to be of similar thicknesses.

The compositions are 8Pd for column 2 and column 1 must be (6Pd + 2Pt at the bottom). The intensity comprising the “shell” is likely due to preferential deposition of Pt at step-like edges of the nanoparticle (shown schematically in Figure 6.13). Steps can be seen along another facet in projection in the top left of the particle (indicated by the red box in Figure 6.12).

Column 1 (6.4Mb)			Column 2 (5.2 Mb)		
Pd	**Pt**	**thickness**	**Pd**	**Pt**	**thickness**
10	0	10	8	0	8
0	5	5	0	4	4
9	1 (top)	10	7	1 (top)	8
8	2 (top)	10	5	2 (top)	7
6	3 (top)	9	3	3 (top)	6
8	1 (bot)	9	6	1 (bot)	7
6	2 (bot)	8	4	2 (bot)	6
6	3 (bot)	9	2	3 (bot)	5
7	1 (sandw)	9	4	1 (sandw)	6
2	2 (sandw)	6			

Table 6.3 Possible composition and thickness values for column 1 and 2 marked in Figure 6.12.

Comparison of cross section values in the region indicated by the blue box show that there is little variation in the scattering, indicative of either a flat, plate like structure, or Pt decoration that corresponds exactly to the difference in height between the columns. The latter interpretation seems an unlikely coincidence.

It is interesting to note that there is increased scattering in some areas in the central plane which could correspond to Pt decoration (see blue box Figure 6.12). Subsequent images of the same area show variation in the location of these brighter columns, suggesting mobile Pt on the surfaces of the particle.

However, as can be seen from the integrated line profile in the same figure, the background is significant and so the columns are not well resolved enough to have a large difference in the cross section values even though the peak intensity (and thus the contrast) may be brighter in some columns.

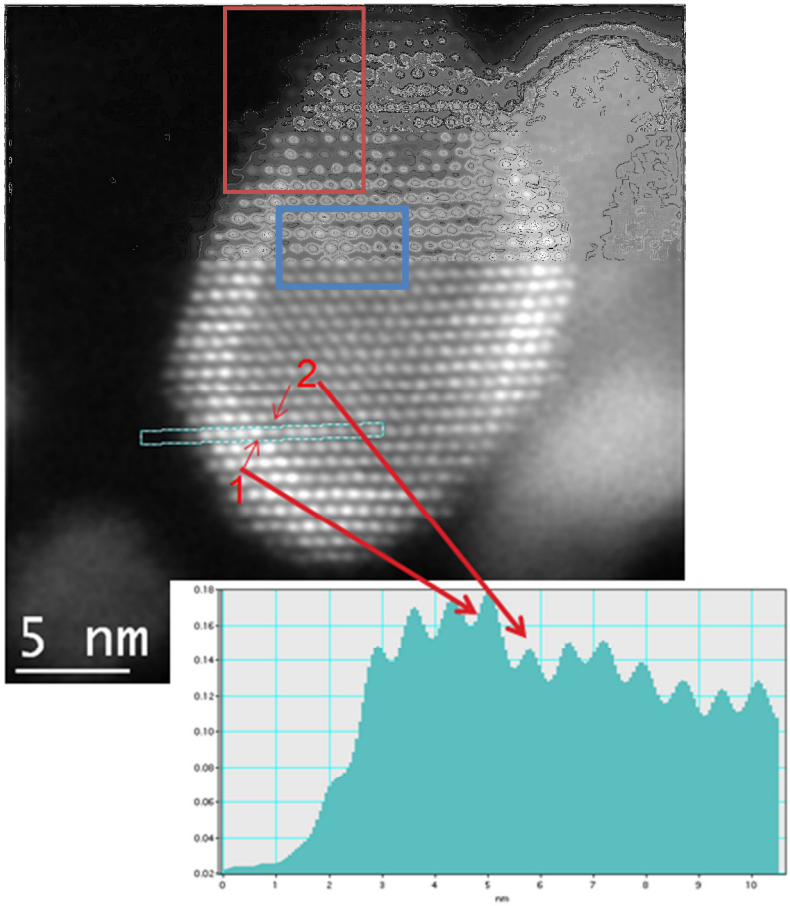

Figure 6.12 A 2ML design particle imaged using the Oxford JEOL 2200MCO at 200kV. The bright intensity at the edges are indicative of a shell of Pt. An integrated line profile shows the scattering from two neighbouring columns, marked 1 and 2, which vary significantly.

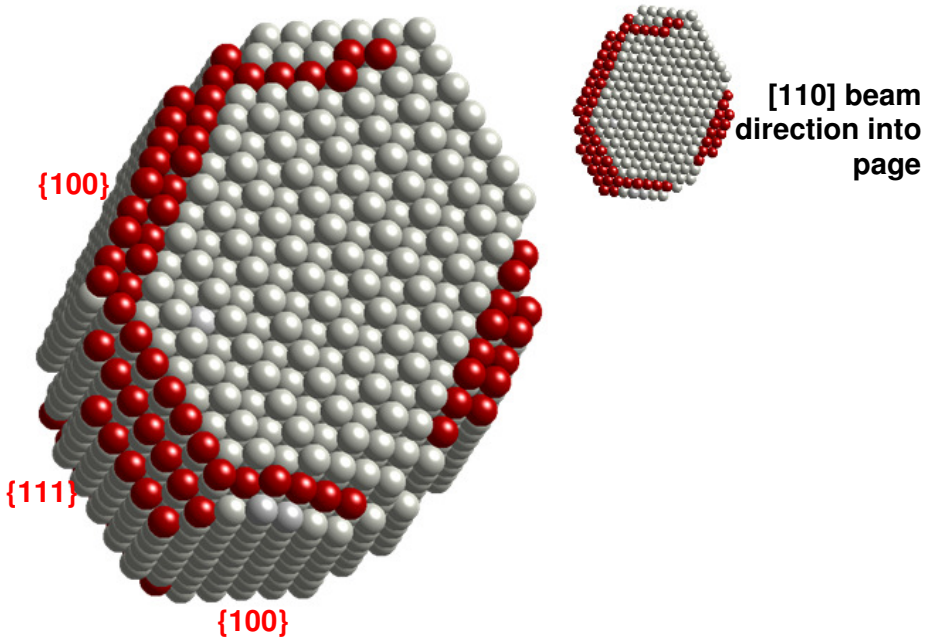

Figure 6.13 Atom model (scaled down) showing sites of preferential Pt deposition at step-like edges

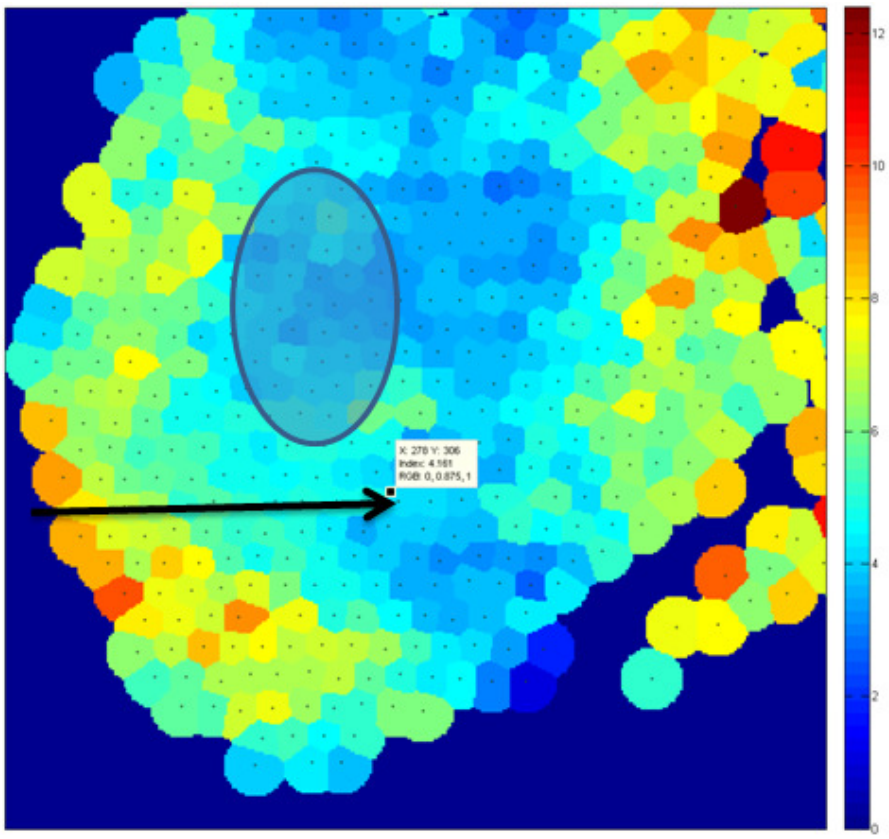

Figure 6.14 cross section analysis of particle in Figure 6.12 The value of one Voronoi polygon is shown. The overly aggressive background subtraction on the right due to the presence of other particles underneath has resulted in a decreased. cross section of columns in the shaded region show similar values. The black arrow indicates the line profile take in Figure 6.12.

6.6 Large nanoparticle

As size increases, the number of possible combinations of composition and thickness increases as a geometric progression, thus the matching becomes increasingly difficult. Particles of size in the region of 8-10nm show more complicated structures and more twinning, further complicating image interpretation.

The particle in Figure 6.15 was imaged using the Oxford JEOL 2200MCO at 200kV and shows two clear grains. From the FT (see Figure 6.16), it can be seen that one in the [110] orientation on the left, (marked a), is twinned with a higher order $[\bar{1}14]$ orientation on the right (marked b). The region in the middle is not well resolved and could be a third grain. Clear Pt segregation is seen by the increased

scattering intensity at the edges of the particle, particular in the right grain and the top left of the left grain. A line profile, summed over 10 pixel widths (Figure 6.15 bottom) clearly shows an increase in scattering. An increase due to thickness in such a short lateral distance, a 'cliff edge' is thermodynamically unlikely and so the contribution to the intensity must be attributed to composition.

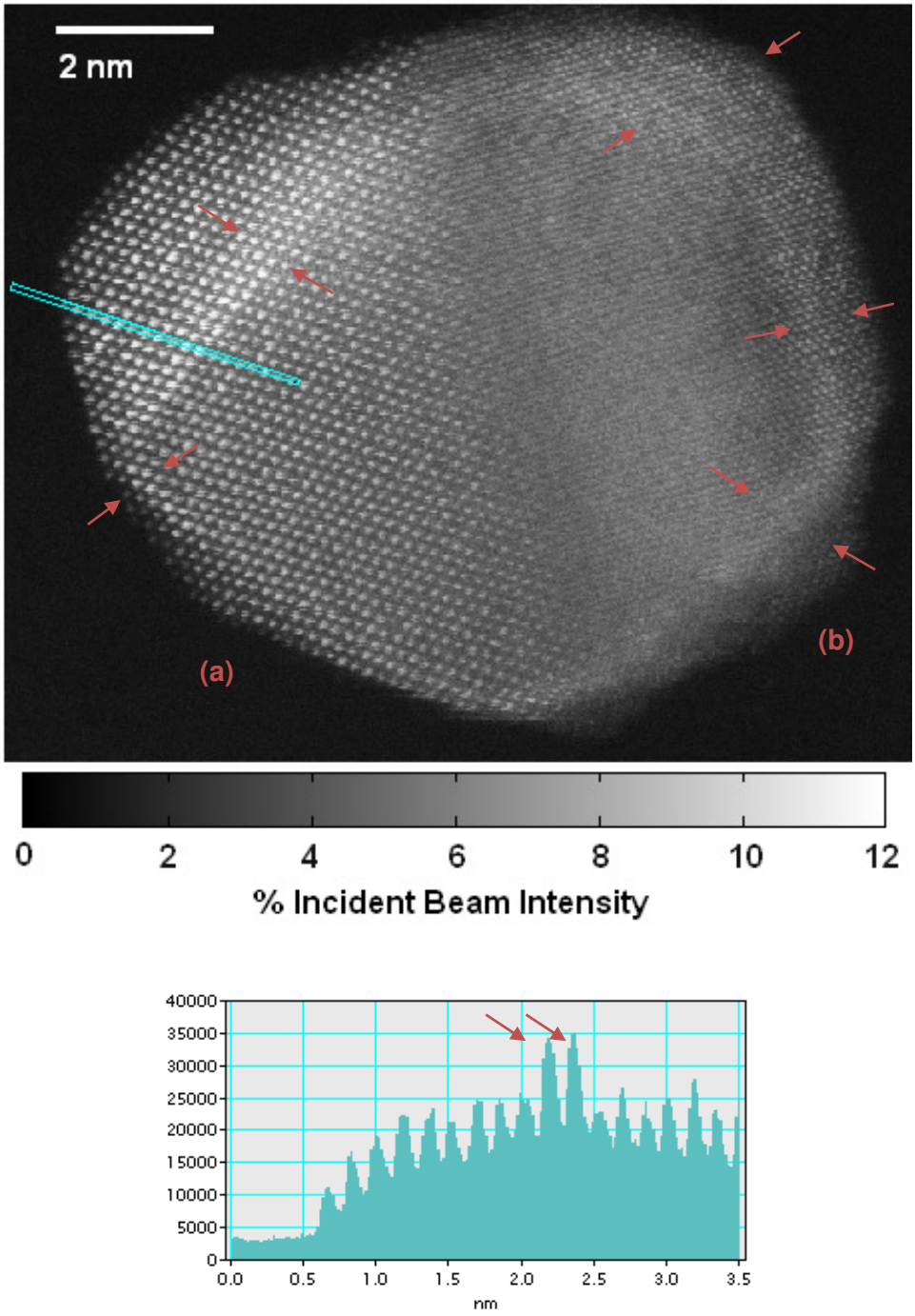

Figure 6.15 (top) a large 2ML design particle showing evidence of Pt decoration marked by red arrows **(bottom)** Line profile of intensity shown by blue line in top figure.

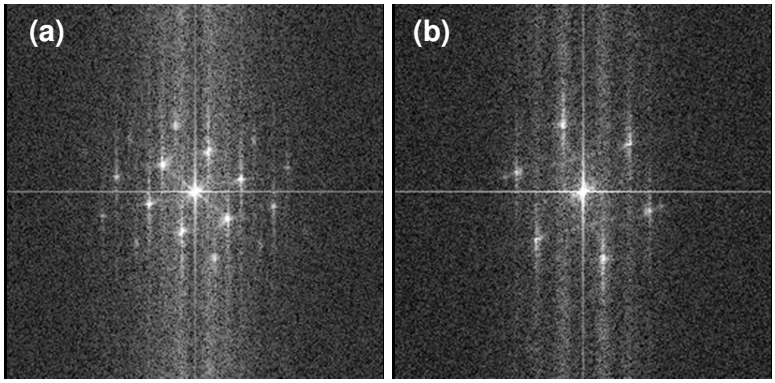

Figure 6.16 FT of two grains marked as (a) and (b) in Figure 6.15, showing the different orientations.

To ascertain the amount of Pt present, a quantitative analysis must be carried out. An analysis of the cross section values (see Figure 6.17) shows that there is indeed a dramatic increase in the scattering in the bright band in the top left of the particle, from cross section of 41Mb to 59Mb within three columns (indicated by the black arrows in Figure 6.17 and red arrow the histogram in 6.15). However, the matching of the absolute values to simulated values does not yield a plausible thickness. Even if the columns of highest cross section were pure Pt, the thickness would still correspond to over 70 atoms, which is greater than the width of the particle. Moreover, given the nature of the synthesis method, it seems unlikely that there would be a few columns of pure Pt neighbouring mixed composition columns, especially some distance from the edge of the particle, but that Pt would at segregate in complete grains or cover the surface of the Pd core.

Thus, it must be concluded that for larger thicknesses, the usage of cross section appears to break down as the probe can no longer be treated as constant in the z direction. Judging from the micrograph in Figure 6.15 and the increased background seen in the histogram, significant probe spreading and cross talk, and multiple scattering effects have occurred, which would go some way to explaining the increased cross section values observed.

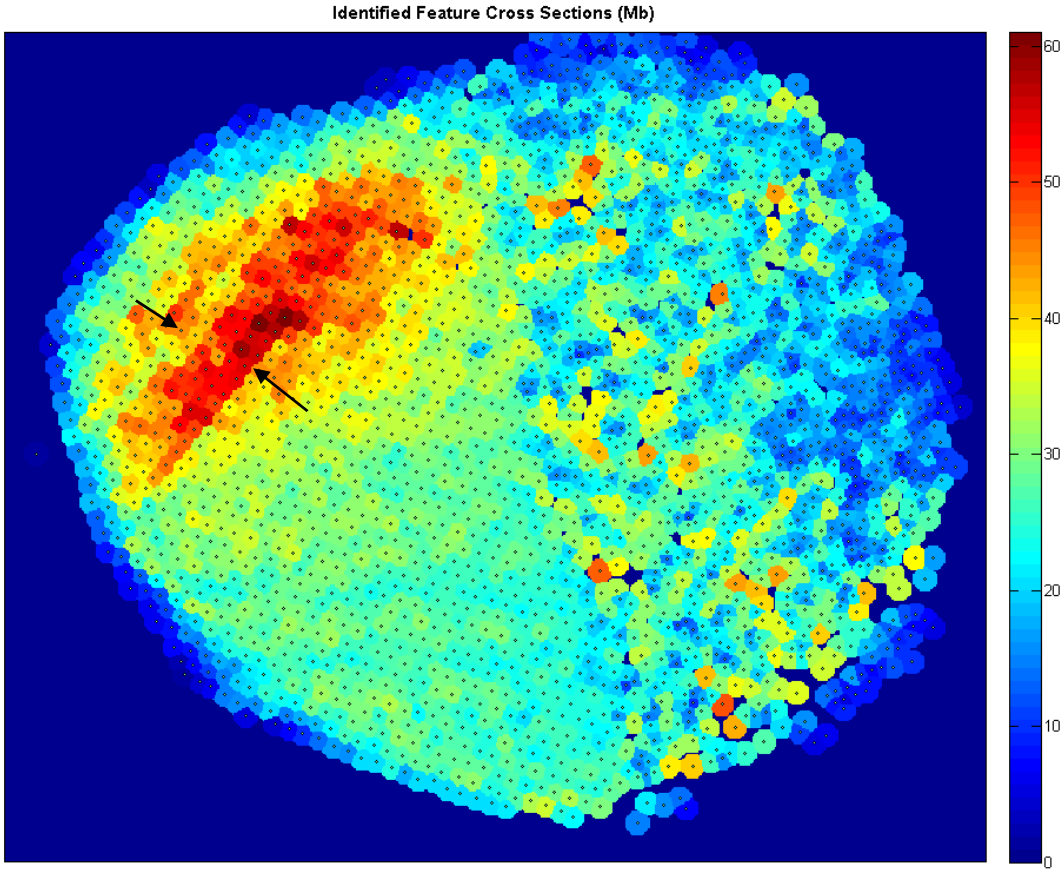

Fi**gure 6.17** cross section analysis of the particle in Figure 6.15. Black arrows show the areas of significant change in cross section values across a short lateral distance, indicative of the presence of Pt. However, the absolute values do not match plausible thicknesses, even of pure Pt columns.

6.7 Complete particle analysis of a core-shell particle

The micrograph in Figure 6.18, of a 2ML pre-cycled sample, was taken at 200kV with a JEOL ARM 200F. The beam current was 6.1pA and the image collected over 1024 x 1024 pixels with a dwell time of 19µs per pixel. The HAADF detector was mapped with a current of 1.03pA over 512 x 512 pixels with a dwell time of 38µs per pixel. Therefore, an extra conversion factor of 2 was required to scale the image to the incident beam current to account for the difference in real dwell time across the particle.

There is clear variation in the intensity to one side of the particle, indicative of a possible core-shell structure, especially along the bottom of the particle (indicated between the red arrows). However, since this is a projected image, the thickness in the beam direction could be any number and moreover, the three atomic planes could be a facet covered by an even distribution of Pt rather than three [$\overline{111}$] planes of Pt.

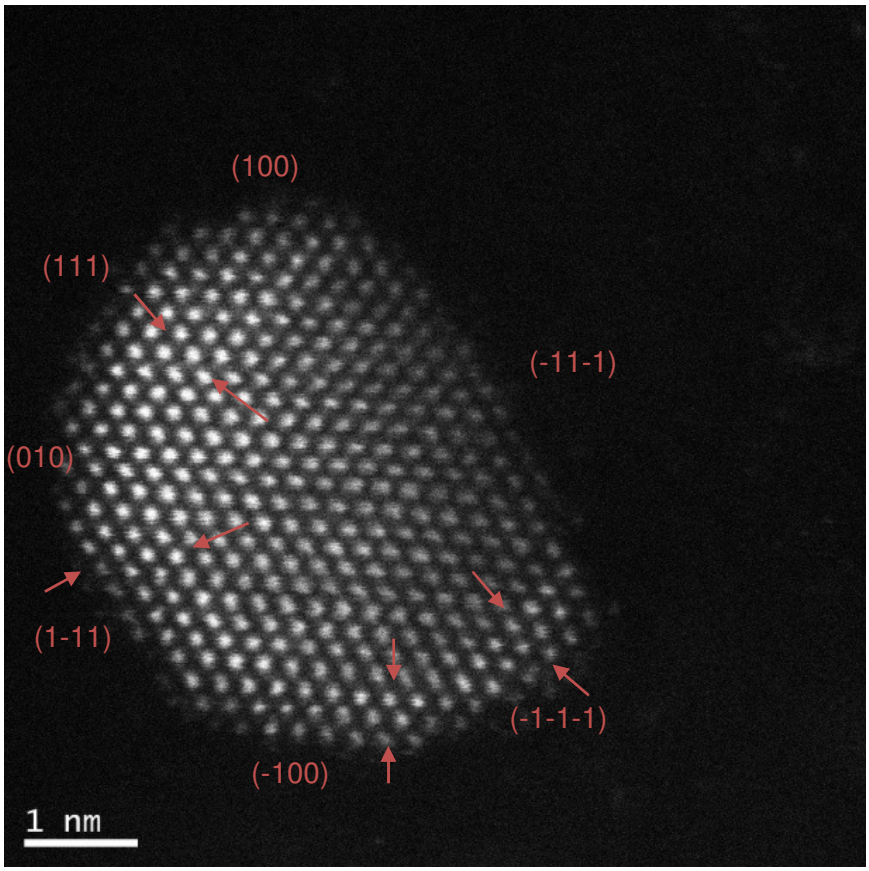

Figure 6.18 2ML particle viewed down the [110] direction. Facets are marked; red arrows indicate the likely Pt segregation from the intensity distribution.

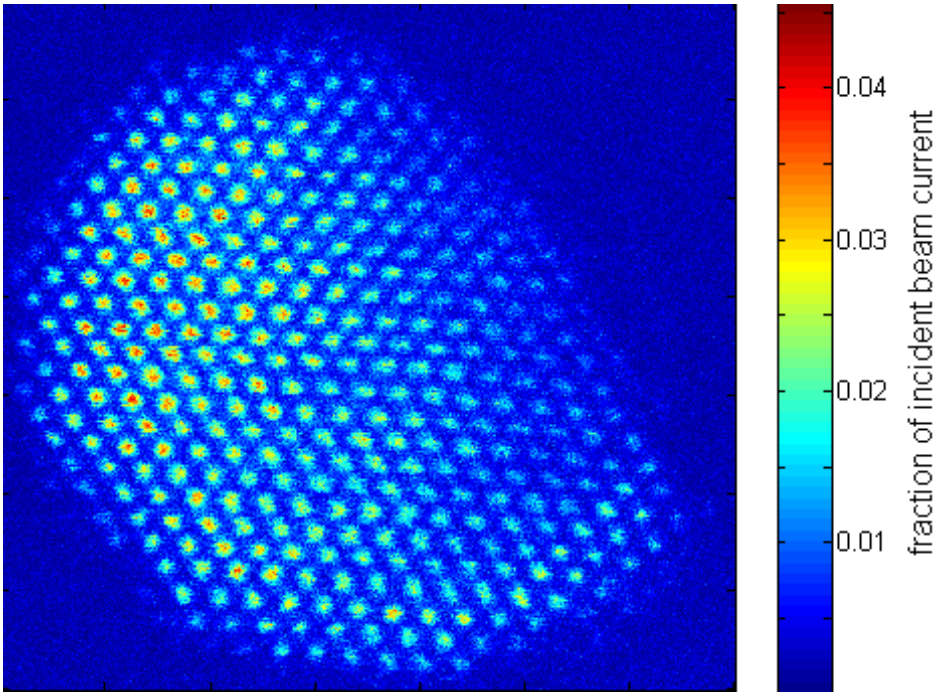

Figure 6.19 A false colour representation of the micrograph in Figure 6.18. Indication of a core-shell structure can be seen.

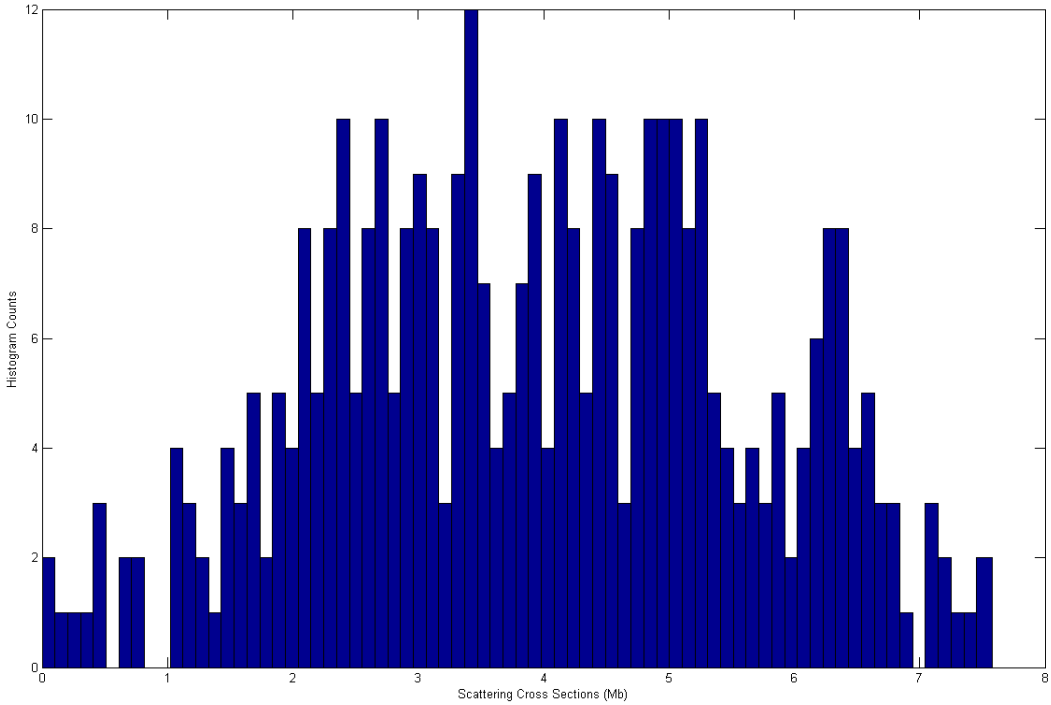

Figure 6.20 Histogram of calculated probe integrated cross section values. Clear clustering of values can be seen though it is difficult to determine how many combinations of thickness and compositions are present

From Figure 6.20, it is evident that extraction of distinct clusterings of values is challenging. The method of fitting Gaussian distributions to the histogram scatter, as done by Van Aert et al [17,18], is hampered by the large number of possible combinations of thickness and composition in the columns of a bimetallic particle. In addition, because of the 10% experimental error, the proximity of cross section values and also the differing effects of dopant atoms at the top of bottom of a column (as explored in Section 5.6), often more than one possible combination of compositions exist within the uncertainty for a single cross section value.

By grouping the data in such a histogram representation, the potential to use the spatial location of the peaks to aid interpretation of the measured intensity value is lost. By matching the cross section value to the location of the column, whether near an edge, surface or in the middle of the particle, it is possible to gain further insight by taking into account the likely thickness and composition of the column in question given its neighbouring columns (see Figure 6.21) to reveal Pt islands and corners.

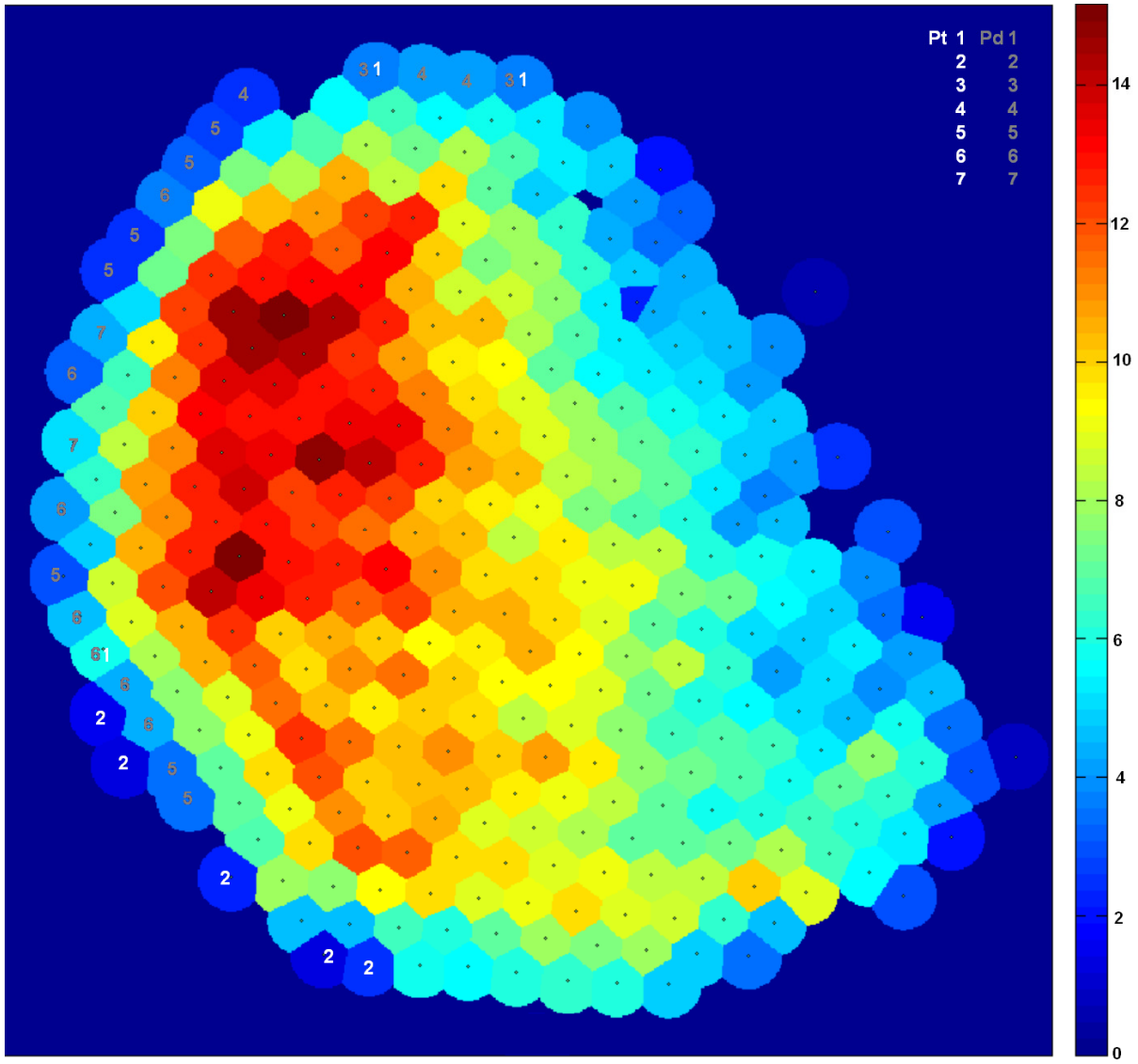

Figure 6.21 Map of probe integrated cross sections of the particle in Figure 6.18. An indication of likely compositions in some areas of less ambiguity is shown with the white numbers corresponding to number of atoms of Pt and grey numbers corresponding to number of atoms of Pd. Pt islands can be seen on some faces and corners.

However, even the cross section analysis cannot unambiguously identify the composition ***and*** thickness of each column. A best estimate model is made in Figure 6.22, where the likely columns which contain Pt are marked in red. Assumptions are made about the thickness of the nanoparticle as detailed in Section 5.6.1.

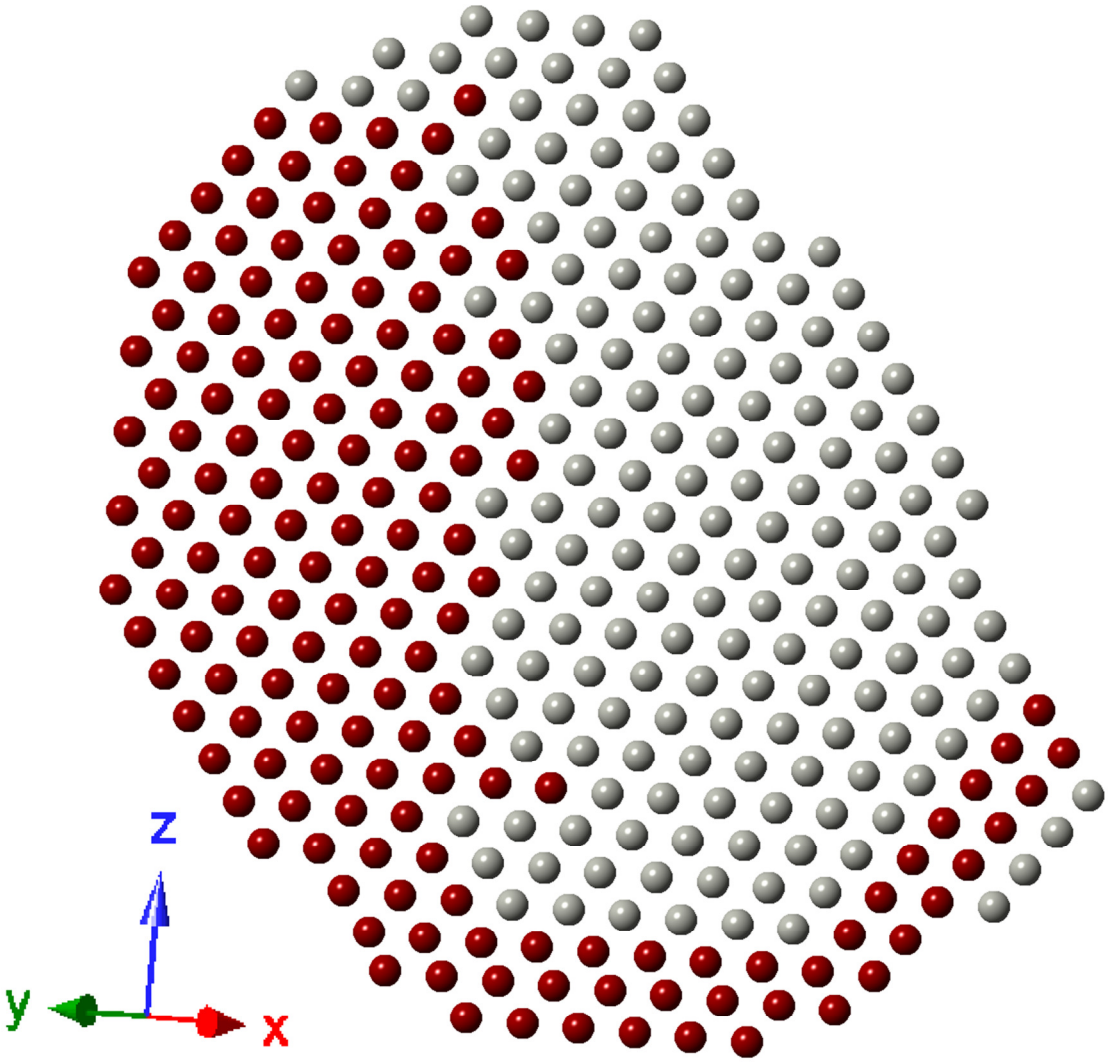

Figure 6.22 Best estimate model of the 2ML particle in Figure 6.18 based on the cross section values analysis of thickness and composition. Location of Pt is marked in red. It is not possible to extract the exact number and location of Pt within the columns as the match library of cross sections as there were too many combinations of thickness and composition.

6.8 Conclusions

While cross sections are a robust measure in the comparison of experimental images to simulation, it is difficult to interpret the scattered signal and separate the contributions to contrast from thickness and composition. The cross section analysis of a test case of a small pure Pt particle shows good agreement with a subsequent simulated model. However, the introduction of another atomic species gravely complicates matters as the number of possible thickness and composition possibilities makes identification of columns intractable given the experimental uncertainties.

Possible accountable errors give a typical 10% margin of combined error on the comparison of experimentally extracted cross sections with simulation, which gives a large selection of possible column compositions and thickness. Furthermore, mistilt presents a grave problem in real samples as it greatly reduces the channelling effects and often cannot be identified through visual clues such as elongation of the column profile, since channelling effects will mitigate this. Finally, since the thermal behaviour of nanoparticles cannot be assumed to be identical to that of a bulk crystal, the DWF could have a significant effect on the cross section values, especially for larger particles.

While it is possible to draw some conclusions about the Pt segregation from cross section analysis and assumptions about morphology, and best estimates of the structure allow for a plausible model to be constructed, more compositional information is necessary to obtain a more certain structural solution. This is explored in the next chapter, where we will apply EDX to the analysis of core-shell nanoparticles.

References

[1] J.M. Lebeau, S.D. Findlay, L.J. Allen, S. Stemmer, Standardless atom counting in scanning transmission electron microscopy, Nano Letters. 10 (2010) 4405–8.

[2] S. Van Aert, K.J. Batenburg, M.D. Rossell, R. Erni, G. Van Tendeloo, Three-dimensional atomic imaging of crystalline nanoparticles., Nature. 470 (2011) 374–7.

[3] P. Hartel, H. Rose, C. Dinges, Conditions and reasons for incoherent imaging in STEM, Ultramicroscopy. 63 (1996) 93–114.

[4] P.M. Voyles, Imaging Single Atoms with Z-Contrast Scanning Transmission Electron Microscopy in Two and Three Dimensions, Microchimica Acta. 155 (2006) 5–10.

[5] S.D. Findlay, L.J. Allen, M.P. Oxley, C.J. Rossouw, Lattice-resolution contrast from a focused coherent electron probe. Part II, Ultramicroscopy. 96 (2003) 65–81.

[6] D.O. Klenov, S. Stemmer, Contributions to the contrast in experimental high-angle annular dark-field images., Ultramicroscopy. 106 (2006) 889–901.

[7] S. Hillyard, R. Loane, J. Silcox, Annular dark-field imaging: Resolution and thickness effects, Ultramicroscopy. 49 (1993) 14–25.

[8] C. Dwyer, J. Etheridge, Scattering of A-scale electron probes in silicon, Ultramicroscopy. 96 (2003) 343–360.

[9] P.M. Voyles, D.A. Muller, J.L. Grazul, P.H. Citrin, H.-J.L. Gossmann, Atomic-scale imaging of individual dopant atoms and clusters in highly n-type bulk Si, Nature. 416 (2002) 826–9.

[10] P. Voyles, Depth-dependent imaging of individual dopant atoms in silicon, Microscopy and Microanalysis. 10 (2004) 291–300.

[11] R. Loane, E. Kirkland, J. Silcox, Visibility of single heavy atoms on thin crystalline silicon in simulated annular dark-field STEM images, Acta Crystallographica Section A. 44 (1988) 912–927.

[12] S.C. Ball, S.L. Burton, J. Fisher, R. O'Malley, B.C. Tessier, B. Theobald, et al., Structure and Activity of Novel Pt Core-Shell Catalysts for the Oxygen Reduction Reaction, ECS Transactions. 25 (2009) 1023–1036.

[13] A.E. Russell, B. Tessier, A. Wise, A. Rose, S.W. Price, P.W. Richardson, et al., In Situ XAS Studies of Core-Shell PEM Fuel Cell Catalysts: The Opportunities and Challenges, in: ECS Transactions, The Electrochemical Society, 2011: pp. 55–67.

[14] L. Jones, K.E. MacArthur, P.D. Nellist, Automated Peak Finding, Intensity Integration and Cross-Section Calculation in HAADF STEM Images, In Preparation. (n.d.).

[15] L. Jones, K.E. MacArthur, Detector Non-uniformity, In Preparation. (n.d.).

[16] J.M. Lebeau, S. Stemmer, Experimental quantification of annular dark-field images in scanning transmission electron microscopy., Ultramicroscopy. 108 (2008) 1653–8.

[17] S. Van Aert, J. Verbeeck, R. Erni, S. Bals, M. Luysberg, D. Van Dyck, et al., Quantitative atomic resolution mapping using high-angle annular dark field scanning transmission electron microscopy., Ultramicroscopy. 109 (2009) 1236–44.

[18] S. Van Aert, A. De Backer, G.T. Martinez, B. Goris, S. Bals, G. Van Tendeloo, et al., Procedure to count atoms with trustworthy single-atom sensitivity, Physical Review B. 87 (2013) 064107.

Chapter 7

Energy dispersive X-ray spectroscopy

As discussed in Chapter 2, energy dispersive X-ray (EDX) spectroscopy is the preferred method for chemically sensitive information about the heavier (higher Z-number) platinum group metal samples of the core-shell nanoparticles investigated in this work. In this chapter, point analysis of particles confirms the presence of platinum and palladium at specific points of the particle. From these initial observations, the feasibility of gaining quantitative compositional information from EDX is explored. The following is investigated:

- necessary parameters to consider in quantification
- experimental limitations of unstable, beam sensitive samples
- various potential sources of error

Then the feasibility of determining shell thickness is probed by taking line scans across particles. Next, the ways the microscope settings can be optimised to obtain maps of particle composition is presented. Finally, drawing these threads together, insights into and recommendations for the practicalities of setting up real world experiments, its limitations and how one could gain the most information from such samples using EDX is presented.

7.1 Usage of EDX for catalyst samples

While it would be possible to get a sense of the overall elemental distribution of Pt and Pd across a large number of particles with EDX, illuminating a large area in the case of this sample, is not an efficient, or in fact, sensible use of microscope time. The loading of the particles on the support is very low (see Figure 7.1). This would make a broad view EDX map very inefficient and time consuming in order to generate and collect enough X-rays to get a sense of the composition of the sample. Instead, the real power of STEM-EDX in an aberration corrected instrument is in being able to map the distribution of different elements within a single nanoparticle at high spatial resolution.

The characteristic X-rays usually used for quantification in this and following chapters are the Pd $L_{\alpha 1}$ line at 2.84keV and the $L_{\beta 1}$ line at 2.99keV; and the Pt M_{α} line at 2.05keV, Pt $L_{\alpha 1}$ at 9.44keV and $L_{\beta 1}$ at 11.07keV. Others higher in energy also exist (see section 2.7) but are less likely to be generated and thus have poorer count statistics.

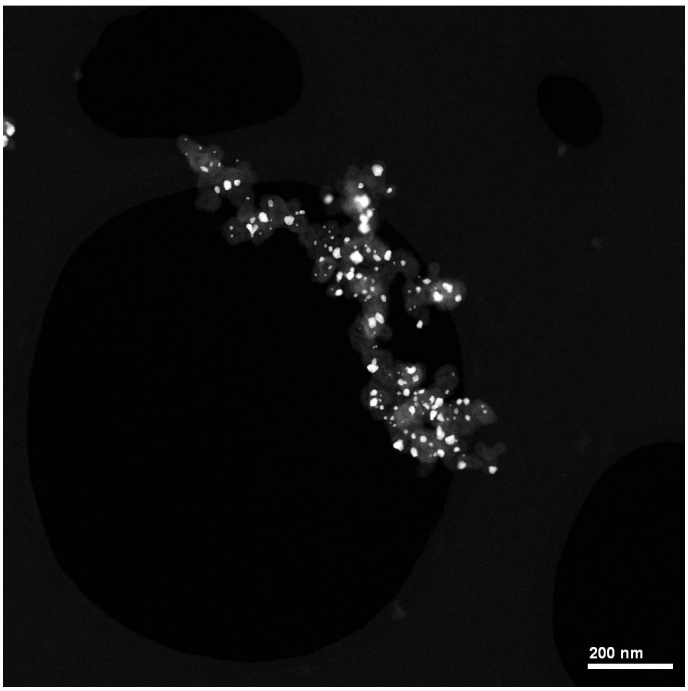

Figure 7.1 low magnification HAADF image of a typical nanoparticle catalyst sample on a holy carbon TEM grid. The heavy Pt and Pd particles show up strongly against the carbon black support and the carbon film of the grid. The loading of the particles is not very dense within the carbon black support in this instance. Moreover, the sample preparation process breaks up the clusters of carbon supported particles into small areas, which is optimal for studying single particles.

7.2 Presence of Pt and Pd by point analysis

The quickest way to confirm the presence of elements within a sample, across various particles or at a specific area of interest, is to perform a point analysis by locating a stationary electron beam on a certain area. This provides a good sense of the composition at a single point and is often easy to accomplish to complement a high-resolution HAADF image. Using this mode, it is easy to establish the existence of core-shell morphology by comparing spectra obtained in the centre of a particle and near the edge, where a shell could be located (see Figure 7.2). From the spectra it is clear that there is both Pt and Pd in the edge of the particle; this suggests the presence of a Pt shell.

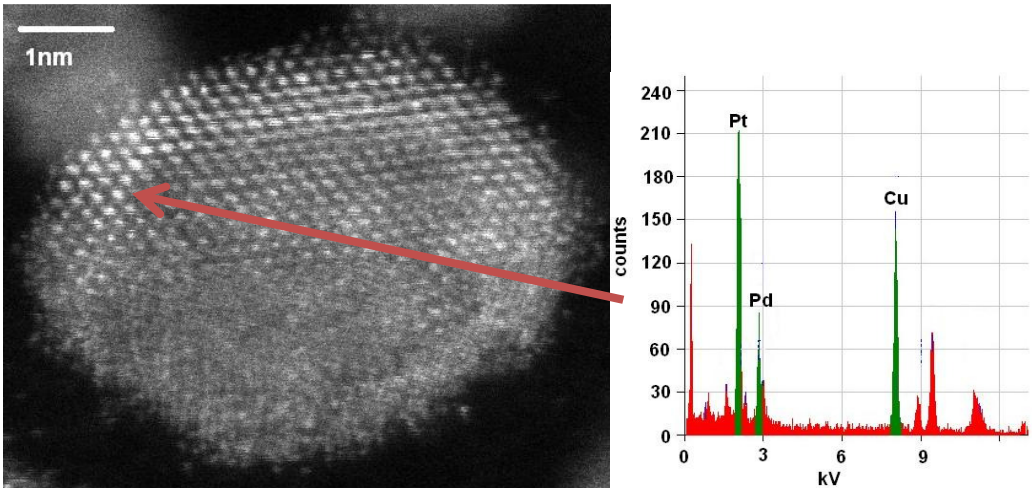

Figure 7.2 (left) particle under investigation, imaged at 200kV. (Right) the EDX spectrum from a point acquisition at the specified point on the particle shows the presence of both Pt and Pd at the shell area. The Cu peak is from the copper of the TEM sample grid. Experiment performed on the Oxford-JEOL 2200MCO with a probe size of 1nm and probe current of 600pA.

Alternatively, a line scan can be performed where sequential spectra are taken across the profile of a particle to give a sense of the compositional variation (see Figure 7.3). The distribution of the Pd and Pt along the line clearly indicates a core shell structure. However, it is not possible to infer the ratios of composition without further quantitative analysis of the spectral data since there is not a one-to-one correspondence between the number of counts and the concentration of the element.

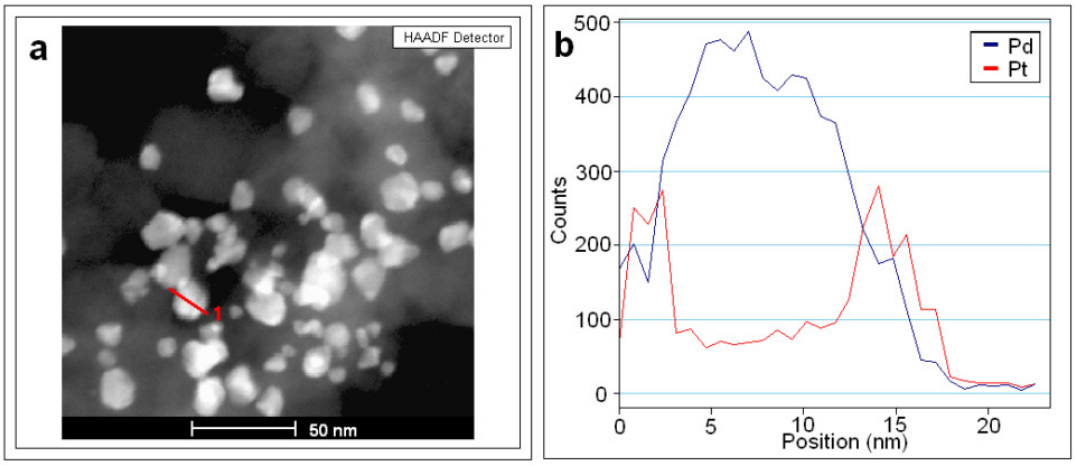

Figure 7.3 a) HAADF image of a cluster of 2ML design nanoparticles, **b)** EDX line profile taken across the nanoparticle marked in red in (a). A clear core-shell structure can be seen. Data taken with an FEI Tecnai F20 at Johnson Matthey Technology Centre at 200kV with a 1nm probe of current 0.6nA. The EDX detector is Si(Li) with a Be window and a solid angle of 0.13 steradians. The linescan was performed with a dwell time of 10s per point.

7.3 Quantification

While point analysis clearly shows the presence of the elements we are investigating, it is more interesting to explore the ratio of elements present in order to gain a quantitative picture of the distribution of Pt and Pd across the particle and obtain catalytically relevant information about the coverage and thickness of the Pt shell.

Most commonly, the concentration of an element in a material is of interest. In this thesis the mass or weight fraction is used for composition (C_{weight} measured in units of kg/nm^3) and converted to the number concentration for use when modelling atomic structures. The software packages that come with modern microscopes, which are used to perform quantification of EDX spectra, are often "black-boxes". The method of quantification and how it is applied is often not clear.

In samples where the generation of X-rays is not efficient and the count rates are likely to be very low, the sensitivity of various factors, such as the way the peaks are integrated, or the way the background is subtracted, becomes crucial in determining the final calculated element ratios. Further, the method of calculating the ratio of element concentrations inherently has sources of error and needs to be well understood. With such thin samples as nanoparticles, it is possible to assume that there is negligible

fluorescence and absorption [1]. Thus applying the standard Cliff-Lorimer ratio method is a feasible approximation. Throughout the following work, theoretical k-factors from the Digital Micrograph software-packages are used, unless otherwise stated. In section 7.9, the accuracy of quantification is explored.

7.3.1 Attributing X-ray counts to specific energy peaks

There is necessarily some scatter in the energies measured with each characteristic X-ray emission. This can be due to various mechanisms:

- Loss of energy as X-rays pass through the sample
- Noise in the detector channels
- Errors in attributing the detected X-ray to a specific energy

This leads to a spread in the signal in the form of a non-delta function peak at the transition energy of the particular characteristic energy (see Figure 7.3). A careful and systematic method of peak integration is therefore needed to determine the number of counts taken into account for the quantification.

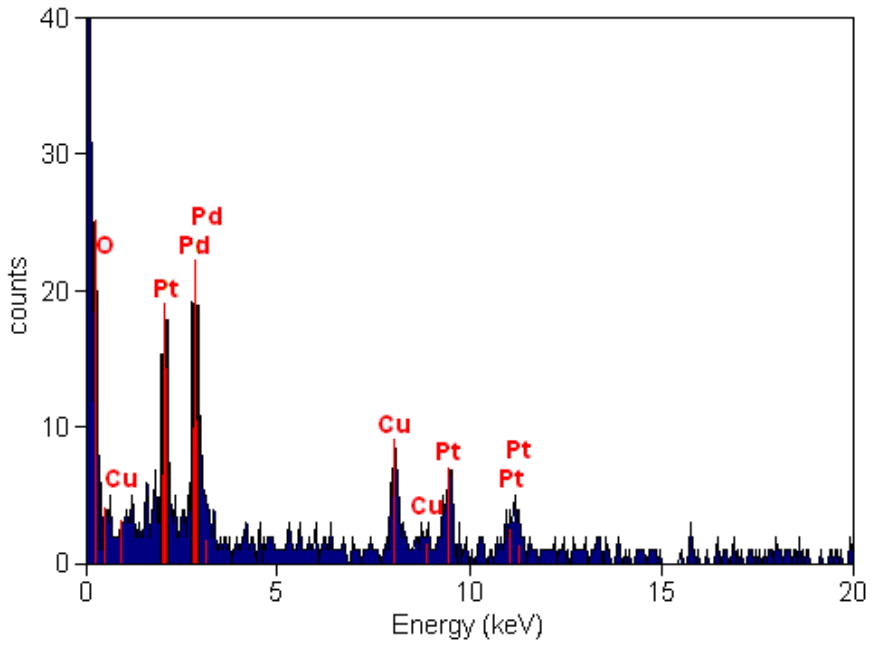

Figure 7.4 Typical EDX spectrum showing non-delta function peaks and background noise.

7.3.2 Background subtraction

The background due to Bremsstrahlung, discussed in section 2.7.1, needs to be effectively subtracted from the characteristic peaks, as it is only the latter that is useful for quantification of the element under investigation. The shape and size of this background is largely dependent on the detector: its placement, orientation, window thickness and efficiency. Since the background is not constant but varies with the X-ray energy, a local background subtraction is necessary.

One approach would be to acquire a "control" spectrum from a nearby region, which does not have the elements of interest. However, this method is time consuming and, in the case of nanoparticles on thin carbon support, impractical.

Gatan's Digital Micrograph software allows for the conversion of EDX spectra to an EELS spectra format. The inbuilt software for background subtraction for EELS spectra can then be used. A smoothed interpolated curve fit from a manually selected window of background can be carried out using the software (See Figure 7.5). This approach is superior to subtracting a background found by

using a simple linear interpolation from the area neighbouring the characteristic peaks, and is the one used in all subsequent analysis unless otherwise stated.

7.4 Quantification techniques

Once the spectrum is processed for background and the counts integrated for each characteristic peak, it is necessary to find the cross-section for X-ray excitation by the electron beam for each element in the sample so a ratio of concentrations can be found.

7.4.1 Cliff-Lorimer k-factor

The Cliff Lorimer ratio method [2], as described in Section 2.8.1, is the most common way of quantifying the ratio of two elements from the integrated signal of two elements' characteristic peaks. Use of tabulated values for k-factors typically results in an uncertainty of about ±10%. Experimentally determined k-factors, determined from a sample of precisely known composition, offer the best handle on error for a particular instrument and microscope conditions, with errors down to as low as ±1%.

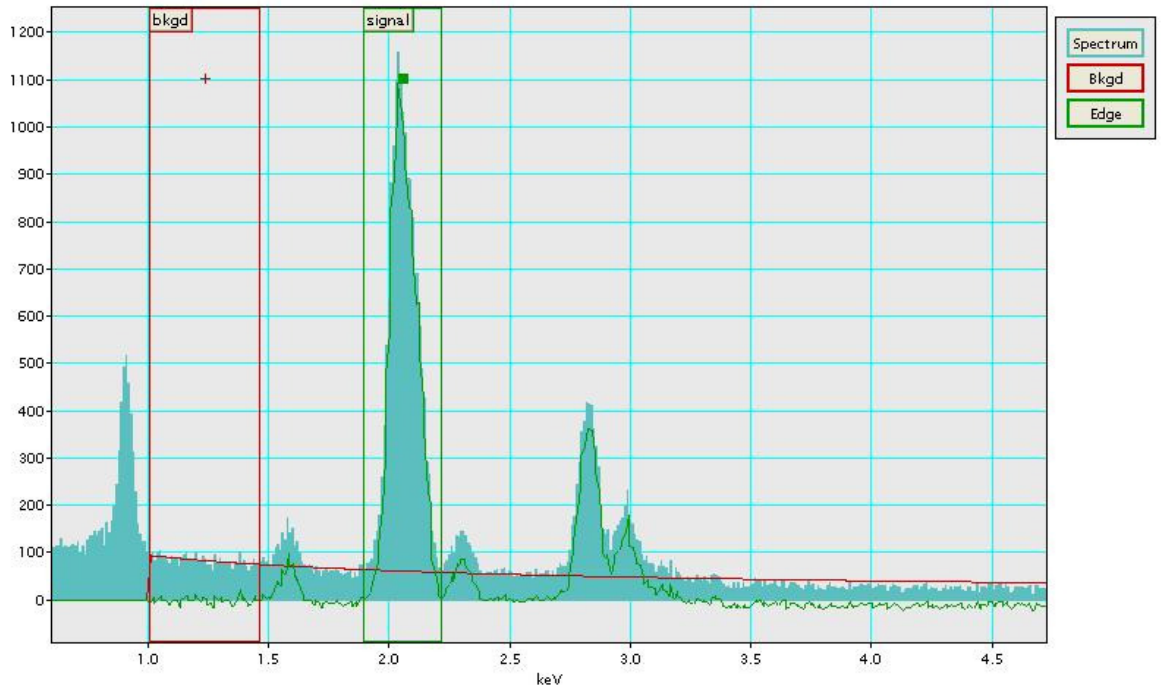

Figure 7.5 Background subtraction for a Pt M edge using the "Convert to EELS spectrum" method. The signal in the manually selected background (red window, labelled "Bkgd") is used to extrapolate a curve for the background in the peak area to its right (green window, labelled "Edge"). The background corrected spectrum is shown superposed as a green line. This data is taken from the particles presented in Section 6.7.3.

7.4.2 ζ-factor

As discussed in section 2.8.2, quantification using the ζ-factor [3], which can be measured from a pure element standard using a probe of known current, removes the requirement for a standard with a known composition.

By comparing the intensity of the peaks from two different mass thicknesses under the same experimental conditions, the ζ-factor for an element A can be calculated simply by:

$$\zeta_A = \rho N_e I_{probe} \tau \frac{(t_1 - t_2)}{(I_1 - I_2)} \qquad 7.1$$

where ρt is the mass thickness of the sample with the thickness taken at two points 1 and 2. N_e is the number of electrons in the unit electron charge[1], I_{probe} and τ are the beam currents and acquisition times and I is the intensity of the X-ray peak for the element A from spectra collected at each of the two thicknesses 1 and 2.

This expression (derived in Appendix H) is sufficient for thin samples where the effects of absorption and fluorescence can be ignored [4][2].

Once a ζ-factor is known for both elements, the concentration can be determined using the relationship:

$$\rho t = \frac{\zeta_A I_A + \zeta_B I_B}{D_e} \qquad 7.2$$

where

$$C_A = \frac{\zeta_A I_A}{\zeta_A I_A + \zeta_B I_B} \qquad 7.3$$

$$C_B = \frac{\zeta_B I_B}{\zeta_A I_A + \zeta_B I_B} \qquad 7.4$$

so long as $C_A + C_B = 1$.

A wedge shape sample with a 1° angle was fabricated by Sergio Lozano-Perez from a Pd wire using a FEI FIB200 focussed ion beam and attached to a TEM grid. An EDX line spectrum was collected across various thicknesses (see Figure 7.6) with a 1nA probe in the JEOL 3000F and 60s dwell time per point. This was repeated for a Pt wire sample (see Figure 7.8).

The relative thickness was calculated by the simple geometric relation of distance from the edge of the sample to the position of the probe *x,* by $t = x \,.\sin\theta$, where $\theta = 1^o$. The ζ-factor calculated from the

[1] This is simply 1/e, the elementary charge, = 6.24 x 10^{18}

[2] For cases where absorption and fluorescence is an issue, a modification of the equation is necessary and an iterative approach is needed to reach a converged solution.

inverse of the gradient[3] of a plot of the thickness and the counts from a particular peak (see Figures 7.7 and 7.9). The Pd $L_{\alpha 1}$ and Pt M_{α} peaks were chosen for their strengths and ease of identification.

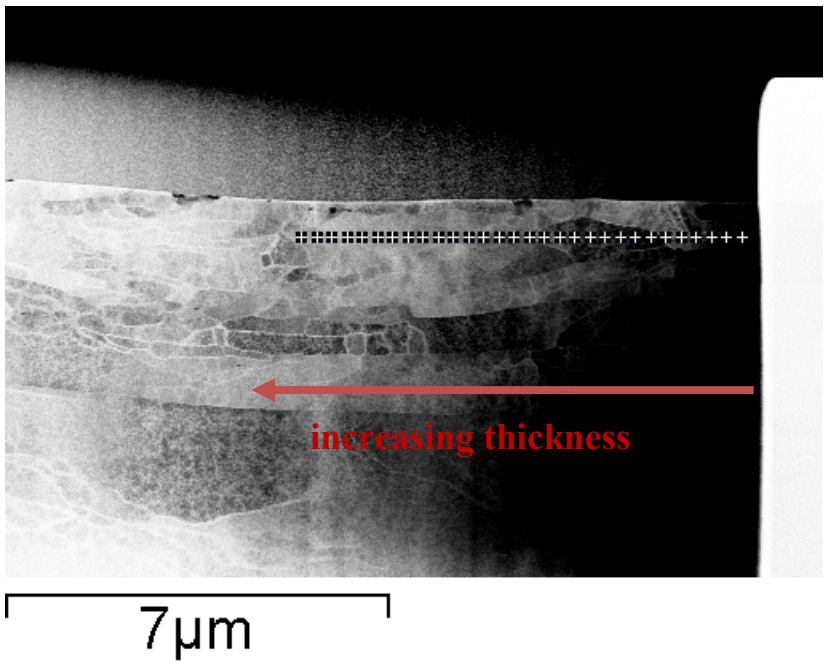

Figure 7.6 HAADF image of the Pd wedge sample showing the probe positions where EDX data was collected

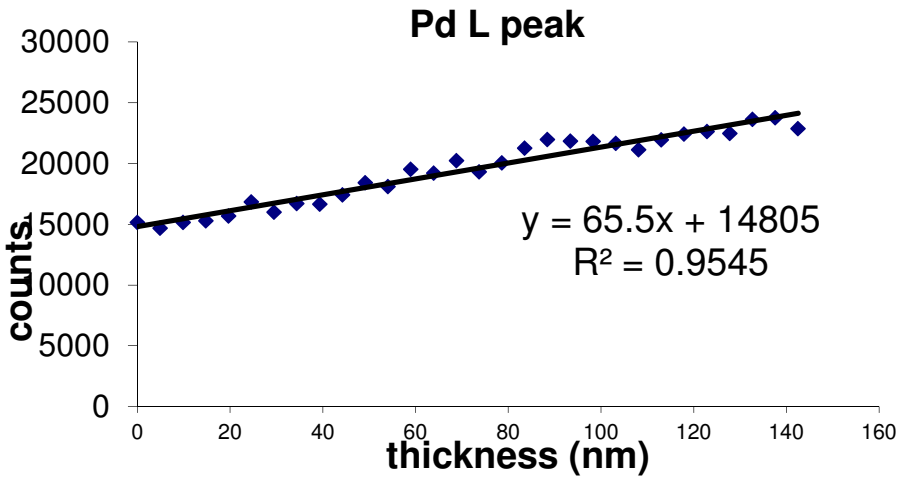

Figure 7.7 Plot of count intensity from the Pd L peak of the line scan of the Pd wedge.

[3] Where the gradient is $\frac{(I_1-I_2)}{(t_1-t_2)}$.

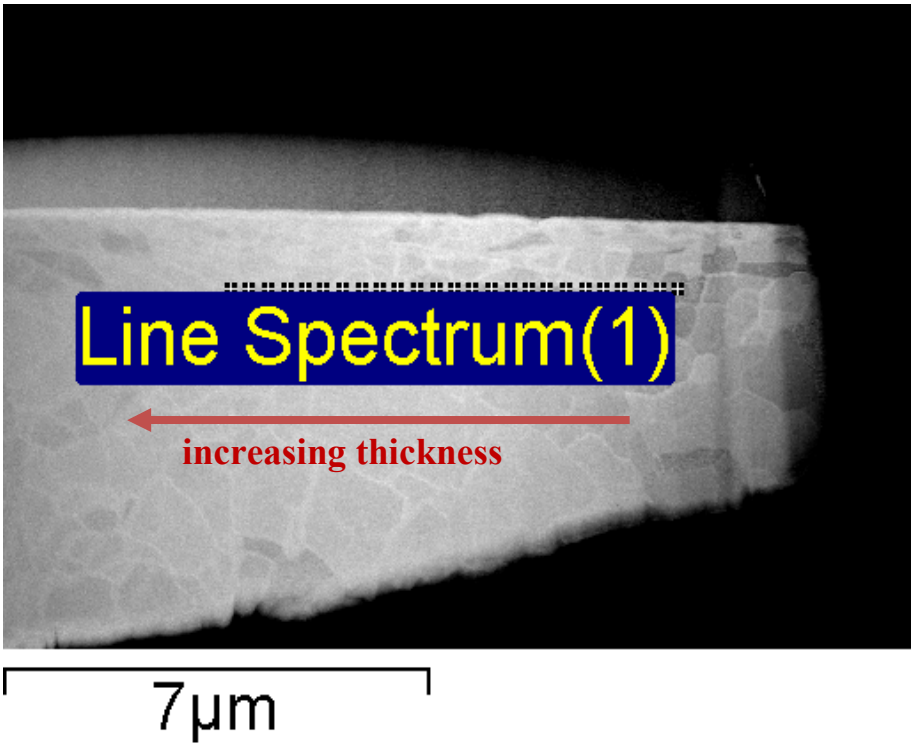

Figure 7.8 HAADF image of the Pt wedge sample showing the probe positions where EDX data was collected

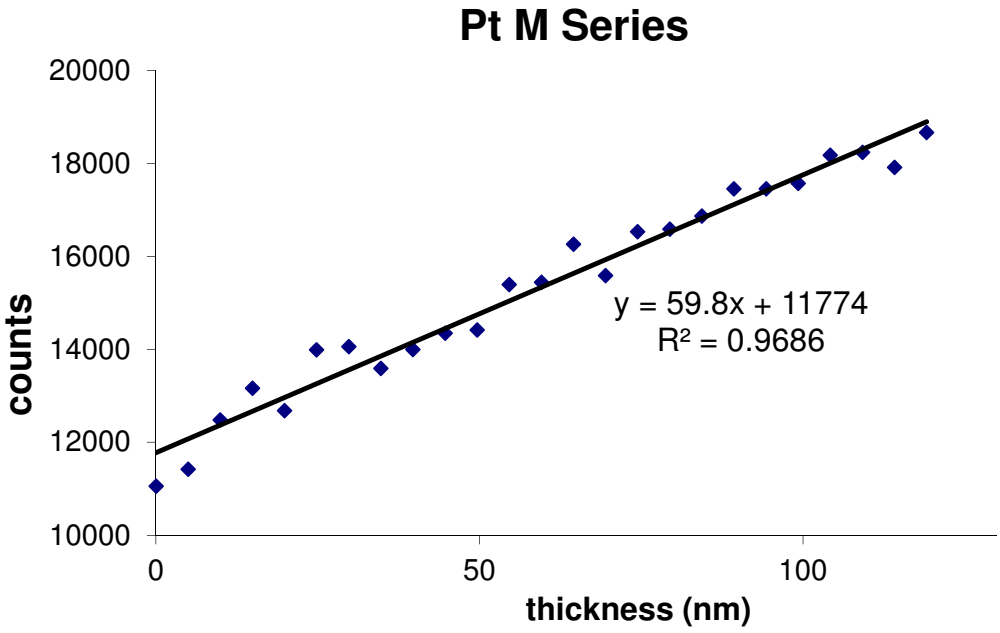

Figure 7.9 Plot of count intensity from the Pt M peak of the line scan of the Pt wedge

The ζ-factors for the Oxford JEOL 3000F are:

	ρ (kg/m^3)	ζ-factor
Pd	12,020	6.87 x 10^{13}
Pt	21,450	7.53 x 10^{13}

Table 7.1 Density and calculated ζ-factor of Pd and Pt for the JEOL 3000F microscope.

Unfortunately, the pure element samples were not available to characterise the detectors on the Oxford JEOL 2200MCO or the ARM-200F so tabulated theoretical Cliff-Lorimer k-factors from the INCA software are used in the quantification of data from those microscopes.

7.4.3 Comparison of ζ-factor and Cliff-Lorimer

A line scan was performed in the JEOL 3000F of a 2ML design nanoparticle (see Figure 7.10) with 10 positions in order to compare the two different quantification methods: the theoretical Cliff-Lorimer k-factors in the INCA software and the ζ-factor method described in Section 7.4.1. The probe current was 400pA and probe size was 3Å. The dwell time was 60s per pixel. The L_α peaks for both Pt and Pd were used for both methods.

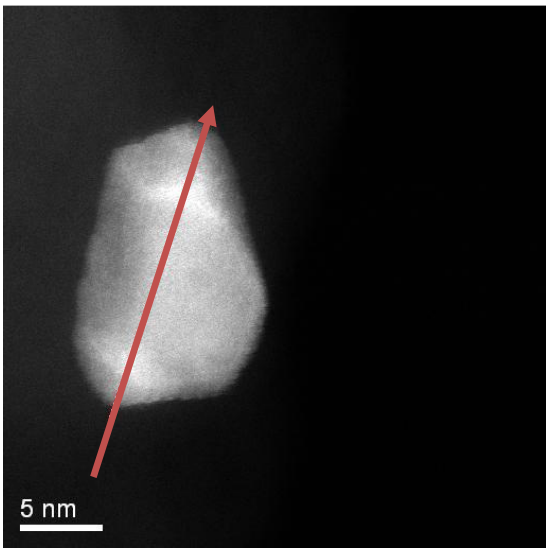

Figure 7.10 Line scan of a 2ML design nanoparticle (marked in red).

It can be seen in Figure 7.11 that both methods give a similar estimation of the general trend, confirming the core-shell structure, the Cliff-Lorimer method overestimates the concentration of the Pt by up to 5%. This is however, not a significant deviation given the paucity of detected signal (counts of the order of 40 – 80 for Pt), the error due to shot noise is 16% for the spectrum with the largest difference in quantification.

In this case, the usage of the ζ-factor method does not greatly improve the accuracy of quantification over the use of software standard theoretical k-factors, even with their assumed error of 10%. The challenge of acquiring sufficient signal to justify the validity of any quantification is of chief concern.

7.5 Quantifying errors and limitations

The two main sources of error are count statistics and the error in the method used to determine the concentration ratio of two identified X-ray peaks. The errors for a relation such as the Cliff-Lorimer equation are combined in quadrature since the variables are independent. Assuming Poisson statistics for the shot noise error in counting X-rays, the number of counts necessary such that the error in the k-factor dominates can be calculated (see Figure 7.12). The results are shown in Table 7.2.

While there is poor signal to noise due to count rates lower than 500 per integrated peak, the theoretical k-factors, with an error of 10%, are a sufficiently good approximation to the true k-factors or the ζ-factor. With better statistics, the method of determining the concentration ratio needs to be carefully calibrated with standards of known composition (for k-factors) or pure element with thickness variation (for the ζ-factors).

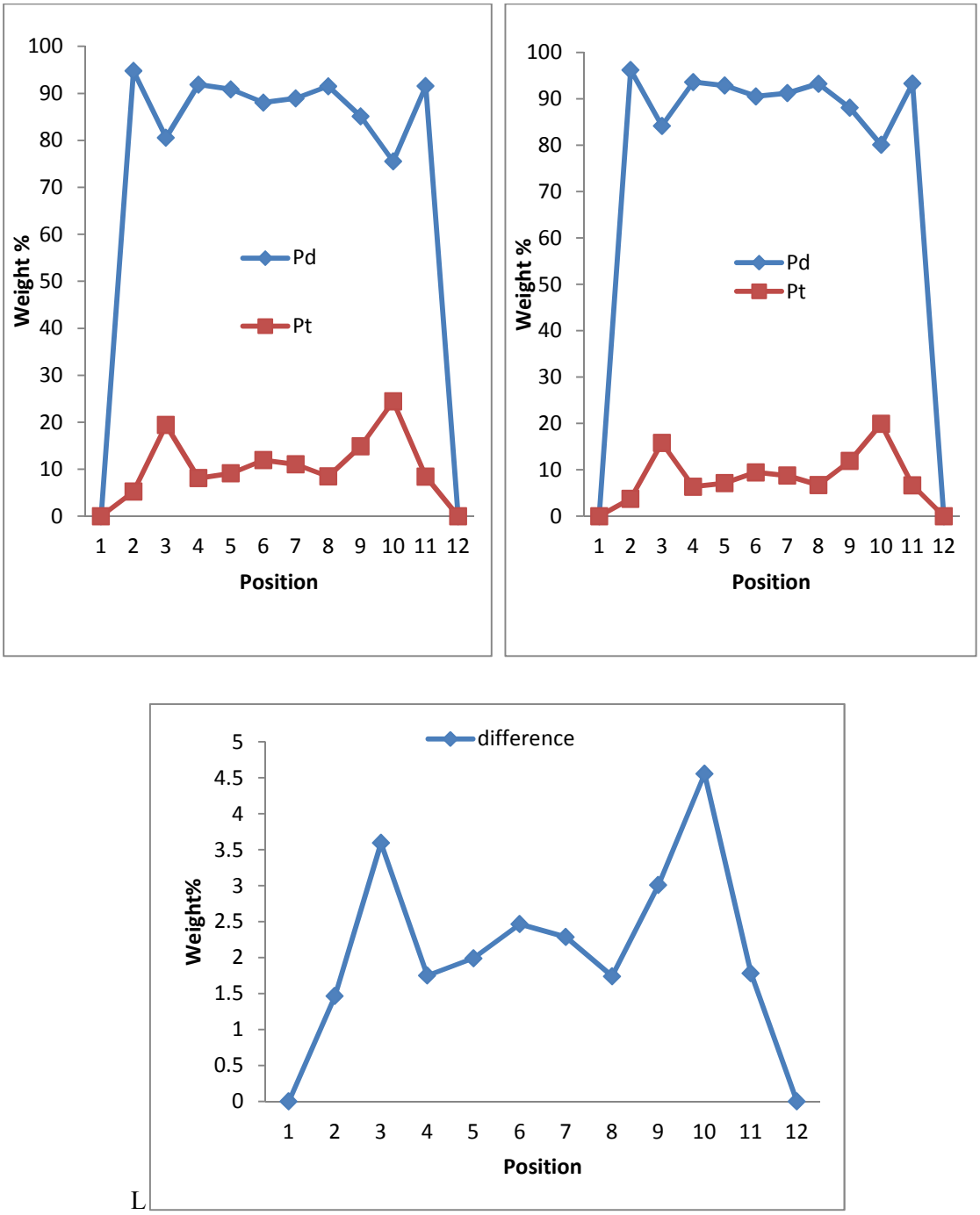

L

Figure 7.11 Quantification of the line spectrum in Figure 7.10 using a theoretical Cliff-Lorimer k-factors (left) and the ζ-factor (right). The difference shows an overestimation of the concentration of the Pt in the Cliff-Lorimer case of up to 5% (bottom). Note that the Pt signal peaks inside the particle boundaries, further suggesting edge decoration and not complete shell coverage.

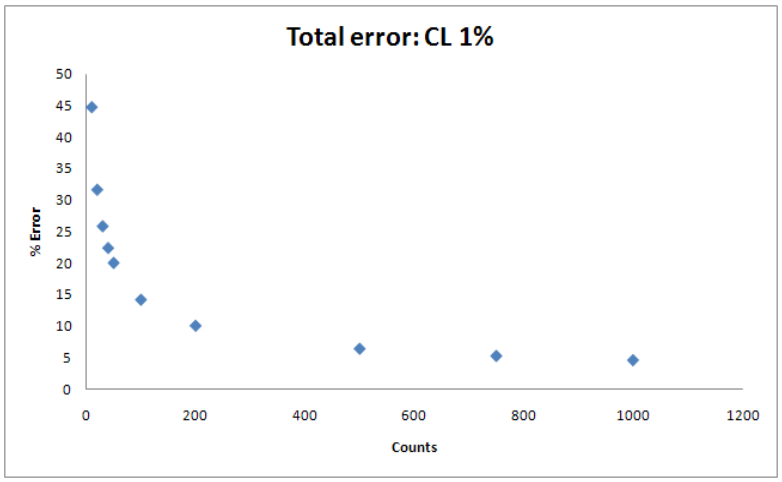

Figure 7.12 Total error in the concentration calculated by the Cliff-Lorimer ratio, given an error in the k-factor of 1% (right), as a function of the number of counts detected.

k-factor error %	Number of counts
20	200
10	500
1	1000

Table 7.2 Number of counts needed such that the error in the k-factor dominates over the shot noise.

7.6 The problem of signal

The other major source of error in quantification of nanoparticles is that of low count rates and poor signal to noise. The trade-off necessary with a high spatial resolution probe for HAADF imaging and also chemical analysis is that the number of X-rays generated and thus collected is severely limited. The extremely small interaction volume of the fine probe with a thin sample of a few nanometres restricts generation. Probe sizes are typically on the scale of one or two nanometres or less. Thus the interaction volume is typically on the scale of 10 nm^3; this volume is 9 orders of magnitude smaller than the interaction volume typical in lower resolution bulk material techniques such as SEM.

Assuming that the probability of X-rays being generated by the beam-sample interaction and detected by the detector in a given time frame of acquisition, τ, follows a Poisson distribution (i.e. the events occur with a known average rate, and independently of the time since the last event), the shot noise level is simply *square root* of the signal collected. Thus, increasing the number of X-rays collected significantly decreases the intrinsic statistical error on the measurement. The poor statistics generated from such small samples means that quantification to an acceptable level of accuracy is difficult.

To increase the amount of X-rays collected for a given sample, the following parameters could be varied:

- Probe current (i.e. the number of incident electrons which could generate an emitted X-ray)
- Sample geometry (optimised to minimise obstructions in the flight path of X-rays to the detector)
- Detector geometry (efficiency of collection due to the placement of the detector)
- Acquisition time (decomposed into dwell time and multiple scans)
- Accelerating voltage (lower accelerating voltages increase the cross section of ionisation, as discussed in Section 2.7)

Each comes with benefits and drawbacks for nanoparticle samples and the capabilities of available microscopes. The optimal conditions for the best count statistics for such beam sensitive samples requires careful balance between many competing factors.

7.6.1 Probe current

Increasing the probe current is the most accessible way of increasing the number of incident ionizing electrons on the sample, therefore increasing the number of possible generated X-rays. Typical currents for nano-analysis in TEM can be as high as 1nA, two orders of magnitude greater than the current typically used for high resolution HAADF imaging. However, increasing the current also brings a greater probability of damage to the sample. This is especially an issue for beam sensitive specimens such as nanoparticles.

On most modern microscopes, the most practical way of achieving a higher probe current is either to use a larger probe-forming aperture or to decrease the demagnification of the probe by weakening the

C1 lens just below the gun and balancing this by adjusting the C3 lens just below the gun. This is often simply accomplished by changing the "spot size" in STEM mode, which loads pre-set lens settings. Both these methods create a larger electron probe, which results in a lower possible lateral spatial resolution. Alternatively, it is possible on a cold-FEG microscope (such as the JEOL JEM ARM-200F) to increase the extraction voltage from the gun. This creates a larger current without compromising the spatial resolution achievable by having a larger probe.

7.6.2 Be-holder and sample geometry

The design of most conventional sample holders limits the collection of generated X-rays. The sides of the Be holder surrounding the sample grid area is removed to allow more of the generated to reach the detector. Tilting the sample holder 10° in the x-direction on most microscopes angles the sample towards the EDX detector. This greatly increases the number of X-rays collected as the sample holder blocks fewer X-rays.

The lacy carbon coated copper grid itself has intrinsic geometry considerations. Depositing the sample on top of the carbon film and then orienting the sample grid such that the carbon film is facing up towards the incoming beam minimises the number of generated X-rays being blocked by the grid itself.

7.6.3 Detector geometry

The physical requirements of the instrument design necessary for high spatial resolution limits the detector geometry: the short focal length necessary for the objective lens to operate at such conditions means that the distance to the sample is necessarily small. Thus the high-resolution objective lens pole-piece has a relatively small gap, which restricts the possible physical size of the X-ray detector and also the proportion of X-rays that can escape the pole-piece area to be detected.

Since the pole-piece is a fixed part of the instrument and cannot be readily changed, the capabilities of a microscope have often been biased towards high-resolution imaging. Since X-rays generated within the sample are scattered isotropically, there is no preferential direction of scatter. However, EDX

detectors are typically positioned in only one direction relative to the sample and can only be a finite distance away from the pole-piece, the solid angle of collection is limited. Until a few years ago, they typically only subtend a solid angle of approximately 0.3 steradians in the best case. This means that only up to 1% of all emitted X-rays are ever collected since only those X-rays that directly enter the detector count towards the acquired spectrum.

Recent improvements in electronics have allowed up to 4 separate detectors to be placed around the pole piece in some instruments such as the Super-X detector on the FEI Chemi-STEM microscopes. The signal is integrated into the computer software to create a single spectrum, which effectively increases the solid angle by a factor of 4, giving up to 0.88 steradians. This however, still only accounts for up to 7% of total emitted X-rays[4].

7.6.4 Acquisition time

Increasing the dwell time increases the number of incident electrons on the sample and thus proportionally the number of generated X-rays. However, since increasing the dwell time also increases the probability of damage to the sample, this is often not a useful method of increasing the count rate since nanoparticles are extremely beam sensitive. In addition, sample drift is a common problem with long dwell times since the drift correction software requires the shift of the beam to another location.

Figure 7.13 shows the damage done to a particle by performing a simple line scan with a dwell time of 60s per pixel. The probe was 3Å in size and had a beam current of 1nA and the accelerating voltage of the JEOL 2200 MCO was 200kV. The beam has left a clear mark on the sample, such that it is not possible to tell whether the composition of the area under investigation is still the same after beam exposure.

[4] 0.88 steradians / 4π steradians

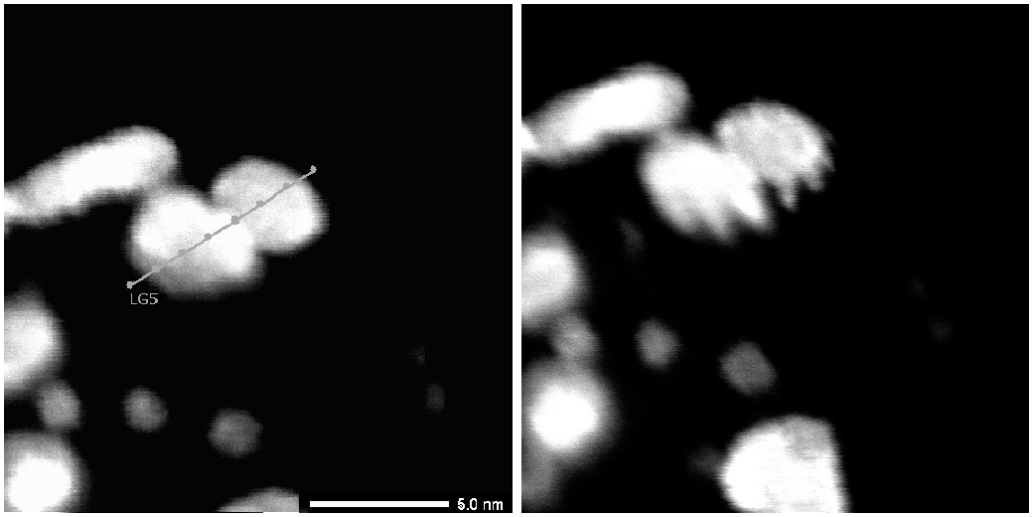

Figure **7.13** A line scan of a particle (left) with an acquisition time of 60s at 1nA, combined with sample drift has destroyed the particle (right), leaving a trail of material in the path of the beam.

Since prolonged exposure of the sample to a stationary beam causes significant damage, constantly moving the beam is a natural alternative. Using short dwell times and repeating the scan over several acquisitions while drift correction software ensures that the same area is being covered on each repeat scan is now possible with the improved beam control capabilities offered by microscope manufacturers.

7.7 Sample-related stability

Since the most easily increased source of X-rays comes from the acquisition of a spectrum over an extended period of time or over multiple scans of the same area, this requires the stability of the sample in location, orientation and configuration for accurate structure determination. Several factors affect the feasibility of this stability. The three main concerns are:

- sample drift due to the microscope,
- the inherent sample stability,
- sample damage due to exposure to the electron beam

7.7.1 Sample drift

The drift of the sample away from the initial position means that the area of acquisition is constant with time. Thus attributing the X-rays to a specific part of the particle and consequently, the analysis of the composition of a specified area, is made very challenging. At the high magnifications necessary to investigate nanoparticles of a few nm, the stability of any mechanical stage is severely tested.

Specific methods of care can minimise the amount of movement. When winding the goniometer to a particular area for investigation, allowing the sample to settle reduces drift in the direction of stage movement. This directional drift can be exacerbated when movement around the grid is done quickly at low magnifications and the sample stage not allowed time to settle before magnification is increased. Some rewind in the opposite direction also aids the stage in settling.

Most modern microscopes come with EDX software that has drift correction capabilities. A HAADF image is used as a reference before an EDX scan. An area can be chosen as a reference for the drift correction, away from the area of interest for the EDX scan to minimise beam damage (see Figure 7.14).

The EDX acquisition is periodically halted so a new HAADF scan can be taken and a cross correlation yields an amount of movement that can be compensated for by the beam scan coils. However, this is obviously limited to a certain range as a cross correlation cannot be performed if the drift is too large or the scan coils run out of range of deflection. Thus the magnification of the initial scan needs to be chosen with care, as a lot of drift means that a lower magnification, and a larger field of view, would be necessary.

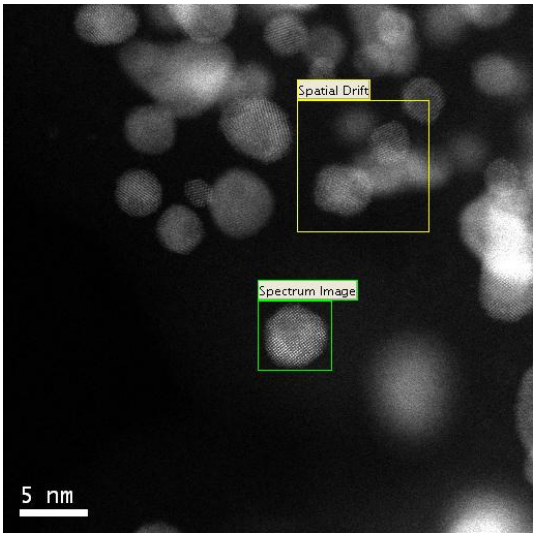

Figure 7.14 Spatial drift is corrected by taking a cross correlation of the area in the yellow box with a previous image of the same area. The calculated displacement is then fed into the scan coil deflectors to move the probe to the position commensurate with no sample drift.

7.7.2 Sample stability

As discussed in section 3.8.1, nanoparticles are inherently structurally unstable at these small dimensions. This presents a challenge for EDX as the long collection times necessary to acquire statistically significant spectra mean that it is possible for significant change to occur. This is worse for particles smaller than 5nm. Therefore, EDX analysis of smaller particles was in general avoided, unless the total dose is limited.

7.7.3 Sample damage

As explored in Section 3.8, nanoparticles of this size are extremely beam sensitive. EDX, with its large probe currents and longer acquisition times will necessarily damage the particles more.

Various techniques can be employed to minimise damage. Short dwell times coupled with sequential cycled scanning can give sufficiently long total acquisition times in order to produce adequate statistics. Essentially, this is the same as summing consecutive images for HAADF images and has been shown to be very effective in the acquisition of atomic resolution EELS data [5]

More recently, sub-pixel scanning has allowed the beam to be controlled and moved across the sample rapidly and continuously within a pixel, allowing dwell time to be increased while still letting the sample relax. This also circumvents worries of undersampling the specimen since a trade-off between total acquisition time and spatial resolution means that often the step sizes between probe positions is smaller than the Å-scale size of the probe, leaving large areas between probe points unilluminated.

Sample heating due to the prolonged exposure to the high current beam used for EDX analysis caused the particle in Figure 7.13 to reconstruct. The most obvious way of minimising this is by decreasing the inelastic scattering cross section by using the highest available voltage, however a lower accelerating voltage is beneficial for minimising knock-on damage and also increasing the count rates, so a balance needs to be struck.

7.8 Composition of catalyst designs

The amount of the raw materials that is used to make the nanoparticles of different designs is given in Table 7.3. The weight % W_A of element A can be converted to atomic % At_A using the formula:

$$At_A = \frac{W_A}{Amass_A \sum_i \left(\frac{W_i}{Amass_i}\right)} \times 100\% \qquad 7.6$$

where $Amass_A$ is the atomic mass of element A and $\sum_i \left(\frac{W_i}{A_{r_i}}\right)$ is the sum over all i elements in the sample.

	Weight%		Atomic%	
	Pt	**Pd**	**Pt**	**Pd**
Pd core	-	100	-	100
0.5 ML	31.2	68.8	19.8	80.2
1 ML	50.3	49.7	35.6	64.4
2 ML	65.0	35.0	50.3	49.7
4 ML	77.6	22.4	65.4	34.6

Table 7.3 Weight% and atomic% of the various designs on catalyst nanoparticles from the raw materials used in synthesis.

While the weight % is useful in the process of synthesis, the atomic % is of more interest in determining the composition and structure for a 3D model.

7.9 EDX spectrum imaging

Spectrum imaging (SI) is the collection of a map of an area of interest where each pixel is an individual EDX spectrum; a 3D data cube is built up, where the third dimension is an EDX spectrum. Since the probe is stopped at each pixel location to acquire the spectrum, the total amount of time required to perform a SI can be significant and on the order of hours.

7.9.1 Initial SI

A probe current of 75pA was used and the acquisition was cycled 20 times to build up counts while maintaining a short dwell time of 0.05s. In addition, to minimise damage, the accelerating voltage was dropped to 80kV, which conveniently also increases the ionisation cross section for a better EDX signal.

This combination of accelerating voltages, beam current, dwell time and acquisition setup resulted in no visible damage to the particle. However, because the resolution was not sufficient for atomic resolution, it is not possible to confirm this. It is always possible that there is some structural change or slight mass loss.

The extracted spectrum maps of the Pt M peak and Pd L peak were then analysed in Matlab using theoretical Cliff-Lorimer k-factors to produce composition maps (see Figure 7.15), showing quantitatively the distribution of Pt and Pd.

The particle is Pt rich, especially around the shell areas, with a total composition of Pt of 86.6±8.7% and 13.4±1.3% Pd, which is predominantly concentrated in the core. The uncertainty is due to the error in the Cliff-Lorimer ratio.

The concentration of Pt is 21.6% higher than expected from the design of the 2ML particle (see Table 7.3), which indicates that there is *more* Pt segregation on the shells than the originally designed 2ML.

The increased activity of these particles could be due to the heavier loading of Pt in combination with the catalytically sensitive edge decoration seen in Chapter 6.

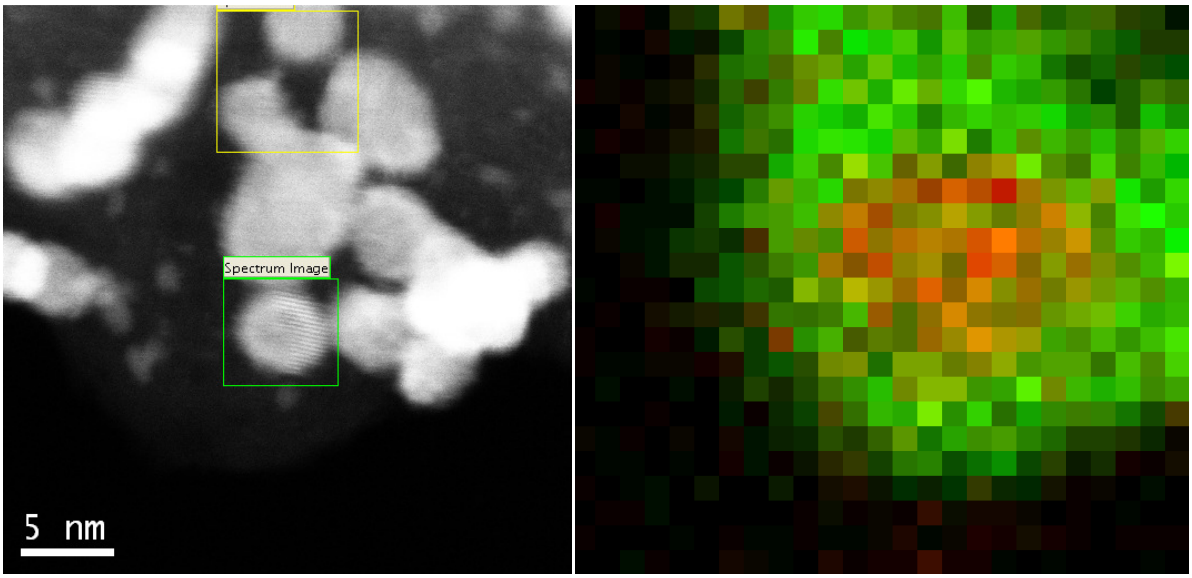

Figure 7.15 An area of interest scanned (green box) and spatial drift area (yellow box) are selected from a HAADF image (left). A RGB composite of the extracted Pt (green) and Pd (red) integrated peak values from a SI of a 2ML design nanoparticle using the Pt M peak and Pd L peak.

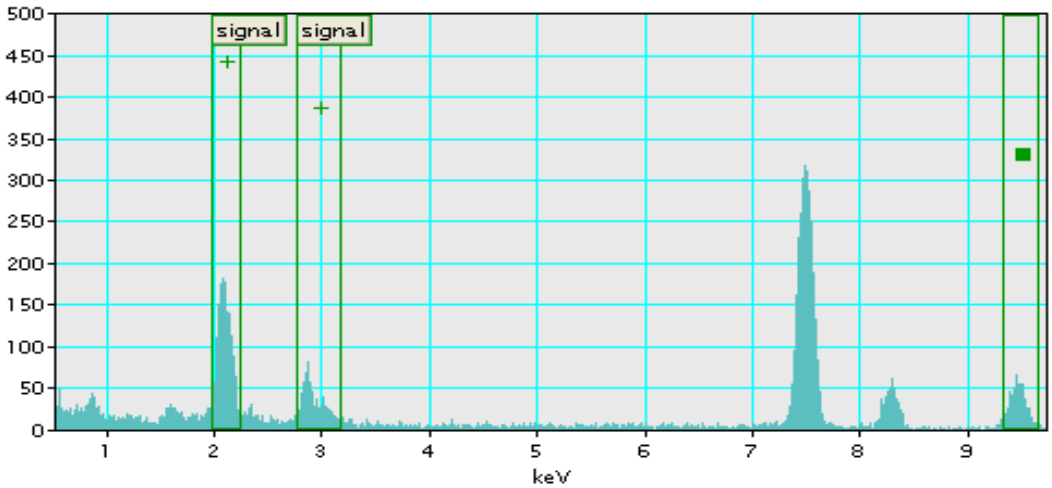

Figure 7.16 Cumulative spectrum from whole SI. A Cliff-Lorimer k-factor quantification using the inbuilt theoretical k-factors in DM give a concentration ration of 80±8% Pt to 20±2% Pd.

There is also the possibility that the large probe size, due to the decreased demagnification of the source to boost the beam current, has meant that the beam is scanning over the same area of Pt multiple times. However, since the atomic % (i.e. number of atoms) of Pt and Pd for 2ML is almost identical, any beam profile related extra scattering should equally affect the counts of both elements, which is not the case.

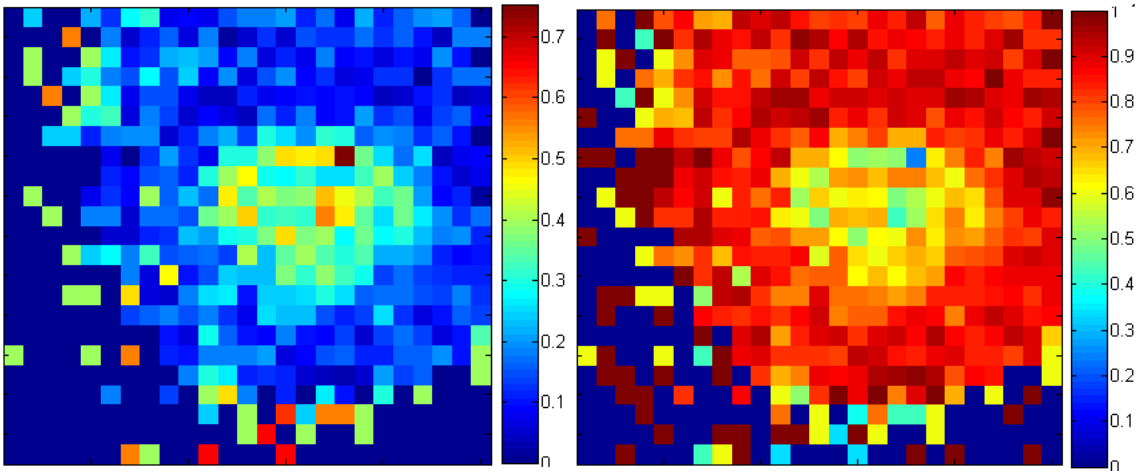

Figure 7.17 Pd concentration (left) and Pt concentration from a Cliff-Lorimer quantification using theoretical k-factors. The total concentration across the whole particle is 18.4±1.8% Pd and 81.6±8.2% Pt. The errors are due to the Cliff-Lorimer quantification technique.

The error in each pixel is significant, due to poor count statistics. Where the signal is as low as 15 in the core area of the Pt map and 2 in the shell area of the Pd map, the uncertainty can be as high as ±30% and ±70% of the pixel value. This dominates the Cliff-Lorimer error so quantification in those areas should be carefully considered.

7.9.2 Higher probe current

An alternative recipe for SI acquisition was tried, which also resulted in no visible damage to the particle. By keeping the same dwell time of 0.05s per pixel and collating only 5 cycles of the SI, the total acquisition time was reduced by a factor of 4. Increasing the current to 200pA scaled the count rate by a factor of 3. A 2ML particle was investigated at 80kV using these conditions (see Figure 7.17).

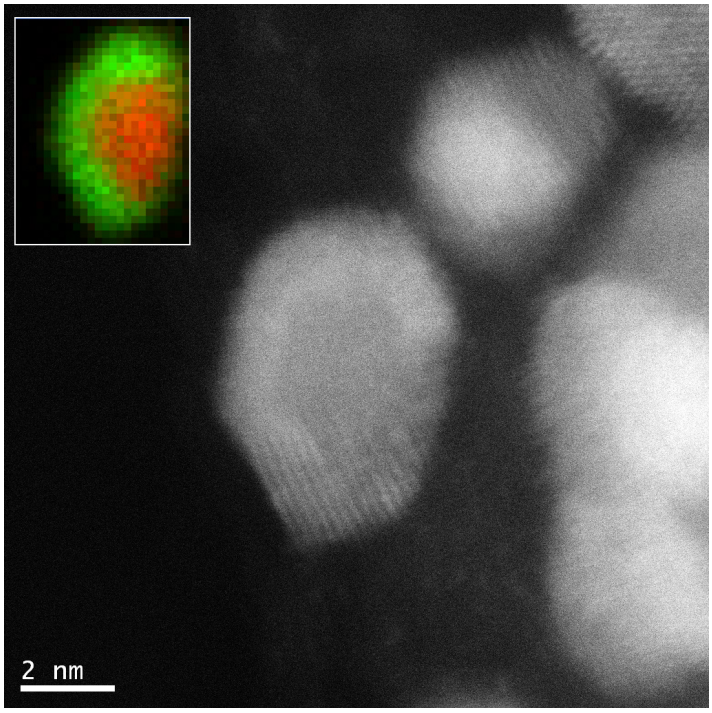

Figure 7.18 HAADF image of a 2ML design nanoparticle with clear core-shell structure. A RGB composite of the extracted Pt (green) and Pd (red) integrated peak values from a SI using the Pt M peak and Pd L peak (insert) confirms this.

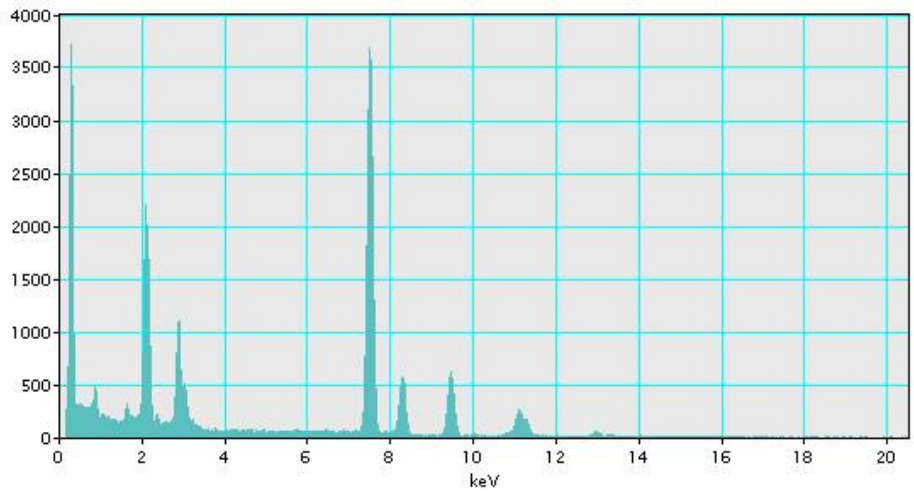

Figure 7.19 Cumulative spectrum from whole SI from Figure 7.17 (inset)

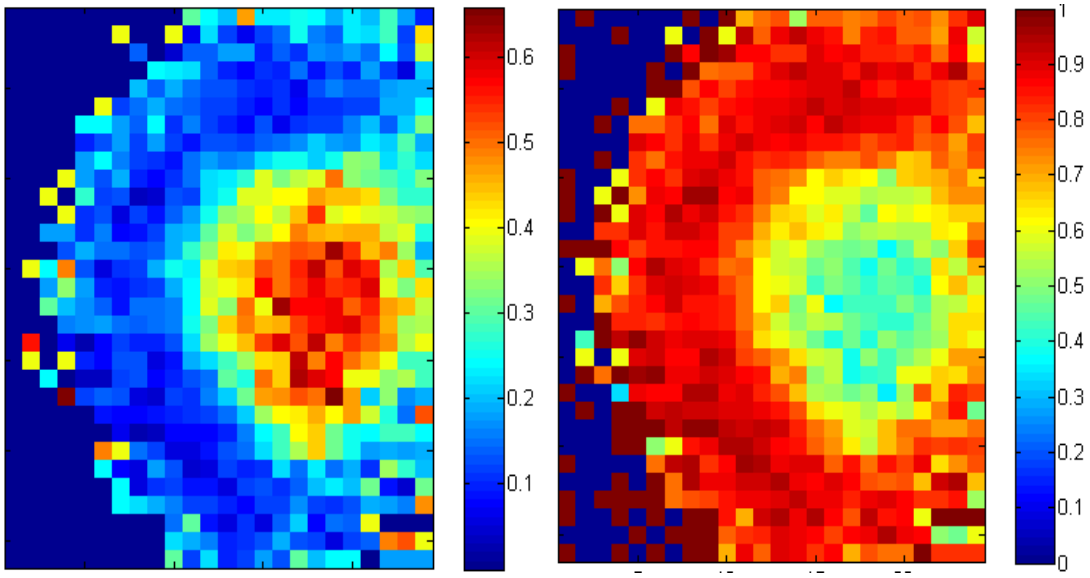

Figure 7.20 Pd concentration (left) and Pt concentration from a Cliff-Lorimer quantification using theoretical k-factors. The average concentration across the whole particle is 22.5±2.3% Pd and 77.5±7.8% Pt, errors due predominantly to the Cliff-Lorimer quantification. Uncertainty in each pixel of high concentration is ±13% of pixel value. Areas of low concentration have much higher uncertainty due to poor count statistics.

A similar result can be seen, whereby the loading of the Pt is higher than expected given the shell design. Moreover, since the weight % of the raw materials was calculated to give full shell coverage, the absence of Pt from one side of the particle (see Figures 7.17 and 7.20) would mean that the loading on the shell like areas is even higher.

The elongated profile and non-uniform shell coverage of the nanoparticle can be easily understood from the synthesis methods; the visible Pd core is supported on one side in the carbon and thus cannot be coated on that side with deposited Pt.

7.9.3 Higher solid angle detector

The following experiment was performed at 80kV and using a Centurio detector, which has a collection solid angle of 0.8sr. This dramatically increases the counts detected and thus gives better signal to noise (see Table 7.3), even without cycling the scan. The higher than expected concentration of Pt in the particle, particular on the shell, is once again seen here.

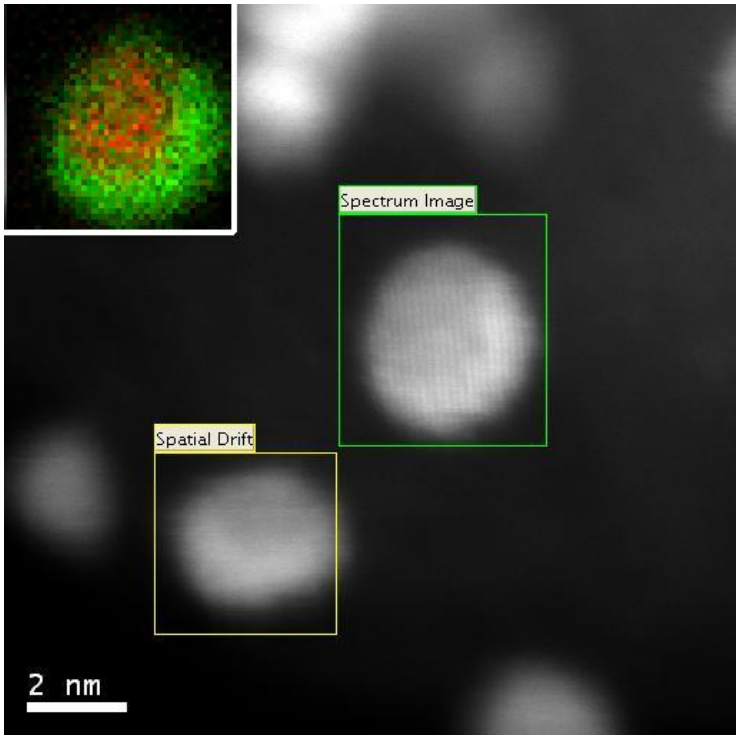

Figure 7.21 HAADF image of a 2ML design nanoparticle with clear core-shell structure. A RGB composite of the extracted Pt (green) and Pd (red) integrated peak values from a SI using the Pt M peak and Pd L peak (insert) confirms this.

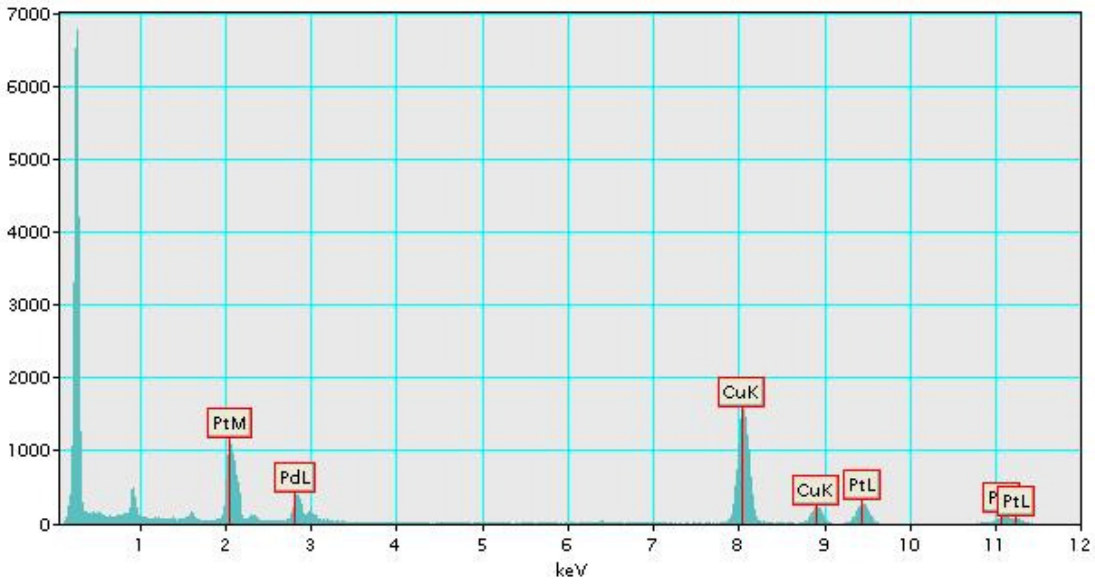

Figure 7.22 Cumulative spectrum from the whole SI from Figure 7.21 (inset).

		Energy Windows /keV		Counts		
X-ray peak		**Background**	**Peak**	**Subtracted Background**	**Corrected Peak**	**Difference between background and peak /%**
Pt	M_α	0.98 – 1.52	1.89 – 2.22	2,185	14,183	13
	L_α	9.05 – 9.25	9.26 – 9.65	326	16	95
	L_β	9.63 – 10.69	10.73 – 11.47	956	9014	10
Pd	L_α	2.40 – 2.58	2.71 – 2.92	1,050	3,864	21
	L_β	2.40 – 2.58	2.92 – 3.09	771	1,623	21

Table 7.4 Background subtraction using the convert to EELS method. The background accounts for typically 10 – 20 % of the total counts integrated for a characteristic peak. For smaller signals, this can be up to 95% of the raw data. For the spectra, see Appendix J.

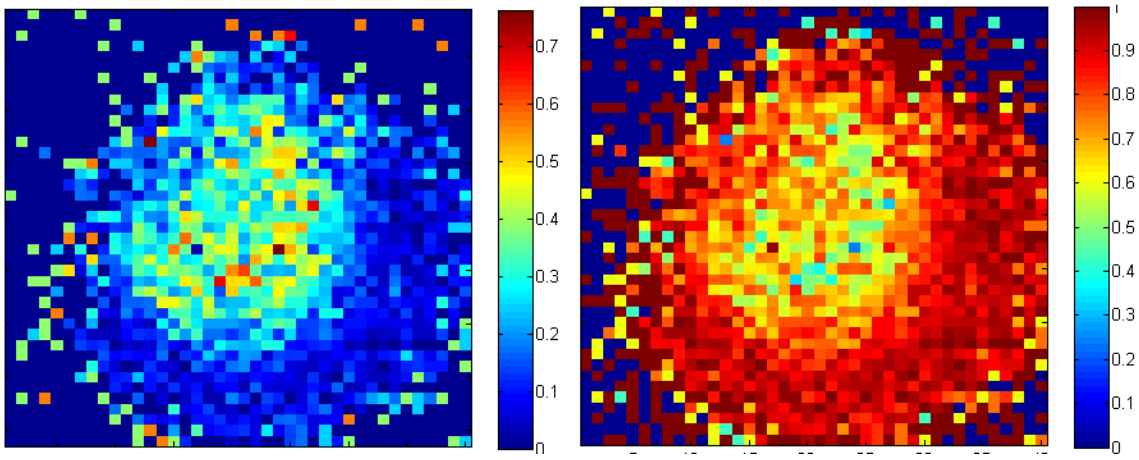

Figure 7.23 Pd concentration (left) and Pt concentration from a Cliff-Lorimer quantification using theoretical k-factors. The average concentration across the whole particle is 16.3±1.6% Pd and 83.7±8.4% Pt. The error in each pixel is on the order of ±20% in the high concentration areas.

Multivariate statistical analysis was carried out on the SI data in order to improve the signal to noise. However, because there were too many pixels which contained very poor signal (one or two counts) above the noise, the PCA algorithm did not show its full potential.

7.10 Optimum parameters for EDX of nanoparticles

Drawing on all the experimental data, it is possible to project what the optimal parameters are for error minimisation. Once the ζ-factor or k-factor error is minimised by various means, the experimental parameters need to be optimised in order to potentially achieve atomic resolution EDX for nanoparticles.

Given that detector efficiency, accelerating voltage, pixel dwell time and probe currents are difficult to vary for hardware of sample sensitivity issues, the only recourse left is to vary the acquisition time. For the limiting case of optimum hardware (low accelerating voltage, less than 200pA of beam current, shortest possible dwell time, subpixel scanning, as large a solid angle of collection for the detector as possible), the relative error in identifying 1 atom, 10 atoms and 100 atoms from an individual spectrum can be seen in figure 7.25. The outlook is fairly bleak for SI to achieve atom by atom sensitivity at 20% error, since for a single spectrum, acquisition needs to be on the order of hundreds of seconds. A full SI of only 10 x 10 pixels, at 800s per pixel, would require 22 hours; a nanoparticle is unlikely to remain undamaged for that period of time.

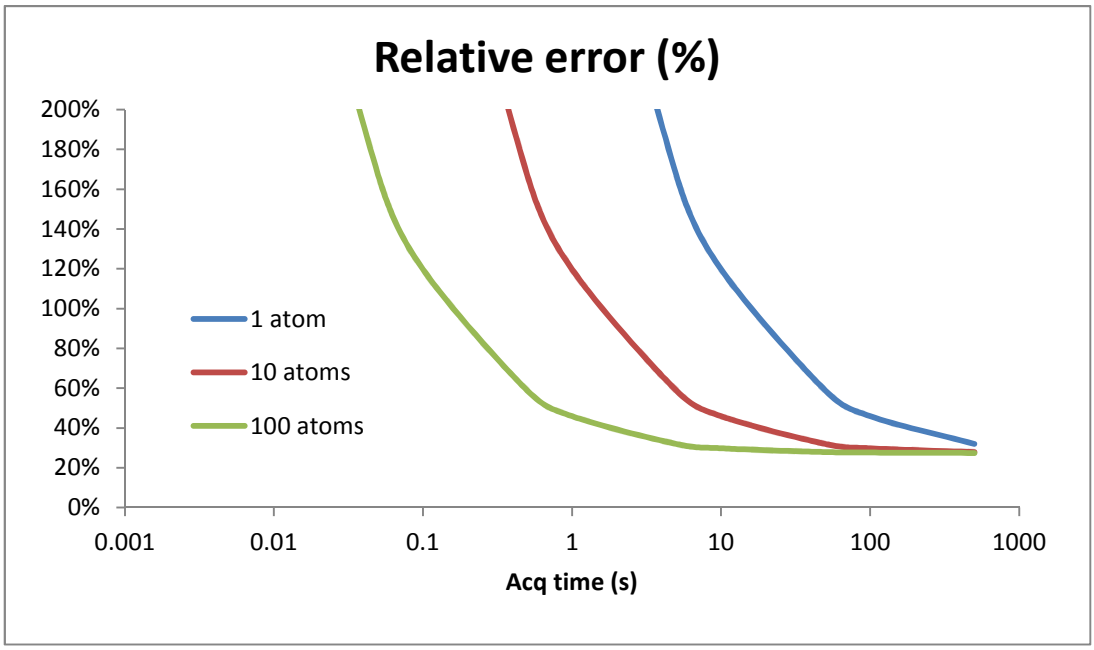

Figure 7.24 Relative error in identifying 1, 10 or 100 atoms given different acquisition times.

A custom Matlab program was coded to determine the number of repeated scans necessary to achieve reasonable signal to noise such that the limiting error is the error in the k-factor ration. The total acquisition time is also calculated to give the user a sense of practical feasibility. By optimising these conditions, the future goal is to achieve compositional sensitivity on an atomic scale from nanoparticles.

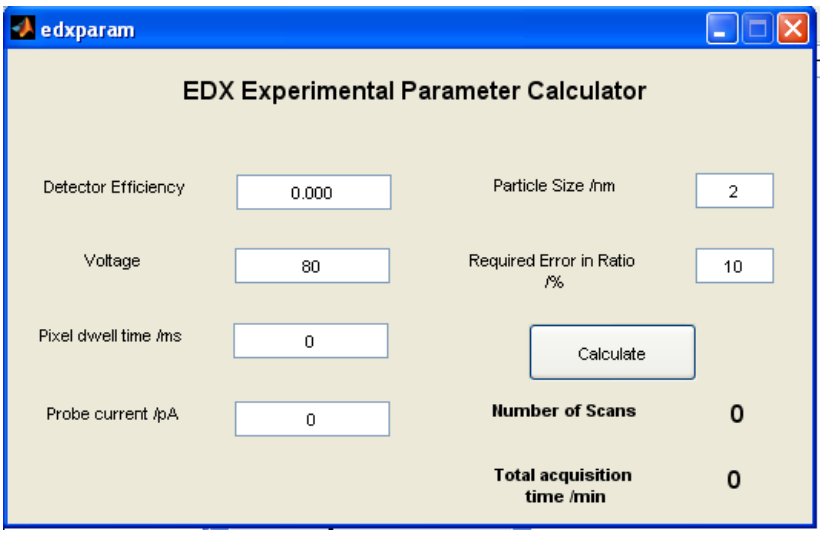

Figure 7.25 User interface of the custom Matlab program which allows the optimum parameters for acquisition of EDX spectra of a particular nanoparticle size to be determined, given the required error in the k-factor ratio.

7.11 Conclusions

Aberration corrected STEM has allowed new possibilities for quantification of EDX spectra of small nanoparticle samples. However, limitations of the current technology and methods of quantification are still appreciable. While optimum conditions found for the acquisition of spectrum images with good signal to noise, spatial resolution is greatly limited by the need to use a larger probe for a higher current beam, which also increases the possibilities of sample damages. A detailed analysis of errors showed that where X-ray counts in individual peaks were below 500, errors in the poor signal dominated.

Current standard quantification methods (Cliff-Lorimer k-factors) are usually carry an uncertainty of 10% as they are of unknown theoretical source or are extracted from bulk samples not nanoparticles. Even manually processing spectra to make sure background subtraction and peak integration are sensible does not eliminate this source of limiting uncertainty. More sophisticated methods such as the ζ-factor approach do not yield any benefits until sufficient signal (over 1000 counts) is reached and so for the current limitations of probe size and current, were not useful.

2ML design nanoparticles were explored, showing uniformly higher concentrations of Pt than expected in the particles identified as core-shell from the HAADF, compared to the synthesis design. In the next chapter, EDX and HAADF STEM are combined to exploit the advantages of each and mitigate their respective drawbacks.

References

[1] D.B. Williams, C.B. Carter, Transmission Electron Microscopy: A Textbook for Materials Science, Springer; 2nd ed. 2009 edition, 2009.

[2] G. Cliff, G.W. Lorimer, The quantitative analysis of thin specimens, Journal of Microscopy. 103 (1975) 203–207.

[3] M. Watanabe, D.W. Ackland, a. Burrows, C.J. Kiely, D.B. Williams, O.L. Krivanek, et al., Improvements in the X-Ray Analytical Capabilities of a Scanning Transmission Electron Microscope by Spherical-Aberration Correction, Microscopy and Microanalysis. 12 (2006) 515.

[4] D. Williams, D. Ackland, M. Watanabe, Quantification of X-ray Spectrum Images in the Analytical Electron Microscope: Progress Toward Single-Atom-Detection Limits, Microscopy and Microanalysis. 13 (2007) 1348–1349.

[5] S.J. Pennycook, M. Varela, A.R. Lupini, M.P. Oxley, M.F. Chisholm, Atomic-resolution spectroscopic imaging: past, present and future., Journal of Electron Microscopy. 58 (2009) 87–97.

Chapter 8

Combining HAADF STEM and EDX

Combining HAADF STEM and EDX is a route to exploiting their respective strengths. In this chapter, both methods are applied to samples of 0.5ML, 2ML and cycled 2ML design particles in order to evaluate the feasibility of answering the following questions:

- Can actual particle composition be correlated with that of the design?
- What can be said about the 3D morphology of the particle?
- What is the degree of Pt segregation to the surface in particles of different sizes?
- What changes have occurred to the particle composition and Pt segregation after cycling?

First a cumulative EDX spectrum from the whole particle is used to give an indication of overall composition and cross section is used to extract compositional information for specific columns. Then, the possibilities for using spectral maps in conjunction with cross section analysis are explored. All the data presented in this chapter was taken on the JEOL ARM 200F at 200kV unless otherwise stated.

8.1 Pt distribution of different designs

One of the key questions that HAADF STEM and EDX can aptly address is the characteristics of Pt distribution on individual particles. Understanding the structure *and* composition of particular particles

as well as the precise location of the Pt on an atomic scale can reveal important understandings of catalytic behaviour that is lost when considering bulk averaging techniques.

8.1.1 Composition of a 2ML design nanoparticle

Not all particles in the samples exhibit clear core-shell structures in HAADF STEM images; some smaller particles on the order of 2 - 3nm in size, such as that in Figure 8.1, do not show the increased scattering intensity at edges which give clear structural information about the location of the Pt. A naïve assumption would be that they are Pd cores left undecorated by the Pt deposition step in the synthesis.

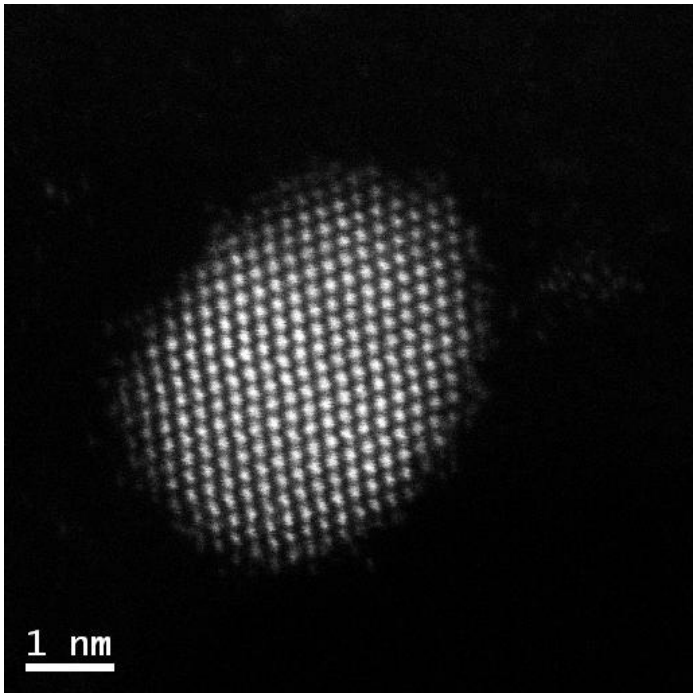

Figure 8.1 HAADF STEM image of a 2ML design nanoparticle taken on the JEOL ARM 200F at 200kV. Variations in intensity are not significant enough to suggest a core shell structure.

A simple histogram analysis of the integrated intensities of the columns does not indicate a clear bimodal distribution (see Figure 8.2) since the thickness variations around the edges of the particle would account for the lower scattering values. Without calibration of the image intensity, it is difficult to attribute the scattering to a particle composition or thickness.

Cross section analysis suggests that there is a significant amount of Pt present in the particle. If the particle was purely or predominantly Pd, the columns in the centre with cross sections in the range of 14 - 16Mb (see Figure 8.3) would correspond to 30 – 40 Pd atoms, which would give the particle a flakiness of 0.5 – 0.38, i.e. significantly thicker than it is wide. Pure Pt columns would be 13 – 15 atoms thick, which would give a much more rounded particle structure. Unfortunately, a full particle model could not be constructed from the cross section analysis since the library does not contain the necessary combinations of Pd and Pt for a Pt rich particle.

In order to confirm the compositional analysis, a cumulative EDX spectrum was taken by scanning the beam across the whole particle (see Figure 8.4) with a beam current of 150pA with a dwell time of 0.05s. The spectrum clearly shows that Pt is present in significant amounts, with very little Pd. Relative concentrations were found using the inbuilt JEOL quantification software, which Cliff-Lorimer k-ratios. The results are given in Table 8.1.

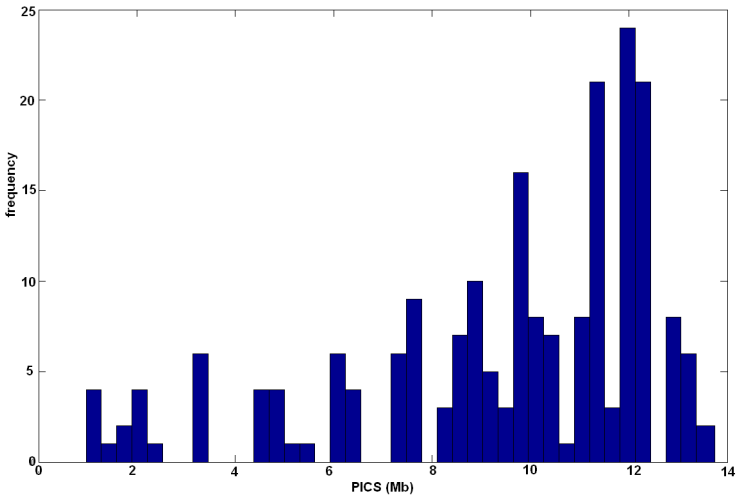

Figure 8.2 Histogram of cross section values from the columns identified in Figure 8.1

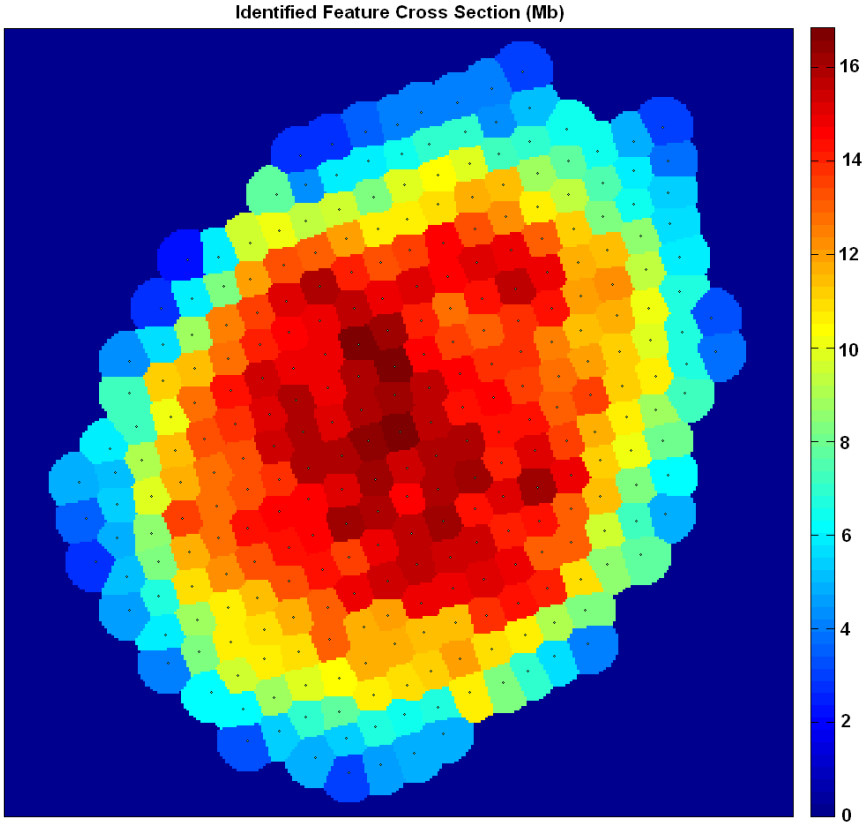

Figure 8.3 cross section analysis suggests that the strong scattering in the centre of the particle is likely to be from columns of Pt.

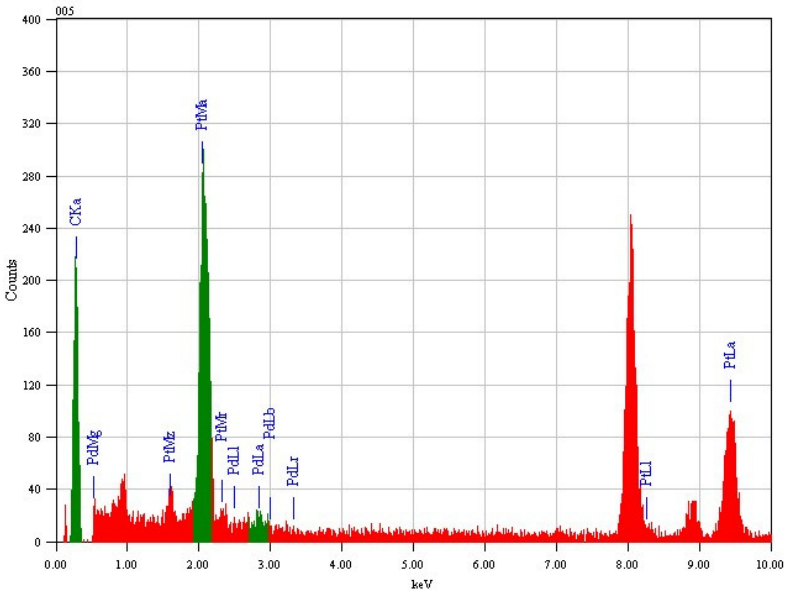

Figure 8.4 Cumulative EDX spectrum from the whole particle

Peak	Weight %	Error in wt%	Atomic %
Pd L	9.85	2.58	16.69
Pt M	90.15	0.95	83.31

Table 8.1 Quantification results of the spectrum in Figure 8.4 from the JEOL analysis software. Theoretical Cliff-Lorimer ratios were used, so an error of 10% must be assumed in addition to the error due to counting statistics reported above. The atomic % is calculated from the weight%.

From these results, it is apparent that the 2ML design catalysts are is in reality not always decorated by 2ML of Pt. Therefore, the increased activity seen in the electrochemical results could be due to the presence of smaller Pt-rich particles, whose behaviour is different from core-shell or pure Pt particles; this requires further electrochemical investigation.

8.1.2 Pt decoration on a 0.5ML design particle

A similar experiment was carried out for a particle of 0.5ML design. The strong scattering of the Pt decoration can be clearly seen on the edges of the particle (see Figure 8.5, left), where the intensity is too strong to be purely Pd. Step-like edges between the (100) and (111) faces are clearly visible (red box) which suggest non-perfect faceting, commonly seen in nanoparticles and the site of increased catalytic activity [1].

A probe of size 3Å and current of 48pA was used to scan an area encompassing the nanoparticle (see Figure 8.5 right, blue box), with sub-pixel scanning to ensure the whole area of interest was covered. The dwell time per pixel was 3s, so the total acquisition time was 300s. The spectrum can be seen in Figure 8.6.

This recipe unfortunately left the particle visibly structural reconstructed. For the purposes of extracting some compositional information from the spectra, it is assumed that the main damage mechanisms are sample heating and not sputtering, so there is negligible mass loss. The total electron dose was 4.5 x 10^7 electrons / $Å^2$.

An estimate of the number of atoms in the particle can be made by assuming a pseudo-spherical shape. A calculation from the width of the particle and atomic density of Pd gives approximately 3600 atoms. The total number of counts from the whole set of identifiable peaks (Pt M_{α}, Pt-L_{β}, Pd-L_{α}, Pd-L_{β}) after background subtraction is 3427. From this structural estimate, 0.95 X-rays per atom does not give sufficient sensitivity to be able to accurately measure the composition ratio of Pt and Pd on an atom-by-atom scale, even assuming that each atom only excites exactly one detected X-ray.

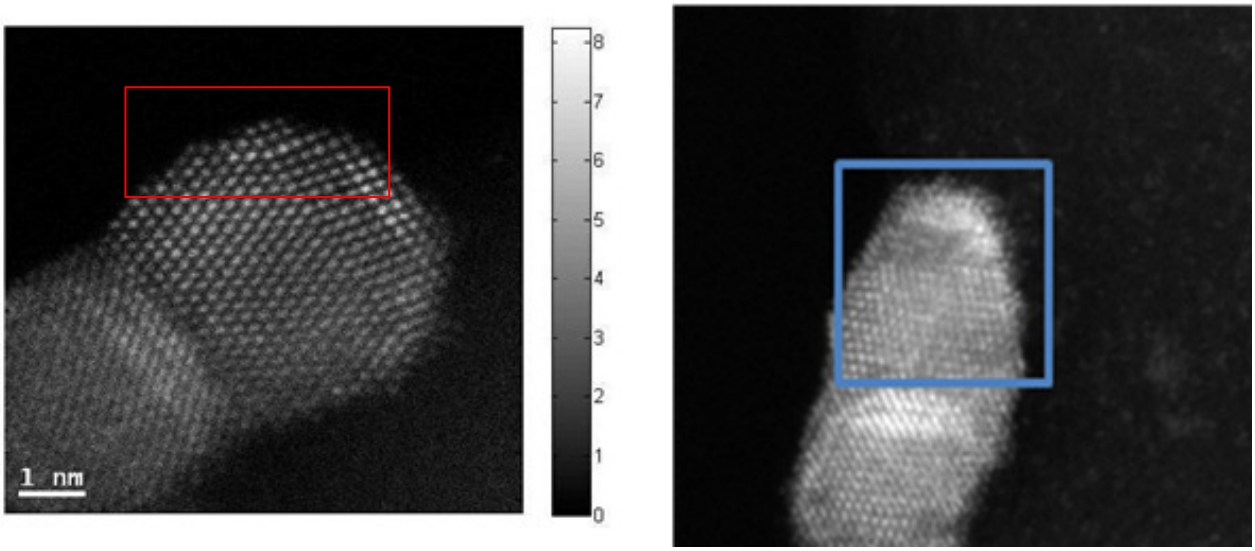

Figure 8.5 (left) particle before EDX acquisition, imaged at 200kV. Catalytically favourable steps are indicated in the red box. (Right) The same particle imaged after a EDX map is acquired, where a significant structural change has occurred.

However, the spectrum can still give an indication of the overall composition of the particle. The inbuilt quantification in the JEOL EDX software uses a thin film quantification standard and tabulated theoretical Cliff-Lorimer ratios (see Table 8.2). The k-factors used by the software are not known and the method of peak integration and background subtraction is not transparent, so it is possible that the results hold more uncertainty than the 10% error due to the uncertainty in the Cliff-Lorimer ratio.

The spectrum was extracted and independently analysed with the methods described in section 8.4. The peak integration allowed all identifiable X-ray lines to be accounted for and included, thus increasing the potential count statistics. Cliff-Lorimer quantification with theoretical k-factors gives a weight% ratio of Pd/Pt of 83%/17%. Both correspond closely with the catalyst design for ½ML

coverage of 80.2% / 19.8%, suggesting that the background subtraction in the in-built software gives minimal errors.

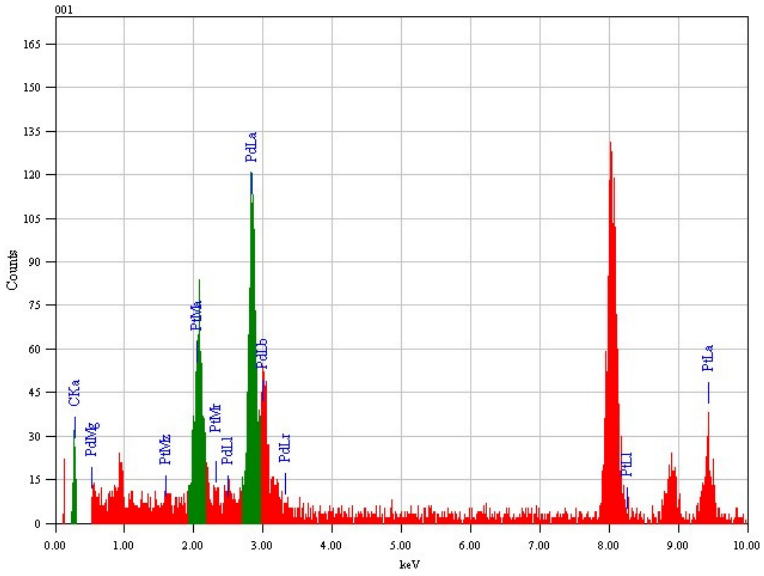

Figure 8.6 EDX spectrum collected from the whole particle shows the strong presence of Pt.

With count statistics here of 500 X-rays giving statistical errors on the order of 4.5%, the dominant error is in the Cliff-Lorimer ratio's 10% uncertainty. Applying the ζ-factor quantification method would give smaller errors in future experiments.

Element	Quantification using JEOL software		Expected Pd / Pt ratios from synthesis	
	Atomic %	Mass %	Atomic %	Mass %
Pd	80.3	69.0	80.2	68.9
Pt	19.7	31.0	19.8	31.2

Table 8.2 Quantification results from built-in JEOL software using a theoretical Cliff-Lorimer ratio compare favourably to the expected ratio of Pd / Pt from the raw materials used in synthesis.

Cross section analysis (see Figure 8.7) shows that scattering from the edges is visibly strong in the HAADF image, especially around the top of the particle. It is possible to extract some information about the potential Pt decoration using cross section analysis. Grey numbers correspond to Pd atoms and white (or black where the background polygon is light) indicates the number of Pt atoms. It is assumed that the particle is as round as possible and that neighbouring columns differ by a maximum of 3 atoms in thickness, as can be seen in the projected direction in step like structures indicated with the red arrows. The combination of thickness and composition is chosen which most closely matches the experimental cross section value ±10% of its value to account for the experimental error. Matches which are heavily Pt-rich are discarded since EDX results show that the overall composition of the particle is Pd-rich.

The total scattering from columns in the bottom right region is also very strong, suggestive of more Pt coverage. However, since the column profiles in that region are elliptical in shape, there has clearly been some mis-tilt of the particle during imaging. As discussed in Chapter 5, this further complicates the identification of column composition and thickness since channelling conditions now broken. Mis-tilt acts to lower the observed scattering intensity compared to on-axis so the scattering from these columns is likely even stronger when the particle is on axis. However, the amount of diminution is not easily calculated when the thickness or mistilt is not known and both cannot be solved from a single image of an elliptical column as the amount of elongation in the column profile will depend on the number of atoms in the column and also the mistilt. Further knowledge of either parameter is required to understand how the mistilt factor.

Since the error in the cross section value of 10% offers more than one likely match for composition and thickness, without further local knowledge of the ratio of concentrations, it is difficult to attribute an overall ratio of Pd/Pt from the whole particle to specific areas.

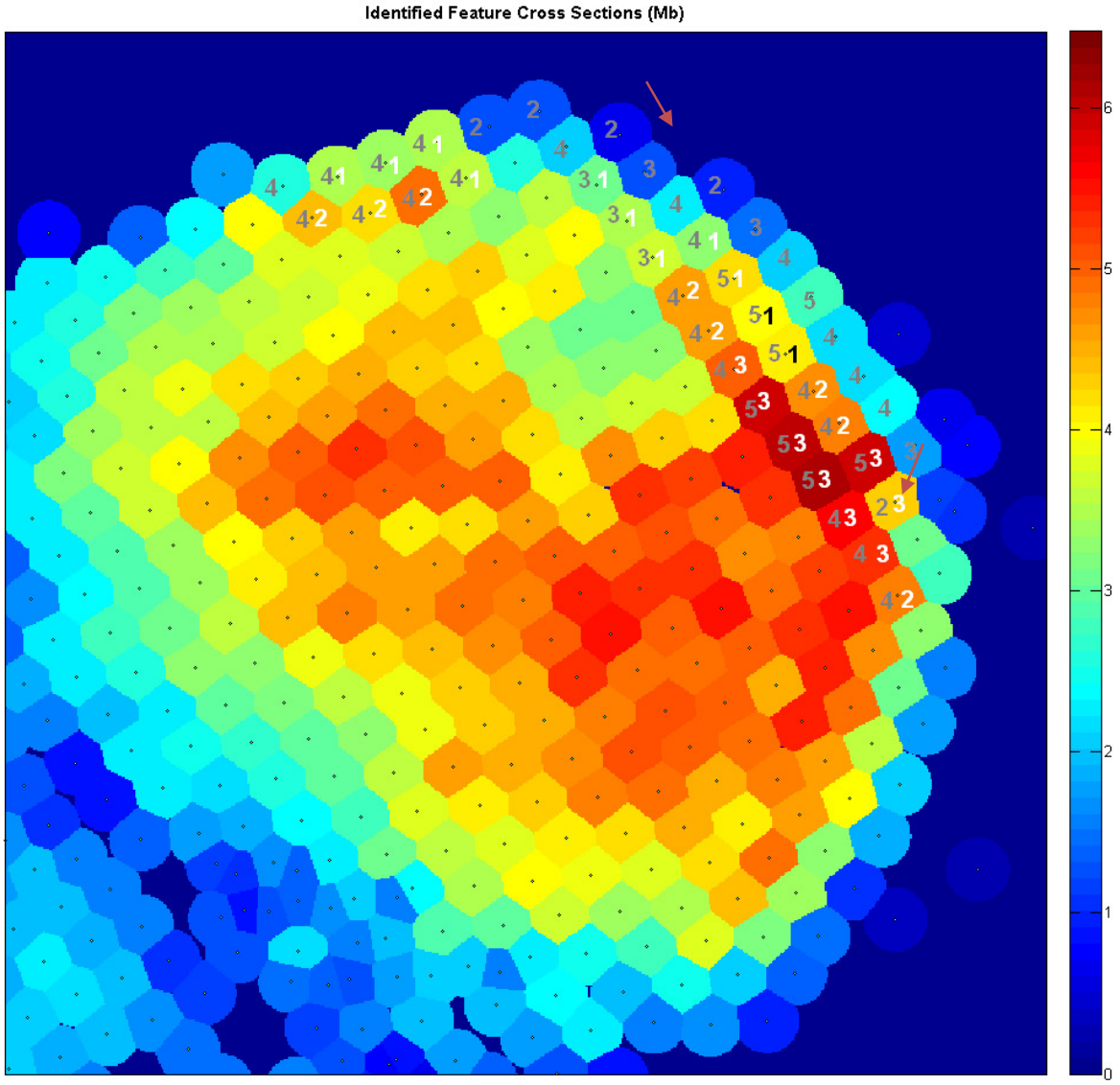

Figure 8.7 Best estimates of composition from cross section values: Pt (white/black numbers) is clearly segregated in two lines across the top right and one across the top. Pd (grey numbers) only columns make up one edge of the particle (red arrows), suggesting uneven coverage of Pt. Moreover, the predominately Pd columns at the edges suggest that the Pt has not been deposited on the faces but rather on steps and edges.

8.2 Alloying in smaller particles

As explored in Chapter 5 and 6, the cross section analysis becomes increasingly intractable at larger thicknesses because the combinations of possible composition and thicknesses are too many for distinction within the errors of the experiment. While EDX can give a good sense of composition, it lacks the sensitivity to thickness.

A small 0.5ML design particle of 2nm diameter was imaged by the JEOL ARM200F at 80kV with a probe current of 14.6pA and the detector mapped with a current of 2.6pA (see Figure 8.8). An SI was acquired (see Figure 8.8 inset) with an 85pA beam because the size of the particle placed a limit on the dose before damage occurred.

The extracted concentration maps from the Pt M and Pd L peaks in the SI show that there is no clear core-shell structure and that, moreover, the elements are quite uniformly alloyed (see Figure 8.9). This behaviour is expected since smaller particles, with their larger surface to volume ratio, have more surface free energy. The bonds of the surface atoms are weaker and intermixing of the Pt in any shell structure with Pd of the core could be expected.

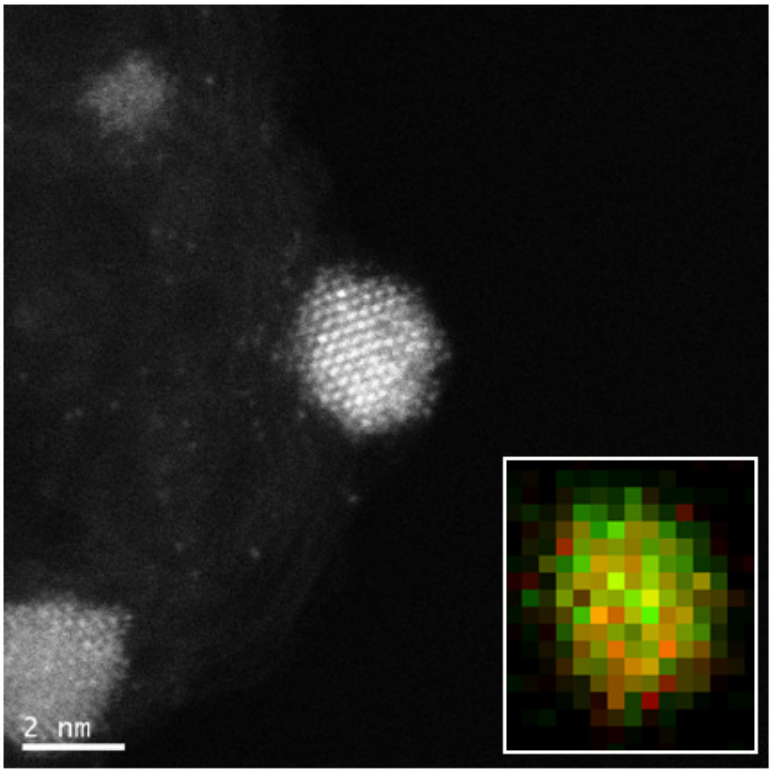

Figure 8.8 HAADF image of nanoparticle with extracted Si Pt / Pd distribution composite (inset).

Matching the cross section values from the experimental image to the library of values compiled by simulation (see Chapter 5) and also the EDX concentration profile, the thickness of each column in the particle could be analysed. In Figure 8.10 the grey numbers indicate the number of Pd in the column

and the white (and black) numbers indicate the presence of x numbers of Pt. The bottom left corner of the particle has higher than expected cross section values because the less well resolved peaks were not successfully found by the automated peak integration software.

In general, the cross section analysis and EDX give similar results in terms of Pd and Pt distribution. Where the EDX cannot give insight into the position of the Pt in the column, cross section has the chance of doing this. However, since only Pt at the entrance or exit surface of the column was considered, more simulations are required to determine whether complete alloying has occurred. In addition, the sensitivity of the cross section analysis, limited by the experimental error to an uncertainty of ±10% may not be sufficient to give a clear indication of the height of Pt atoms in the column.

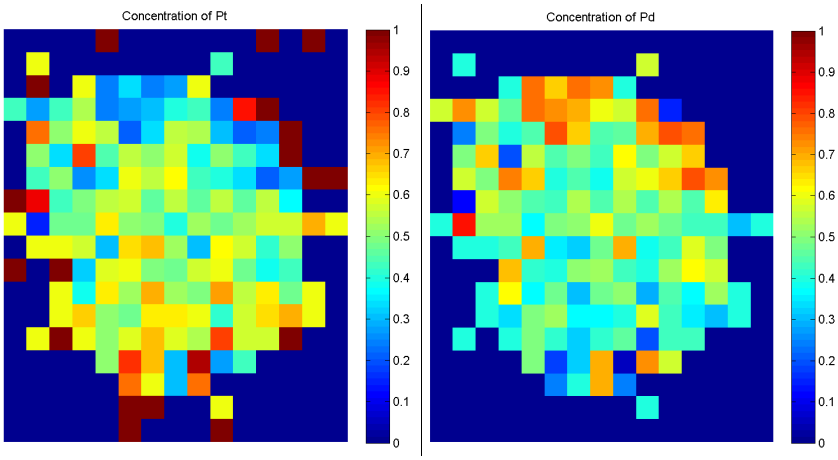

Figure 8.9 Concentration of Pt (left) and Pd (right) calculated from the SI's Pt M and Pd L peaks respectively.

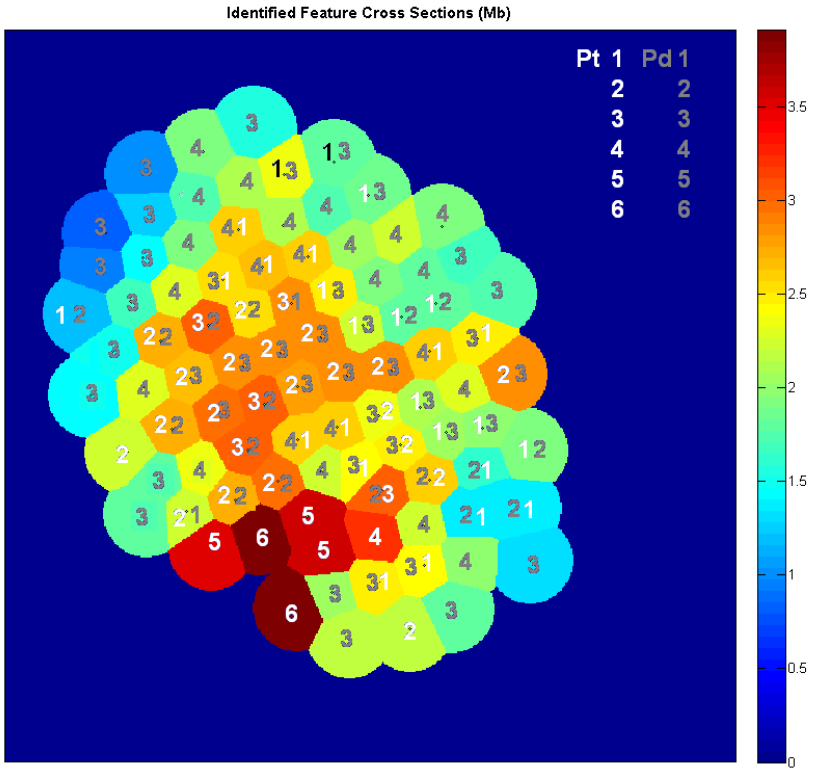

Figure 8.10 Map of composition in each column of the HAADF cross section analysis. Number of Pd atoms per column is in grey, Pt in white (or black). Numbers for the Pt, to the left of the Pd number indicate an entrance surface species and the number to the right, an exit surface species. There is little difference between the two at this thickness.

8.3 Effect of cycling on morphology

For larger particles, where cross talk and mistilt become a greater issue, the 80kV probe on the JEOL ARM 200F was not fine enough to deliver crisp atomic resolution HAADF images,. Since well resolved columns is an important condition for the validity of the cross section approach (see Chapter 5), combined HAADF and EDX exploration at 200kV was necessary.

After cycling, several particles were seen to have coalesced (see Figure 8.11), with the regions where two particles have joined showing higher intensity (marked by red box). A SI was taken of the conjoined particles with a probe current of 45.2pA and dwell time of 0.05s per pixel to minimise damage and cycled 15 times to acquire sufficient counts.

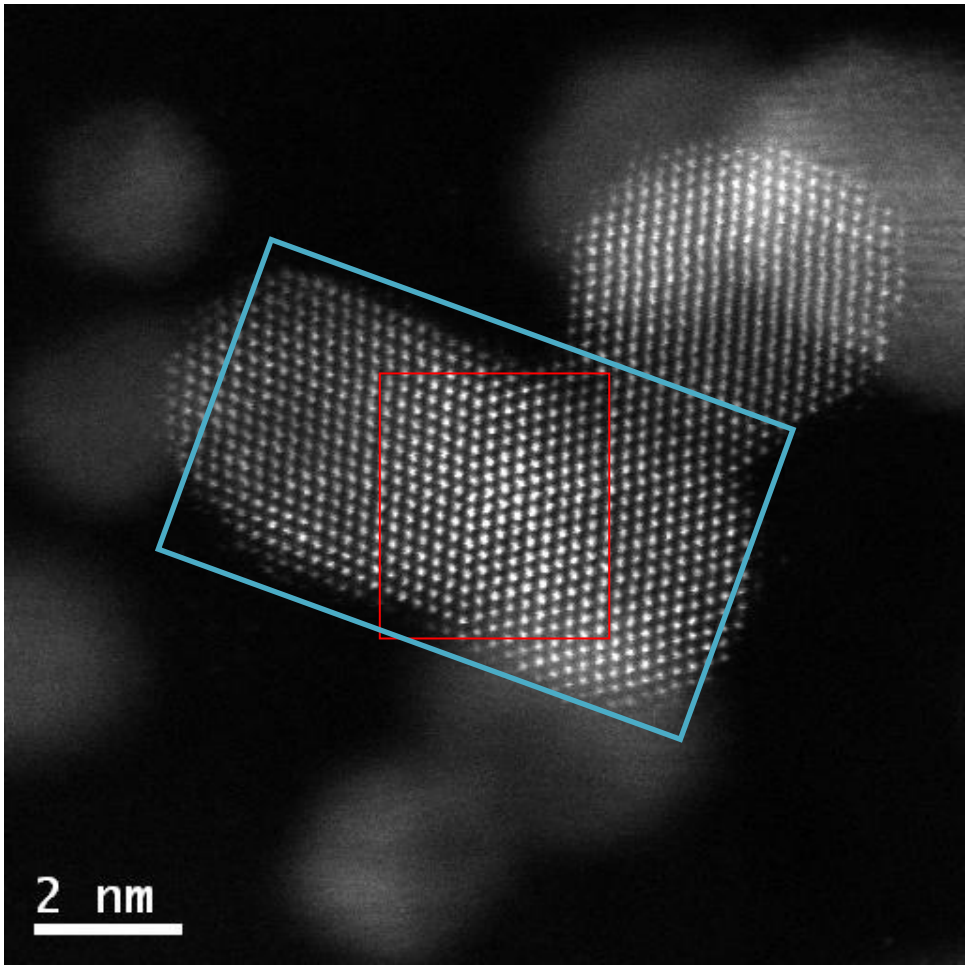

Figure 8.11 HAADF image of a 2ML cycled sample, showing particle coalescence. The areas of the join show brighter intensity (red box). SI taken from area in blue box.

The calculated concentrations of Pt and Pd (see Figure 8.12) show that the particles are predominantly Pt, with very little Pd in the core areas. This matches observations from electrochemical tests which show the dissolution of Pd after cycling as the CV behaviour clearly becomes more Pt-like with fuel cell aging [2].

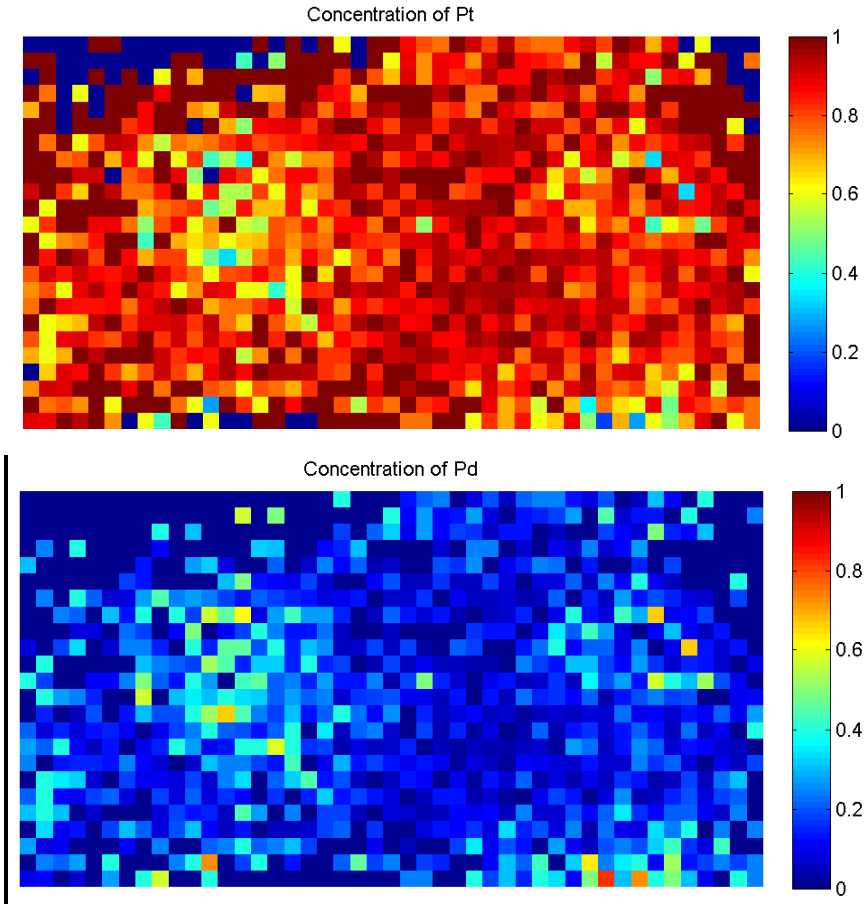

Figure 8.12 Calculated concentrations of the area selected in red in Figure 8.13 from the SI using theoretical Cliff-Lorimer k-ratios. The particles are predominantly Pt, with very little Pd, even in the core areas.

The cross section values of the join area are between 11.2±1.1Mb and 15.5±1.6Mb. Here the EDX map shows that the composition is strongly Pt. The cross section values can then be interpreted to give a thickness measurement of between 10 and 14 Pt atoms (see numbered columns in Figure 8.13). Given that the edges of the particles individually would be thinner than the diameter, this value might at first seem to thick. However, given that the two particles have coalesced, it is conceivable that the new particle would be of a similar thickness to its diameter of 14 atoms (indicated by the black line in Figure 8.13)

For the areas where there is a more mixed composition, the possible combinations are larger and assumptions would need to be made about the particle morphology in order to characterise the

structure. Moreover, the area to the left of the particle on the left shows lower cross section values because of the particle mis-tilt, seen by the elongated column profiles.

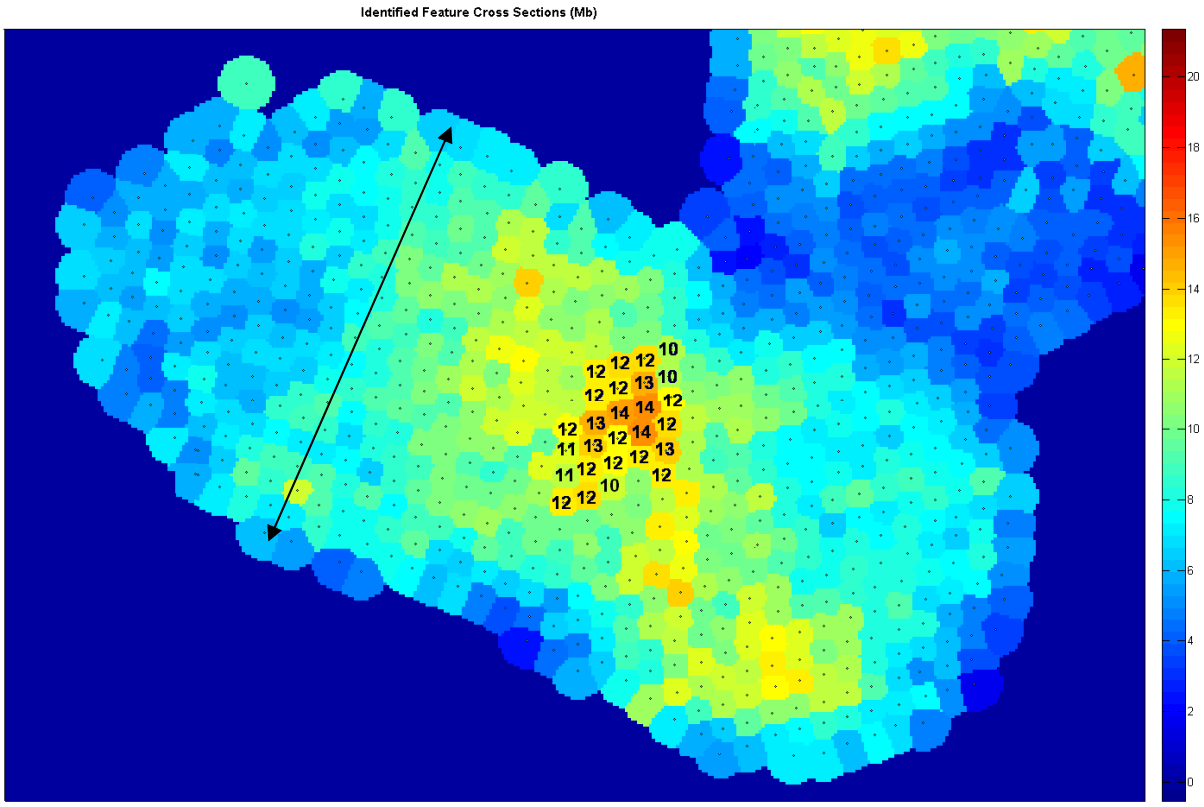

Figure 8.13 The cross section analysis results, showing higher values for the area where the particles are joined. Comparison to simulations identifies them as between 10 and 14 Pt in thickness.

8.4 Effect of cycling on Pt distribution

A 2ML design particle was imaged at 200kV. The [100] orientation and clear core-shell structure can be seen in Figure 8.14. An SI map was collected with a dwell time of 0.05s per pixel and probe current of 45.2pA. The acquisition was cycled 15 times, which provided good count statistics for the whole particle (see Figure 8.15)

The overall concentration across the whole particle was calculated as 82.7±8.3% for Pt and 17.3±1.7% for Pd, which is significantly more Pt-rich than the design of the 2ML particle (see Table 8.3 and Figure 8.16). This would, on first inspection, further support the electrochemical findings of Pd dissolution and Pt aggregation with fuel cell cycling. However, the uncycled fresh samples investigated in Chapter 6 are also Pt rich with the same concentrations In addition, there does not seem to be significant mass loss from the central core, as would be expected of Pd leaching, nor is there significant intermixing of Pt and Pd as would be expected if the particle had reconstructed due to loss of mass from the core.

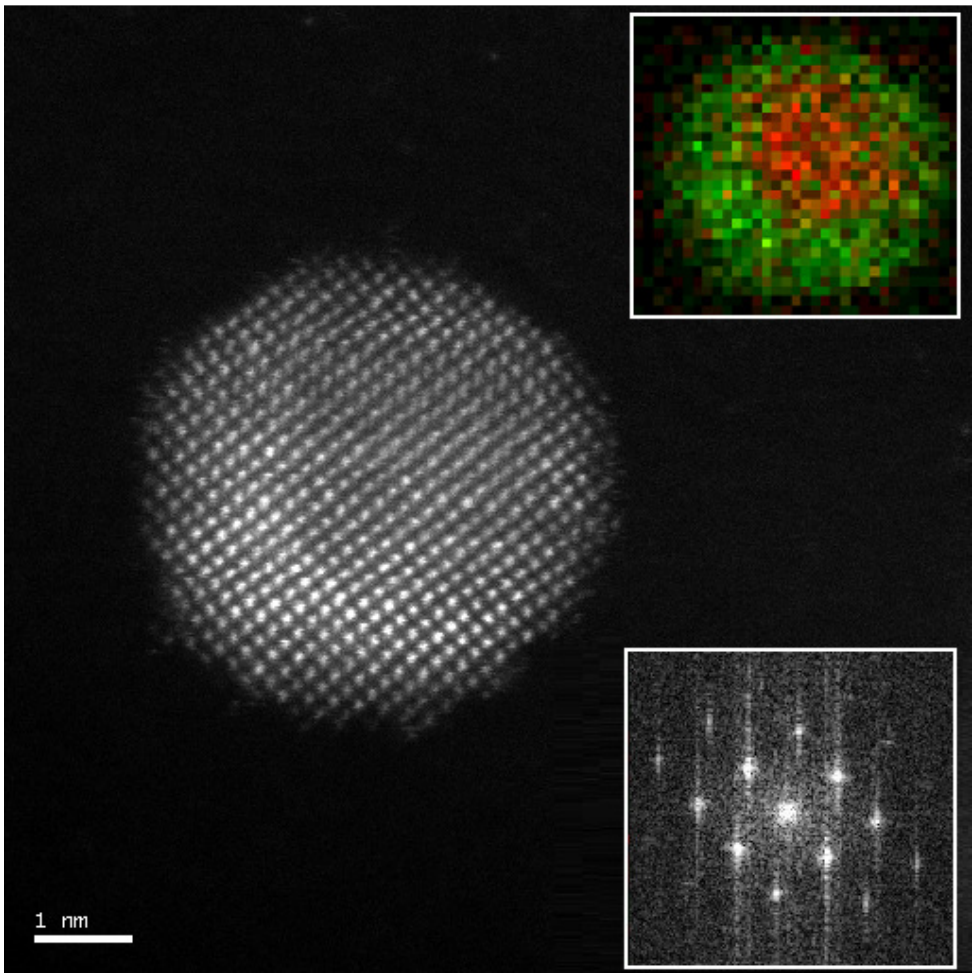

Figure 8.14 Micrograph of a 2ML nanoparticle after fuel cell cycling, imaged at 200kV. (top inset) A RGB composite of the extracted values of the Pt M (green) and Pd L (red) peaks from the SI. (bottom inset) FT of the HAADF image showing the [100] orientation.

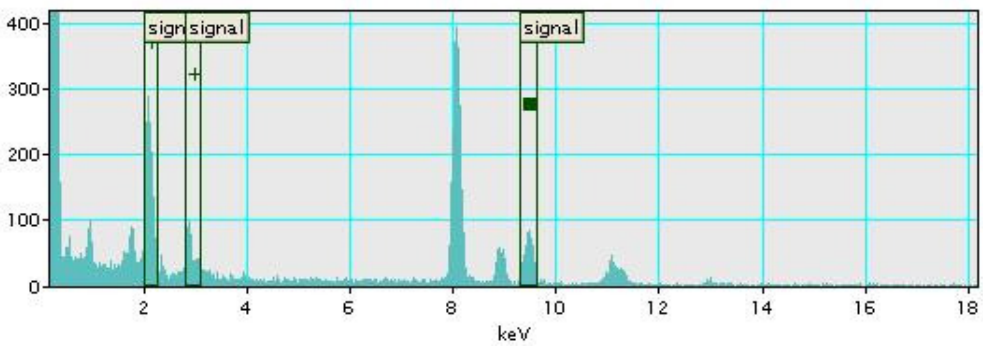

Figure 8.15 Spectrum extracted from summing all the spectra in the SI. Peaks selected are, in order of increasing energy: Pt M, Pd L, Pt L.

	Pt M	**Pd L**	**Pt L**
Integrated Peak Area	4100	1556	1576
Background	476	348	134
True X-ray counts	**3624**	**1208**	**1442**
Error	60.2	34.8	38.0
% error in counts	**1.7%**	**2.9%**	**2.6%**

Table 8.3 Error analysis from the extracted peaks in Figure 8.15.

The cross section analysis (see Figure 8.17) showed that scattering was not intense enough to warrant a full spherical particle; the particle is 26 x 28 atoms wide in the image plane. The PIC value of the column marked by the black arrow in Figure 8.17 is 11.5±1.1Mb, which corresponds to a column thickness of 23 atoms if all the atoms were Pd. However, since the EDX analysis shows that this area contains some Pt, it is likely that the column is thinner. Taking into account the Pt and Pd distribution from the EDX maps, the cross section values suggest that the thickness in the centre of the particle is between 16 – 21 atoms. Given the full shell of Pt seen in the EDX map here and not in other particles (see for example Figure 7.19, 8.20, 8.23), it is feasible that the particle is sitting on top of the carbon support and the undecorated, embedded side is in the plane of the image.

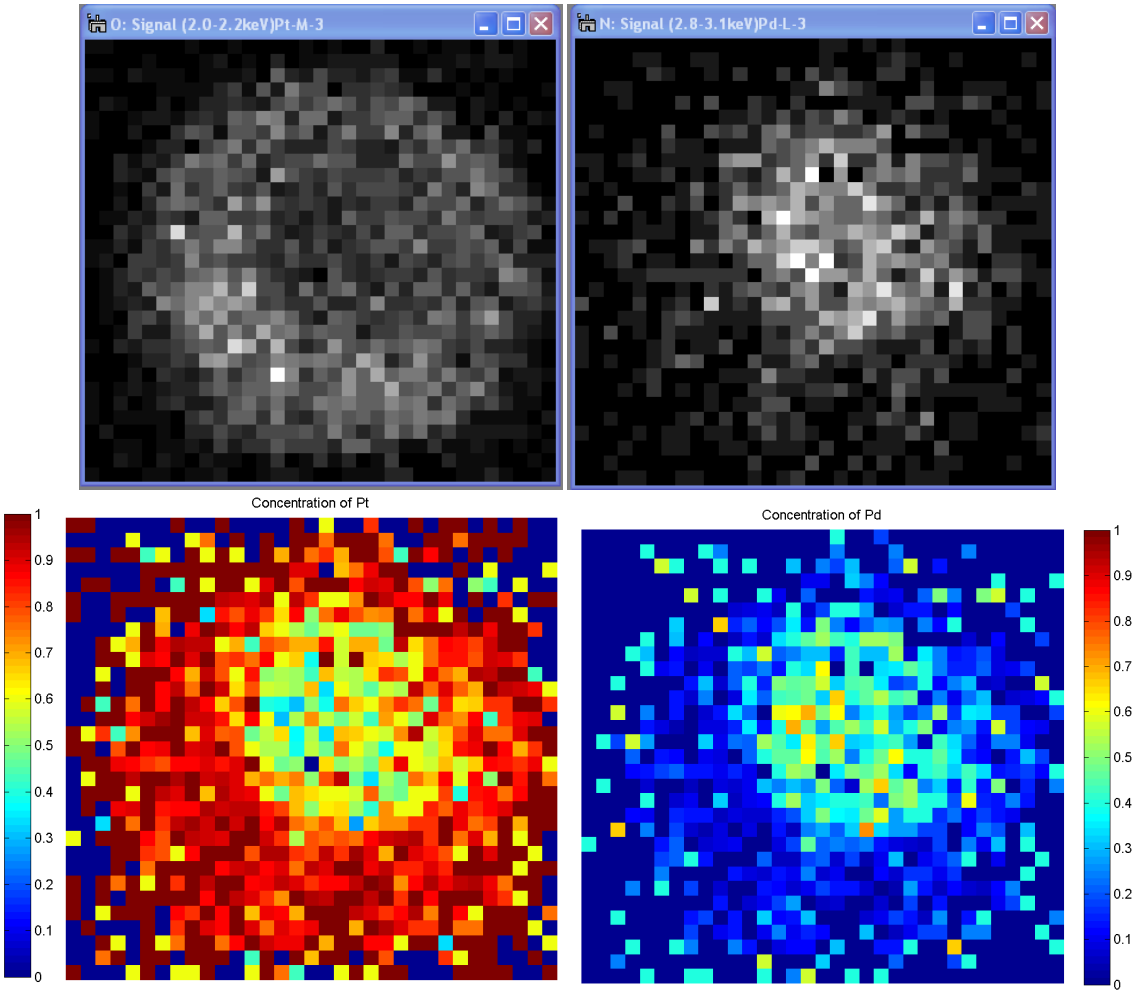

Figure 8.16 Extracted SI maps (clockwise from top left): signal from the Pt M peak from 2.0–2.2keV; signal from Pd L peak from 2.8–3.1keV; calculated concentration profile of Pd; calculated concentration profile of Pt. Clear Pt segregation to a shell can be seen, with very little Pd at the shell and very little Pt seen in the core.

The areas of purely Pt concentration have a cross section value of between 18.1±1.8Mb and 21.3±2.1Mb, which corresponds to a thickness of between 18 and 22 Pt atoms. Unfortunately, a full reconstruction of the particle column-by-column composition could not be modelled as the library constructed in Chapter 6 does not include the necessary Pt concentrations.

The first step of a structural model of the projected image has been created (see Figure 8.18). This initial model can then modified by altering each column's thickness once more detailed information about the column composition and thickness can be extracted from the cross section values. This

model can then be fed into a simulation and the output compared to the experimental cross section analysis. Adjustments can be made until a converged solution emerges.

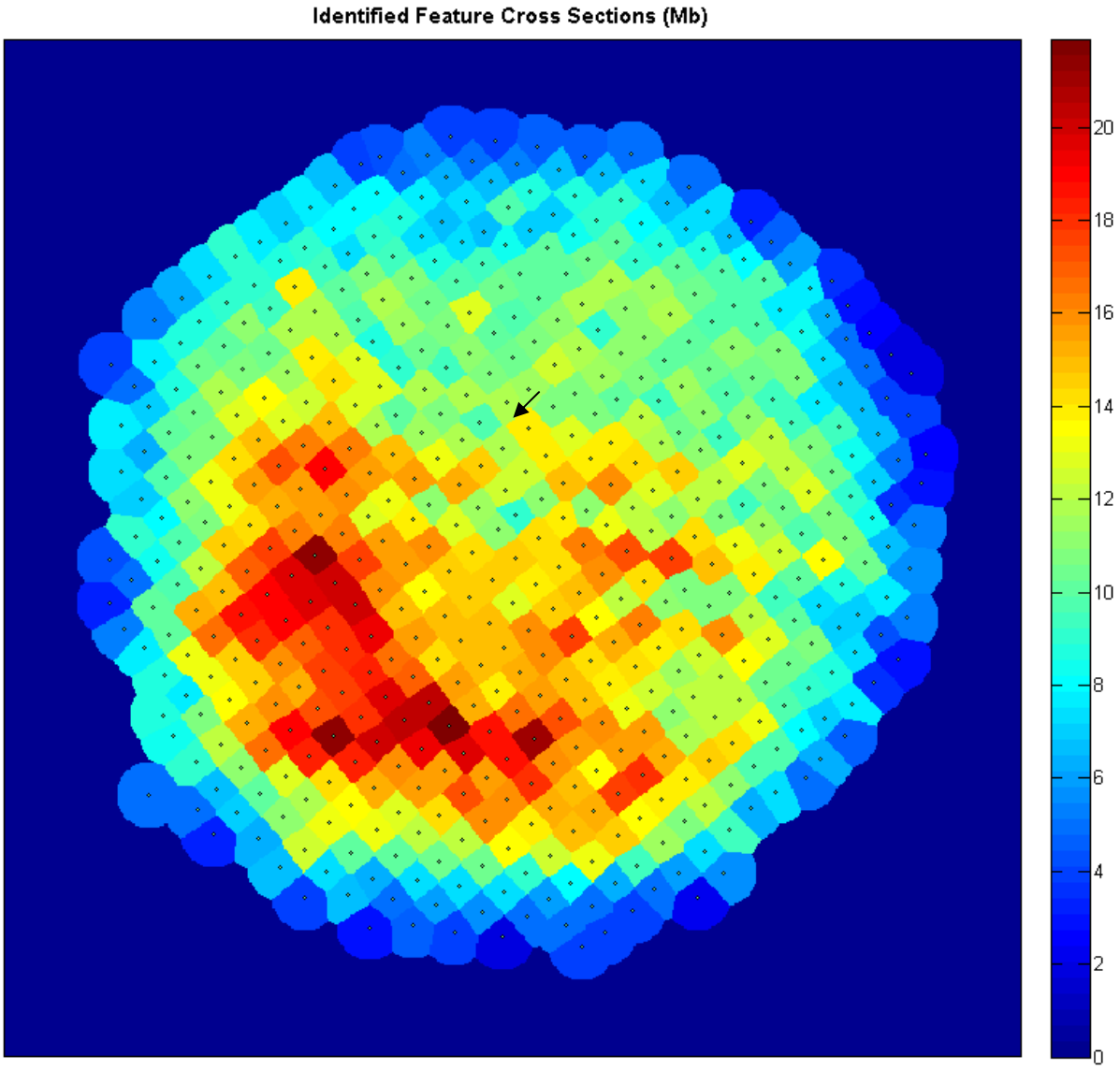

Figure 8.17 Cross section analysis of particle in Figure 8.14

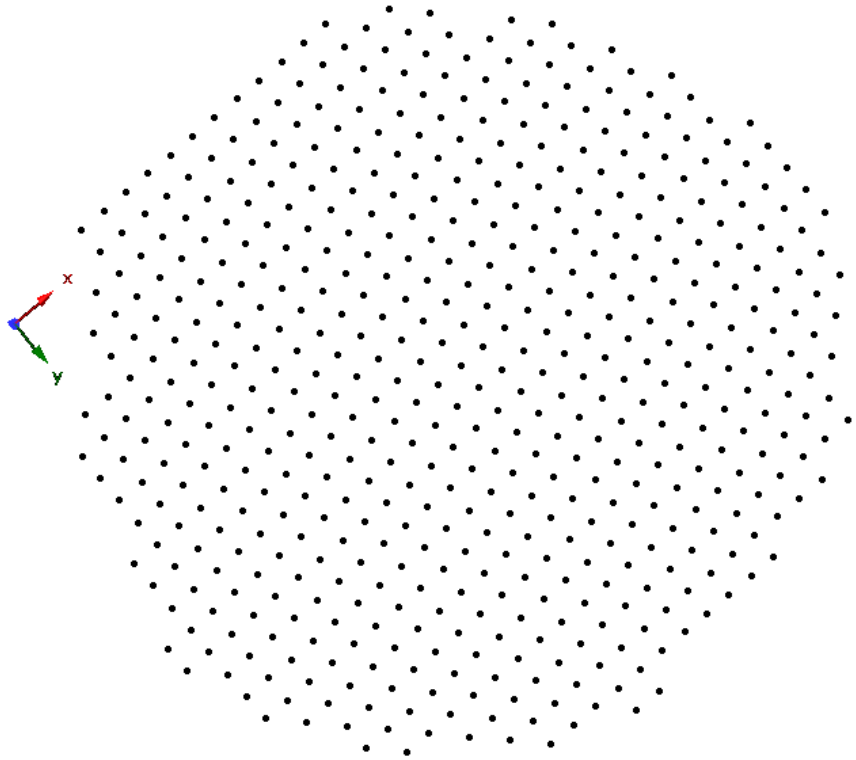

Figure 8.18 First step of the model of the particle in Figure 8.14 made in Crystal Maker. The projected structure in the image plane is constructed. Once more information about each column's composition and thickness is known, each column can be adjusted.

8.5 Conclusions

The combination of cross section and EDX spectrum image maps gives complementary information in order to solve the thickness / composition problem in interpreting HAADF STEM images.

Core-shell nanoparticles of 2ML design have shown large concentrations of Pt in a clear shell-like structure in EDX maps. The concentration is higher than the synthesis design would suggest for complete shell coverage. Coupled with observations of edge only Pt decoration from the lower resolution work in Chapter 3 and the cross section analysis in Chapter 6, it is evident that the coverage of Pt on the Pd cores is not homogenous across the sample.

Smaller particles show a more even alloy of Pt and Pd and 0.5ML design. Post fuel cell cycling, 2ML nanoparticles have been seen to coalesce and become more Pt rich at the joins. This observation would support the results from other techniques which attribute the loss of activity to the dissolution of Pd from the core. However, previously uncycled fresh samples were also observed to be equally Pt rich. The error on the analysis from the poor signal to noise and insufficiently accurate quantification factors mean that there is not enough analytical sensitivity to determine if there is true Pd dissolution.

Factors hampering a full determination of column-by-column, atom-by-atom structure include mistilt, signal to noise of the EDX maps, EDX quantification ratios, and the stability of the particle under the electron beam.

References

[1] L.Y. Chang, A.S. Barnard, L.C. Gontard, R.E. Dunin-Borkowski, Nano Letters 10 (2010) 3073–6.

[2] B.C. Tessier, Preparation, Characterisation and Evaluation of Core-Shell Electrocatalysts for PEMFCs, University of Southampton, 2009.

Chapter 9

Conclusions and Future Work

9.1 Conclusions

This thesis has explored the application of aberration corrected high angle annular dark field (HAADF) scanning transmission electron microscopy (STEM) and energy dispersive X-ray (EDX) analysis to the problem of quantifying Pd-Pt core-shell nanoparticle catalysts. Understanding the structure of nanoparticle catalysts, particularly the surfaces and active sites, is a vital step to understanding the processes which govern their effectiveness. This work opens up a new understanding of analysis of atomic resolution HAADF STEM images and has explored some of the boundaries at the cutting edge of this technique and also EDX.

9.1.1 Efficacy of core-shell design

Platinum group metal core-shell nanoparticles, specifically Pt-shell, Pd-core structures offer significant increases in the activity and selectivity over traditional pure Pt nanoparticles in the oxygen reduction reaction, which is the limiting factor to the effectiveness of a proton exchange membrane fuel cell. In addition, usage of the precious Pt-metal is decreased, leading to more cost-effective precious metal usage. Traditionally, as a heavily surface dependent technique, understanding the location of Pt shell decoration as well as the structure of the surfaces and the particle's morphology, is vital to understanding its associated catalytic behaviour. In addition, due to the increase in activity because of the core-shell design, understanding the full 3D structure of the particle is necessary to explain these effects.

9.1.2 Characterisation techniques

While bulk averaging techniques such as XPS and EXAFS give statistical information about size distributions and bonding co-ordinations, the bulk averaging nature means that only an ensemble average is returned and individual structures cannot be investigated. Local techniques such as SEM do not have the lateral resolution necessary to image these 3-5nm sized particles. Transmission electron microscopy gives good lateral information but its phase contrast based image formation mechanisms limit the ease of interpretability of the images.

High angle annular dark field (HAADF) scanning transmission electron microscopy (STEM), with its incoherent imaging mechanism, strong composition sensitivity (so called Z-dependence) and now also the finer, brighter probes made available through aberration correction, offers the best tool for simultaneously mapping the structure and composition of these structure nanoparticles at high spatial resolutions. This is combined with EDX, which provides compositional sensitivity at lower spatial resolutions.

9.1.3 Size and morphology findings

Pd-Pt core shell nanoparticles with different shell designs on a 3nm Pd core were investigated for the first time with electron microscopy. Designs were half a monolayer (ML), 1ML, 2ML and 4ML, where a ML is a complete coverage of one layer of atoms. The samples were subsequently also investigated post cycling in a fuel cell and the results compared to information obtained through other techniques.

Using HAADF STEM images to measure the diameter of the particles, the Pd core was seen to be larger than the 3nm design, with increasing thickness of shell design corresponding to increases in diameter, as expected. Cycling increases the diameter for all particles. All both pre-and post cycling designs showed a similar aspect ratio of approximately 1.4. This corresponded to the higher resolution images, which showed the particles to be in general oblate rather than circular. The roundness also revealed that particles are in general convex and the more stable designs retain their roundness, while the less active ones become rougher with cycling.

9.1.4 Identification of the shell

Increased scattered intensity was observed in bands on non-atomically resolved micrographs of 2ML nanoparticles, suggestive of Pt decoration on stepped edges of particles rather than complete coverage of facets, as designed. This corresponds to the observed increases in catalytic activity from electrochemical tests since active sites are higher in number at stepped edges.

Atomic resolution images showed that columns of greater intensity often lay within the outline of the particle, again suggestive of stepped edges decorated with Pt However, not enough composition or thickness information could be extracted to determine the thickness of the columns or the precise distribution of Pt in the individual columns without further analysis.

9.1.5 Analysis of calibrated HAADF STEM images by 'cross section' approach

With the novel quantification techniques developed for a commercially available microscope, it is possible to place the scattered intensity on an absolute scale and measure the scattering in a parameter-robust manner for the first time. By integrating the signal scattered from all probe positions corresponding to a single column, the experimentally measured cross section of HAADF scattering is a new measure which is insensitive to the form of the probe, so long as the column is well resolved and the sample sufficiently thin. Good agreement is shown for thin 2D layered materials and partial agreement for isolated single atoms. The latter is hampered by the stability of the atoms under the beam.

Application of the cross section analysis to a single element Pt nanoparticle has shown its power to reveal a 3D structure. However, when applying it to a single image of a bimetallic particle, the dependence of scattered intensity on both composition and thickness restricts the possibility of the technique in identifying both simultaneously from one value. A first estimate can be made given approximations and assumptions of the particle morphology, but this is not a truly satisfying result.

9.1.6 Compositional information from EDX

A study into the various EDX quantification techniques revealed that below a total of around 500 counts in each peak, the use of the more sophisticated ζ-factor method over the inbuilt Cliff-Lorimer k-ratio in the standard Gatan DM software does not improve the accuracy of the result, since poor signal statistics is the limiting factor on the error.

It is only with EDX to give compositional information is it revealed that Pt content in 2ML design nanoparticles is much higher than expected values from the designed chemistry, whereas the 0.5ML designs match the nominal concentrations. Since edge-only decoration is also seen in the 2ML design, it is clear that the coverage of Pt is not homogenous across the different particles within a sample.

Further, spectral images of the particles from certain orientations showed that there was coverage of only ¾ of the sides due to the Pd core being partially embedded in the carbon support before disposition of Pt occurred. Thus, more Pt was available to cover the unsupported areas of the Pd core than the nominal design would suggest. Investigations of smaller particles showed that the sample contained predominantly Pt nanoparticles and that the shell coverage of some core-shells was Pt rich.

Unfortunately, often the poor signal to noise of the individual pixels in the EDX maps meant that information about the composition on a column-by-column basis could not be revealed within the experimental uncertainties.

9.1.7 The final combination

Smaller particles are seen to be not shell decorated but alloyed, and column by column compositions can be extracted from the cross section by matching to the EDX maps. Cycling is seen to cause the particles to coalesce and the joins are detected by EDX and cross section analysis to be Pt only. Further, the composition and structure of 2ML design particles is seen by combined EDX and cross section analysis to be unchanged pre- and post-cycling. This contradicts findings from electrochemical and EXAFS data, suggesting that other mechanisms are at work to reduce the activity of the catalysts with cycling.

The limitations of the technique on such a challenging sample are real. The small length scales, the complexity of the morphology and compositional uncertainty are all exacerbated by the beam sensitive nature of the nanoparticles. Prolonged exposure is often not possible due to ready damage mechanisms. However, there is still scope for exploiting the available data or techniques in other ways:

9.2 Future work

Within the scope of this thesis, a small section of the possible parameter space was explored in order to highlight the main points of interest of analysis by HAADF cross section. Further investigation into the following could yield fruitful results.

9.2.1 Size and composition correlation

An initial investigation of the trend of composition with particle size has been carried out, showing that smaller particles are more often alloyed and concentrations more uniform across the two elements. Further studies could yield a method of investigation whereby composition can be classified by particle size, leading to a "single-particle" microscopy approach akin to those used in biological EM. Averaging over multiple particles would give better count statistics for EDX and thus more likelihood of accurate compositional determination. This information of particle composition can then be used to determine thickness and composition of individual columns in an atomic resolution HAADF image.

9.2.2 Improvements on HAADF image analysis

Assuming adequate signal to noise in the HAADF image, which can be achieved by using a fine beam with a higher probe current, the main sources of quantifiable experimental errors in the technique are measuring the smaller probe current used to map the detector, measuring size of the detector inner angle, the detector non-uniformity and the sample mistilt. Detector non-uniformity should be modelled from the detector map and taken into account in the simulations. This work is already underway with

collaborators but was not in the scope of this thesis. A smaller error on the probe current can be accomplished by technical improvements which allow smaller probes with higher beam currents, or by improvements on the A/D convertors, which have necessitated this calibration method. More careful calibration of the inner angle could be done in diffraction space if the lenses allow it.

The variation of cross section with mistilt is a real and intricate issue. The possibility of determining the degree of mistilt from the ellipticity of columns of various thicknesses could give a further handle on the thickness measurement across the particle. Enhanced stability of the particle on the support by embedding the catalyst in a matrix, or supporting it on a flat support such as graphene, could greatly aid the cross section analysis. This would further decrease the errors due to subtraction of an unknown background.

9.2.3 Other material effects

Dopant top-bottom effects are seen to be significant, hampering the unambiguous matching of experimental cross sections to simulations. While reducing the errors in experimental measurements will go some way to reducing the number of thickness / composition possibilities for a single measured cross section value, some sort of spectral analysis or thickness determination is needed. Since there is a difference in the behaviour of the peak value and the cross section, it may be possible to use both parameters together to map the dopant height. In addition, mistilt could be used as a metric, since the channelling conditions would differ depending on the height of the dopant atom.

The Debye Waller factor has an appreciable effect at larger thicknesses; indeed they are often not known for nanoparticle systems and traditionally figures for bulk materials are used. For industrial nanoparticles of sizes of 10nm or greater, more detailed understanding of the true DWFs and their effects on the cross section is needed.

Ideally, a match between tabulated cross sections and experiment would reveal a first approximation model, which would then be simulated and compared to the original experimental image. This could then be iterated until a converged structural and compositional solution can be found.

9.2.4 Improvements on damage limitation

Beam effects have been shown to be of great concern. High accelerating voltages result in knock-on displacement of the less tightly bound surface atoms, especially at edges. However lower accelerating voltages have in practice, reduced spatial resolution, and one of the key requirement of the cross section analysis is that columns are well-resolved so that cross-talk effects, which are difficult to account for, are minimal. Where the background between columns is high, the cross section analysis overestimates the scattering from individual columns. The continual push to improve electron optics and microscope stability should render this less problematic in future.

In addition, particles are regularly seen to reconstruct under the beam, giving rise to questions of the fidelity of the image with the real sample. If material is lost during the acquisition of EDX maps, especially where the maps are cycled to increase count statistics, then the associated error in the quantification needs to be taken into account for a true column-by-column compositional analysis.

Decreasing the overall dose on the particle, allowing it to relax between successive scans are all possibilities to mitigate these effects. Lowering the temperature to “freeze” structures could be a route to circumventing this, though temperature changes would also result in potential structural changes and different DWF might be necessary for the simulations.

9.2.5 Improvements on EDX

Simulations of EDX generation have often been neglected in the literature. Further work to enhance the understanding of the detected spectra using available software such as the DTSA and Monte Carlo methods could add insight into the quantification. Currently, EDX is most popularly modelled for bulk samples. Theoretical modelling of the cross section of ionisation and real absorption and florescence effects in thin samples would also be interesting. While these considerations are minimal given the current limitation of signal to noise, they could prove necessary as detectors improve and count rates increase.

While experimental Cliff-Lorimer k-factors from known alloy calibration samples would decrease the error in quantification, in practice a ζ-factor calibration with a pure element wedge sample is a better

alternative to characterising a microscope's EDX detection system for a particular element and sample geometry, as it gives similarly good errors of 1% in the quantification and also provides an easier method of calibration.

9.3 Outlook

Combining the matching of absolute scattering cross sections with high resolution EDX maps is, in the author's opinion, the path to successful atom-by-atom compositional mapping. This thesis has developed the methodology and shown a proof of principle. The next steps towards this goal now is to limit the aforementioned errors and applying the cross section and EDX quantification techniques to the same Pt-Pd particle viewed in two or more orientations.

Although discrete tomography was not successful in the current work due to particle reconstruction under the beam, this is a promising area of development and has been shown in the literature to hold great promise in revealing the 3D structure of embedded model catalysts and single element supported catalysts. So far, it has only been applied to HAADF images. With the addition of compositional information from either EELS or EDX, it may be possible to determine cross-boundary alloying or inter-diffusion between the core and the shell. In addition, other compositional techniques should be explored, such as high resolution EELS of samples of lighter elements.

Ideally, a complete set of data from all scattered signals should be collected: EELS, EDX, HAADF, BF and BS to truly utilise the full power of electron microscopy in analysing core-shell nanoparticle catalysts. Ultimately, a full 3D structural and compositional characterisation of a nanoparticle catalyst in a gaseous environment, perhaps even in a miniature fuel cell in real working conditions, would unlock the true nature of the catalytic process. With the exciting research being carried out in environmental atomic resolution HAADF STEM, this may one day be realised.

Appendices

Appendix A

Other characterisation techniques

A.1 Optical spectroscopy

Optical spectroscopy, including UV-Vis, Raman and infra-red, involves measurement of the elastic/inelastic scattering of a particular incident wavelength of light. UV-Vis spectroscopy can provide information on the electronic structure particularly important for oxide supports or measuring the degree of oxidation within the metallic nanoparticles themselves. Raman spectroscopy is well known as a technique to discriminate between multiple molecular structures whilst infra-red spectroscopy provides important information on identifying surface species [8].

A.2 Inductively Coupled Plasma Emission Spectroscopy (ICP-ES)

ICP-ES is a technique used to determine the concentration of a particular element within a sample. By decomposing the sample using the high temperatures generated by the ICP source, it is possible to determine the compositional distribution of the free atoms and ions by collecting the photons emitted from the excited atoms returning to ground state. It is the most sensitive technique to obtain exact average chemistry of a sample. ICP-MS (mass spectroscopy) version can detect trace elements to parts per billion.

A.3 Scanning Tunnelling Microscopy (STM)

Scanning tunnelling microscopy has long been used as surface sensitive technique which maps the local density of electronic states. In application to nanoparticles, it has been used to show the catalytically important edges, kinks, vacancies and other defects [57], but is only applicable to certain sample geometries and classes of supports [58] and is not suitable for industrial samples supported on amorphous carbon due to large height differences in an irregular structure.

A.4 Atomic force microscopy (AFM)

Atomic force microscopy is, like its precursor scanning tunnelling microscopy, a topographical tool, probing surface layers only [59]. Forces between the nano-scale tip and the sample cause the cantilever on which the tip is mounted to be deflected according to Hooke's law. While AFM can achieve atomic resolution and is useful as a particle size characterisation tool, it is still limited by slow scan times and sample drift and piezo hysteresis, Furthermore, the tip curvature radius needs to be much smaller than both the particle sizes and distances between the particles to allow for accurate characterisation [60].

A.5 Atom probe tomography

Recent advances in field ion microscopy have led to the use of atom probe tomography to study catalyst nanoparticles [61,62] as well as core-shell structures [63]. However, the technique is a destructive one and requires dedicated and involved sample preparation, not suitable for the investigation of industrial catalysts.

Appendix B

Microscope Operating Parameters

	JEOL 3000F	Oxford-JEOL 2200 MCO	JEOL ARM 200F	
Basic Specifications				
Gun	Schottky FEG	ZrO/W (100) Schottky FEG	Cold FEG	Cold FEG
Spherical Aberration Correctors	none	Upper Lower	Upper	Upper
Basic Parameters				
Accelerating voltage (kV)	300	200	80	200
Wavelength (pm)	2.0	2.5	4.2	2.5
Imaging Parameters				
Point resolution (0.61λ/α) (nm)	1.4	0.08	0.08	0.08
Probe convergence semi-angle (mrad)	18	22.5	25	25
Camera length for HAADF STEM imaging (cm)	12	100	6	8
HAADF detector angles (mrad)	90	90 – 180	91 – 170	55 – 170
Analytical Instrumentation				
Spectrometer	Oxford Instruments	JEOL	JEOL	
Detector type	SATW	Si(Li)	SDD	
Take off angle (°)	unknown	unknown	18	
Solid angle of collection (sr)	0.22	0.22	0.22 0.8 (Centuro detector)	

Table B.1 Microscope operating parameters used for the experiments in this thesis. Unless otherwise detailed in the thesis, values are taken from manufacturer's specifications.

Appendix C

Matlab code written to analyse particle size (adapted for HAADF STEM images from [1])

```
% Selecting an image
[file,folder]=uigetfile({'*.bmp';'*.jpg';'*.tif'},'Select an image');
cd(folder);
fc=imread(file(:,:,1));

%Selecting subimages
[N,M]=size(fc);
ns=input('Number ofdivisions=');
or=input('Minimum size=');

x=fix(N/ns); y=fix(M/ns);

for sx=1:x:N-x
        for sy=1:y:M-y
                sp=fc(sx:sx+x-1,sy:sy+y-1);
%Thresholding
                T=graythresh(sp);
                spT=im2bw(sp,T);
                g(sx:sx+x-1,sy:sy+y-1)=spT;
        end
end

g2=imopen(g,strel('disk',or));
[labeled,a]=bwlabel(g2,4);
points=regionprops(labeled,'Centroid','PixelList');
[B,L2,N2]=bwboundaries(labeled,4,'noholes');

%Draw segmentedparticles
imshow(fc);
hold on;

for s=1:numel(points)
        boundary=B{s};
        if(s>a)
                plot(boundary(:,2),boundary(:,1),'g','LineWidth',1);
        else
                plot(boundary(:,2),boundary(:,1),'r','LineWidth',1);
        end
end
hold off

%Histogram
graindata=regionprops(labeled,'basic');
areap=[graindata.Area];
t=0;
for s=1:numel(points)
        t=t+1;
        sizes(t)=2*sqrt(areap(s)/pi);
end

figure; hist(sizes,30)
Mean=mean(sizes)
Standard_deviation=std(sizes)
```

Appendix D

Identification of diffraction spots in a FT (Figure 3.14) by using the angle between spots

Indices	Angle (°)		
	Top grain	***Bottom grain***	***Ideal crystal***
$\bar{2}00$ and $\bar{1}1\bar{1}$	54.3	56.6	54.7
$\bar{1}1\bar{1}$ and $11\bar{1}$	74.2	68.4	70.6
$11\bar{1}$ and 200	52.9	57.6	54.7
200 and $1\bar{1}\bar{1}$	55.1	54.6	54.7
$1\bar{1}1$ and $\bar{1}\bar{1}1$	73.9	66.8	70.6
$\bar{1}\bar{1}1$ and $\bar{2}00$	50.2	54.1	54.7
total	*360.6*	*358.1*	*360*

Table D.1 Table showing angles between the spots of the diffractogram in Figure 4.13

Appendix E

Possible <110> orientations of the particle in Figure 3.13

$[0\bar{1}1]$ 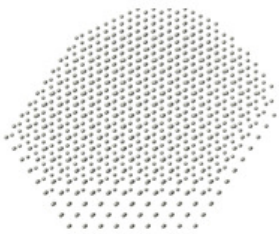	$[1\bar{1}0]$ 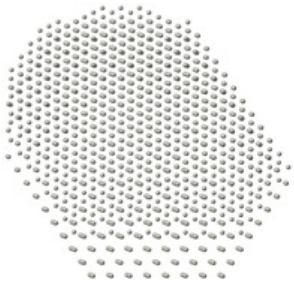
[011] 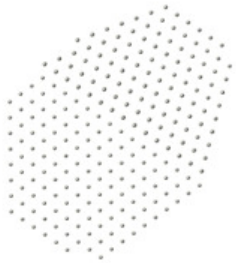	$[10\bar{1}]$ 
[101] 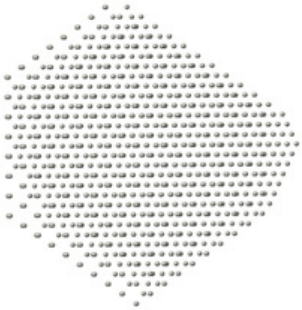	[110] 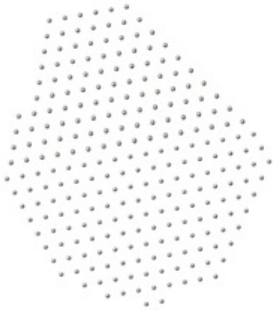

Table E.1 Possible <110> orientations of the particle in Figure 3.13

Appendix F

Recipe for quantification of experiments

Detector Mapping Method for the Oxford-JEOL 2200MCO

1. Without scanning, move the sample so that the probe is going through vacuum (a large hole in the sample).
2. Switch on the TEM lenses below the sample (click 'Alignment' button in the ASID control panel).
3. Use a probe current to map the detector that is 10% of the current used in imaging. This ensures that the same contrast and brightness settings can be used for sample imaging in order to circumvent the nonlinear behaviour of the A/D convertors on standard microscopes with the gain settings.
4. Measure the probe current.
5. Adjust the contrast and brightness settings of the A/D convertor so that the signal is not saturated on the detector and the black level is detectable.
6. Insert the detector
7. Adjust the camera length and post specimen magnification until the detector can be seen.
8. Use post specimen deflectors (e.g. PLA) to shift the detector image to the centre of the screen. Zoom in and adjust the focus until a good map is obtained.
9. Make a note of the brightness and contrast settings.
10. Image the detector using the same exposure and image size that you use for image. Take a several maps at each setting if you use several.
11. Switch back to normal STEM mode with the usual beam current used for imaging.
12. Adjust the brightness and contrast settings to match those used for the detector map.
13. Measure the beam current after every image of the sample. This is particularly important for cold FEG instruments where the current decays with time.

Image Calibration

Using the corresponding detector image to the image to be calibrated, calculate the average pixel intensity, I_D, of the detector pixels. In order to transform the imaged intensity to a fraction of incident beam current, Int_{frac}, the following conversion needs to be performed:

$$Int_{frac} = Int_{Spec} \frac{I_{Det}}{I_{Spec} \times Int_{Det}} \quad \text{F.1}$$

where Int_{Spec} is the unscaled intensity collected from the scattering of the specimen in the raw experimental image; I_{Spec} is the probe current used to image the specimen in the experiment; and Int_{Det} is the mean intensity of the detector response when mapped with a probe current of I_{Det}.

Appendix G

Concerning simulations

G.1 Input for Melbourne Absoprtive Potential Code

Example crystal specification file: "PtPd110.xtl"

```
1     Pt(Pd) Core Shell 110 zone axis
2     20.0000    20.0000    20.0000    90.000     90.0000    90.0000
3             200.00
4           2
5     Pd
6           38 46 1.000 0.005784
7     0.500000   0.568766   0.293702
8     0.500000   0.431234   0.706298
      .          .          .
      .          .          .
44    0.402750   0.500000   0.500000
45    Pt
46          78 78 1.000 0.004835
47    0.500000   0.706298   0.706298
48    0.500000   0.293702   0.706298
      .          .          .
      .          .          .
124   0.597250   0.362468   0.775065
125   1
126         0      0      1
127         1      0      0
128         0      1      0
129          0      0      0
```

Line 1: header that is skipped by the simulation code and is useful for comments describing the crystal

Line 2: dimensions of unit cell in Å (x, y, z) and angles of the unit cell (α, β, γ).

Line 3: accelerating voltage of microscope (kV)

Line 4: number of elements in crystal structure

Line 6: number of atoms; Z number of element; occupancy; mean square displacement value

Line 7+: coordinates of atom in fraction of unit cell, note padding around structure to avoid artefacts from periodic boundary conditions of FFTs

Line 125: end of specification of atomic positions

Line 126-9: direction of the unit cell which describes the beams used in the calculation

Record of inputs to set up simulation:

```
Main menu selection
          1
 Crystal (middle layer) file name
 input1.xtl
 Surface layer file name
 input1.xtl
 Main menu selection
          2
 <1> zone axis,<2> systematic row
          1
 npix in supercell along x
        512
 npix in supercell along y
        512
 no of unit cells along x
         8           // tiling the unit cell to form a supercell
 no of unit cells along y
         8
 Accept summary <1> yes <2> no
          1
 <1> zone axis,<2> systematic row
          1
 npix in supercell along x
        512
 npix in supercell along y
        512
 no of unit cells along x
         8
 no of unit cells along y
         8
 Accept summary <1> yes <2> no
          1
 TDS calculation menu
          1          //adding TDS
 Save form factors <1> yes <2> no
          2          //option to save calculated TDS
 Main menu selection
          3
 Psuedo holz <1> Yes <2> No
          2          //also implements auto slicing of supercell
 Layer 1 thickness
  0.000              //amorphous first layer, set to 0
 Number of subslices z1
          1
 Accept the choices for z1
          1
 Layer 2 thickness
   98.000       //crystalline middle layer, thickness of sample in Å
 Number of subslices in layer 2
          25         //to put atoms at correct heights
 Accept the choices for z2
          1
 force z1=z3
```

```
          1          //amorphous bottom layer
 Spherical Abberration mm
  0.000000000000000E+000
 Use scherzer defocus <1> yes <2> no
          1
 Accept Cs and aperture
          2          //1=yes, 2=no
 New cutoff aperture
   0.9000000000000          //changes convergence angles used
 Accept Cs and aperture
          1
 Use 5th order Cs <1> yes <2> no
          2
 Change probe paramaters <1> no <2> yes
          1
 BWL <1> Yes <2> No
          1          //bandwidth limiting to avoid aliasing
 Shift probe? <1> Yes <2> No
          2    //yes allows scanning of smaller area in supercell
using fractional step sizes to determine location and scan range
 Accept size and orientation of scan vectors
          1          //1=yes
 Main menu selection
          4
 ADF inner angle
   90.0000000000000          //mrad
 ADF outer angle
   180.000000000000          //mrad
 Calculate ADF pot <1>, read in <2>
          1
 Save form factors <1> yes <2> no
          2
 Number of x probe positions
         36          // 4-6 pixels per Å for round atoms
 Number of cells to scan over
          1
 Number of y probe positions
         36
 Number of cells to scan over
          1
 Main menu selection
         11
 STEM xo simulation menu
          1
 Print N slice potentials  <1> yes <2> no
          2
 Output file name
 PtPd_core-shell_110       //output is x by y array of intensities
calculated at each probe position as a fraction of the incident beam
 ADF output menu selection
          2
```

G.2 Sampling in simulations

Typically, the simulations require a 'unit cell' to be tiled, creating a supercell, or a large supercell to contain a nanoparticle to meet adequate sampling criteria. The large real space supercell increases the sampling in reciprocal space.

The real space pixel size Δx must be small enough to resolve the shape of the probe and the atomic columns. A good guide is to use:

$$\Delta x < \frac{d_{probe}}{4} \qquad \text{G.1}$$

where d_{probe} is the probe diameter. However, this is usually trivially met since the reciprocal space sampling requires more pixels.

In reciprocal space, the pixel size Δk should be fine enough to sufficiently sample the probe aberrations, the Fresnel propagator and the scattering potential accurately. A good guide is to have 1mrad sampling of the size objective aperture, which is given by Equation 2.5. For a 25mrad objective aperture forming a probe at 200kV, this corresponds to a 25Å x 25Å supercell.

Since the use of Fourier transforms imposes that the number of pixels in the real space cell and the reciprocal space cell is the same, the choice of the fineness of sampling grid needs to be carefully considered. The number of pixels in one direction N_x must be greater than:

$$N_x > \frac{2ak_{max}}{\lambda} \qquad \text{G.2}$$

where a is the size of the supercell in Å, λ the wavelength of the electrons in $Å^{-1}$ and k_{max} is the maximum angle in radians to which signal is scattered. The calculations described in Chapter 6 have a supercell of 31.12 Å x 31.12 Å sampled by 512 x 512 pixels. This gives a maximum reciprocal space angle of 206mrad, which is much larger than the objective aperture and enough to encompass all the scattering to high angles.

Appendix H

Recipe for analysis of images by cross sections

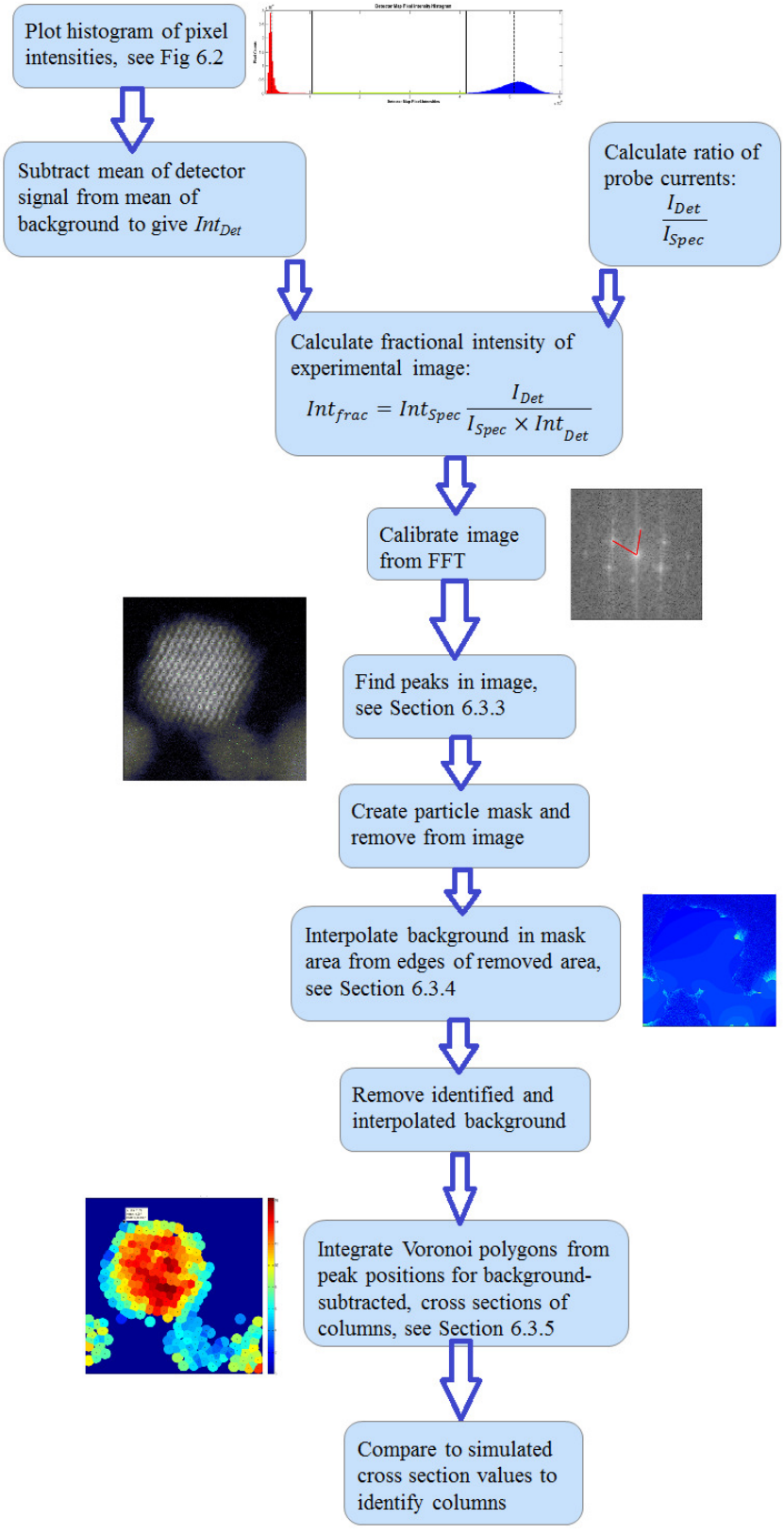

Appendix I

Derivation of the ζ-factor formula in Equation 7.2

The mass-thickness ρt of a sample can be related to the X-ray intensity for an element *A* [4] by:

$$\rho t = \zeta_A \frac{I_A}{C_A D_e} \quad \text{I.1}$$

Where ζ_A is the proportionality factor, I_A is the intensity of the X-ray peak for element *A* which has a concentration C_A in the sample, and D_e is the total electron dose during the acquisition, defined as:

$$D_e = N_e I_{probe} \tau \quad \text{I.2}$$

Where N_e is the number of electrons in the unit electron charge[1] and I_{probe} and τ are the beam currents and acquisition times. The measured X-ray intensity I_A can be theoretically described by:

$$I_A = N_v \frac{Q_A \omega_A a_A}{M_A} C_A \rho t D_e \left(\frac{\Omega}{4\pi}\right) \varepsilon_A \quad \text{I.3}$$

Where is N_v Avogadro's number, Q_A is the ionisation cross section, ω_A is the fluorescence yield, a_A is the relative transition probability (i.e. the relative line weight), M_A is the atomic weight, Ω is the detector collection angle in steradians and ε_A is the detector efficiency.

Combining Equations F.2 and F.3, the ζ-factor can be seen to be

$$\zeta_A = \frac{M_A}{N_v Q_A \omega_A a_A [\Omega/4\pi] \varepsilon_A} \quad \text{I.4}$$

This expression requires the knowledge of several key parameters, which are often difficult to determine. However, from Equation I.1 at two thicknesses 1 and 2:

$$\rho t_1 = \zeta \frac{I_1}{C D_e} \quad \text{I.5}$$

$$\rho t_2 = \zeta \frac{I_2}{C D_e} \quad \text{I.6}$$

[1] This is simply 1/e, the elementary charge, = 6.24 x 10^{18}

The difference gives:

$$\rho t_1 - \rho t_2 = \zeta \frac{I_1}{CD_e} - \zeta \frac{I_2}{CD_e} \quad \text{I.7}$$

$$\rho(t_1 - t_2) = \zeta \frac{(I_1 - I_2)}{CD_e} \quad \text{I.8}$$

Which rearranges to give:

$$\zeta = \rho CD_e \frac{(t_1 - t_2)}{(I_1 - I_2)} \quad \text{I.9}$$

Combining Equations I.2 with I.9 (where C has been assumed to be 1 since the sample is a pure element), the expression for ζ_A is then:

$$\zeta_A = \rho N_e I_{probe} \tau \frac{(t_1 - t_2)}{(I_1 - I_2)} \quad \text{I.10}$$

Appendix J

Background subtraction from Section 7.3.2

Pd L_α @ 2.84keV

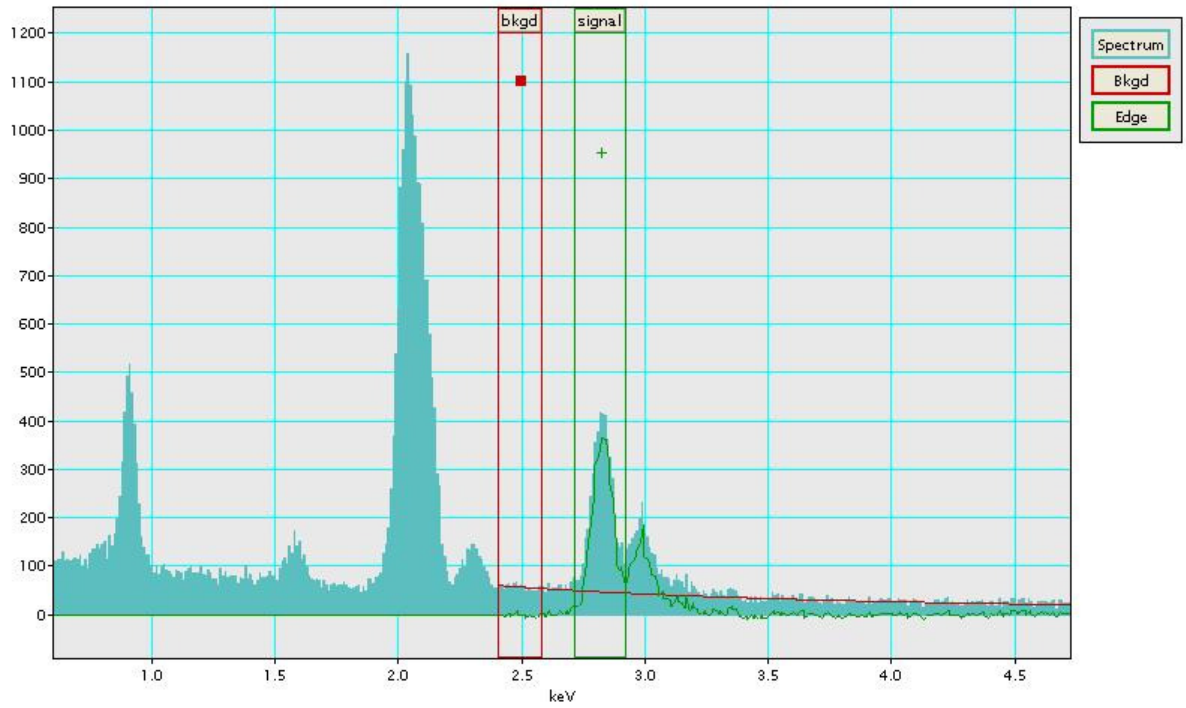

Pd L_β @ 2.99 keV

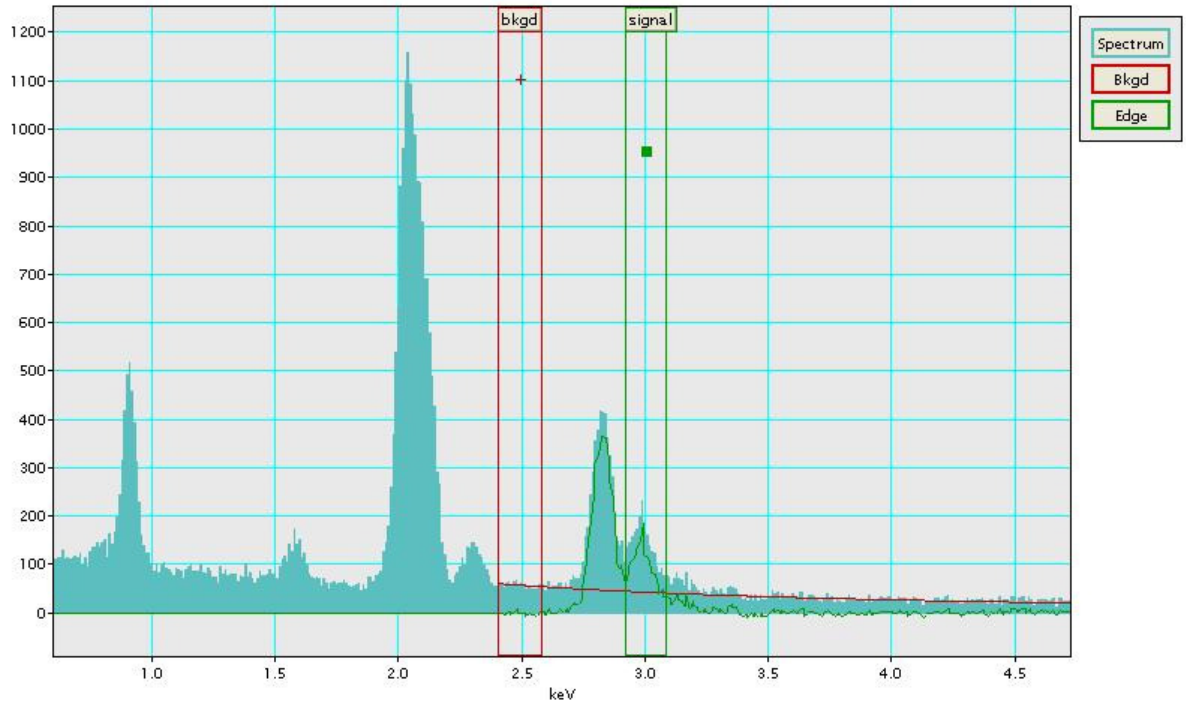

Pt L_{α} @ 9.44 keV

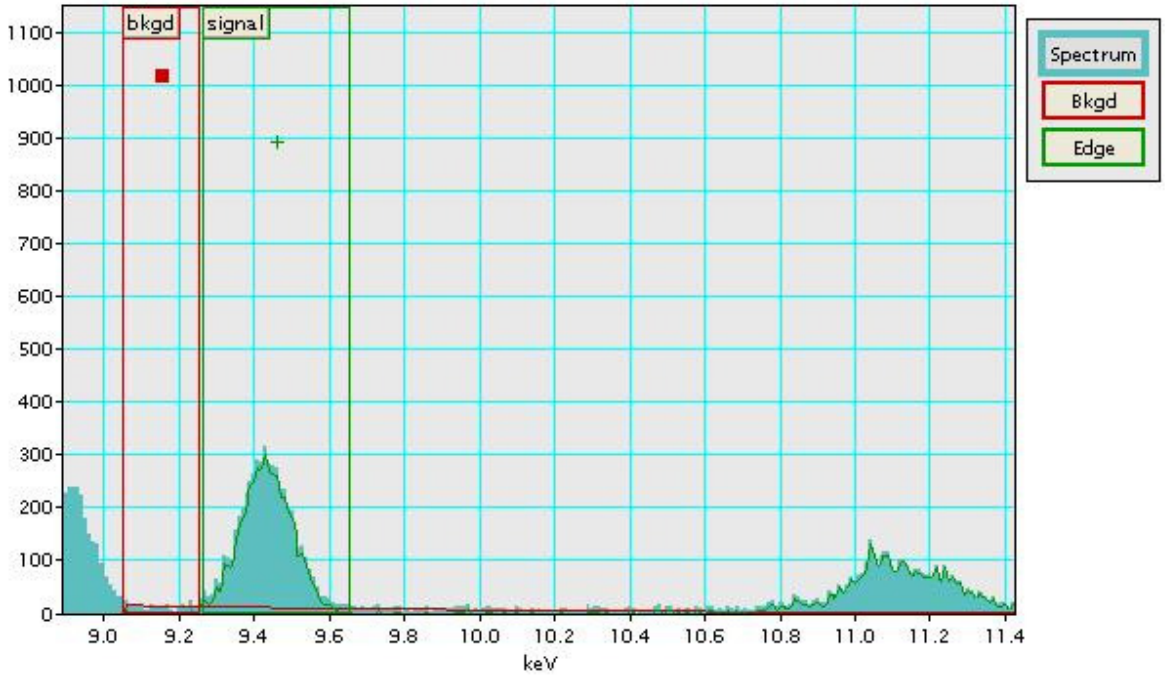

Pt L_{β} @ 11.07 keV